



TECHNISCHE
UNIVERSITÄT
WIEN
Vienna University of Technology

DISSERTATION

The Weyl-Kondo semimetal

$Ce_3Bi_4Pd_3$

Conducted for the purpose of receiving the academic title

“Doktor der Naturwissenschaften”

under the supervision of

Univ. Prof. Dr. Silke Bühler-Paschen

Institute of Solid State Physics

by

Msc. Sami Dzsaber

Matriculation No.: 1525918

Pezzlgasse 72.

1170 Vienna, Austria

Vienna, August 2020

Abstract

Topological phases of matter describe electronic structures that can be continuously tuned into one another while being characterized by a well defined global (topological) invariant. Recently, noncentrosymmetric Weyl semimetals have emerged as one of the few such phases hosting 3D relativistic fermions in the bulk; therein, pairs of Weyl nodes – each node characterized by a well defined Chern number – are stabilized by broken inversion symmetry and strong spin-orbit interaction. So far, Weyl semimetals as well as most other topologically nontrivial phases were studied in noninteracting systems, or in settings that are adiabatically connected to them. On the other hand, exploring topologically nontrivial phases in systems where electron correlation effects are strong may open the way towards entirely new quantum phases. Heavy fermion materials are canonical representatives of strongly interacting electron systems. Therein, a plethora of novel quantum phases emerge due to the Kondo entanglement of conduction electrons and a sublattice of localized magnetic moments. Therefore, they constitute an ideal setting for exploring the interplay of topology and strong electron correlations.

In this work, I show that tuning the spin-orbit interaction in the canonical noncentrosymmetric Kondo insulator $\text{Ce}_3\text{Bi}_4\text{Pt}_3$ via Pd-Pt substitution drives the system into a semimetal. Low-temperature specific heat experiments for the novel Pd end compound $\text{Ce}_3\text{Bi}_4\text{Pd}_3$ demonstrate that this compound hosts Kondo interaction-driven Weyl cones, thus realizing a new groundstate dubbed Weyl-Kondo semimetal. To probe the Berry curvature of $\text{Ce}_3\text{Bi}_4\text{Pd}_3$, zero-field temperature dependent Hall resistivity measurements were carried out. They reveal a giant nonlinear spontaneous Hall effect in this material exposing a diverging Berry curvature at the Fermi energy. Whereas this effect was predicted for time-reversal preserving Weyl semimetals – though with orders of magnitude smaller magnitude than observed here – I show that it features additional terms that are beyond this

theoretical framework, and whose description requires a non-perturbative treatment of the effect. Finally, I present magnetotransport and magnetization experiments of $\text{Ce}_3\text{Bi}_4\text{Pd}_3$ and magnetization experiments of $\text{Ce}_3\text{Bi}_4\text{Pt}_3$, both done in high magnetic fields and at low temperatures. The data evidence that the groundstate of $\text{Ce}_3\text{Bi}_4\text{Pd}_3$ is driven across a two-step quantum phase transition with increasing magnetic field. In the first step, the Weyl-Kondo semimetal state collapses at a topological quantum phase transition. In the second step, the system undergoes an abrupt metallization featuring quantum critical behaviour, thus exposing a Kondo insulator gap underlying the Weyl nodes.

The results discussed in this thesis demonstrate that strong electron correlations can drive new topologically nontrivial electronic phases with properties beyond what could have been anticipated from weakly interacting systems. I anticipate that this insight will trigger further work, both experimental and theoretical, thereby helping to establish correlation-driven electronic topology as a new field of fundamental research, with potential also in quantum applications.

Contents

1	Introduction	5
2	Background	8
2.1	The Kondo effect	8
2.2	The Kondo lattice	10
2.3	Topological classification of matter	14
2.4	Weyl semimetals	18
2.4.1	Theoretical model	18
2.4.2	Experimental signatures	21
2.5	Muon spin rotation and relaxation spectroscopy	24
2.6	Crystal growth from liquids	27
3	Hall effect	30
3.1	Introduction and symmetry aspects	30
3.2	The normal Hall effect	33
3.3	Skew scattering in heavy fermion systems	35
3.4	The anomalous Hall effect	37
3.5	The nonlinear Hall effect	39
3.6	Hall effect in quantum critical systems	42
4	The Kondo insulator $\text{Ce}_3\text{Bi}_4\text{Pt}_3$	44
4.1	Crystal structure	44
4.2	Physical properties	46
4.3	High magnetic field studies	49
5	Results	53
5.1	Tuning the spin-orbit coupling in $\text{Ce}_3\text{Bi}_4\text{Pt}_3$	53

CONTENTS

5.1.1	Introduction and principles	53
5.1.2	Crystal growth of $\text{Ce}_3\text{Bi}_4(\text{Pt}_{1-x}\text{Pd}_x)_3$	56
5.1.3	Structural and chemical characterization of $\text{Ce}_3\text{Bi}_4(\text{Pt}_{1-x}\text{Pd}_x)_3$	62
5.1.4	Electrical transport in $\text{Ce}_3\text{Bi}_4(\text{Pt}_{1-x}\text{Pd}_x)_3$	67
5.1.5	Magnetic susceptibility in $\text{Ce}_3\text{Bi}_4(\text{Pt}_{1-x}\text{Pd}_x)_3$	72
5.1.6	Conclusions	77
5.2	Surface superconductivity in $\text{Ce}_3\text{Bi}_4\text{Pd}_3$	79
5.3	Probing the Weyl-Kondo semimetal state in $\text{Ce}_3\text{Bi}_4\text{Pd}_3$	87
5.3.1	The Weyl-Kondo semimetal	87
5.3.2	Specific heat	91
5.3.3	Magnetic field-dependent resistivity	97
5.3.4	Spontaneous Hall effect	102
5.3.5	In search for magnetic phase transition in $\text{Ce}_3\text{Bi}_4\text{Pd}_3$	111
5.3.6	Muon spin rotation experiments	112
5.3.7	Magnetic field dependence of the Hall effect	115
5.3.8	Nonlinearity in the Hall effect	123
5.3.9	Density functional theory for $\text{Ce}_3\text{Bi}_4\text{Pd}_3$	133
5.3.10	Discussion	135
5.4	Collapse of the Weyl-Kondo semimetal state in $\text{Ce}_3\text{Bi}_4\text{Pd}_3$ in high magnetic fields	143
5.4.1	Magnetic field-dependent electrical resistivity	143
5.4.2	Hall effect and quantum criticality	151
5.4.3	Torque magnetometry	160
5.4.4	Discussion	165
6	Summary and outlook	169
7	List of abbreviations	173

8 Contributions of collaborators	174
----------------------------------	-----

1 Introduction

The triumph of band theory in solids, put forward by Felix Bloch and colleagues in the 1930's, set grounds for modern solid state physics and formulated a framework to understand and predict electronic properties of materials. Remarkably, this theory proved to be not only correct but quantitatively accurate (in case of simple metals), despite taking only the electron's kinetic energy into account, and completely neglecting the Coulomb interaction between electrons. Yet, more and more compounds emerged such as Mott insulators and heavy fermion compounds, where such a simple, single electron approach breaks down, and where including the electron-electron interaction is essential to understand the microscopic mechanism stabilizing their ground state. Among the many families of compounds hosting strongly interacting electrons, heavy fermion systems stand out due to their remarkable richness of novel ground states and phenomena. In these systems, the Kondo interaction between itinerant electrons and localized magnetic moments leads, at low temperatures, to the formation of a truly quantum manybody ground state with extremely heavy fermionic quasiparticles, whose mass can be enhanced by orders of magnitude over the free electron mass (hence their name). Most intriguingly, due to the competing energy scales that typically govern these systems (Kondo vs. RKKY), the ensuing richness in novel physics exceeds by far that of a simple renormalized band picture. Tipping the balance between the low-energy scales of these systems, which can be frequently achieved by readily accessible tuning parameters (such as magnetic field or pressure) realizes many novel quantum states of matter such as "strange metals" or unconventional superconductors. Thus, starting from the initial experimental work on dilute Kondo systems in the 1930's, through the discovery of heavy fermion superconductivity in the 1970's, via the study of quantum criticality in the last two decades, heavy fermion systems still continue to be a fertile ground of novel physics and phenomena. Certainly,

many new and exotic effects await identification.

In parallel to the advances in strongly correlated electron systems, another major progress beyond a simple band classification of solids – albeit still within a single particle picture – was put forward by the theory of topology and topological classification of matter. Motivated by the remarkable discovery of the quantum Hall effect in 1982 by von Klitzing *et al.*, it was quickly realized that the quantum mechanical geometrical phase (also known as the Berry phase) of an electron in a solid gives rise to fundamentally new quantum phenomena on a macroscopic scale, similar to superconductivity and Bose-Einstein condensates. At the heart of these systems are degenerate electronic states that disperse like massless, ultrarelativistic particles, similar to light. The richness of novel quantum states of matter and related phenomena that followed with the discovery of graphene, topological insulators and Dirac and Weyl semimetals, led to a spectacular proliferation of this field, and put topology (traditionally a discipline of mathematics) at the spearhead of modern condensed matter physics. Discoveries include quantum phenomena such as the spin Hall effect or high mobility protected electrical transport that are the working principles of next generation electronic technologies, but also the detection of massless chiral Weyl fermions, long sought for in high energy physics.

The investigation of topology in condensed matter systems has so far focused on weakly interacting systems. However, introducing strong electron correlations is expected to further expand the horizon as far as novel states of matter are concerned, the same way it did for topologically trivial systems. In this quest, heavy fermion systems are ideal candidates due to their extreme correlation strength. Thus exploring the nontrivial topology of these systems is of great interest. Initial studies – focused on exploring topological surface states in the Kondo insulator SmB_6 – proved to be challenging, and provided in part ambiguous and conflict-

ing results. Exploring topologically nontrivial states in Kondo semimetals, on the other hand, represents an entirely different approach, where novel topological responses and phenomena are expected in the bulk.

The focus of this thesis is to explore the interplay of strong electron interactions and electronic topology as shown in Fig. 1. Emphasis is given to novel phenomena beyond a simple noninteracting picture. In the first part of the thesis, I show that the spin-orbit coupling strength can be readily tuned by Pd-Pt substitution in the Kondo insulator $\text{Ce}_3\text{Bi}_4\text{Pt}_3$. This tuning is a powerful way to search for electronic states with nontrivial topology, as was done in the case of the topological insulator $\text{Bi}_x\text{Sb}_{1-x}$. I show, that as a result a novel, strongly interacting ground state emerges that is neither insulating nor metallic, and the emergence of which can be directly attributed to the change of the spin-orbit coupling strength. In the second part of the thesis, I address this novel ground state by means of thermodynamic and electrical transport probes, and show that it represents a topologically nontrivial, strongly interacting Weyl semimetal state dubbed Weyl-Kondo semimetal. In particular, I discuss the transport evidence of topologically nontrivial states detected in the Hall response of $\text{Ce}_3\text{Bi}_4\text{Pd}_3$, and discuss that this state is not adiabatically connected to a noninteracting Weyl semimetal. Finally, in the third and last part, I present a high magnetic field study of $\text{Ce}_3\text{Bi}_4\text{Pd}_3$. I show that the small energy scales present in this compound are readily tuned by accessible magnetic fields, revealing the richness of its phase diagram, and the underlying mechanism stabilizing the Weyl-Kondo state.

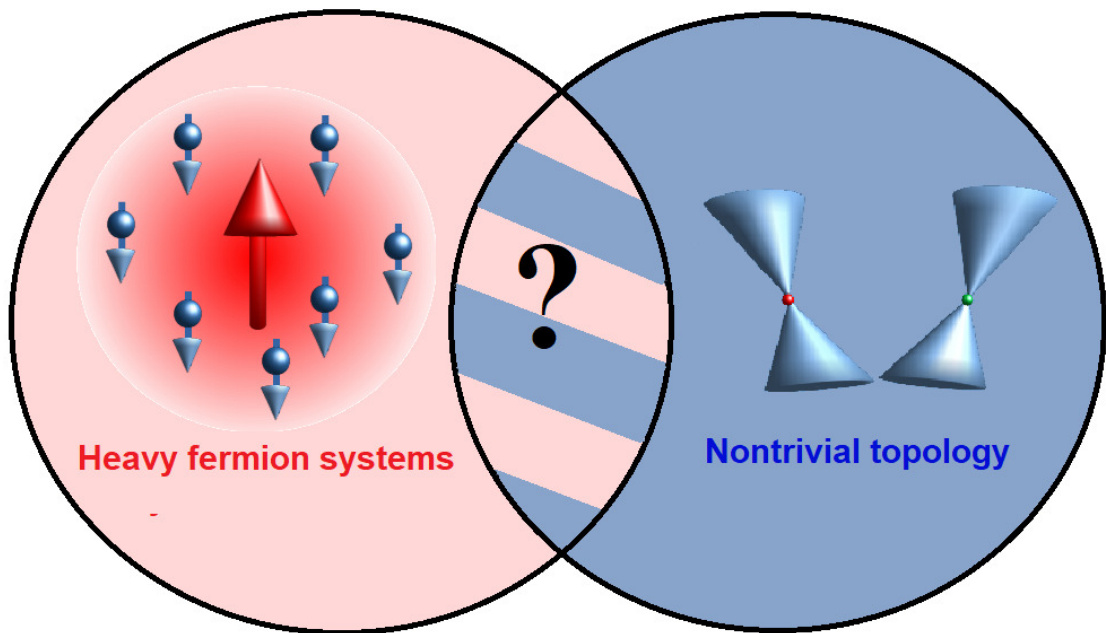


Figure 1: The aim of this work to explore the interplay of strong electron interaction in heavy fermion systems and nontrivial topology.

2 Background

2.1 The Kondo effect

Conventional electron scattering mechanisms in simple metals such as electron-impurity, electron-phonon and electron-electron scattering result in resistivities that decrease with decreasing temperature. It thus came as a surprise, when early experiments on the low-temperature resistivity of certain metals evidenced a local minimum of the electrical resistivity followed by a logarithmic increase as temperature further decreased [1]. The first model to successfully address this puzzling observation was the single-ion Kondo model [2]. Recognising that such a minimum correlates with the presence of magnetic impurities, Jun Kondo demonstrated that second order perturbation theory of the antiferromagnetic $s - d$ model, with the

Hamiltonian

$$H_{s-d} = J\boldsymbol{\sigma}(\mathbf{r}) \cdot \mathbf{S} , \quad (1)$$

indeed leads to a $\rho(T) \sim -\log T$ contribution, in agreement with the experimental results [2]. Here J is the coupling constant, $\boldsymbol{\sigma}(\mathbf{r})$ is the spin density of the conduction electrons and \mathbf{S} is the spin of the localized moment. Subsequent theoretical work by Abrikosov *et al.* [3] has identified a characteristic temperature T_K , the Kondo temperature, as given by

$$k_B T_K = D e^{-1/2Jg(E_F)} , \quad (2)$$

where $g(E_F)$ is the electronic density of states at the Fermi energy, and $k_B T_K$ the characteristic energy scale of the Kondo interaction. Jun Kondo's original (perturbation theory) approach holds only for $T \gg T_K$. The regime $T \ll T_K$ represents a strong-coupling regime, where conduction electrons screen the spin of the magnetic moment to form a many-body nonmagnetic singlet state [4] (Fig. 2 a).

A related model for the interaction of magnetic impurities with conduction electrons is the Anderson model [4]

$$H = \sum_{\mathbf{k},\sigma} \epsilon_{\mathbf{k}} c_{\mathbf{k},\sigma}^\dagger c_{\mathbf{k},\sigma} + \sum_{\sigma} \epsilon_d n_{d,\sigma} + U n_{d,\uparrow} n_{d,\downarrow} + \sum_{\mathbf{k},\sigma} \left(V_{\mathbf{k}} c_{d,\sigma}^\dagger c_{\mathbf{k},\sigma} + V_{\mathbf{k}}^* c_{\mathbf{k},\sigma}^\dagger c_{d,\sigma} \right) . \quad (3)$$

Here the first term is the usual kinetic energy of the conduction electrons, the second term is the bare energy of the d -electrons that represent the localised species, the third term describes the interaction between d -electrons by an onsite-interaction term U , and the last term captures the interaction between the conduction and d -electrons with an amplitude $V_{\mathbf{k}}$. For a large U and in the local moment limit ($n_d \approx 1$) this model was shown to be equivalent to the antiferromagnetic Kondo model [6]. At low temperatures, the formation of the Kondo singlet, that

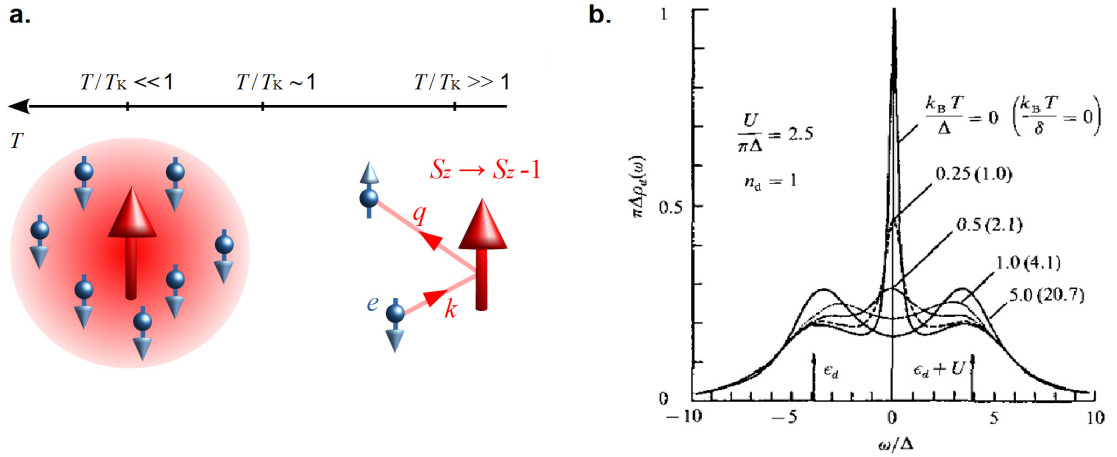


Figure 2: **The Kondo effect.** **a:** Crossover of the Kondo effect from weak ($T/T_K \gg 1$) to the strong ($T/T_K \ll 1$) coupling regimes as temperature is lowered. Incoherent scattering at high temperatures crosses over to a nonmagnetic singlet where the local moment (red arrow) is screened by conduction electrons (blue arrows). k , q and S_z denote electron wavevectors and the local moment spin state, respectively. **b:** Spectral density of the Anderson model (Eqn. 3) at various temperatures. Corresponding to the Kondo-singlet, a many-body Kondo resonance develops at low temperatures. Δ and δ are the widths of the Hubbard bands and Kondo resonance, respectively. Panel **b** is taken from [5].

results also from the Kondo model in treatments beyond the perturbative one, leads to a narrow many-body resonance at the Fermi energy, with a characteristic width of $\delta \sim k_B T_K$ (Fig. 2 b).

2.2 The Kondo lattice

In systems where the localized magnetic moments form a sublattice as opposed to being dilute and randomly distributed impurities, the physical properties at high-temperatures can still be explained with the single-ion Kondo model discussed so far, because in this temperature range incoherent scattering dominates. However, at low temperatures, the sublattice periodicity suppresses the incoherent scattering, and coherent Bloch bands emerge.

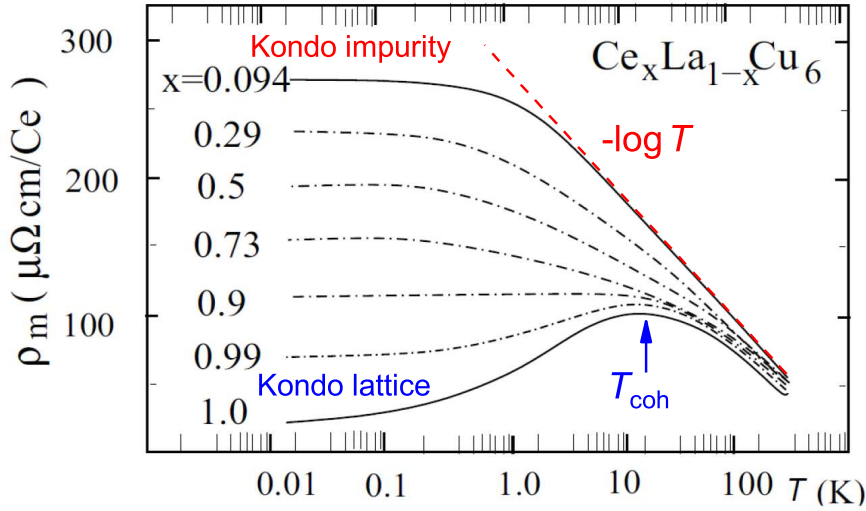


Figure 3: **Temperature-dependent resistivity of $\text{Ce}_x\text{La}_{1-x}\text{Cu}_6$.** For $x = 1$, the system represents a Kondo lattice. In the coherent regime below T_{coh} , the $-\log T$ behaviour turns into a metallic behaviour. Figure adapted from [7].

As a result, the $-\log T$ trend in $\rho(T)$ turns into the usual metallic behaviour (with the resistivity decreasing with decreasing temperature) below a characteristic coherence temperature T_{coh} (Fig. 3) [7]. A cartoon of the band picture with d -electrons derived flat band pinned to the Fermi energy and hybridizing with the conduction electron band is shown in Fig. 4.

As a result, a gap Δ opens in the Kondo resonance peak with a characteristic scale of $\Delta \sim k_B T_K$ (Fig. 4) [8]. The enhanced density of states then manifests as a sizeable increase in the quasiparticle effective mass (Fig. 4), reaching up to $m^* \sim 1000 m_e$, where m_e is the bare electron mass. Such a heavy fermion state is realized in numerous iso-called heavy fermion compounds. Therein, $4f$ ($5f$) electrons residing on a sublattice of lanthanide atoms such as Ce or Yb (actinide such as U) represent the localized species (d -electrons in the above discussed models). Such a sublattice is located in a metallic host (typically containing transition metals) that provides the broad conduction band.

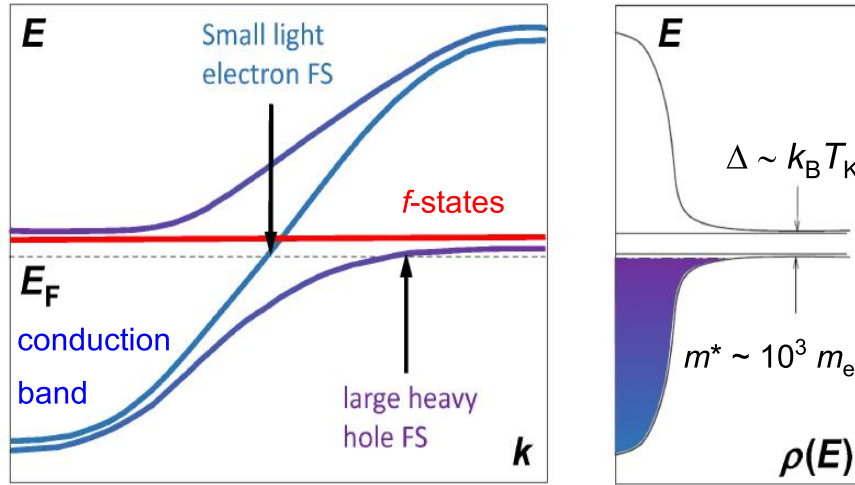


Figure 4: **Cartoon of the Kondo lattice band structure.** The hybridization of a wide conduction band (blue) with localized-electron derived flat-band. The localized states (d -states in the Kondo and Anderson models discussed above) typically represents f -electrons of certain lanthanides (actinides). The hybridization gives rise to a large Fermi surface of coherent, heavy quasiparticles dubbed heavy fermions. The corresponding density of states displays a Kondo resonance similar to the single-ion case (Fig. 2 b) but now featuring a gap Δ , which is in the order of magnitude of the Kondo energy $k_B T_K$. The enhancement of the density of states manifests as an increased quasiparticle mass m^* , that was experimentally shown to reach values as large as $\sim 1000 m_e$. Figure adapted from [8].

At low temperatures, the ground state of heavy fermion metals are usually well described by Fermi liquid theory where the electrical resistivity, heat capacity and magnetic susceptibility follow the forms

$$\rho(T) = \rho_0 + AT^2, \quad (4)$$

$$C(T) = \gamma_0 T, \quad (5)$$

$$\chi(T) = \chi_0. \quad (6)$$

The coefficients A , γ_0 and χ_0 are enhanced via the strongly enhanced quasiparticle

mass. This boosts the physical properties described in Eqns. 4-6 to a level where the low-temperature properties are dominated by the Fermi liquid behaviour. For example, only in heavy fermion compounds is the A -coefficient large enough to overcome the $\sim BT^5$ contribution of electron-phonon scattering.

An aspect not addressed so far is that in addition to the Kondo interaction, also the inter-moment RKKY interaction needs to be considered in (dense) Kondo lattice systems [9]. The competition between these two energy scales makes these system responsive to external stimuli such as magnetic field or pressure. It allows to tip the balance between different ground states, most typically a fully Kondo-screened paramagnet and an (itinerant or local-moment) antiferromagnet. The continuous suppression of magnetic order at a quantum critical point (QCP) leads to quantum critical fluctuations, that lead to non-Fermi liquid behaviour. Particularly interesting is the situation where the ordered phase is not itinerant, with a spin-density wave order parameter [10, 11], but features local moments. This requires Kondo destruction to occur at the QCP [12]. The main characteristic of such a Kondo destruction QCP is that it involves critical electronic modes, and defines an additional temperature scale T^* associated with the Kondo destruction of the ground state [12, 13].

Finally, in some Kondo lattices, the Fermi energy falls within the hybridization gap, giving rise to a strong correlation-driven insulating state known as the Kondo insulator [16]. The salient features of such systems are the simultaneous quenching of the spin and charge degrees of freedom at low temperatures. The hybridization gap gives rise to an activated temperature-dependent resistivity and a suppression of the magnetic susceptibility [16]. A more detailed discussion of the archetypal Kondo insulator $\text{Ce}_3\text{Bi}_4\text{Pt}_3$ is presented in Sect. 4.2.

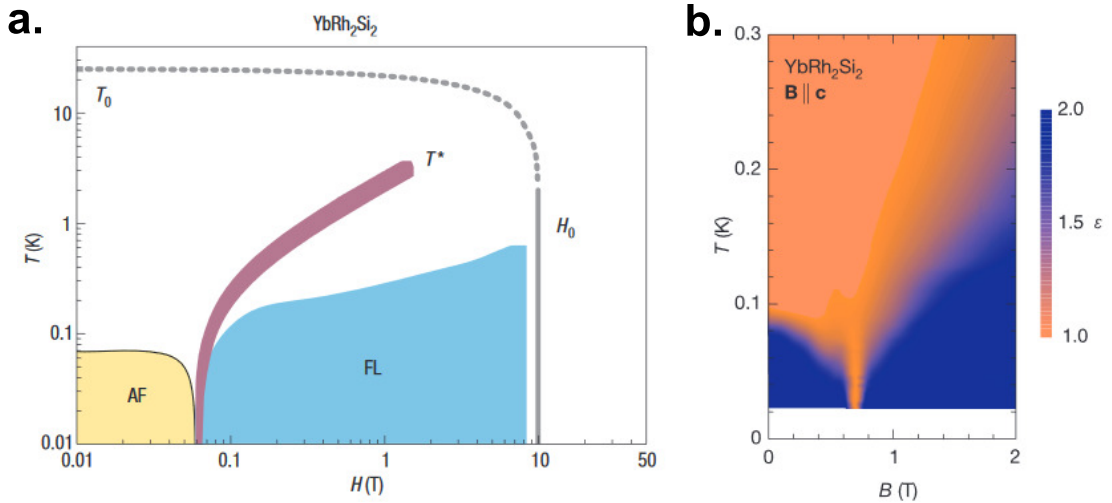


Figure 5: **Unconventional quantum criticality in heavy fermion systems.** **a:** Temperature – magnetic field phase diagram of the heavy fermion compound YbRh_2Si_2 for fields along the crystallographic c direction. It features a Kondo destruction QCP at $B = 70$ mT separating an antiferromagnetic (AF) phase from a paramagnetic phase where Fermi liquid (FL) behaviour is seen below a certain temperature. Across the scale T^* the static Kondo screening is destroyed. **b:** The resistivity exponent ϵ of the measured $\rho \sim T^\epsilon$ law in the same phase diagram as panel **a**. Non-Fermi liquid behaviour with $\epsilon = 1$ emerges from the QCP, in a background of Fermi-liquid behaviour ($\epsilon = 2$). Panels **a** and **b** are taken from [14] and [15], respectively.

2.3 Topological classification of matter

Condensed matter systems are traditionally classified into phases dictated by spontaneously broken symmetries [17]. An important step in the way beyond this paradigm was provided by the remarkable discovery of the quantum Hall effect by von Klitzing *et al.* [18], which demonstrated a robust quantization of the Hall resistivity in a 2D electron gas with an unprecedented accuracy, and most notably, without any apparent breaking of the system’s symmetries. Subsequent theoretical investigations showed that it is in fact the Bloch electron’s well-defined geometrical phase that provides the key for understanding these phenomena [19]. These

advances uncovered a novel classification scheme of matter that is based on the topology of the system under consideration. In this section, I will present the basic concepts.

Topology is an abstract mathematical discipline that describes properties of space that remain unchanged upon continuous deformation such as stretching and bending.

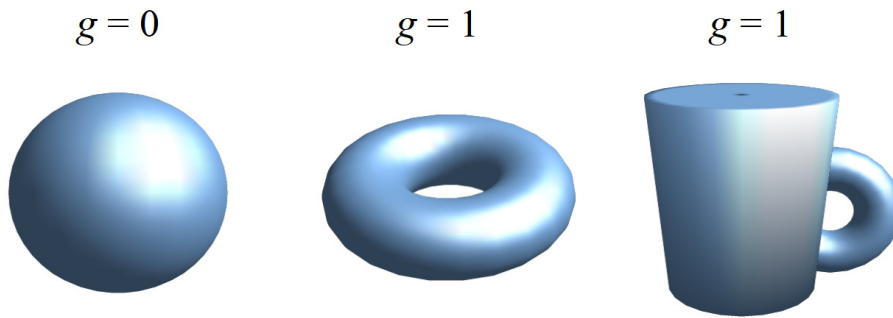


Figure 6: **Concept of topology.** Topological classification of a sphere, a torus and a mug characterized by their genus g (number of holes). Whereas a sphere and a torus are topologically distinct ($g = 0$ and $g = 1$, respectively), a torus and a cup are topologically equivalent. The latter two can be transformed continuously into one another without encountering singularities (creating or destroying holes).

For example, the continuous deformation of a sphere into a torus is not possible, as a singularity is encountered in the form of creating a hole (Fig. 6). Thus, these two objects are topologically distinct. On the other hand, a torus and a mug are topologically equivalent (Fig. 6), as no such singularity is encountered. Generally, a topological class is characterized by the existence of a well-defined topological number, which in the previous example corresponds to the genus (number of holes) of the various objects. This number then remains invariant upon continuous deformations.

In condensed matter systems, topological classification was first introduced for 2D insulators. Based on their Bloch-Hamiltonian $H(\mathbf{k})$, they can be classified

into topological phases that are continuously deformed into one another without closing of the gap [20]. Each of these topological phases are then characterized by a well-defined topological invariant. For example, in the case of the quantum Hall state [19] and related Chern insulators [21], such a topological invariant is the Chern number C_n , that assumes a nonzero value. It is defined as the surface integral of the Berry curvature [22]

$$\mathbf{\Omega}_n(\mathbf{k}) = i \nabla_{\mathbf{k}} \times \langle u_n(\mathbf{k}) | \nabla_{\mathbf{k}} | u_n(\mathbf{k}) \rangle , \quad (7)$$

over the Brillouin zone (BZ) so that

$$C_n = \frac{1}{2\pi} \int_{\text{BZ}} \mathbf{\Omega}_n(\mathbf{k}) d\mathbf{k}^2 . \quad (8)$$

Here n indicates the band index and $|u_n(\mathbf{k})\rangle$ the corresponding Bloch wavefunction at a wavevector \mathbf{k} . As can be seen from Eqn. 8, C_n is a measure of the Berry flux in the Brillouin zone, and is interpreted as the Berry phase [22] of the Bloch state divided by 2π .

Because the transition between two distinct topological phases occurs via a quantum phase transition where the gap collapses, interfaces of such systems are particularly rich in novel quantum phenomena. For example, since the adjacent vacuum to a quantum Hall state ($n \geq 0$) has a Chern number $n = 0$, the gap collapse at their interface gives rise to chiral, conducting edge states (Fig. 7 a-b). Such edge states are required by the bulk topology of the system, known as the bulk-edge correspondence and, thus, are protected against scattering. It is this topological protection that drives the precise quantization of the Hall conductance and maintains dissipationless electron transport [23] (Fig. 7 c).

Motivated by the quantum Hall effect and Chern insulators, topologically non-trivial phases of matter were demonstrated in time-reversal symmetric setting and

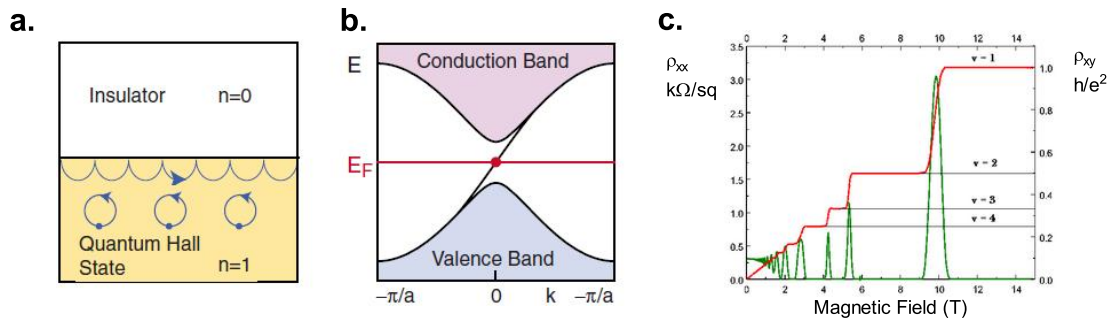


Figure 7: **Topology of the quantum Hall effect.** **a:** Schematic draw of the quantum Hall state at the interface of a trivial insulator such as the vacuum. Closed orbits around an external magnetic field (blue circles) are disrupted at the edge forming a chiral, 1D conduction channel. Here n denotes the Chern number of the medium. **b:** Corresponding schematic bandstructure displaying a chiral edge state that crosses the Fermi energy. **c:** Quantization of the Hall resistivity (red, right axis) in the universal units of h/e^2 . Each plateau is accompanied by dissipationless edge conductivity where the bulk resistivity vanishes (left axis, green). Panels **a** and **b** are adapted from [20]. Panel **c** is taken from [24].

higher dimensions. For example, the spin-orbit interaction driven band inversion in Z_2 topological insulator allows to define a topological number ν beyond the Chern number n (that is zero for these systems) [25]. The bulk-boundary correspondence in these systems drives spin polarized edge states, such as in the case of gate tuned HgTe/CdTe heterostructures [26]. A related topological number in three dimensional topological insulators, on the other hand, drives metallic surface states with well-defined spin texture [27]. Early representatives of this novel state of matter were $\text{Bi}_{1-x}\text{Sb}_x$ [28] and Bi_2Se_3 [29] bulk crystals as shown by bandstructure calculations and angle-resolved photoemission spectroscopy (ARPES) experiments.

Finally, the topologically equivalent classes discussed so far are defined in the presence of a gap. Thus, the identification of such phases in itinerant systems is not straightforward. Whereas ungapped, itinerant systems may form topological

classes in a sense that certain features in their band structure are stable against continuous deformations. In the next section, I present such a phase known as the Weyl semimetal.

2.4 Weyl semimetals

2.4.1 Theoretical model

In solids with two relevant orbitals, the Hamiltonian of the resultant bands is uniquely given by a linear combination of the Pauli matrices so that [30]

$$H(\mathbf{k}) = f_1(\mathbf{k})\sigma_x + f_2(\mathbf{k})\sigma_y + f_3(\mathbf{k})\sigma_z , \quad (9)$$

where the $f_i(\mathbf{k})$ are general functions. The corresponding bandstructure then features an energy gap of

$$\Delta(\mathbf{k}) = \sqrt{f_1^2(\mathbf{k}) + f_2^2(\mathbf{k}) + f_3^2(\mathbf{k})} . \quad (10)$$

The aspect defining the Weyl semimetal physics are points in k -space where the two bands are degenerate. It is realised for \mathbf{k}_0 values where the gap closes, $\Delta(\mathbf{k}_0) = 0$, which requires that all $f_i(\mathbf{k}_0)$ terms in Eqn. 10 simultaneously vanish (Fig. 8). Notably, when introducing perturbations to the Hamiltonian (e.g., via a tuning parameter) such degeneracy points persist robustly, and are merely displaced in the Brillouin zone [30] (Fig. 8 b).

The low-energy sector in the vicinity of such points is then obtained by linearising the Hamiltonian in Eqn. 9, yielding [30]

$$H(\mathbf{k}) = \sum_{i=1, 2, 3} \hbar v_i \mathbf{q} \sigma_i . \quad (11)$$

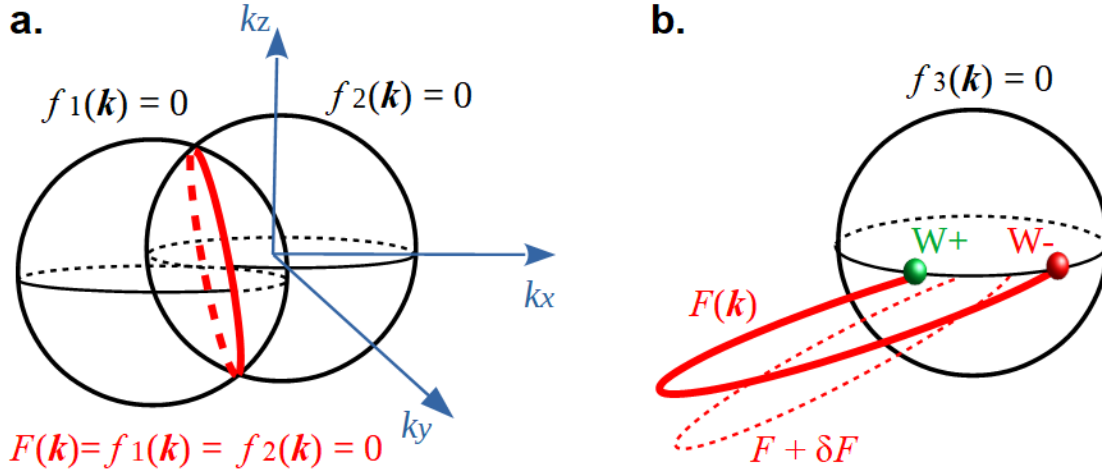


Figure 8: **Accidental degeneracies in a 3D.** **a:** The intersection of the two surfaces (black spheres) that describes the $f_{1,2}(\mathbf{k}) = 0$ conditions, respectively (Eqn. 10), define the curve $F(\mathbf{k})$ in 3D (red). **b:** The simultaneous condition of $f_{1,2,3}(\mathbf{k}) = 0$ holds at the intersection of $F(\mathbf{k})$ and $f_3(\mathbf{k}) = 0$. It defines (pairwise) Weyl points W^+ and W^- (green and red dots, respectively). A change in the Hamiltonian leads to the shift of $F(\mathbf{k})$ by δF (red dashed line), and the mere displacement of the Weyl nodes.

Here $\mathbf{v}_i = \partial f_i(\mathbf{k})/\partial \mathbf{k}$ are the quasiparticle velocities and $\mathbf{q} = \mathbf{k} - \mathbf{k}_0$ is the k -space distance measured from the degeneracy point. The effective Hamiltonian in Eqn. 11 has the form of the Weyl Hamiltonian that describes mass-less, ultrarelativistic Dirac fermions with well-defined chirality $\chi = \pm 1$ [31].

The robustness of the Weyl nodes is deeply rooted in the topological properties of Weyl semimetals. The Berry curvature $\mathbf{\Omega}(\mathbf{q})$ around a single Weyl node goes as $\mathbf{\Omega}(\mathbf{q}) = \mathbf{q}/(2q^3)$ [22, 32]

Then, it follows directly that the integral over any closed Fermi surface (FS),

$$\int_{\text{FS}} d^2\mathbf{q} \mathbf{\Omega}(\mathbf{q}) = \pm 2\pi n, \quad (12)$$

yields an integer valued topological index n , that is ± 1 if the FS encloses a Weyl node, and 0 otherwise. Thus, it is this Gauss law that captures the topological

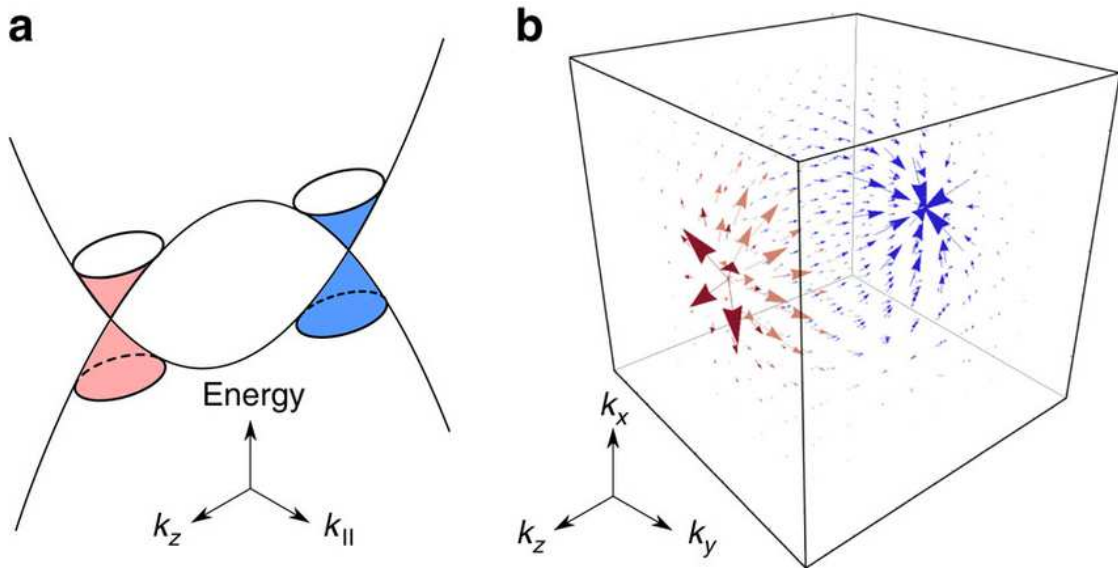


Figure 9: **Berry curvature structure of a Weyl semimetal.** **a:** Schematic of a pair of a Weyl and anti-Weyl nodes **b:** The Berry curvature distribution in the Brillouin zone shows sinks and sources (monopoles) at the Weyl points. The figure is taken from [33].

stability. It detects a Weyl point through its Berry monopole that disappears only if another Weyl node with an opposite charge enters the surface integral. As this surface can be arbitrarily small, Berry monopole charges disappear only when two Weyl nodes with opposite chiralities meet, at which point they annihilate and a gap opens in the bandstructure.

Finally, the arguments presented so far inherently exploit the fact that the spin degree of freedom is frozen out. As a consequence, Weyl nodes discussed so far are expected in systems that break either time-reversal or inversion symmetry [30]. For example, in the noncentrosymmetric zincblende structure, the interplay of spin-orbit interaction and inversion symmetry breaking was demonstrated to stabilize a Weyl semimetal state over a broad range of parameter values [34] (Fig. 10).

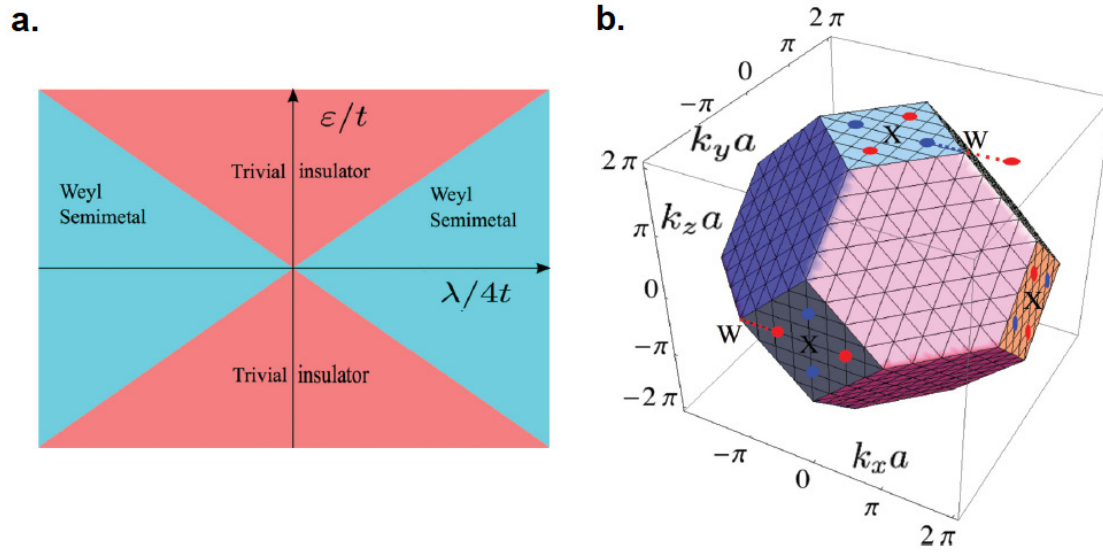


Figure 10: **Noncentrosymmetric Weyl semimetals.** **a:** The phase diagram of the noncentrosymmetric zincblende model as function of the inversion symmetry breaking and spin-orbit interaction parameters ϵ and λ , respectively [34]. Both are measured in units of kinetic energy, t and $4t$, respectively. The Weyl nodes are stable over a broad range of parameters. **b:** Position of Weyl node pairs of opposite chiralities (blue and red dots) in the Brillouin zone of the zincblende lattice. The nodes correspond to a specific value of ϵ and λ in the Weyl semimetal phase. Panels **a** and **b** are taken from [34].

2.4.2 Experimental signatures

Key techniques in the search for novel Weyl semimetals have been the identification of Weyl nodes in density functional theory (DFT) bandstructure calculation of candidate materials [35–38], followed by the direct confirmation of the Weyl bands using ARPES [37–39]. In addition, the nontrivial topology of these systems gives rise to novel quantum phenomena that go beyond the standard textbook description of conductors. In this section, I will address three salient topological responses of Weyl semimetals: the chiral anomaly, Fermi arc mediated transport and the anomalous Hall effect.

Although the chirality is a good quantum number for Weyl fermions, the si-

multaneous pioneering works by Adler, Bell and Jackiw demonstrated that the conservation of the chiral current breaks down under the action of a weak electromagnetic field [40,41]. This anomaly, known as the Adler-Bell-Jackiw (ABJ) anomaly (or simply the chiral anomaly), has been extended to Weyl fermions in condensed matter systems [42] (Fig. 11 a), where it manifests as an additional longitudinal magnetoconductivity

$$\sigma(B) = \sigma_0 + \frac{e^4 B^2 \tau_a}{4\pi^2 g(\epsilon_F)}, \quad (13)$$

that is absent in the transverse configuration [30].

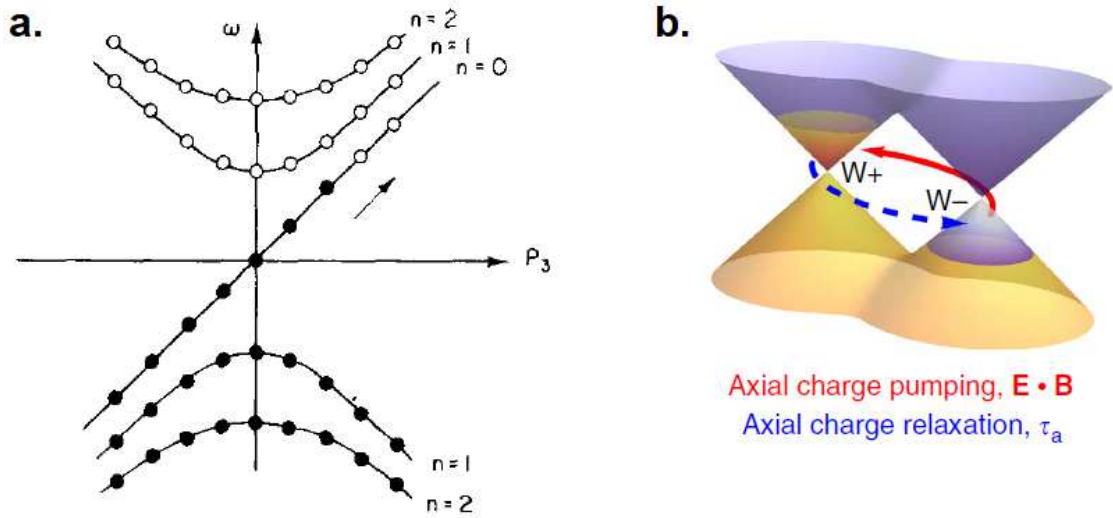


Figure 11: **The chiral anomaly in Weyl semimetals.** **a:** For a Weyl cone in a magnetic field along the p_3 direction, the lowest Landau level ($n=0$) remains chiral, and crosses the Fermi energy. Applying a parallel electric field ($\mathbf{E} \parallel \mathbf{B}$) creates chiral fermions on that Landau level (arrow). **b:** For a pair of Weyl cones, the axial charge pumping described in panel **a** is compensated by the axial relaxation rate τ_a . It creates a steady state imbalance of Weyl fermions. Panels **a** and **b** are taken from [42] and [43], respectively.

Here σ_0 is a background conductivity, τ_a is the axial relaxation rate (Fig. 11 b) and $g(\epsilon_F)$ is the density of states at the Fermi energy. Remarkably, the chiral anomaly

induced negative magnetoresistance was indeed observed in representative Weyl semimetals such as TaAs [43], TaP [44], Cd₃As₂ [45] and ZrTe₅ [46], although isolating this effect from other trivial contributions is a major challenge [47]

Another intriguing consequence of the nontrivial topology of Weyl semimetals is the existence of topologically protected surface states required by the bulk-surface correspondence [48]. Such surface states appear in the form of Fermi arcs in the surface Brillouin zone, and extend between Weyl nodes projections of opposite chirality, at which point they merge with the bulk states [48] (Fig. 12 a). Indeed, Fermi arc states have been explicitly identified by DFT bandstructure calculations in candidate materials [38, 39, 48], and assigned to related signals in subsequent ARPES experiments [38, 39]. In addition, their unique magnetotransport features were experimentally demonstrated by Schubnikov-de Haas [49] (Fig. 12 b) and quantum Hall effect [50] (Fig. 12 c) measurements, although microstructured samples are required for such experiments, where the surface-to-bulk ratio is large enough that Fermi arc mediated transport prevails [49–51].

Finally, beside the unusual topological response of the Fermi arcs discussed so far, the Berry curvature singularities at the Weyl nodes are expected to drive a bulk topological Hall effect in Weyl semimetals [52–54]. Indeed, such an effect was experimentally evidenced for representative magnetic Weyl semimetal systems [55–57]. For noncentrosymmetric Weyl semimetals, a spontaneous Hall effect-driven by imbalanced left- and right-handed Weyl fermions was theoretically predicted [53, 54], but so far lacked experimental confirmation until its demonstration in the present work. For a more detailed discussion of both the magnetic and noncentrosymmetric cases, I refer the reader to Sect 3.4 and Sect. 3.5, respectively.

In conclusion, the well-defined chirality and topological index of Weyl bands give rise to novel quantum phenomena such as the chiral anomaly, Fermi arcs mediated charge pumping and various unusual Hall responses that constitute the

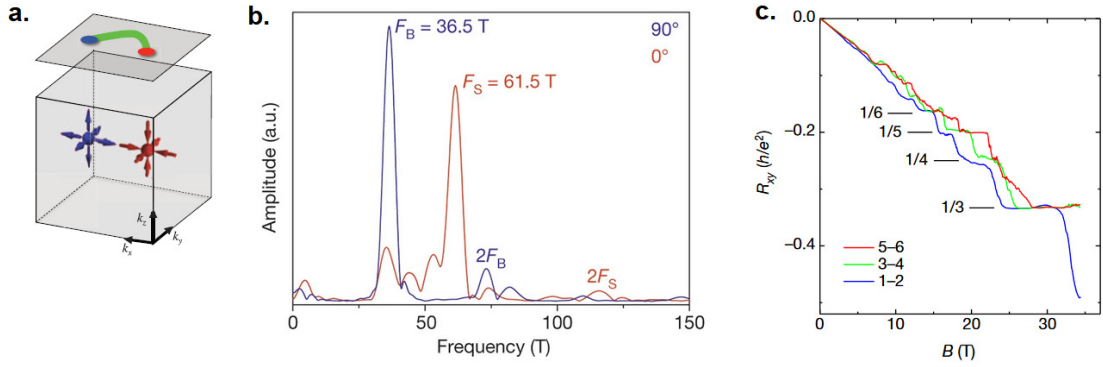


Figure 12: **Topological response of Fermi arcs.** **a:** Schematic of the Fermi arc state at the surface Brillouin zone (green line). It extends between the surface projections (red and blue dots) of the bulk Weyl nodes. **b:** Fourier transform amplitude of the Shubnikov-de Haas effect in a microstructured samples of the Weyl semimetal Cd_3As_2 . Depending on the angle between the magnetic and electric fields, the measurement evidences Weyl orbits related to the surface states (F_S) as opposed to the bulk contribution (F_B). **c:** Fermi arc-driven quantum Hall effect in a similar system as panel **b**. Panels **a**, **b** and **c** are taken from [39, 49, 50], respectively.

intrinsic fingerprints of these exotic systems.

2.5 Muon spin rotation and relaxation spectroscopy

Muon spin rotation (μSR) is a powerful tool to measure the local magnetic field in solids. Because of its high sensitivity (down to $B \sim 1 \text{ G}$ or $M \sim 10^{-3} \mu_B$), this technique has been successfully used to determine the occurrence (or the absence) of time-reversal symmetry breaking in many different materials [58–60]. Contrary to other well established local probes such as nuclear magnetic resonance (NMR) and electron spin resonance (ESR) here experiments can be done in zero applied magnetic field (ZF- μSR), and in the absence of any probing electromagnetic radiation. Instead, as positive muons μ^+ are spin 1/2 ($S = 1/2$) massive ($m \approx 207m_e$) and charged ($q = +e$) particles, μSR phenomena rely on two key points:

1. Due to its large magnetic moment $\boldsymbol{\mu}_\mu$ and gyromagnetic ratio γ_μ , the total spin polarization \boldsymbol{P} of the implanted μ^+ ensemble will precess around the local magnetic field $\boldsymbol{B}_{\text{loc}}$ with a Larmor frequency of $\omega_L = \gamma_\mu B_{\text{loc}}$.
2. The muon decay $\mu^+ \rightarrow e^+ + \nu_e + \bar{\nu}_\mu$ (with a lifetime of $\tau = 2.2 \mu\text{s}$) violates parity conservation, with an asymmetric e^+ emission in the preferential direction of the muon spin (Fig. 13). Thus, by tracking the positron emission $N_{e^+}(t)$, the spin polarisation $\boldsymbol{P}(t)$ can be reconstructed.

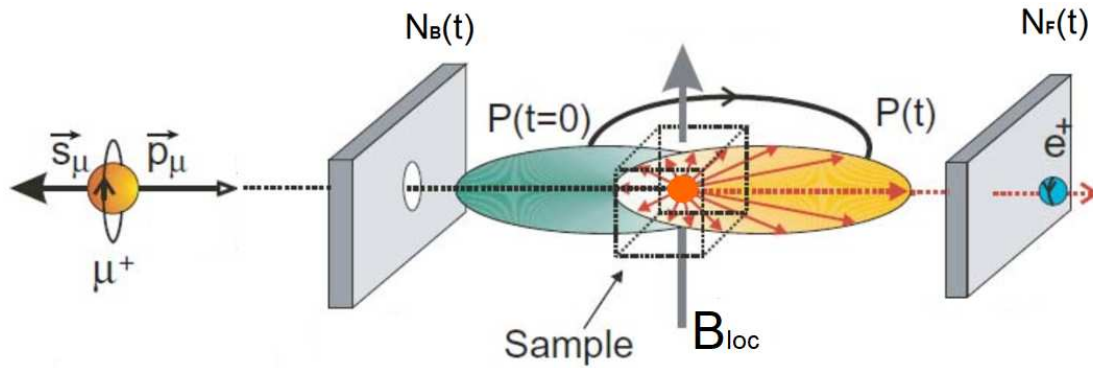


Figure 13: μSR measurement configuration. A spin polarized μ^+ ensemble, with the spin \boldsymbol{S}_μ parallel to the momentum \boldsymbol{p}_μ , is implanted in the sample (orange circle). The spin polarization $\boldsymbol{P}(t)$ is measured via the asymmetric e^+ decay (orange ellipse, red arrows), which rotates (green ellipse) around the local magnetic field B_{loc} (vertical arrow). Finally, time dependent e^+ counts ($N_{\text{F}}(t)$ and $N_{\text{B}}(t)$) are detected at two opposing detectors at the front and back, respectively, and $A(t)$ is obtained (Eqn.14). Figure is taken from [61].

In a μSR experiment, the $N_{e^+}(t)$ asymmetry and, thus, $\boldsymbol{P}(t)$ is recorded via a two detector configuration (Fig. 13), quantified by the asymmetry parameter

$$A(t) = \frac{N_{\text{B}}(t) - N_{\text{F}}(t)}{N_{\text{B}}(t) + N_{\text{F}}(t)}. \quad (14)$$

Here N_{B} and N_{F} are the detected e^+ counts on the backward and forward detectors, respectively (Fig. 13), and the initial, maximum value of $A(t = 0)$ reaches $A_{\text{max}} =$

0.2 – 0.3).

For nonmagnetic materials, the local magnetic field is determined by the spin fluctuation of electronic and nuclear degrees of freedom, resulting in a decoherence of the muon's spin with time. Typically, the relaxation due to the nuclear moments (in case of $\text{Ce}_3\text{Bi}_4\text{Pd}_3$ by the $4.11\mu_{\text{N}}$ nuclear moment of ^{209}Bi), is described by the Gaussian Kubo-Toyabe function [62] characterized by the relaxation rate σ , that is

$$G_{\text{KT}} = \frac{1}{3} + \frac{2}{3}(1 - \sigma^2 t^2)e^{-\frac{\sigma^2 t^2}{2}} . \quad (15)$$

In parallel, the electronic contribution to the ZF- μSR spectrum is modelled by an additional Lorentzian relaxation, with the electronic relaxation rate denoted by Λ [58–60], so that the total relaxation is given as

$$A_{\text{ZF}} = A_{\text{s}}G_{\text{KT}}e^{-\Lambda t} + A_{\text{bkg}} , \quad (16)$$

where A_{s} and A_{bkg} are the sample- and background-related constant asymmetries, respectively.

Finally, additional information of the system under investigation can be extracted if the μSR relaxation is measured while applying an external magnetic field parallel to the initial spin polarization, that is, in a so-called longitudinal-field configuration (LF- μSR). Clearly, if the applied field is zero, the spin precession is determined by the internal field of the solid. On the other hand, if the longitudinal field is dominating, then the spins are pinned to it, and no precession occurs. Thus, in a typical LF- μSR experiment, one determines the magnetic field, where the transition between these two regimes occur. This field is an estimate of the local magnetic field strength in the investigated material.

2.6 Crystal growth from liquids

Crystal growth from a liquid phase is one of the simplest and most wide-spread growth techniques. The liquid phase may be a stoichiometric melt or a solution of the solid in a solvent (flux growth). From a technical point of view, several versions exist such as the Czochralski method or zone melting. The main principle is that, from a thermodynamic point of view, the composition and the temperature are the only control parameters. They select the state of matter with the lowest Gibbs energy G (the maximum amount of extractable work at constant pressure and temperatures).

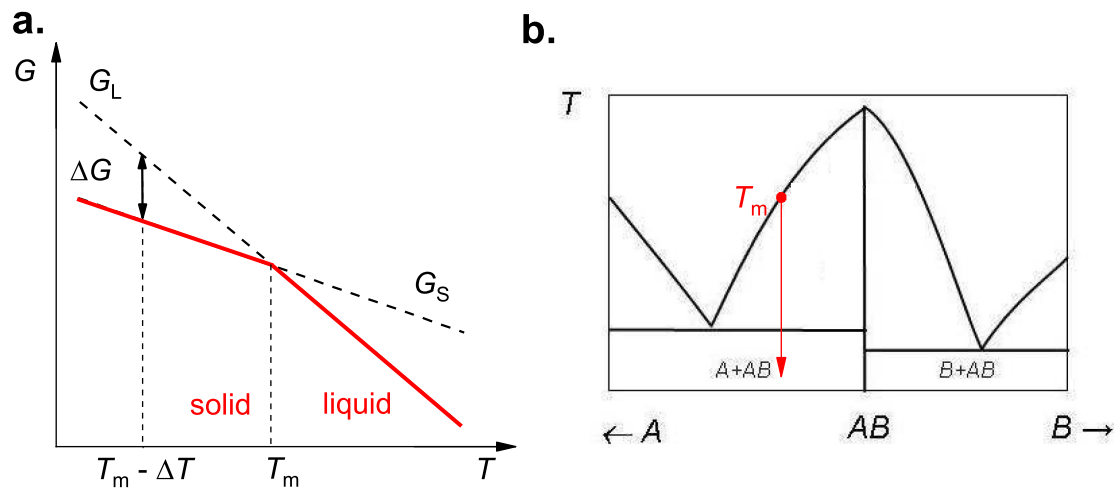


Figure 14: **Principle of crystal growth from the melt.** **a:** Gibbs free energy G vs. temperature for a system that undergoes a liquid to solid phase transition. G_L and G_S are the Gibbs free energies of the liquid and solid phase, respectively, that are equal at the melting temperature T_m . The red line denotes the actual state of matter. At a temperature ΔT below T_m , the solid phase has ΔG energy gain compared to the liquid phase (indicated by a dashed line and an arrow). **b:** Schematic temperature–concentration phase diagram of a binary compound AB . The growth occurs by reducing the temperature from above T_M (vertical red arrow). Figures are taken from [63].

At high temperatures, the Gibbs energy G_L of the liquid phase (L) is lower

than that (G_S) of the solid phase (S) and, thus, the system remains liquid. As temperature decreases, the Gibbs energies of the two phases first become equal at T_M (Fig. 14 a), and the melt starts to crystallize. Consequently, T_M is the melting temperature of the compound. By further decreasing the temperature by ΔT below T_m , the solid phase is lower in energy by ΔG compared to the liquid phase (Fig. 14 a).

The main advantage of the flux method is the controlled reduction of the melting temperature of the compound by introducing a solvent. In the case of self-flux technique, the solvent has offstoichiometric, frequently a strong excess of one of the components, otherwise the flux is an additional foreign element. This concept is presented schematically for a simple case of a hypothetical binary compound AB in Fig. 14 b, where T_M is maximum at the stoichiometric point, and is reduced by introducing an excess of A (or B). By decreasing the temperature from above T_M , the compound AB crystallizes in the melt of A , and is commonly separated from the liquid by centrifuging.

Whereas the flux method is a powerful and simple crystal growth technique, it also offers challenges to be overcome for a successful single crystal growth. Without addressing all of them, I briefly discuss two important aspects that arise due to crystal surface effects, namely: constitutional supercooling and spontaneous nucleation.

Constitutional supercooling arises when different species in the melt are absorbed at different rates. This leads to a difference in the local density C_i of the i -th species near the surface of the growing crystal with respect to its value in the melt. Since T_M of the compound is controlled by the relative ratio of the constituents, its value may be reduced at the surface of the crystal resulting in “spiky” and irregular growth. Constitutional supercooling can be suppressed primarily by reducing the cooling rate, and by introducing a temperature gradient between the

crystal surface and the melt.

Spontaneous nucleation, on the other hand, arises because the energy penalty due to the surface formation of the crystal competes with the energy gain of the volume. For an initial nucleus with radius r_N , the former scales with $\sim r_N^2$ and the latter with $\sim r_N^3$. Thus, the surface contribution will prevail at small r_N and crystals will form only at a temperature T^* below T_m . However, when the nucleation rate increases, the bulk growth rate is already large, resulting in an uncontrolled crystal growth and the formation of polycrystals. To avoid the spontaneous nucleation, and promote single crystal growth, the growth procedure must take place in the so-called Ostwald-Miers region [63]. In a first step the temperature is reduced below the bulk T_m to T^* , and kept there. This helps the formation of some initial seeds. Thereafter, the temperature is not reduced further, resulting in the stop of nucleation and the oversaturated state is relieved. Finally, single crystal growth based on the initial nucleus proceeds according to the bulk liquidus line.

3 Hall effect

3.1 Introduction and symmetry aspects

The Hall effect is defined as a transverse current response to an applied electric field. Here, and throughout this thesis, I define the Hall effect setting as the electric field excitation being in the x direction, i.e., $\mathbf{E} = \mathbf{E}_x$, and the response being in the y direction, i.e., $\mathbf{j} = \mathbf{j}_y$ (Fig. 15). the associated Hall conductivity σ_{xy} in the linear response regime is then defined as

$$\sigma_{xy} = \lim_{E_x \rightarrow 0} \frac{j_y}{E_x}. \quad (17)$$

Due to its extreme low-energy scales (with respect to the Fermi energy), the Hall effect stands out as sensitive tool to probe the ground state of condensed matter systems. It has delivered invaluable insight in quantum critical systems [13, 64–66], topologically non trivial 2D [18, 21, 67] and 3D [55, 57, 68] states of matter, and in novel magnetic materials such as skyrmion lattices [69, 70] and non-collinear magnets [71, 72]

In an experiment, the Hall contacts represent an open circuit condition, thus no net current can flow in the y -direction. This is ensured by the fact that the Hall current $j_y = \sigma_{xy}E_x$ leads, after an initial transient period, to an accumulation of charge on one side of the sample (Fig. 15). Subsequently, the charge separation gives rise to an electric field E_y in the y -direction that drives, via the usual Ohmic conductivity σ_{yy} , a current density $j^* = \sigma_{yy}E_y$, so that $j^* = -j_y$. In this case, the equilibrium condition for E_y is given by

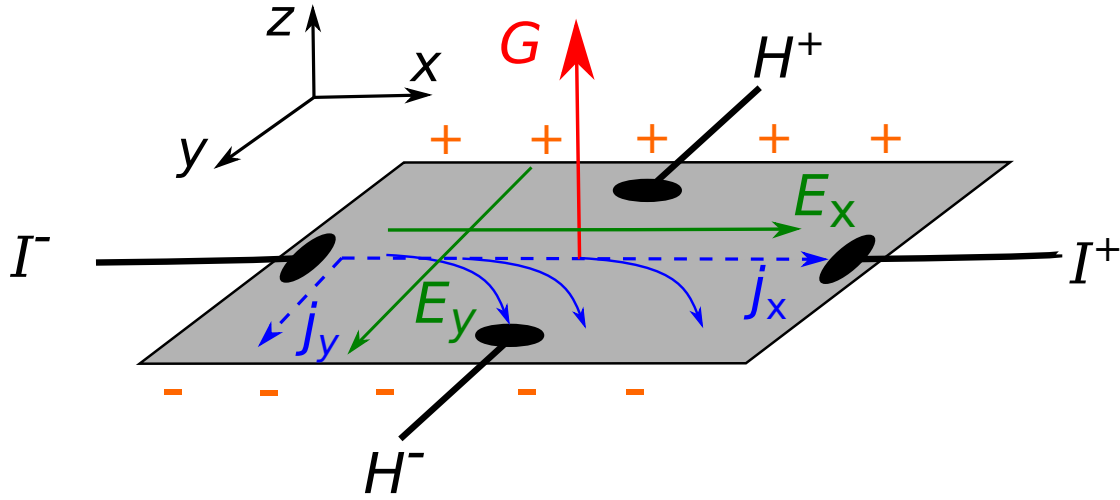


Figure 15: **Sketch of the Hall effect.** Electron current density (dashed blue arrow) flows between contacts I^- and I^+ . It leads to the build up of an x -direction electrical field E_x (green). Electrons coupled to a time-reversal breaking quantity described by the out of plane vector \mathbf{G} (red arrow) leads to a bending of j_x and, thus, to a y component current density j_y . This results in a subsequent charge imbalance along the y direction (orange + and -). The associated y -direction electrical field E_y (green arrows) is then measured with the Hall voltage contacts H^- and H^+ .

$$j_y + j^* = \sigma_{xy}E_x - \sigma_{xx}E_y = 0 , \quad (18)$$

$$|E_y| = \frac{\sigma_{xy}}{\sigma_{xx}}|E_x| = \tan\Theta_H|E_x| .$$

Here I have used that in a cubic system $\sigma_{yy} = \sigma_{xx}$. As can be seen from Eqn.18, the strength of the response E_y due to E_x , and a figure of merit for the Hall effect, is given by the ratio σ_{xy}/σ_{xx} , known as the tangent of the Hall angle $\tan \Theta_H$. Thus, in an experiment, it is E_y that is directly measured with respect to a current density excitation j_x (Fig. 15), defining the Hall resistivity as

$$\rho_{xy} = \lim_{j_x \rightarrow 0} \frac{E_y}{j_x} . \quad (19)$$

Another important aspect related to a finite Θ_H is that it leaves its fingerprint on the electrical resistivity ρ_{xx} . This is because the Hall conductivity enters the expression of ρ_{xx} directly as

$$\rho_{xx} = \frac{\sigma_{xx}}{\sigma_{xx}^2 + \sigma_{xy}^2} = \frac{1}{\sigma_{xx}} \frac{1}{1 + (\tan \Theta_H)^2}. \quad (20)$$

In case of a negligible Hall angle, the resistivity is simply the inverse of the conductivity $\rho_{xx} = 1/\sigma_{xx}$, whereas if the Hall angle is $\pi/2$ ($\tan \Theta_H = \infty$), such as in the case of the quantum Hall effect [18], the (bulk) resistivity vanishes.

Finally, I discuss aspects of time-reversal symmetry (TRS) that imposes strict constraints on the Hall effect. Generally, σ_{xy} is driven by a physical parameter \mathbf{G} that is perpendicular to the plane defined by E_x and j_y , so that $\mathbf{j}_y \sim \mathbf{G} \times \mathbf{E}_x$. Here \mathbf{G} can be an external magnetic field \mathbf{B} , magnetization \mathbf{M} or the integral Ω of the Berry curvature $\Omega(\mathbf{k})$ over occupied electronic states in the Brillouin zone (see Fig. 16 and Sects.3.2, 3.3, 3.4).

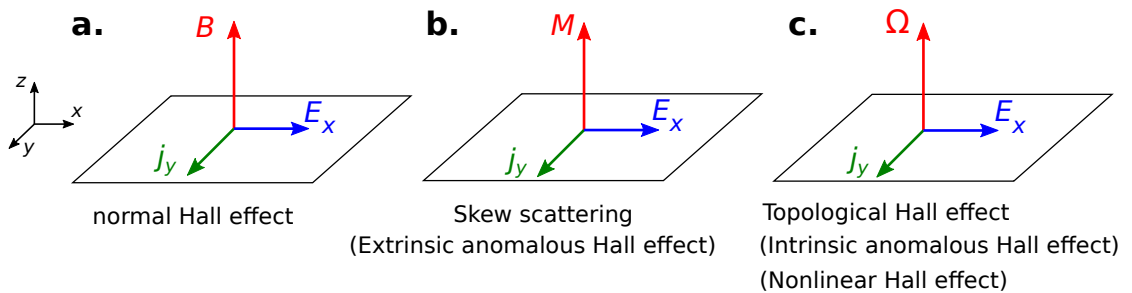


Figure 16: **Different types of Hall effect.** A Hall response is due to an out of plane vector \mathbf{G} that breaks TRS (Fig.15). In the case of the normal Hall effect (panel **a**), this is an external magnetic field ($\mathbf{G} = \mathbf{B}$, Sect.3.2). In case of skew scattering (panel **b**, also known as the extrinsic anomalous Hall effect) \mathbf{G} is the internal magnetization ($\mathbf{G} = \mathbf{M}$, Sect.3.3). For the topological Hall effect (panel **c**) such as the intrinsic anomalous Hall effect and the nonlinear (quantum) Hall effect, \mathbf{G} is the integral Ω of the Berry curvature distribution $\Omega(\mathbf{k})$ over the occupied states in the Brillouin zone ($\mathbf{G} = \Omega$, Sect.3.4).

Since E_x is invariant under time-reversal operation \mathcal{T} ($\mathcal{T}E_x = E_x$) but j_y changes sign ($\mathcal{T}j_y = -j_y$), it directly implies that $\mathcal{T}\mathbf{G} = -\mathbf{G}$. Thus, σ_{xy} is finite only if \mathbf{G} explicitly break TRS, otherwise j_y is forced to vanish. As a consequence, this restricts σ_{xy} to be a fully antisymmetric function of \mathbf{G} such as $\sigma_{xy}(G) = -\sigma_{xy}(-G)$, known as the Casimir-Onsager relations [73]. Here I note that this argument does not apply for the usual electrical conductivity, as therein, dictated by the third law of thermodynamics, TRS is inherently broken due to the entropy production ($\dot{S} = j_x E_x$). For the Hall current $\dot{S} = 0$ since j_y and E_x are orthogonal.

3.2 The normal Hall effect

In a conductor, applying an external magnetic field perpendicular to the current ($\mathbf{G} = \mathbf{B}$ see Fig. 16 a) gives rise to a Lorentz force $\mathbf{F}_L = -e\mathbf{v} \times \mathbf{B}$ acting on the charge carriers and, thus, leads to a Hall voltage. Here \mathbf{v} is the electron velocity. In this case, the corresponding dependence of $\rho_{xy}(B)$ is linear-in-field at low fields, determined by the Hall coefficient R_H , which is defined as the initial slope and reads

$$R_H = \lim_{B \rightarrow 0} \frac{\partial \rho_{xy}}{\partial B} . \quad (21)$$

In the case of a single Fermi pocket (one band case), such as in simple metals and semiconductors, R_H is inversely proportional to the charge carrier concentration n and charge q so that

$$R_H = \frac{1}{nq} . \quad (22)$$

The associated Hall angle in a simple Drude picture, where $\rho_{xx} = 1/(nq\mu)$, is then a good measure for the mobility μ and reads

$$\tan \Theta_H = \frac{R_H B}{\rho_{xx}} = \mu B . \quad (23)$$

For systems with two (multiple) bands intersecting the Fermi level (Fig. 17 a), $\rho_{xy}(B)$ is a complicated function of n_1 , n_2 , μ_1 , μ_2 , q_1 and q_2 (i sets of parameters if i bands), and is given by [74]

$$\rho_{xy}(B) = \frac{n_1 q_1 \mu_1^2 + n_2 q_2 \mu_2^2 + (n_1 q_1 + n_2 q_2) \mu_1 \mu_2 B^2}{(n_1 q_1 \mu_1 + n_2 q_2 \mu_2)^2 + (n_1 q_1 + n_2 q_2)^2 \mu_1^2 \mu_2^2 B^2} B. \quad (24)$$

This may deviate considerably from simple linear behaviour (Fig. 17 b). Here the parameters denote the carrier densities, mobilities and the type of the two bands, respectively.

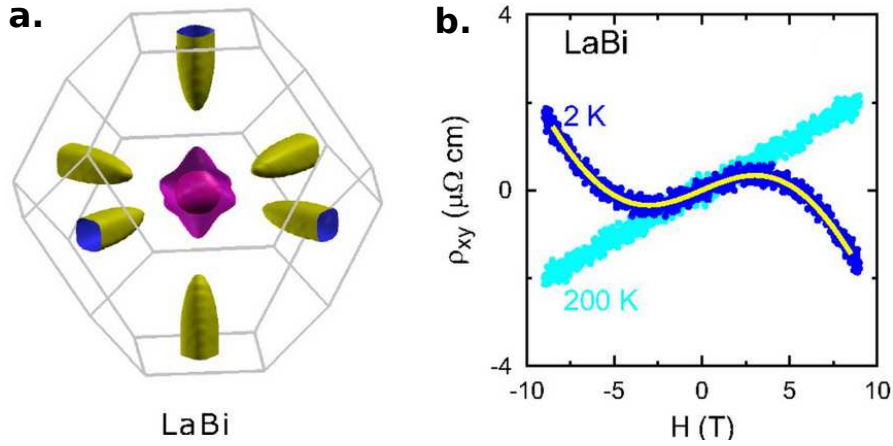


Figure 17: **Hall effect in a two-band system.** **a:** Calculated Fermi surface structure of LaBi showing a central hole pocket and peripheral electron pockets. **b:** Hall resistivity in the same material showing strong nonlinearities at low temperatures (2 K) captured by a two-band fit (yellow line). Panels **a** and **b** are taken from [75].

Finally, whereas a nonlinearity in $\rho_{xy}(B)$ may have many possible sources, the two-band model offers a strict consistency check: Two-band parameters obtained from fits to $\rho_{xy}(B)$ according Eqn.24 uniquely determine the magnetic field-dependent electrical resistivity $\rho_{xx}(B)$ given as [74]

$$\rho_{xx}(B) = \frac{n_1 q_1 \mu_1 + n_2 q_2 \mu_2 + (n_1 q_1 + n_2 q_2) \mu_1 \mu_2 B^2}{(n_1 q_1 \mu_1 + n_2 q_2 \mu_2)^2 + (n_1 q_1 + n_2 q_2)^2 \mu_1^2 \mu_2^2 B^2}. \quad (25)$$

Thus, a strong disagreement between the calculated and the measured MR curves indicates that nonlinearity of the $\rho_{xy}(B)$ curve is driven by a mechanism other than the presence of multiple bands.

3.3 Skew scattering in heavy fermion systems

Magnetic moments embedded in a metallic host – whether as impurities or as an integral part of the lattice – serve as scattering centres for conduction electrons. If spin-orbit interaction is non-negligible, the left-hand right-hand symmetry of the scattering is broken, and is described by an asymmetric transition rate $W_{\mathbf{k},\mathbf{k}'}^A$ [68] so that

$$W_{\mathbf{k},\mathbf{k}'}^A = \frac{1}{\tau_A} \mathbf{k} \times \mathbf{k}' \cdot \mathbf{M} . \quad (26)$$

Here \mathbf{M} is the magnetization vector, whereas \mathbf{k} and \mathbf{k}' denote the wave vector of the initial and final Bloch states. Thus, in a Hall effect experiment, skew scattering leads to the appearance of a Hall voltage that is proportional to the out-of-plane magnetization (Fig. 16 b). In such a case the Hall resistivity is given by

$$\rho_{xy} = R_0 B + R_1 M(T, B) , \quad (27)$$

where R_0 and R_1 are the normal and anomalous Hall coefficients, respectively [68]. A distinctive feature of this type of scattering is that it is proportional to the momentum scattering rate $\rho_{xy} \sim \tau$ and, thus, the coefficient R_1 scales linearly with ρ_{xx} [68]. This provides a most direct way to isolate this contribution from other Hall effect contributions that are independent of ρ_{xx} .

In heavy fermion systems, the strong interaction between conduction electrons and magnetic moments gives rise to a sizeable skew scattering contribution in the incoherent regime [76]. It leads to a Hall coefficient that is dominated by R_1 at high temperatures (Fig. 18), and that scales linearly with the product of the magnetic

susceptibility and the magnetic contribution to the resistivity [76] such that

$$R_1 = \gamma_1 \chi^* \rho_{\text{mag}} . \quad (28)$$

Here χ^* is the reduced magnetic susceptibility $\chi^* = \chi/C$ where $C = n_{\text{mag}} \mu_{\text{eff}}^2 / (3k_B)$ is the Curie constant, n_{mag} is the magnetic moment density, μ_{eff} is the effective moment and k_B is the Boltzmann constant.

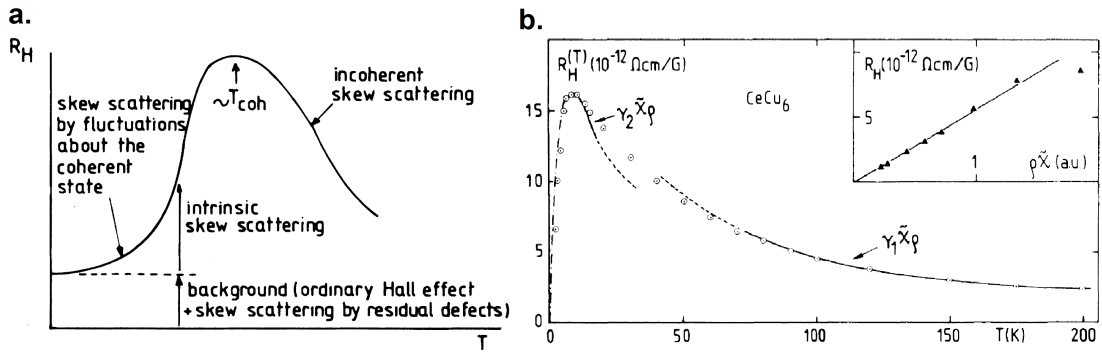


Figure 18: **Skew scattering in heavy fermion compounds.** **a:** Sketch of the Hall coefficient R_H vs. T . The coherence temperature T_{coh} separates two regimes: A high-temperature part dominated by incoherent skew scattering, and a low-temperature part where the latter is suppressed. **b:** Experimental R_H vs. T for the heavy fermion metal CeCu_6 (symbols). Lines indicate fits according to Eqn. 28. Inset shows the data plotted vs. $\chi^* \rho$. Figures are taken from [76].

Most importantly, the constant γ_1 is determined by the microscopic properties of the scattering, and has an overall maximum value of $|\gamma_1| < 0.21$, which reduces to $\gamma_1 < 0.1$ for the specific case of Ce containing Kondo systems [76]. Indeed, experimentally determined γ_1 values of $\gamma_1 = 0.082, 0.075, 0.016,$ and 0.01 K/T for prototypical heavy fermion metals $\text{CeCu}_6, \text{CeAl}_3, \text{CeCoRh}_5,$ and $\text{CeCoIr}_5,$ respectively [76, 77], are in good agreement with the theory. Finally, below the characteristic coherence temperature T_{coh} , conduction electrons and magnetic moments form heavy quasiparticles that propagate coherently and, thus, the skew scattering is suppressed [76] (Fig. 18 a)

3.4 The anomalous Hall effect

In systems hosting a finite Berry curvature distribution $\mathbf{\Omega}(\mathbf{k})$, applying an electric field \mathbf{E} gives rise to an additional, anomalous component $\mathbf{v}_a(\mathbf{k})$ to the electron velocity, given by [32]

$$\mathbf{v}_a(\mathbf{k}) = \frac{e}{\hbar} \mathbf{E} \times \mathbf{\Omega}(\mathbf{k}) . \quad (29)$$

Here \mathbf{k} denotes the wavevector of a single Bloch state of the Brillouin zone. Integrating $\mathbf{v}_a(\mathbf{k})$ with respect to the occupied state in the Brillouin zone leads to a macroscopic Hall current $j_y = \sigma_{xy} E_x$, with the Hall conductivity determined as [32]

$$\sigma_{xy} = \frac{e^2}{\hbar} \int_{BZ} \frac{d^3k}{(2\pi)^3} \Omega_z(\mathbf{k}) f(\mathbf{k}) . \quad (30)$$

Here $f(\mathbf{k})$ is the electron distribution function under an applied electric field \mathbf{E} . It can be generally written as $f(\mathbf{k}) = f_0(\mathbf{k}) + g(\mathbf{k})$, where $f_0(\mathbf{k})$ and $g(\mathbf{k})$ are the equilibrium (Fermi-Dirac) and nonequilibrium contributions to the distribution function, respectively.

The nature and properties of the Hall effect described in Eqn.30 depend on whether $\mathbf{\Omega}(\mathbf{k})$ is driven by a broken time-reversal symmetry (TRS), or by a broken inversion symmetry. In this section, I will focus on the former, commonly known as the intrinsic anomalous Hall effect (AHE) [68].

For systems with broken TRS, the Berry distribution is an even function of \mathbf{k} so that $\mathbf{\Omega}(\mathbf{k}) = \mathbf{\Omega}(-\mathbf{k})$ [32]. Since $f_0(\mathbf{k})$ is even- whereas $g(\mathbf{k})$ is odd-in- \mathbf{k} , the integral in Eqn.30 is finite only for the former case. Then, the integrand is determined by the perfect crystal, and the Hall conductivity is independent of the scattering time, i.e., $\sigma_{xy} \sim \tau^0$. As a consequence σ_{xy} is constant (Fig. 19 a) and results in a Hall resistivity $\rho_{xy} \sim \sigma_{xy}/\sigma_{xx}^2$ that is proportional to ρ_{xx}^2 [68].

For the intrinsic anomalous Hall effect discussed so far TRS can be broken in several ways. In case of 2D electron gases, TRS is broken either by applying a

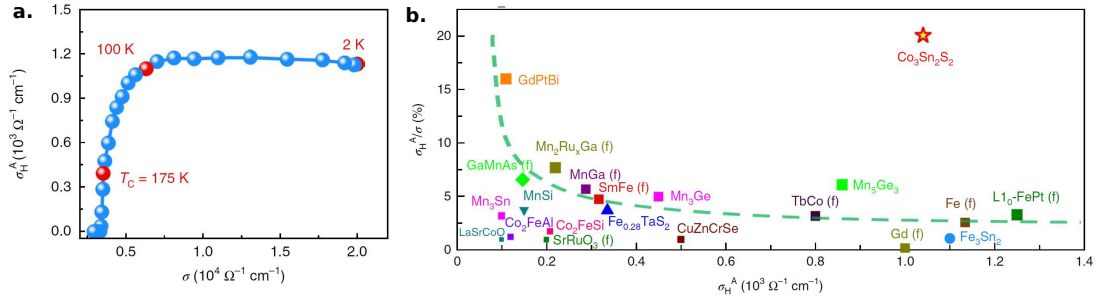


Figure 19: **Intrinsic anomalous Hall effect in TRS broken systems.** **a:** Anomalous Hall conductivity vs. electrical conductivity in $\text{Co}_3\text{Sn}_2\text{S}_2$. Temperature is an implicit variable. The Hall conductivity appears after a ferromagnetic phase transition at a Curie temperature T_C , and is independent of the electrical conductivity. **b:** The tangent of the Hall angle for various TRS breaking materials. Magnetic Weyl semimetals such as GdPtBi and $\text{Co}_3\text{Sn}_2\text{S}_2$ stand out due to their largely enhanced Berry curvature distribution. Panels **a** and **b** are taken from [57].

strong external magnetic field that gives rise to the quantum Hall effect (QHE) [18,67], or spontaneously, e.g., due to a ferromagnetic phase transition, giving rise to an anomalous QHE [21]. In bulk 3D systems, the Berry curvature-driven AHE was demonstrated for simple ferromagnets [78], non-collinear antiferromagnets [71, 72], skyrmion lattices [69,70], and even systems without any long range magnetic ordering [79]. The common aspect in all these systems is that the Berry curvature is proportional to the TRS breaking (order) parameter.

Finally, as the AHE is driven by $\mathbf{\Omega}(\mathbf{k})$, it is expected to be substantially enhanced by its singularities in a magnetic 3D Weyl semimetal [52]. Indeed, the AHE evidenced in these systems, such as GdPtBi [55], ZrTe_5 [56] and $\text{Co}_3\text{Sn}_2\text{S}_2$ [57], shows that the associated Hall angle is greatly enhanced with respect to systems lacking linear band crossings (Fig. 19b).

3.5 The nonlinear Hall effect

As mentioned in the previous section, in TRS broken systems, a Berry curvature-driven AHE carried by the equilibrium Fermi-Dirac distribution has been experimentally demonstrated and theoretically understood. In systems with preserved TRS but broken IS, however, the Berry curvature is odd-in- \mathbf{k} [$\Omega(\mathbf{k}) = -\Omega(-\mathbf{k})$] and, thus, its integral with $f_0(\mathbf{k})$ (Eqn. 30) vanishes. It was, however, theoretically demonstrated that when the out of equilibrium part of the distribution function $g(\mathbf{k})$ is considered (that is also odd-in- \mathbf{k}), such systems display a Berry curvature-driven Hall effect [53]. In this case the Hall current density is given by

$$j_y = \sigma_{xy} E_x = \frac{e^2}{\hbar} \int \frac{d^3 k}{(2\pi)^3} g(\mathbf{k}, E_x, \tau) \Omega_z(\mathbf{k}) E_x . \quad (31)$$

Equation 31 clearly shows that the salient feature of this Hall effect is the nonlinearity in the driving electric field, and the explicit dependence on the momentum scattering time. Both of these features are in sharp contrast to the AHE in TRS broken systems and, thus, can be used to uniquely identify this mechanism.

The exact dependence of σ_{xy} on E_x , and the functional form of the nonlinearity is given by the specific form of $g(\mathbf{k})$ (Eqn.31), which in the simplest case, is obtained perturbatively by solving the Boltzmann equation in the relaxation time approximation [53]. $g(\mathbf{k})$ is then simply the first order term of a Taylor series around the equilibrium Fermi-Dirac distribution [80], and is given by

$$g(\mathbf{k}) = \frac{e\tau}{\hbar} E_x \frac{\partial f_0(\mathbf{k})}{\partial k_x} , \quad (32)$$

so that the Hall current reduces to

$$j_y = \frac{e^3 \tau E_x^2}{\hbar^2} \underbrace{\int \frac{d^3 k}{(2\pi)^3} \frac{\partial f_0(\mathbf{k})}{\partial k_x}}_{D_{xz}} \Omega_z(\mathbf{k}) . \quad (33)$$

In this approximation, the Hall current is quadratic in E_x and proportional to the Berry dipole D_{xz} of the material [53].

For an AC excitation with an angular frequency of ω , i.e., $E_x(t) = E_x \cos \omega t$, the E_x^2 term results in a Hall current that is composed of a rectified DC and a second-harmonic (2ω) response [53] as shown by

$$j_y = \frac{e^3 \tau E_x^2}{\hbar^2} D_{xz} \cos^2(\omega t) = \frac{e^3 \tau E_x^2}{\hbar^2} D_{xz} \left(\underbrace{\frac{1}{2}}_{\text{DC}} + \underbrace{\frac{\cos(2\omega t)}{2}}_{2^{\text{nd}} \text{harmonic}} \right). \quad (34)$$

For Weyl semimetals, Berry curvature singularities at the Weyl nodes are expected to boost the nonlinear Hall effect. Indeed, first principle calculations for several weakly interacting Weyl semimetals have predicted a nonlinear Hall effect that is enhanced if the Fermi energy is in the vicinity of the Weyl points (Fig. 20 g) [54]; this effect remains to be experimentally confirmed. Most importantly, it was shown that this effect is finite only in case of tilted and type-2 Weyl semimetals (Fig. 20 a-f) [54]. This is because for a given Weyl cone, the integrand in Eqn. 33 is symmetric in the k_x - k_y plane and integrates to zero for the symmetric Fermi surface of a Weyl cone without a tilt (Fig. 20 a).

Another important aspect of this effect is TRS breaking. Whereas the nonlinear Hall effect occurs in systems with microscopically preserved TRS, it is the experiment itself that breaks TRS: Since $g(\mathbf{k})$ is driven by E_x , σ_{xy} can be maintained only at the cost of entropy production $\dot{S} = j_x E_x$, thus breaking the TRS at the thermodynamic level via the third law of thermodynamics. To be more explicit, the Hall effect discussed here is a nonlinear response, defined only in this entropy producing state, and is suppressed to zero if entropy production is suppressed, i.e., $\sigma_{xy} \rightarrow 0$ if $E_x \rightarrow 0$ (Eqn.31). This is in sharp contrast to conductivities described in the linear response limit, where σ_{xy} remains finite in the $E_x \rightarrow 0$ ($\dot{S} = 0$) limit (Eqn. 17).

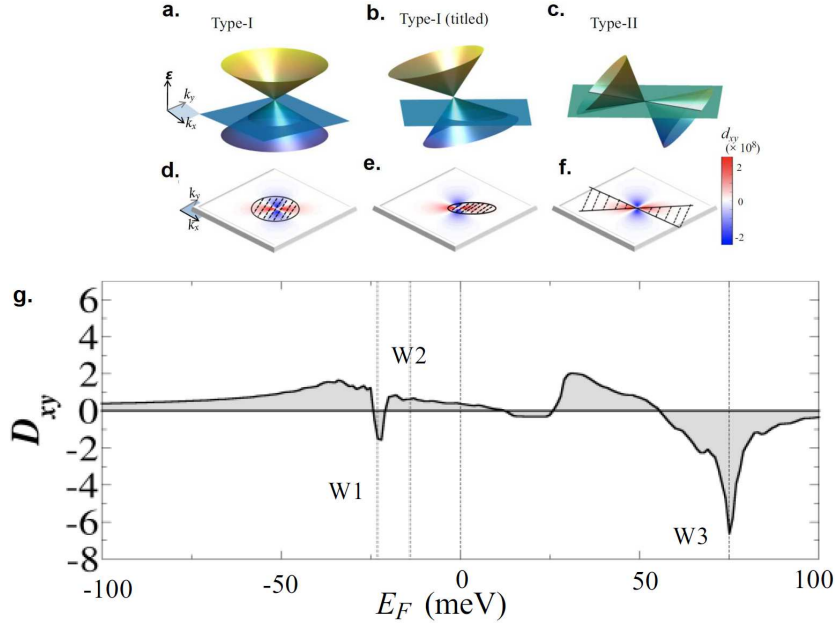


Figure 20: **Nonlinear Hall effect in noncentrosymmetric Weyl semimetals.** **a-c:** Sketch of Weyl cones with various tilts intersecting the Fermi energy ($\epsilon = 0$ plane). **a-c:** Berry curvature dipole density (integrand in Eqn.33) in the $k_x - k_y$ plane, with respect to the occupied states (black shaded area). For a non-tilted Weyl cone (**a**), the occupation function is symmetric over the Berry dipole distribution and hence its integrand vanishes. Only in the case of a tilt is this symmetry broken (**b-c**, **e-f**), resulting in a finite nonlinear Hall conductivity. **g:** Calculated Berry curvature dipole for the Weyl semimetal TaAs as function of the Fermi energy position in a rigid band model. D_{xy} is strongly enhanced in the vicinity of the Weyl points (W1, W2, W3). All panels are taken from [54].

Finally, I discuss the limitations of the perturbative treatment presented in [53, 54]. As seen in Eqn. 32, $g(\mathbf{k})$ is a Taylor expansion around the equilibrium (Fermi-Dirac) distribution function $f_0(\mathbf{k})$, where the expansion parameter $\delta\mathbf{k}$ is determined by the electric field and scattering time as $\delta\mathbf{k} = e/\hbar \cdot \tau \mathbf{E}$. Clearly, the validity of this approach is fulfilled if the absolute value δk is much smaller than that of the characteristic wave vector determining $f(\mathbf{k})$, the Fermi wavevector k_F . This is indeed the case: For an ideal metal with a single, half filled band and a spherical Fermi surface, k_F is of the order of the inverse lattice length $1/a$. As

$a \sim 10^{-9}$ m, k_F is of the order of $k_F \approx 10^9$ m $^{-1}$. For a value of $\tau = 10$ ps (typical for good metals), and an electric field $E = 100$ V/m (a large value to provide an upper limit of δk) the expansion parameter is of the order of $\delta k = 10^4$ m $^{-1} \ll k_F$. Thus, a linearised Boltzmann approximation is clearly justified. A second aspect of the linearised Boltzmann approximation is that it traces the observable quantity back to a surface integral in k -space at the equilibrium Fermi surface (Eqn. 33). Such an approximation is only valid if the observed microscopic quantity, in this case $v_a(\mathbf{k})$ or equivalently $\Omega(\mathbf{k})$, does not change considerably on the scale of δk . Weyl semimetals do not generically satisfy this requirement; if the Fermi energy is pinned to the Weyl points the singular $\Omega(\mathbf{k})$ dictates a diverging $v_a(\mathbf{k})$ at the Weyl nodes and, thus, its change on the scale of δk cannot be neglected. If, by contrast, the Fermi energy is far from the Weyl points, this divergence does not play an important role, and the electric field can be considered as a perturbation.

3.6 Hall effect in quantum critical systems

As discussed in Sect. 2.2, heavy fermion systems have been found where the static Kondo effect breaks down at a quantum critical point [12, 13]. This leads to pronounced features in the Hall effect. For magnetic field-driven quantum criticality in such systems, R_H can no longer be considered as the initial slope of $\rho_{xy}(B)$. This is because the magnetic field here plays a two-fold role of tuning the ground state, and providing the Lorentz force acting on the current. Thus, instead of R_H , the relevant quantity is the local slope \tilde{R}_H at any finite field B_0 , i.e.,

$$\tilde{R}_H(B_0) = \left. \frac{\partial \rho_{xy}}{\partial B} \right|_{B=B_0}, \quad (35)$$

leading to a Hall resistivity defined as

$$\rho_{xy}(B_0) = \int_0^{B_0} \tilde{R}_H(B) dB. \quad (36)$$

Indeed, in such systems, the initially linear $\rho_{xy}(B)$ shows a crossover to a second linear regime with a different slope (Fig. 21 a) [13, 64–66].

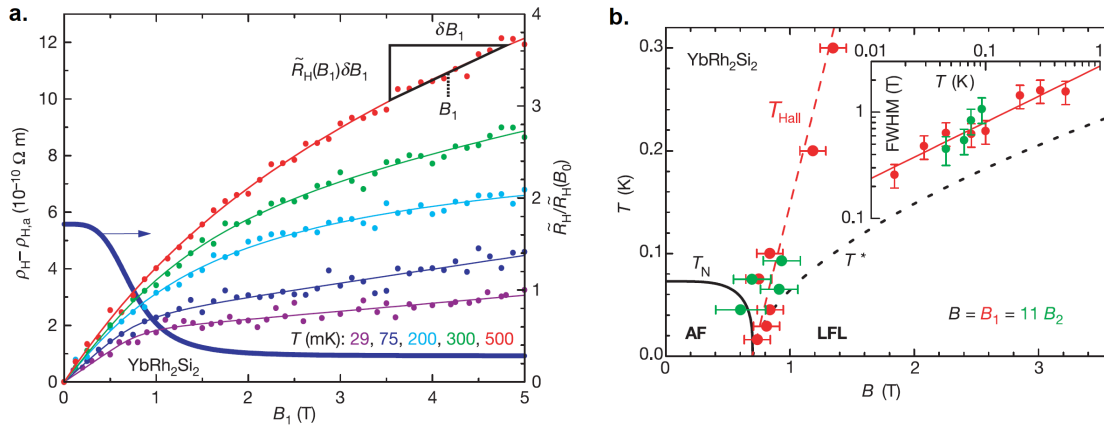


Figure 21: **Hall resistivity across a Kondo destruction quantum critical point in a heavy fermion system.** **a:** Isothermal $\rho_{xy}(B)$ curves across the quantum critical point of YbRh_2Si_2 at $B_c = 0.7\text{ T}$ (symbols, left axis). The field-dependent Hall coefficient corresponds to the local slope of the curve (black triangle on the red curve). Fits according to Eqn.36,37 are shown as solid lines. \tilde{R}_H obtained at $T = 75\text{ mK}$ according to Eqn.35 shows a broadened step at B_H (right axis). **b:** T - B Phase diagram of YbRh_2Si_2 . Both the temperature dependence of B_H (plotted as T_{Hall} , red symbols) and the FWHM of the crossover (inset) extrapolate to B_c and 0, respectively, in the zero temperature limit. Panels **a** and **b** are taken from [13].

A distinctive feature is that the crossover extrapolates to a sharp kink in $\rho_{xy}(B)$, and a step in $\tilde{R}_H(B)$, in the $T \rightarrow 0$ limit (Fig. 21 a). At finite temperatures, these features are broadened. In such a case, \tilde{R}_H is described by the empirical crossover function

$$\tilde{R}_H = R_H^\infty - (R_H^\infty - R_H^0) \left[1 + \left(\frac{B}{B_H} \right)^p \right]^{-1} \quad (37)$$

(see Fig. 21 a and [13]). Here B_{H} is the crossover field, R_{H}^0 and R_{H}^{∞} are the initial and final Hall coefficients at zero and infinite fields (below and above B_{H} , respectively), and p is a parameter related to the width of the crossover. Quantitatively, the latter is captured by the full width at half maximum (FWHM) of the second derivative of $\rho_{xy}(B)$ curves, that resembles a peak function in the low-temperature limit [13, 64]. Then, a tell-tale of a QCP scenario is that in the $T \rightarrow 0$ limit, B_{H} and the FWHM extrapolate to B_c and zero, respectively (Fig. 21 b).

4 The Kondo insulator $\text{Ce}_3\text{Bi}_4\text{Pt}_3$

Among the few known Kondo insulator systems [16] $\text{Ce}_3\text{Bi}_4\text{Pt}_3$ stands out due to the lack of any controversy regarding its Kondo insulating ground state. Indeed, a long series of studies spanning a wide range of experimental techniques, such as transport [81–84], thermodynamics [81, 82], magnetization [81, 82], spectroscopy [85–87], neutron scattering [88] and tuning studies [89–92], have firmly established the Kondo insulator ground state of $\text{Ce}_3\text{Bi}_4\text{Pt}_3$. Thus, while including all essential ingredients for correlation-driven topology, the clarity offered by this systems makes it especially attractive as a starting point in the path of realizing it. In this section, I present the most important properties of this compound based on the pioneering works cited above.

4.1 Crystal structure

$\text{Ce}_3\text{Bi}_4\text{Pt}_3$ crystallizes in the cubic noncentrosymmetric Th_3P_4 phase of space group $I\bar{4}3d$ (space group Nr. 220) with a lattice constant of $a = 10.051 \text{ \AA}$ (Sect. 5.1.3). Here, I stands for a body center structure, $\bar{4}$ denotes a 4-fold roto-inversion symmetry around the x -axis (and equivalently y and z), 3 means 3-fold rotational symmetry around the body diagonals (Fig. 22 a) and d indicates the presence of

a glide plane with respect to the face diagonals. This space group belongs to the highly symmetric tetrahedral point group T_d that has 24 symmetry elements in total (E , $8C_3$, $3C_2$, $6S_4$, $6\sigma_d$) [93]. Due to the presence of a glide plane, $\text{Ce}_3\text{Bi}_4\text{Pt}_3$ belongs to the class of nonsymmorphic crystals, that was recently predicted to host symmetry protected, topologically nontrivial electron structures in the strong electron interaction limit [94, 95].

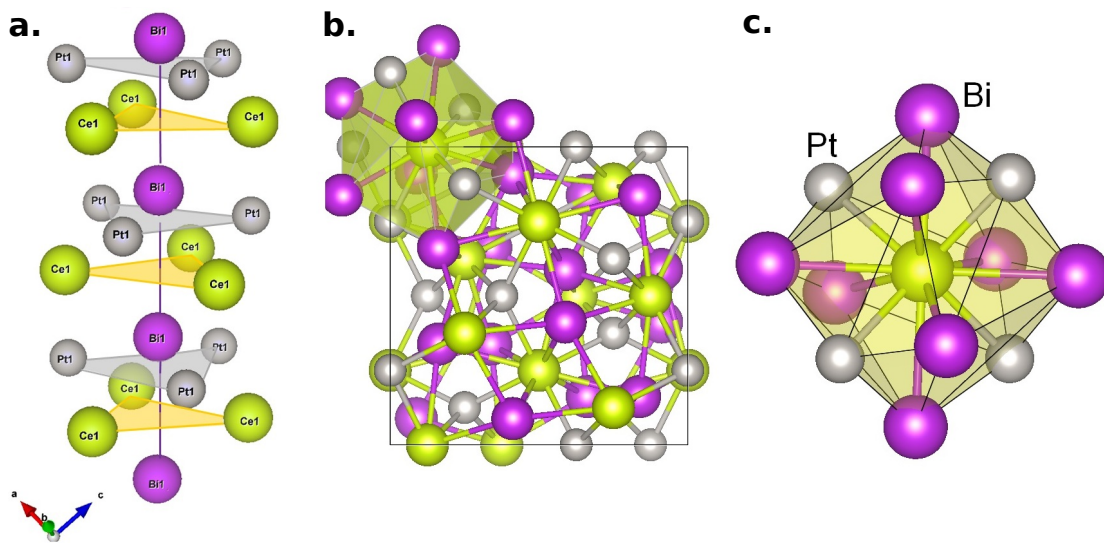


Figure 22: **Crystal structure of $\text{Ce}_3\text{Bi}_4\text{Pt}_3$.** **a:** A chain of Ce, Pt and Bi in the [111] direction demonstrating the 3-fold rotational symmetry of the $I\bar{4}3d$ space group. **b:** Unit cell of $\text{Ce}_3\text{Bi}_4\text{Pt}_3$ and close environment of a Ce atom (yellow polyhedron, top-left part) showing Ce, Pt and Bi atoms in yellow, grey and purple respectively. **c:** The close environment of the Ce atom in details. Four Pt first neighbours are located in a tetrahedral configuration, and eight Bi second nearest neighbours form the polyhedron.

The unit cell of $\text{Ce}_3\text{Bi}_4\text{Pt}_3$ contains four formula units, thus 40 atoms make up the rather complicated structure (Fig. 22 b). To better capture it, the local environment of the Ce atom — which is most essential in shaping the extraordinary physical properties of the compound (Sect. 4.2)— is presented in its position in the unit cell (Fig. 22 b) and alone, emphasizing the Pt and Bi positions (Fig. 22 c).

Each Ce atom is surrounded by 12 atoms (4 Pt and 8 Bi). However, Ce has only Pt atoms as nearest neighbours at 3.01 Å distance, arranged in a tetrahedral configuration. The second nearest neighbours are formed by 8 Bi atoms in a distorted polyhedral structure at a distance of 3.41 Å.

4.2 Physical properties

As mentioned in Sect. 2.2, the prime feature of Kondo insulators is the opening of a hybridization gap at the Fermi energy as temperature decreases. Such a Kondo gap opening is most directly observed in the temperature-dependent resistivity, due to the exponentially activated carrier concentration. Indeed, the electrical resistivity $\rho(T)$ in $\text{Ce}_3\text{Bi}_4\text{Pt}_3$ increases by two orders of magnitude with decreasing temperature down to $T = 4$ K (Fig. 23 a).

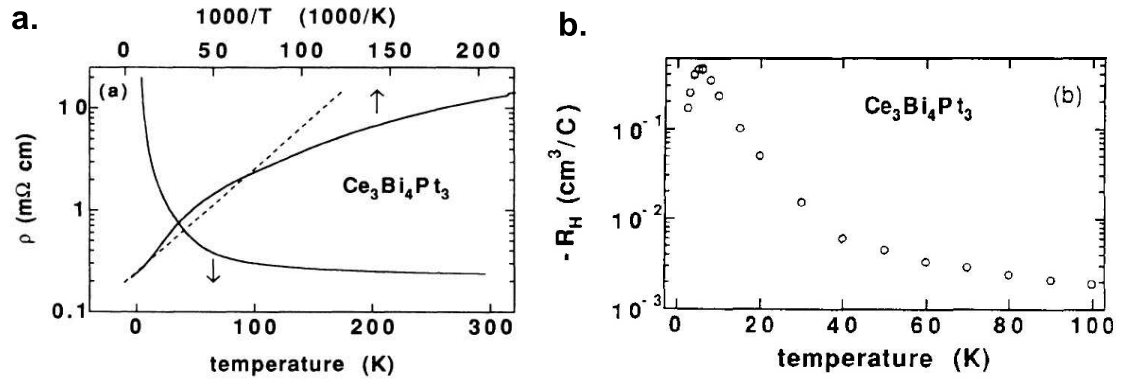


Figure 23: **Transport gap opening in $\text{Ce}_3\text{Bi}_4\text{Pt}_3$.** **a:** Temperature-dependent electrical resistivity in $\text{Ce}_3\text{Bi}_4\text{Pt}_3$ on a semi-logarithmic scale (bottom-left) shows a clear insulating behaviour. Arrhenius plot ($\log \rho$ vs. $1/T$, top scale) reveals an activated behaviour (linear relation, dashed line) down to $T = 50$ K. **b:** Low-field Hall coefficient for $\text{Ce}_3\text{Bi}_4\text{Pt}_3$ on a semi-logarithmic scale. Panels **a** and **b** are taken from [81] and [82], respectively.

The corresponding Arrhenius plot ($\log \rho$ vs. $1/T$) shows a linear regime from 300 to 50 K (Fig. 23 a), indicative of exponential activation across an energy gap

Δ with a characteristic temperature of $\Delta/2k_{\text{B}} \approx 70 \text{ K}$ [81]. Below $T = 50 \text{ K}$, the data cross over to another linear regime with a smaller slope corresponding to $\Delta/2k_{\text{B}} \approx 37 \text{ K}$ [91]. Optical spectroscopy studies confirm that it is this second gap that is associated with the development of Kondo coherence [85], which is further supported by magnetic field-dependent resistivity studies at high magnetic fields (Sect. 4.3). Finally, that the insulating behaviour seen in $\rho(T)$ is due to charge carrier density reduction is confirmed by temperature-dependent Hall coefficient measurements. These show a similar, two orders of magnitude increase on the same temperature scale (Fig. 23 b), which (in a single band picture) correspond to a reduction of the charge carrier concentration n from $n(100 \text{ K}) \approx 6 \cdot 10^{21} \text{ 1/cm}^3$ to $n(4 \text{ K}) \approx 10^{19} \text{ 1/cm}^3$.

That the observed activated behaviour of $\rho(T)$ is indeed driven by the Kondo interaction is supported by the fact that substituting La for Ce in $\text{Ce}_3\text{Bi}_4\text{Pt}_3$ drives the system into a metallic state (Fig. 24 a). Remarkably, even a minuscule value of La concentration amounting to $\sim 1\%$ is enough to suppress the 3 orders of magnitude increase of $\rho(T)$ at low temperatures (Fig. 24 a). This is because even small amounts of La disrupt the translational symmetry of the Ce sublattice, pointing to the importance of Kondo coherence in the gap formation.

The role of the Ce sublattice is further highlighted by temperature-dependent specific heat measurements (Fig. 24 b). C/T in $\text{Ce}_3\text{Bi}_4\text{Pt}_3$ is dominated by the phonon contribution down to the lowest temperatures, with an electronic term ($\gamma = 10 \text{ mJ/mol K}^2$) that is significantly smaller than in the nonmagnetic (and metallic) La reference compound ($\gamma = 30 \text{ mJ/mol K}^2$) [81]. This what is expected from a Kondo insulator, where the finite and small γ value is usually attributed to residual impurity-driven ingap bands [96].

Finally, a unique fingerprint in Kondo insulators is the simultaneous freezing out of charge and magnetic degrees of freedom at low temperatures [97]. Indeed,

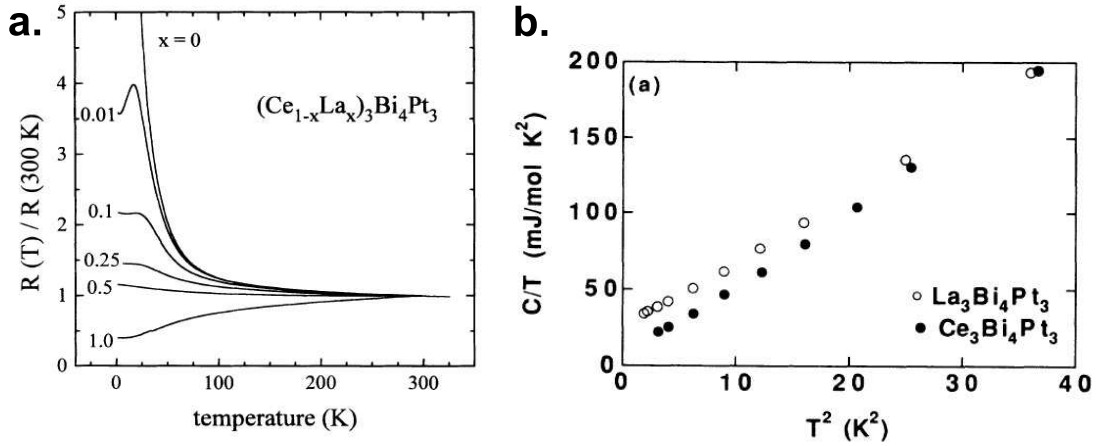


Figure 24: **La substitution in $\text{Ce}_3\text{Bi}_4\text{Pt}_3$.** **a:** Normalized temperature-dependent electrical resistance for various substitution levels x . With increasing La concentration the Kondo insulator gap collapses, and the system eventually turns into a metal. **b:** Temperature-dependent specific heat plotted as C/T vs. T^2 for $\text{Ce}_3\text{Bi}_4\text{Pt}_3$ (full symbols) and $\text{La}_3\text{Bi}_4\text{Pt}_3$ (open symbols). The temperature dependence of both is determined by the phonon background ($C/T \sim T^2$) and a Sommerfeld coefficient γ . The latter is considerably smaller for the Ce compound ($\gamma = 10\text{ mJ/mol K}^2$ vs. $\gamma = 30\text{ mJ/mol K}^2$ respectively). Panels **a** and **b** are taken from [89] and [81], respectively.

magnetic susceptibility measurements in $\text{Ce}_3\text{Bi}_4\text{Pt}_3$ clearly evidence the loss of magnetization at low temperatures (Fig. 25) [81, 86].

The magnetic susceptibility at high temperatures displays a Curie-Weiss ($\chi \sim 1/(T - \Theta)$) behaviour expected from localized moments in the incoherent regime. With further decreasing temperatures, this behaviour is successively suppressed after a local maximum at $T = 70\text{ K}$, (Fig. 25 a). The crossover from local magnetization to a suppressed magnetic state has also been confirmed by complementary techniques such as NMR (Fig. 25 b) [86] and neutron scattering [88] experiments. Notably, the local maximum in these magnetic probes coincides with the upturn of the resistivity and Hall coefficient (Fig. 23) and, thus, is clearly related to the

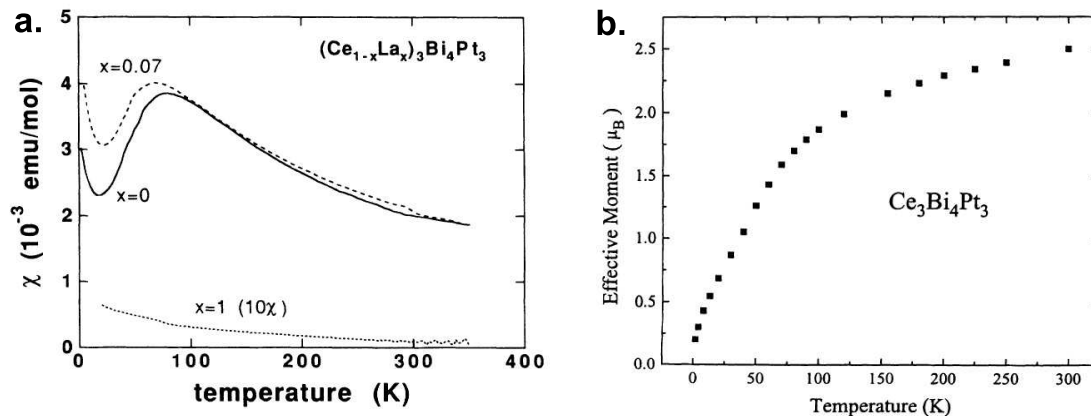


Figure 25: **Magnetic properties of $\text{Ce}_3\text{Bi}_4\text{Pt}_3$.** **a:** Magnetic susceptibility of $\text{Ce}_3\text{Bi}_4\text{Pt}_3$ (black curve), 7% La substituted $\text{Ce}_3\text{Bi}_4\text{Pt}_3$ (dashed line), and $\text{La}_3\text{Bi}_4\text{Pt}_3$ (dotted line). Data for $\text{Ce}_3\text{Bi}_4\text{Pt}_3$ show a local maximum at $T \approx 70$ K. It separates the high-temperature Curie-Weiss regime, from the spin-screened low-temperature regime. An upturn at the lowest temperatures is likely due to un-screened magnetic $4f$ impurities on the Ce site, which are a natural contamination of even high-purity Ce metals. **b:** Effective magnetic moment vs. temperature in $\text{Ce}_3\text{Bi}_4\text{Pt}_3$ shows the suppression of local magnetization. The data are obtained from isotropic Knight shift measurements. Panels **a** and **b** are taken from [81] and [86], respectively.

opening of the charge gap. This confirms the Kondo insulating ground state of this compound.

4.3 High magnetic field studies

Tuning studies in heavy fermion metals have proven essential in unravelling the mechanism stabilizing their exotic ground states [98]. In such an experiment, a non-thermal control parameter is varied to induce transitions between the ground states of these systems. In the Kondo insulator $\text{Ce}_3\text{Bi}_4\text{Pt}_3$, tuning by pressure [90] and chemical composition [89] have provided invaluable information about how the ground state is stabilized therein. In this section, I revisit magnetic field-tuning studies in $\text{Ce}_3\text{Bi}_4\text{Pt}_3$, and summarize how an applied large field collapses

the Kondo insulator gap. Due to the magnitude of the gap energies in Kondo insulators ($\Delta/k_B \approx 50 - 100$ K) [16], such tuning studies are typically done at high magnetic field facilities [91, 92, 99–102].

Because in Kondo insulators the opening of a charge gap is coupled to the opening of a spin gap [88, 97], an applied magnetic field with a corresponding Zeeman energy of $g\mu_B B \approx \Delta$ is expected to collapse the Kondo insulator gap [92]. Indeed, magnetic field-dependent resistivity measurements in $\text{Ce}_3\text{Bi}_4\text{Pt}_3$ confirm this scenario (Fig. 26) [91]. They show that, at low temperatures and high magnetic

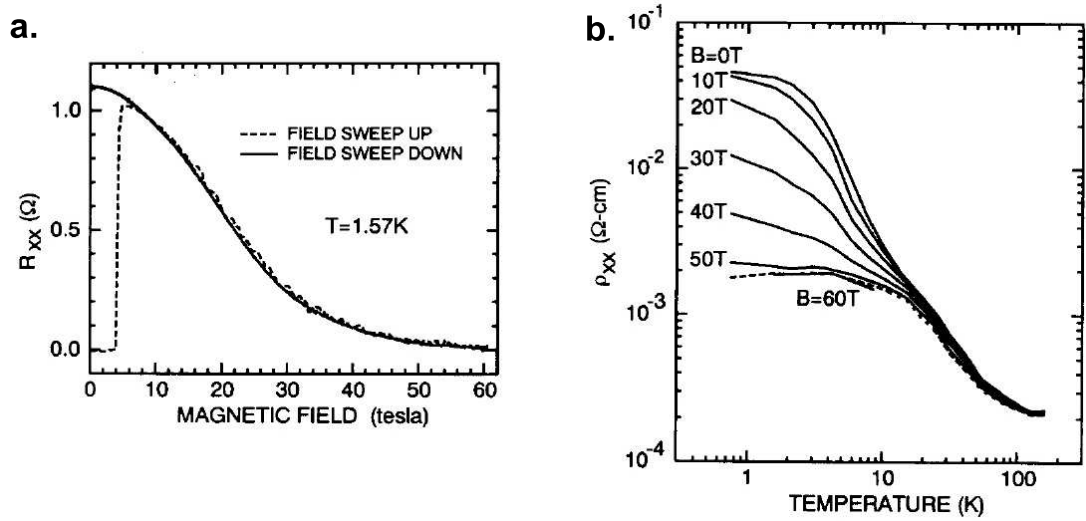


Figure 26: **Collapse of the Kondo insulator gap in $\text{Ce}_3\text{Bi}_4\text{Pt}_3$ at high magnetic fields.** **a:** Magnetic field-dependent electrical resistivity of $\text{Ce}_3\text{Bi}_4\text{Pt}_3$ up to $B = 60$ T at $T = 1.57$ K. The data show a strong suppression of the resistivity with increasing field. Zero resistance values for the sweep up curve is due to intentional grounding of the voltage leads at the beginning of the measurement. **b:** Iso-field electrical resistivity curves show a strong suppression of the resistivity below $T = 20$ K. Panels **a** and **b** are taken from [91].

fields, the resistivity is strongly suppressed above $B \approx 40$ T (Fig. 26 a). Similar behaviour has also been observed in other Kondo insulators such as SmB_6 [102] and YbB_{12} [99, 100]. Interestingly, the collapse of the resistivity upturn is observed

only for temperatures below $T = 20$ K (Fig. 26 b). Even for $B = 60$ T the temperature dependence remains non-metallic (Fig. 26 b). These observations suggest that the Kondo insulator gap opens only below $T \approx 20$ K out of a pseudo-gapped background bandstructure.

The gap collapse seen in the magnetic field-dependent electrical resistivity is also reflected in Hall effect measurements at high magnetic field (Fig. 27). The $\rho_{xy}(B)$ curve at the lowest temperatures shows a continuous suppression of the Hall resistivity with respect to the initial, large slope curve (Fig. 27 a). The extracted

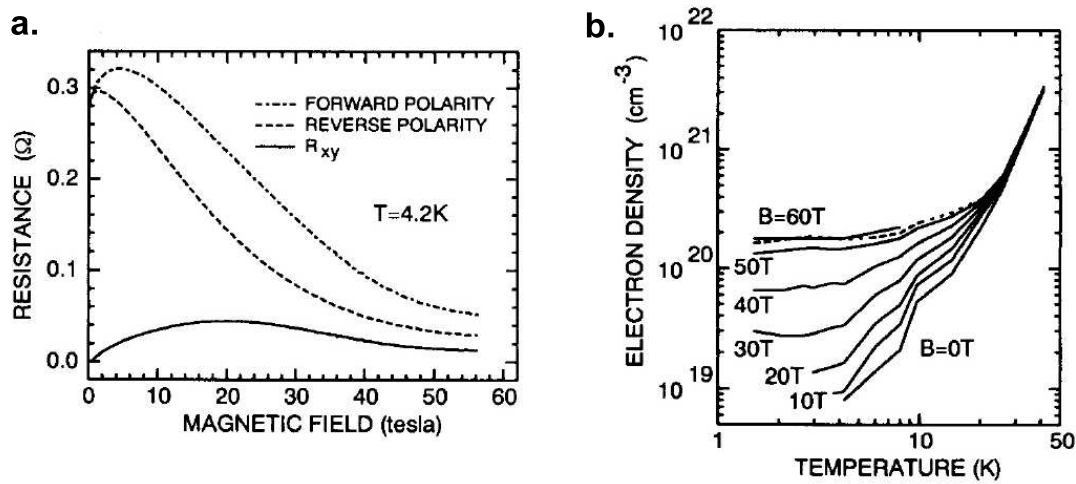


Figure 27: **Hall effect in $\text{Ce}_3\text{Bi}_4\text{Pt}_3$ at high magnetic fields.** **a:** Hall resistance vs. magnetic field (continuous line) obtained by antisymmetrizing the measured curves obtained during increasing and decreasing magnetic field (dash-dotted and dashed lines respectively). The data show a strong suppression of the slope of the curve (the differential Hall coefficient) with increasing field. **b:** Temperature dependence of the carrier concentration at different magnetic fields up to $B = 60$ T. The data are obtained from field-sweep curves such as that in panel **a**. The data show a strong field-induced increase of the carrier concentration below $T = 20$ K. Panels **a** and **b** are taken from [91].

iso-field curves of the carrier concentration (in a simple 1-band model) show a strong increase of the charge carrier concentration with increasing field, amounting

to almost two orders of magnitude at the lowest temperatures (Fig. 27 b). However, similar to iso-field $\rho(T)$ curves (Fig. 26 b), the increase in $n(T)$ is observed only for $T < 20$ K. Its value at $B = 60$ T is still significantly smaller than its room temperature value (Fig. 26 b).

Finally, the collapse of the Kondo insulator gap at high fields is further evidenced by thermodynamic probes [92]. Temperature-dependent specific heat measurements on $\text{Ce}_3\text{Bi}_4\text{Pt}_3$ show that the electronic contribution γ to C/T is enhanced significantly between 30 and 40 T (Fig. 28 a) [92]. This was interpreted as an abrupt emergence of a Fermi pocket in the relevant field range. Recent specific heat measurements in the Kondo insulator YbB_{12} at high magnetic fields show a similar behaviour (Fig. 28 b) [101]. These observations indicate that this characteristic might be generic for Kondo insulators. Finally, as I will show in Sect. 5.4.3, a similar, sharp feature appears also in the magnetization of $\text{Ce}_3\text{Bi}_4\text{Pt}_3$. It confirms that the collapse of the Kondo insulator gap is related to the liberation of the magnetic degrees of freedom, which are frozen in the Kondo insulating state.

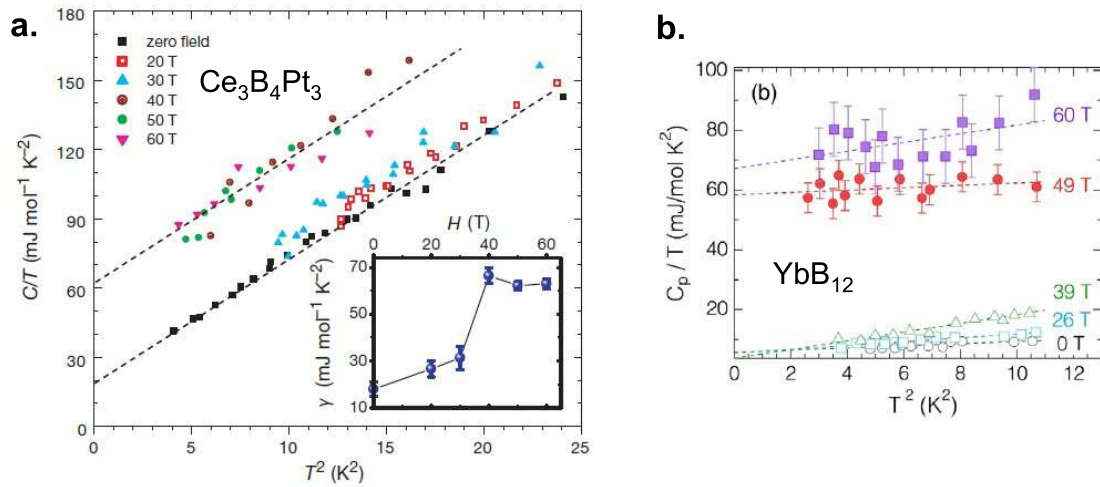


Figure 28: **Specific heat of Kondo insulators at high magnetic fields.** **a:** Iso-field data for $\text{Ce}_3\text{Bi}_4\text{Pt}_3$ are plotted as C/T vs. T^2 . They show a linear behaviour due to the phonon contribution and an abrupt change in the offset between 30 and 40 T. The inset shows the extracted Sommerfeld coefficient γ vs. B that highlights the jump. **b:** Similar data as in panel **a** for the Kondo insulator YbB_{12} . Panels **a** and **b** are taken from [92] and [101], respectively.

5 Results

5.1 Tuning the spin-orbit coupling in $\text{Ce}_3\text{Bi}_4\text{Pt}_3$

5.1.1 Introduction and principles

The proposal that Kondo insulators exhibit topologically nontrivial metallic surface states [103] was taken up enthusiastically and triggered many experimental studies, most notably on SmB_6 [104]. A key ingredient for a topologically nontrivial electronic structure in Kondo insulators is the strong spin-orbit coupling (SOC) of the heavy lanthanide $4f$ elements [103], but the importance of SOC of the conduction electrons that hybridize with the $4f$ electrons has also been demonstrated [105]. In studies of the periodic Anderson model, the latter was shown to tune between different phases, including topological and topologically

trivial Kondo insulators [105], Dirac-Kondo semimetals [106], and most recently, Weyl-Kondo semimetals [107]. To link such studies directly to an experiment, it would be highly desirable to find an experimental “tuning knob” for SOC in Kondo systems. In this thesis, I demonstrate for the first time the experimental tuning of the SOC strength λ_{SOC} in a Kondo insulator. This is achieved while keeping changes to other vital microscopic parameters such as the Kondo interaction strength, and chemical potential minimal.

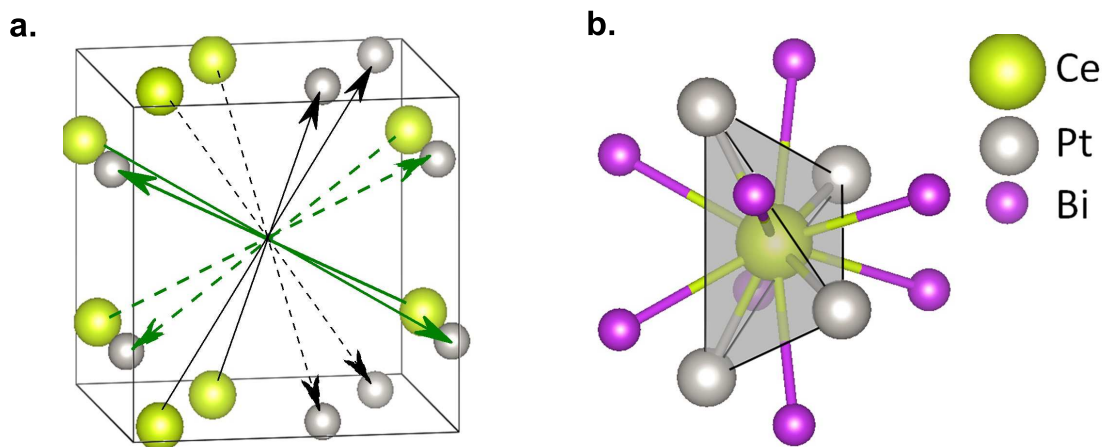


Figure 29: **Lack of inversion center in $\text{Ce}_3\text{Bi}_4\text{Pt}_3$.** **a:** Crystal structure of $\text{Ce}_3\text{Bi}_4\text{Pt}_3$ showing only (selected) Ce and Pt atoms. Both Ce and Pt atoms are directly involved in the broken inversion symmetry. **b:** Local environment of a Ce atom with the four nearest Pt (3.01 \AA) and eight nextnearest Bi (3.41 \AA) neighbours.

Among the archetypal cubic Kondo insulators that have been studied for decades [16], $\text{Ce}_3\text{Bi}_4\text{Pt}_3$ appears as an ideal starting material for tuning the SOC. As a Ce-based system, it represents the conceptually simple situation of a single $4f$ electron as the localized species. Its Kondo insulating ground state is well established and quite robust (Sect.4.2). Also, its noncentrosymmetric crystal structure (Fig. 29 a) makes this compound an ideal system to realize a topologically nontrivial electronic structure by tuning the λ_{SOC} . Interestingly, both the Ce and the Pt atoms

(which are most relevant for the Kondo interaction) are directly involved in defining the noncentrosymmetric structure (Fig. 29 a). Indeed, theoretical studies have suggested that $\text{Ce}_3\text{Bi}_4\text{Pt}_3$ hosts topologically nontrivial surface states [95, 103], but their experimental identification has remained elusive to date [108].

Generally, chemical substitution with atoms of sizeable mass difference seems to be a promising route for SOC tuning because the atomic number Z (or the mass) enters the SOC parameter as $\lambda_{\text{SOC}} \sim Z^4$ [109]. In Kondo insulators, however, a clever choice of the type of substitution has to be made. A substitution of the $4f$ element (Ce) breaks the translational symmetry of the local moment sublattice, which leads to a loss of Kondo coherence. To keep the Kondo lattice intact, substitutions should therefore be limited to the nonmagnetic elements (Bi and Pt). Most relevant for the Kondo interaction are the transition metal d electrons. Indeed, photoemission experiments evidence the presence of Pt $5d$ states near the Fermi level [110], suggesting that a substitution of Pt by another transition element would be most relevant. This is further underpinned by the fact that the Ce atoms in $\text{Ce}_3\text{Bi}_4\text{Pt}_3$ have only Pt as nearest neighbours (Fig. 29 b). The second constraint is that Kondo insulators, just as heavy fermion metals, react sensitively to even small changes of chemical pressure. Thus, to keep the Kondo coupling J_K tuning minimal, iso-size substitutions should be used. Finally, Kondo insulators being insulators naturally makes them react strongly to changes in electron count, and thus, in the chemical potential μ , which favours iso-electronic substitutions (without carrier “doping”).

Up to date no experimental attempts have been made to separate different tuning effects of J_K , μ and λ_{SOC} in chemically substituted Kondo insulators. For instance, in the Kondo semimetal CeNiSn , iso-electronic but non-iso-size substitutions of Ni by Pt or Pd close the Kondo (pseudo)gap as a consequence of the increased unit cell volume, and hence the decreased J_K [111, 112]. The (full) sub-

stitution of Bi in $\text{Ce}_3\text{Bi}_4\text{Pt}_3$ by the much lighter iso-electronic element Sb strongly enhances the Kondo insulator gap to 1080 K [113]. This must be due to the smaller size of Sb, which leads to a lattice constant reduction by 2.3% [113] and, thus, a stronger hybridization, similar to the gap opening under hydrostatic pressure [90]. In $\text{Ce}_3\text{Sb}_4\text{Pt}_3$, the non-isize and non-isoelectronic substitutions of Pt by Cu and Au both suppress the Kondo insulating state, although Cu doping results in a reduced [114] and Au doping in an increased unit cell volume [113]. Thus, here the change in μ dominates.

Surprisingly, no substitution series of $\text{Ce}_3\text{Bi}_4\text{Pt}_3$, other than Ce-La replacements [96, 115] has yet been studied. In this chapter, I present the crystal growth followed by transport and magnetization measurements on the series $\text{Ce}_3\text{Bi}_4(\text{Pt}_{1-x}\text{Pd}_x)_3$, and show that it ideally qualifies to study pure λ_{SOC} tuning in a Kondo insulator. The $4d$ transition metal Pd is much lighter than the $5d$ transition metal Pt (with an atomic weight of 106.42 instead of 195.084) and, thus, an increase of the Pd content x should sizably reduce the conduction electron λ_{SOC} . In fact, preliminary calculations show that $\lambda_{\text{SOC}}^{\text{Pd}}/\lambda_{\text{SOC}}^{\text{Pt}} \approx 0.38$ [116]. By contrast, as Pt and Pd are iso-electronic, there is also minimal μ tuning. Furthermore, as will be shown in the next subsection below, there is minimal J_{K} tuning.

5.1.2 Crystal growth of $\text{Ce}_3\text{Bi}_4(\text{Pt}_{1-x}\text{Pd}_x)_3$

In order to successively map out the effect of Pd substitution, Pd must be introduced to the parent compound $\text{Ce}_3\text{Bi}_4\text{Pt}_3$ lattice gradually. As a natural first step, the crystal growth of $\text{Ce}_3\text{Bi}_4\text{Pt}_3$ using the self flux growth method was adapted from the literature [117], and was further optimized within four steps: Single crystals of $\text{Ce}_3\text{Bi}_4\text{Pt}_3$ were synthesized by putting the elements together in a large (3 cm inner diameter) Al_2O_3 crucible, with a starting molar composition ratio of 1:1:12 (Ce:Pt:Bi). Here clearly the overstoichiometric Bi serves as the self-flux.

For the elemental Ce, care was taken not to introduce any impurities by carefully polishing the surface of the Ce chunk in an Ar glove box until it is shiny. The crucible was then placed in a quartz tube, pumped for 24 h to reach low pressures ($\approx 7 \times 10^{-5}$ mbar), then sealed with a torch under continuous pumping, and placed in a box furnace for the growth.

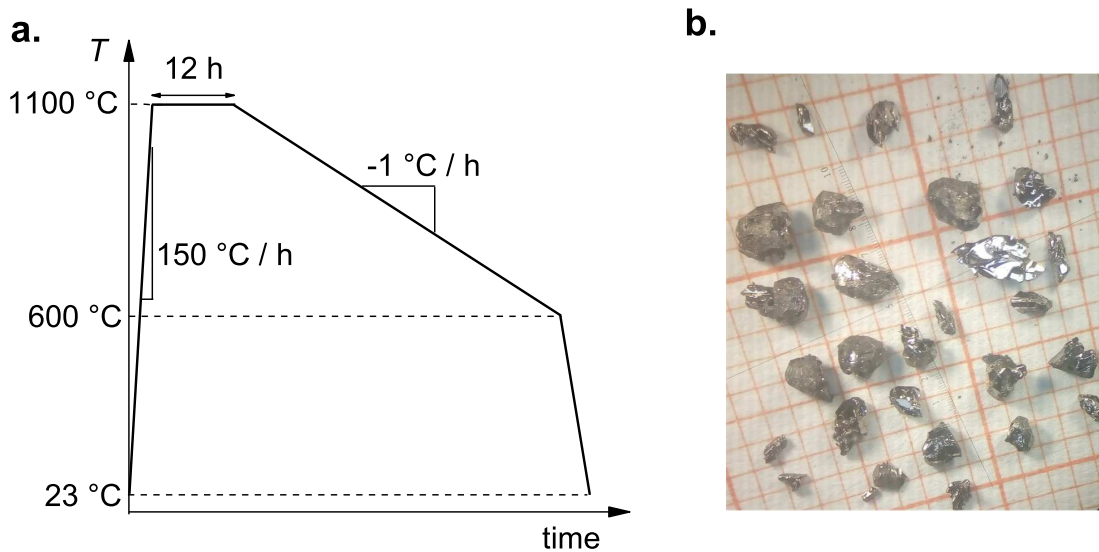


Figure 30: **Single crystal growth of $\text{Ce}_3\text{Bi}_4\text{Pt}_3$.** **a:** Temperature profile used for the growth of both Pt and later Pd compounds. **b:** Photograph of representative single crystals of $\text{Ce}_3\text{Bi}_4\text{Pt}_3$ obtained by the adapted self-flux technique, shown on millimetre paper.

The optimal temperature program is shown in Fig. 30 a. The crucible was heated up fast to 1100 °C and was kept there for 12 h. A very slow cooling rate of 1 °C/h down to 600 °C was found to increase the crystal size. As a result several grams of $\text{Ce}_3\text{Bi}_4\text{Pt}_3$ single crystals were obtained with characteristic sizes of $\sim 1.5 \times 1.5 \times 2 \text{ mm}^3$ as shown in Fig. 30 b.

While this protocol proved to be successful to grow $\text{Ce}_3\text{Bi}_4\text{Pt}_3$ (as far as the starting composition is concerned), it fails when it comes to the full Pd com-

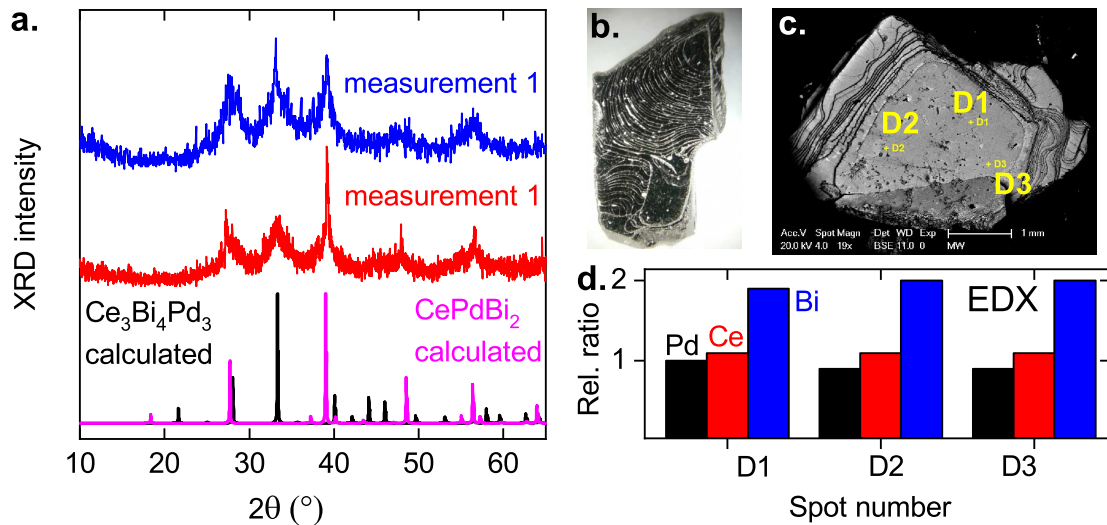


Figure 31: **Initial Bi self-flux attempts to grow $\text{Ce}_3\text{Bi}_4\text{Pd}_3$.** **a:** XRD patterns collected from the bottom and top parts of the crucible (blue and red), and compared with those expected from 3:3:4 and 1:1:2 stoichiometric phases (black and magenta curves). Crystals are obtained from high Bi excess flux (see text). **b:** Photograph of a typical, shiny, plate like crystal obtained from the growth. **c:** SEM image of a selected sample with three spots indicated for the EDX measurements. **d:** Relative atomic ratio of the elements obtained by EDX measurement. The x-axis denotes the three spots where the measurements were carried out as shown in c.

pond $\text{Ce}_3\text{Bi}_4\text{Pd}_3$. This is because for high Bi content, the primary stable phase is CePdBi_2 , as evidenced by powder X-ray diffraction (XRD) and Energy-dispersive X-ray spectroscopy (EDX) measurements obtained from such a growth (Fig. 31). The former shows weak intensity, non-crystalline features corresponding mainly to the 1:1:2 phase next to the minority 3:3:4 one (Fig. 31 a), while the latter identifies the corresponding shiny, plate-like crystals (Fig. 31 b) as the 1:1:2 stoichiometry phase (Fig. 31 c-d).

To check whether $\text{Ce}_3\text{Bi}_4\text{Pd}_3$ crystals grow at all using the Bi self flux method even for different growth parameters, fast polycrystalline growth directly from close-to-stoichiometric starting composition was attempted in an inductive RF-

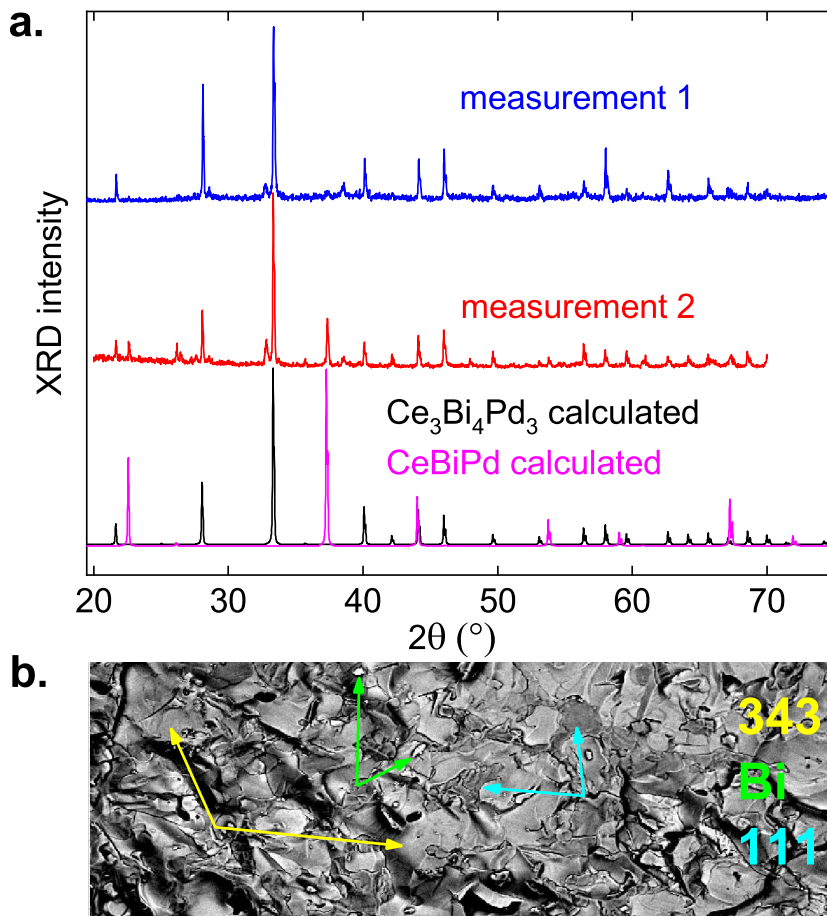


Figure 32: **RF-furnace melting of $\text{Ce}_3\text{Bi}_4\text{Pd}_3$.** **a:** XRD patterns obtained from top and bottom parts of the polycrystalline melt (blue and red) compared to expected patterns of $\text{Ce}_3\text{Bi}_4\text{Pd}_3$ and CePdBi (black and magenta curves). **b:** SEM image of the polycrystalline product, identifying the majority $\text{Ce}_3\text{Bi}_4\text{Pd}_3$ phase (intermediate gray areas, yellow arrows), minority CePdBi (dark gray areas, blue arrows) and Bi inclusions (light gray areas, green arrows).

furnace. The main advantage in this case is that the absence of the excess Bi flux suppress the growth of the 1:1:2 phase. Thus, growth experiments were conducted with only a small overstoichiometric Bi amount in the ratio of $\text{Ce}:\text{Pd}:\text{Bi} = 1:1:1.5$, which is very close to the 1:1:1.33 nominal ratio. XRD measurement on such powdered polycrystalline sample shows a clear signature of the formation of

$\text{Ce}_3\text{Bi}_4\text{Pd}_3$ next to a minority phase CePdBi (Fig. 32 a). By measuring different parts of the melt (measurements 1 and 2 in Fig. 32 a), it is clearly seen that the 3:3:4 phase is uniformly formed all over the melt, suggesting that it is indeed the primary phase. On the other hand the minority 1:1:1 phase formation is inhomogeneous (present only in measurement 2). This indicates, that CeBiPd is the primary stable phase only in the under stoichiometric Bi regime ($1:1:1.33-\delta$), (actually even for $\delta=0$). EDX measurements further confirm this, as they show that the majority of the melt is composed of $\text{Ce}_3\text{Bi}_4\text{Pd}_3$, with minor CePdBi and Bi inclusions as seen in Fig. 32 b.

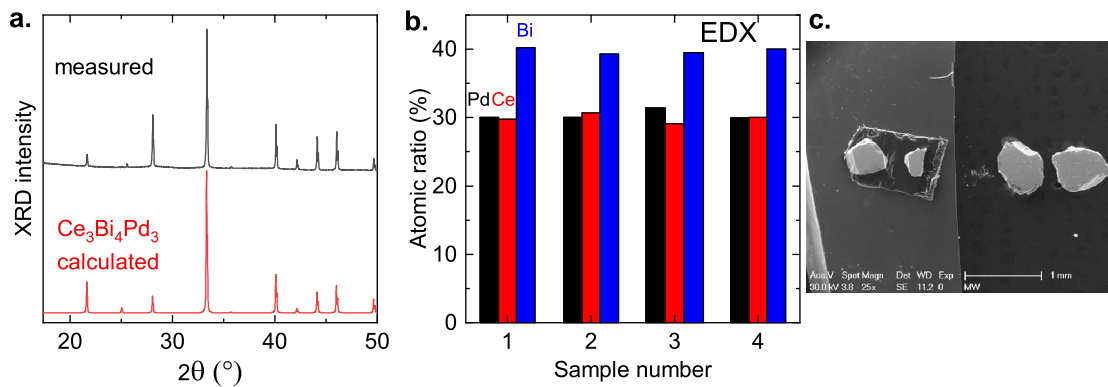


Figure 33: **Growth of $\text{Ce}_3\text{Bi}_4\text{Pd}_3$ using the self flux method.** **a:** Measured XRD pattern of the yielded crystals compared to that expected for $\text{Ce}_3\text{Bi}_4\text{Pd}_3$. **b:** Atomic ratio of Pd, Ce and Bi (black, red and blue bars, respectively) obtained from EDX spectroscopy. The x-axis corresponds to the four crystals (panel c) separated from the flux. **c:** SEM image of the four samples measured by EDX. The scale bar is 1 mm.

The successful crystallization of polycrystalline $\text{Ce}_3\text{Bi}_4\text{Pd}_3$ shows that, in principle, single crystal growth from a melt with a reduced Bi excess is possible. However, the optimal growth condition is dictated by the interplay of two competing mechanisms: 1) Whereas increasing the Bi excess reduces the melting temperature of $\text{Ce}_3\text{Bi}_4\text{Pd}_3$, it nevertheless favours the formation of the CePdBi_2 as the primary

phase and, thus, must be avoided. 2) on the other hand, decreasing the Bi content too much though suppresses the formation of the 1:1:2 phase, but also increases the melting temperature of the 3:3:4 phase, ultimately impeding its growth. As a consequence, the optimal condition (initial Bi concentration) of the growth is defined by the range of the primary crystallization of $\text{Ce}_3\text{Bi}_4\text{Pd}_3$, while every other secondary phase is absent (especially CePdBi_2 and CePdBi).

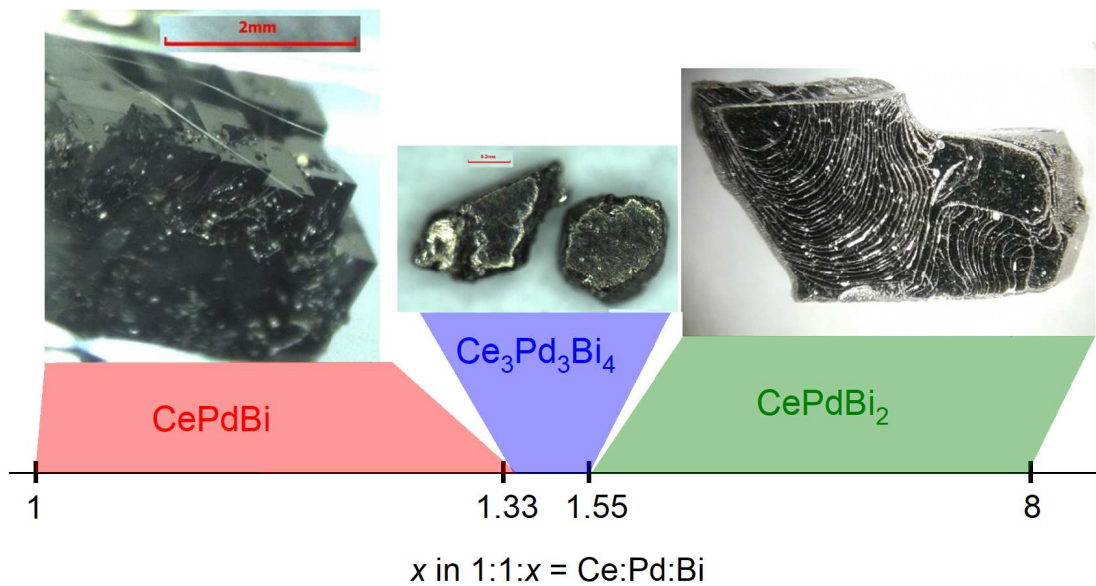


Figure 34: **Primary crystallizing phases of the Ce-Bi-Pd ternary system vs. relative Bi concentration.** The phase diagram is dominated by the 1-1-1 phase at low Bi- and the 1-1-2 phase at high Bi concentration. The desired $\text{Ce}_3\text{Bi}_4\text{Pd}_3$ phase grows only in a narrow range of relative Bi concentration. This phase diagram is experimentally observed for the temperature program shown in Fig. 30 a.

By mapping out the phase diagram, now with self flux method, as function of the relative Bi concentration, and identifying the present primary and secondary phases with XRD and EDX measurements, the optimum condition for the formation of $\text{Ce}_3\text{Bi}_4\text{Pd}_3$ is observed at relative Bi concentration of 1:1:1.55 (Fig. 33 and 34). Finally, I note, that with this protocol, only small single crystals with the

size of $\sim 400 - 500 \mu\text{m}$ in characteristic length, and irregular shape were possible to grow (Figs.33 c).

Table 1: Main crystallographic and ground state properties of various Ce-Bi-Pd ternary compounds obtained from Bi self-flux growth (Fig. 34). FM, AFM and SC denote ferromagnetic, antiferromagnetic and superconducting states, respectively.

compound	spacegroup	centrosymmetric	symmorphic	ordering
CeBiPd	cubic, $F\bar{4}3m$	No	Yes	FM + SC [118]
Ce ₃ Bi ₄ Pd ₃	cubic, $I\bar{4}3d$	No	No	No ordering
CeBiPd ₂	tetragonal $P4/nmm$	Yes	No	AFM [119]

5.1.3 Structural and chemical characterization of Ce₃Bi₄(Pt_{1-x}Pd_x)₃

Although XRD and EDX measurements clearly show the successful formation of both Ce₃Bi₄Pt₃ and Ce₃Bi₄Pd₃ phases, they don't provide information about whether the sample is a (preferred) mono domain or multi domain crystal. In order to investigate the crystal quality of the two end compounds, Laue diffraction measurements were performed on selected crystals of Ce₃Bi₄Pt₃ and Ce₃Bi₄Pd₃ (Fig. 35). Both show good-, mono domain single crystalline quality, evidenced by the discrete, dot like Laue pattern.

By choosing two differing growth techniques, I showed that both Ce₃Bi₄Pt₃ and Ce₃Bi₄Pd₃ can be grown. However, to obtain the solid solution Ce₃Bi₄(Pt_{1-x}Pd_x)₃, crystals with nominal Pd content of $0 > x > 0.4$ were grown using the Bi rich flux adapted to initially grow Ce₃Bi₄Pt₃. To investigate the chemical composition of the substitution, comparative EDX spectroscopy was performed on a series of Ce₃Bi₄(Pt_{1-x}Pd_x)₃ samples corresponding to different nominal x values (Fig. 36). Here, nominal x value means the starting composition of the melt, and true x value the final composition of the solid.

Figure36 shows a clear inverse correlation between the Pd and Pt EDX lines

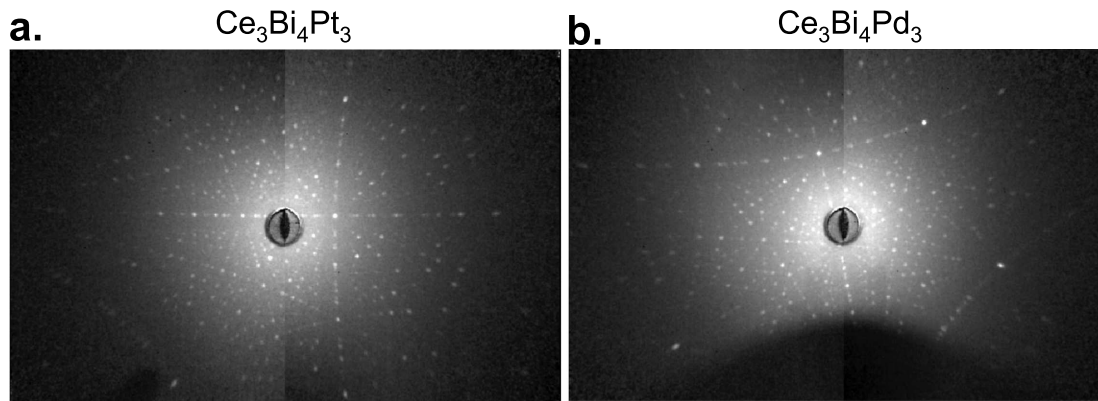


Figure 35: **Laue diffraction patterns of $\text{Ce}_3\text{Bi}_4\text{Pt}_3$ and $\text{Ce}_3\text{Bi}_4\text{Pd}_3$.** Images on representative crystals obtained from optimized growth protocols of $\text{Ce}_3\text{Bi}_4\text{Pt}_3$ (panel a) and $\text{Ce}_3\text{Bi}_4\text{Pd}_3$ (panel b) evidence single crystalline quality by the clear, point like pattern.

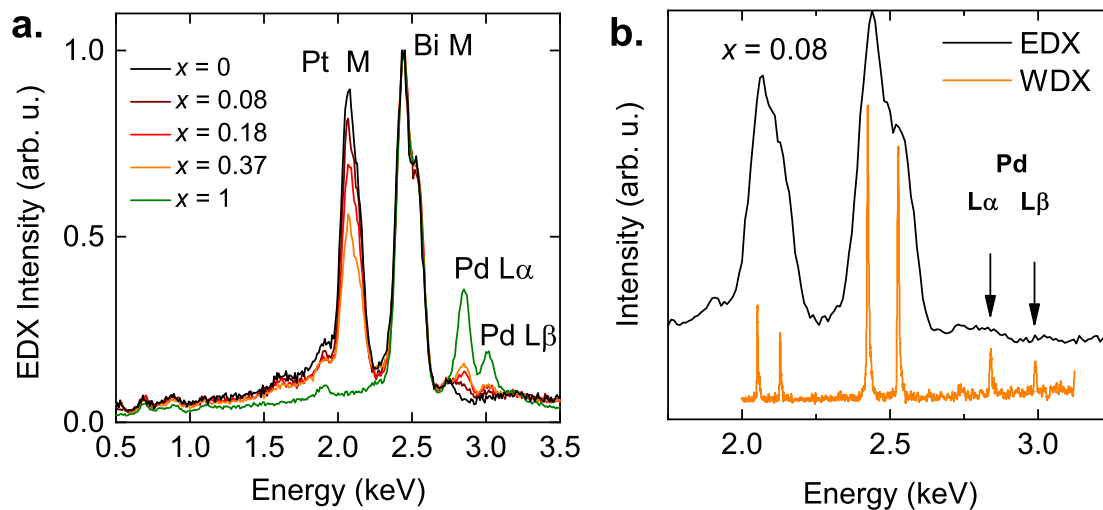


Figure 36: **EDX spectroscopy on $\text{Ce}_3\text{Bi}_4(\text{Pt}_{1-x}\text{Pd}_x)_3$.** **a:** Normalized EDX spectra of a series of $\text{Ce}_3\text{Bi}_4(\text{Pt}_{1-x}\text{Pd}_x)_3$ crystals with varying x values determined by quantitative EDX analysis. The peak intensities are normalized with respect to the Bi M-line. A clear inverse correlation is observed between the Pt M- and Pd L-peaks. **b:** WDX spectrum for the $x = 0.08$ compound (orange) compared to its EDX spectrum. The Pd lines are clearly resolved.

relative to the Bi M-line. This strongly indicates that Pd indeed substitutes Pt in the $\text{Ce}_3\text{Bi}_4(\text{Pt}_{1-x}\text{Pd}_x)_3$ compound. For low Pd content ($x < 10\%$) *Wavelength-Dispersive X-ray* spectroscopy (WDX) is also used (Fig. 36 b) to compensate for the low sensitivity of the EDX method.

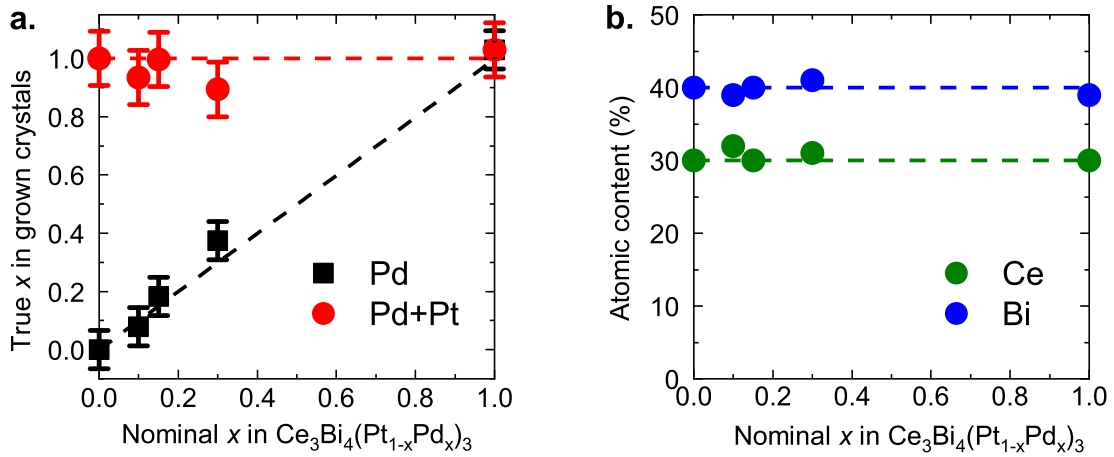


Figure 37: **Quantitative EDX analysis of $\text{Ce}_3\text{Bi}_4(\text{Pt}_{1-x}\text{Pd}_x)_3$.** **a:** Evolution of the Pd content x in crystals as determined by EDX measurements vs. its nominal value in the starting material. Dashed black line indicates the nominal values. Also the sum of the Pd and Pt atomic ratios (red symbols) and the nominal behaviour (red dashed line) are plotted. **b:** The evolution of Ce and Bi atomic ratios vs. nominal Pd content (symbols) compared to the nominal behaviour (dashed lines). Within error bars, the measured and nominal compositions largely agree.

Strong evidence that Pd indeed substitutes Pt in the crystal structure, is provided by the quantitative analysis of the elemental ratios of $\text{Ce}_3\text{Bi}_4(\text{Pt}_{1-x}\text{Pd}_x)_3$ (Fig. 37) as obtained from EDX spectra. The detected Pd quantity expressed in atomic ratio increases in a remarkable agreement with the expected behaviour, while the total Pd+Pt content does not change (Fig. 37 a). For that reason, throughout the remaining parts of this thesis, x indicates the Pd content as measured by EDX spectroscopy. Also evidenced by EDX spectroscopy is that neither the Ce nor the Bi content changes with varying the nominal (and EDX derived)

Pd ratio (Fig. 37b). This is a clear evidence that Pd indeed substitutes Pt on the Pt site, while leaving the Ce and Bi sites unaffected.

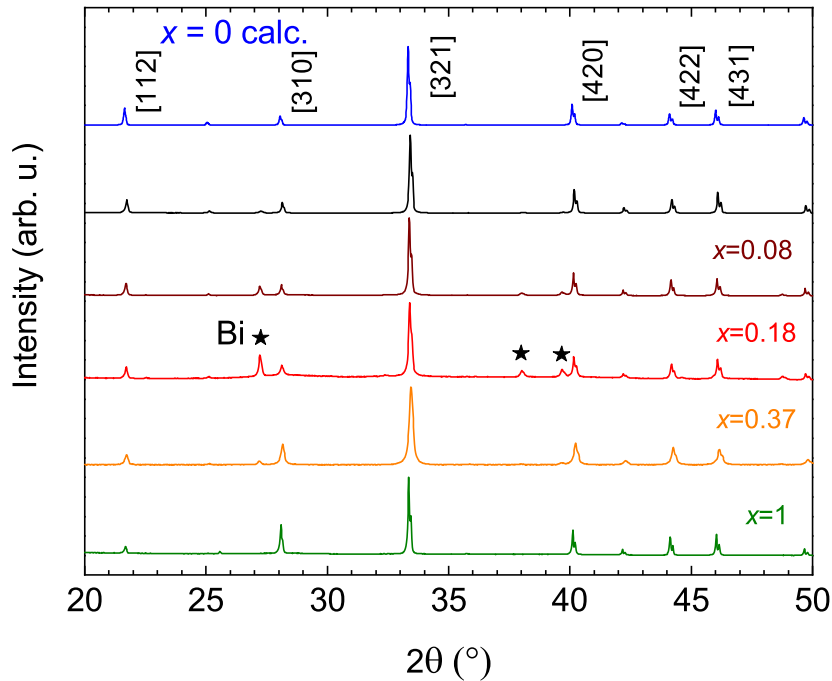


Figure 38: **X-ray diffraction patterns of $\text{Ce}_3\text{Bi}_4(\text{Pt}_{1-x}\text{Pd}_x)_3$.** The patterns for $x = 0 - 1$ agree well with the pattern calculated for $\text{Ce}_3\text{Bi}_4\text{Pt}_3$ (blue, top). No foreign phases are detected except for minor remnant Bi flux denoted by stars.

After discussing the chemical characterization, I address the crystal structure of $\text{Ce}_3\text{Bi}_4(\text{Pt}_{1-x}\text{Pd}_x)_3$. The crystal structure and unit cell parameters for each x composition were obtained from powder XRD diffraction measurements (Fig. 38). The result clearly shows that $\text{Ce}_3\text{Bi}_4(\text{Pt}_{1-x}\text{Pd}_x)_3$ crystallizes in the $I\bar{4}3d$ structure of the $\text{Ce}_3\text{Bi}_4\text{Pt}_3$ parent compound, thus realizing an iso-structural series.

To obtain quantitative information of the lattice constant, Rietfeld analysis on each XRD pattern was performed. In Fig. 39 I show how the lattice constant a changes with varying the Pd content in $\text{Ce}_3\text{Bi}_4(\text{Pt}_{1-x}\text{Pd}_x)_3$. Here, the change is defined as $\Delta a/a = [V(x)/V(x = 0)]^{(1/3)} - 1$, where $V(x)$ is the unit cell volume

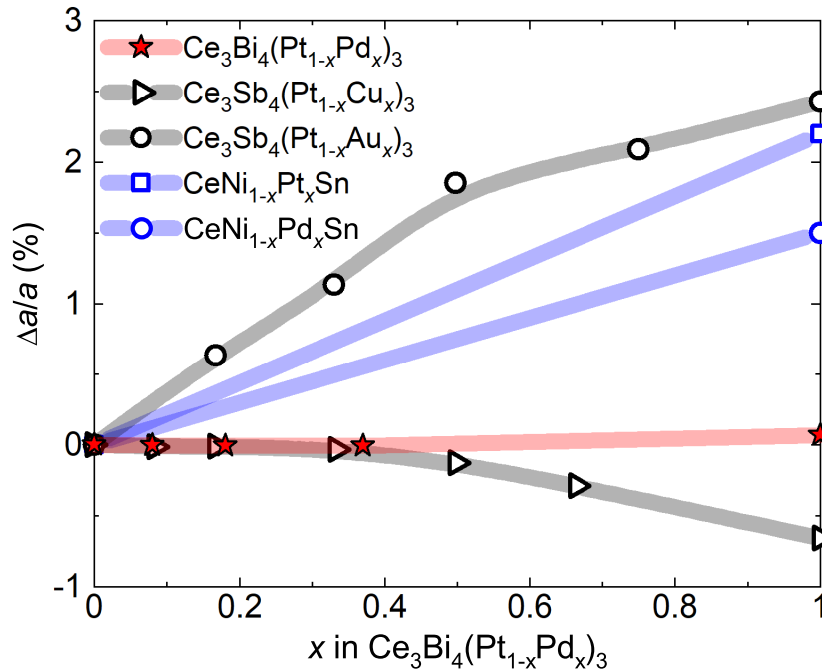


Figure 39: **Lattice constant evolution of $\text{Ce}_3\text{Bi}_4(\text{Pt}_{1-x}\text{Pd}_x)_3$.** The relative change in the average lattice constant $\Delta a/a$ vs. Pd content x . Here a indicates the lattice constant of $\text{Ce}_3\text{Bi}_4\text{Pt}_3$. The scale is defined by non-isosize substitution in related heavy fermion semimetals [111–114]. For $\text{Ce}_3\text{Bi}_4\text{Pd}_3$, the total change is as small as 0.069%.

at x Pd content. Surprisingly $\Delta a/a$ is negligible on a scale typical for non isosize substitutions in representative Kondo insulating/semimetallic systems. This is most prominent for the $\text{Ce}_3\text{Bi}_4\text{Pd}_3$ end compound, where the unit cell changes only 0.069% compared to the Pt compound, thus realizing an iso-size substitution. Here, I note that the obtained $a = 10.058\text{\AA}$ for $\text{Ce}_3\text{Bi}_4\text{Pd}_3$ agrees well with $a = 10.052\text{\AA}$ obtained for crystals grown with different growth technique [120].

In conclusion, qualitative and quantitative EDX and XRD measurements clearly show that Pd substitution in $\text{Ce}_3\text{Bi}_4(\text{Pt}_{1-x}\text{Pd}_x)_3$ represents an iso-structural and iso-size substitution series ruling out the chemical pressure (and hence a change in J_K) as the primary tuning parameter, whereas the identical

electron count of the Pd and Pt rules out charge doping. This allows to directly observe the effects of the changing spin-orbit coupling λ_{SOC} in a Kondo insulator for the first time.

5.1.4 Electrical transport in $\text{Ce}_3\text{Bi}_4(\text{Pt}_{1-x}\text{Pd}_x)_3$

In order to probe the evolution of the Kondo insulating gap with increasing Pd substitution in $\text{Ce}_3\text{Bi}_4\text{Pt}_3$, the temperature-dependent electrical resistivity at zero magnetic field was measured in single crystals of $\text{Ce}_3\text{Bi}_4(\text{Pt}_{1-x}\text{Pd}_x)_3$ with different x values (Fig. 40). Measurements in the temperature range of $T = 2 - 300$ K were done on several commercial and home built setups in ^4He cryostats. Standard four point contact method was used to determine the resistivity, using silver paint and spot welding techniques to secure point like contacts. All crystal surfaces were polished before contacting to avoid spurious surface effects, particularly the surface superconductivity of the $x = 1$ compound (see Sect.5.2). For typical contact geometries see Fig. 40 b. Contact misalignment contributions to the electrical and Hall resistivities are taken care of as discussed in Sect. 5.3.4.

The room temperature values of the resistivity for different x value vary between 180 to 350 $\mu\Omega\text{cm}$, in good agreement with the published value of 220 $\mu\Omega\text{cm}$ for $\text{Ce}_3\text{Bi}_4\text{Pt}_3$ [81]; small differences are attributed to the poorly defined geometrical factors of the small single crystals. Temperature-dependent resistance curves down to $T = 2$ K are plotted normalized to their room temperature values $R(T)/R(300\text{ K})$, and show a gradual suppression of the Kondo insulator gap with increasing Pd substitution (Fig. 40 a). The absolute values of the transport gap $\Delta = 2E_a$ can be quantified by fitting an exponentially activated resistance

$$R(T) = R_1 \exp[E_a/(k_B T)] . \quad (38)$$

Here R_1 is the asymptotic resistance at $T = \infty$, E_a is the activation energy

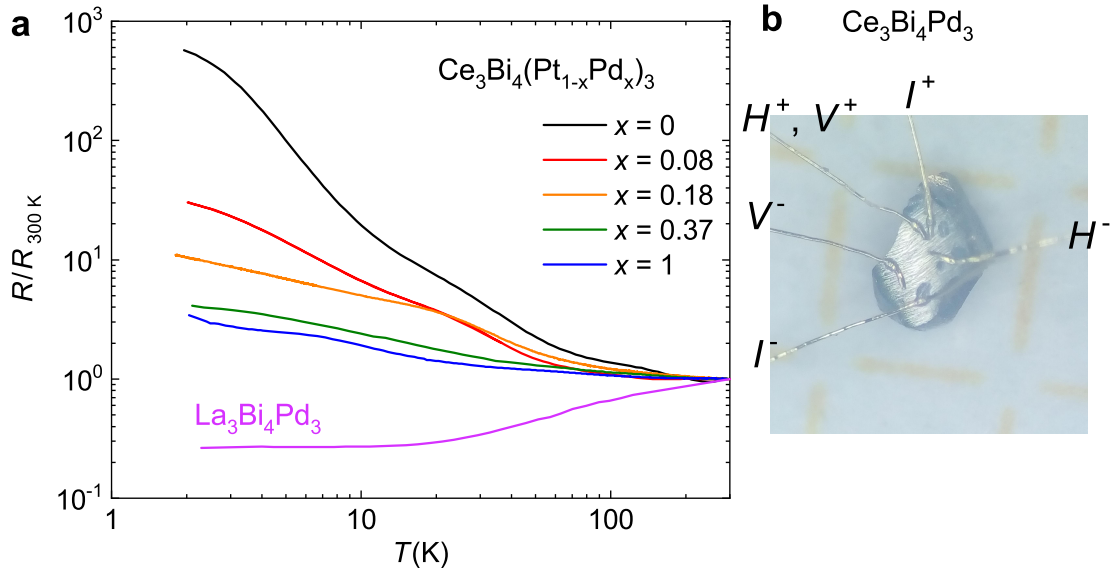


Figure 40: **Temperature-dependent normalized electrical resistance of $\text{Ce}_3\text{Bi}_4(\text{Pt}_{1-x}\text{Pd}_x)_3$.** **a:** The resistance normalized to the respective room temperature value, of all $\text{Ce}_3\text{Bi}_4(\text{Pt}_{1-x}\text{Pd}_x)_3$ samples increases with decreasing temperature, clearly distinct from the metallic behaviour of $\text{La}_3\text{Bi}_4\text{Pd}_3$. **b:** Photograph of $\text{Ce}_3\text{Bi}_4\text{Pd}_3$ single crystal contacted by spotwelding in a 5-wire configuration. I , V and H denotes (with polarity) the current, resistivity voltage and Hall resistivity voltage leads, respectively. Yellow length bar is 0.5 mm.

and k_B is the Boltzmann constant. Such fits hold for the high-temperature ($T = 300 - 50$ K) region of the Arrhenius plots (Fig. 41 a), and clearly show a reduction of E_a with increasing Pd content x (Fig. 41 b-f). For $\text{Ce}_3\text{Bi}_4\text{Pd}_3$, the activation energy of $E_a/k_B = 12.6$ K is smaller than the upper limit of the fit ($T \sim 50$ K) and, thus, rather indicates the absence of a well-defined gap, as will be addressed later in this chapter.

The collapse of the Kondo insulator gap and the emergence of a low carrier density in $\text{Ce}_3\text{Bi}_4\text{Pd}_3$ is also signalled in the temperature-dependent Hall coefficient R_H as shown in Fig. 42. At high temperatures, the R_H values of all studied $\text{Ce}_3\text{Bi}_4(\text{Pt}_{1-x}\text{Pd}_x)_3$ samples essentially coincide, and are $R_H \approx 10^{-3} \text{ cm}^3/\text{C}$

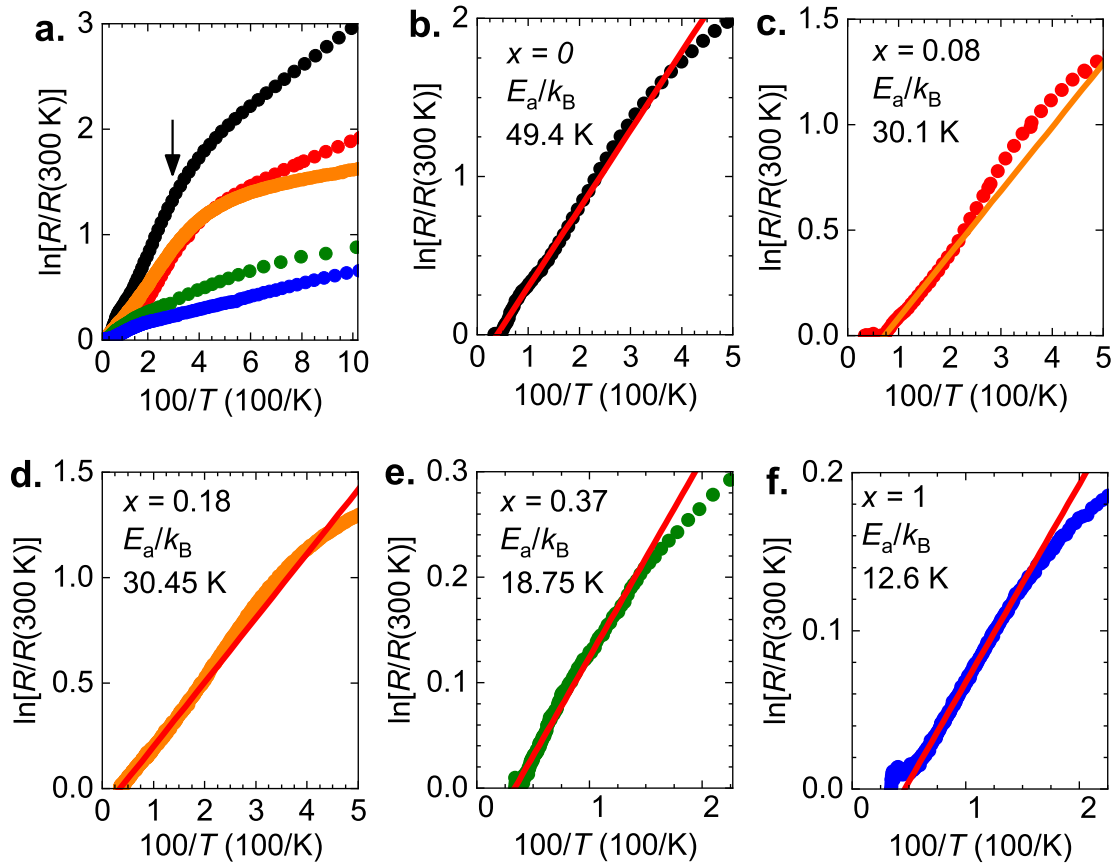


Figure 41: **Arrhenius plots for $\text{Ce}_3\text{Bi}_4(\text{Pt}_{1-x}\text{Pd}_x)_3$.** **a:** Arrhenius plots for all measured $\text{Ce}_3\text{Bi}_4(\text{Pt}_{1-x}\text{Pd}_x)_3$ single crystals in the temperature range of $T = 300 - 10$ K. Black arrow indicates the upper limit in $1/T$ below which, for $x = 0$, a linear behaviour is observed. **b - f:** High-temperature region of the Arrhenius plot for each measured compound of different x . Linear fits corresponding to exponentially activated behaviour (Eqn. 38) are shown as red, solid lines. Fits were made where a linear behaviour in the data is observed (see arrow in panel **a**). Extracted activation energies E_a/k_B are indicated in each panel.

($n = 6 \cdot 10^{21} \text{ cm}^{-3}$) at room temperature. For $\text{Ce}_3\text{Bi}_4\text{Pt}_3$, R_H increases substantially with decreasing temperature due to the Kondo insulator gap opening, and reaches $R_H \approx 2 \text{ cm}^3/\text{C}$ ($n = 3 \cdot 10^{18} \text{ cm}^{-3}$) at $T = 2$ K. On the contrary, for $\text{Ce}_3\text{Bi}_4\text{Pd}_3$ the Hall coefficient reaches only $R_H \approx 10^{-1} \text{ cm}^3/\text{C}$ ($n = 6 \cdot 10^{19} \text{ cm}^{-3}$) at $T = 2$ K, a considerably smaller value than that of $\text{Ce}_3\text{Bi}_4\text{Pt}_3$. This clearly

points to the presence of an extra density of states. That such extra states are Kondo-driven is further confirmed by a comparison with the nonmagnetic reference compound $\text{La}_3\text{Bi}_4\text{Pd}_3$. There the carrier density reaches values as high as $n = 2.1 \cdot 10^{22} \text{ cm}^{-3}$ ($R_H = 2.93 \cdot 10^{-4} \text{ cm}^3/\text{C}$), as seen in Fig. 42.

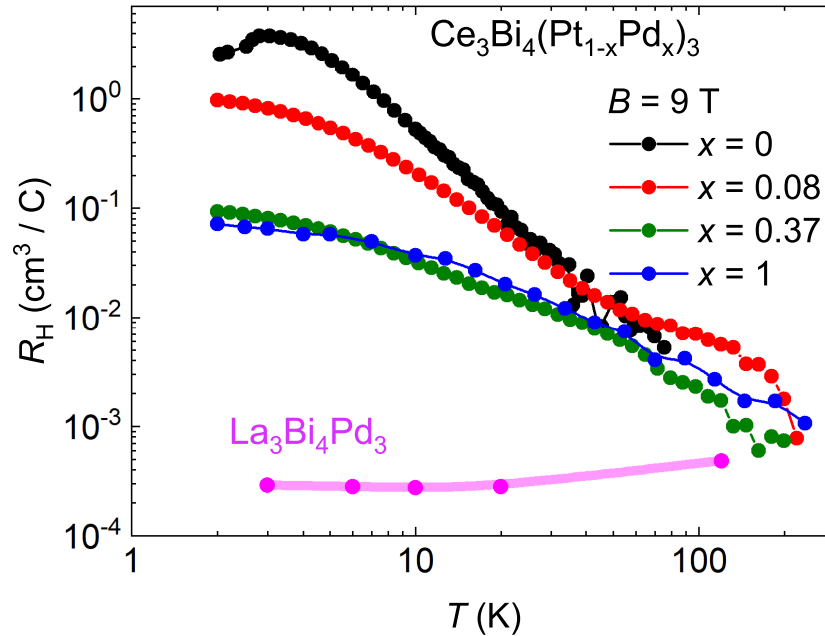


Figure 42: **Hall coefficient of $\text{Ce}_3\text{Bi}_4(\text{Pt}_{1-x}\text{Pd}_x)_3$.** Temperature dependence of the Hall coefficient at $B = 9 \text{ T}$ defined as $R_H = \rho_{xy}(9\text{T})/9\text{T}$. The temperature-dependent Hall coefficient of $\text{La}_3\text{Bi}_4\text{Pd}_3$ is also shown. There, data (magenta symbols) are taken from the slope of linear fits to iso-T $\rho_{xy}(B)$ curves. The magenta line is a guide to the eyes.

In what follows, I show that the weak temperature dependence of the electrical resistivity $\rho(T)$ and Hall coefficient $R_H(T)$ of $\text{Ce}_3\text{Bi}_4\text{Pd}_3$ at low temperatures are incompatible with a gapped ground state. Instead, they provide support for a semimetal ground state of $\text{Ce}_3\text{Bi}_4\text{Pd}_3$. Figure 43 displays the data in Arrhenius plots. Analogues to the temperature dependence of the resistance (Eqn. 38), the Hall coefficient is considered to be described by

$$R_H(T) = R_{H,1} \exp[E_a/(k_B T)] . \quad (39)$$

Two essentially linear regimes, representing activated behaviour of the resistivity and Hall coefficient in panels **a** and **b**, respectively, can be identified at high and intermediate temperatures (red and blue solid lines), but at temperatures below about 10 K, the data tend to saturate and, thus, strongly deviate from these laws. These linear ranges should not be taken as strong evidence for the presence of well-defined energy gaps because they persist only in limited temperature ranges, and the condition that the activation energy is much larger than the lower-temperature bound of the fitting range is not fulfilled in all cases.

If one nevertheless assumes the fits to be meaningful, a possible interpretation goes as follows. The high-temperature behaviour could represent activation across an energy gap ($\Delta = 2E_a$) in the uncorrelated bandstructure, though DFT calculations predict a gap of much larger size (150 meV, see [121]). The activated behaviour at intermediate temperatures might reflect the incipient formation of a Kondo insulator gap of reduced size. The deviation of the data from this law below about 10 K then points to the formation of small Fermi pockets in a gapped (Kondo insulating) background, which is further supported by the small observed residual charge carrier concentration n_0 (Fig. 43 b). Recent DFT+DMFT calculations indeed find $\text{Ce}_3\text{Bi}_4\text{Pd}_3$ to be a topological semimetal [122]. Thus, in conclusion, the limited ranges of activated behaviour seen in the transport experiments, and the deviation from such a law at low temperatures reflect the evolution of a correlation-driven semimetal ground state in $\text{Ce}_3\text{Bi}_4\text{Pd}_3$. This is further supported by the marked difference between the low carrier density, semimetallic character of the resistivity and Hall coefficient of $\text{Ce}_3\text{Bi}_4\text{Pd}_3$ when compared to the metallic, high carrier density nonmagnetic reference compounds $\text{La}_3\text{Bi}_4\text{Pd}_3$ (Figs. 40,42), clearly pointing to the Kondo effect as an important mechanism at play.

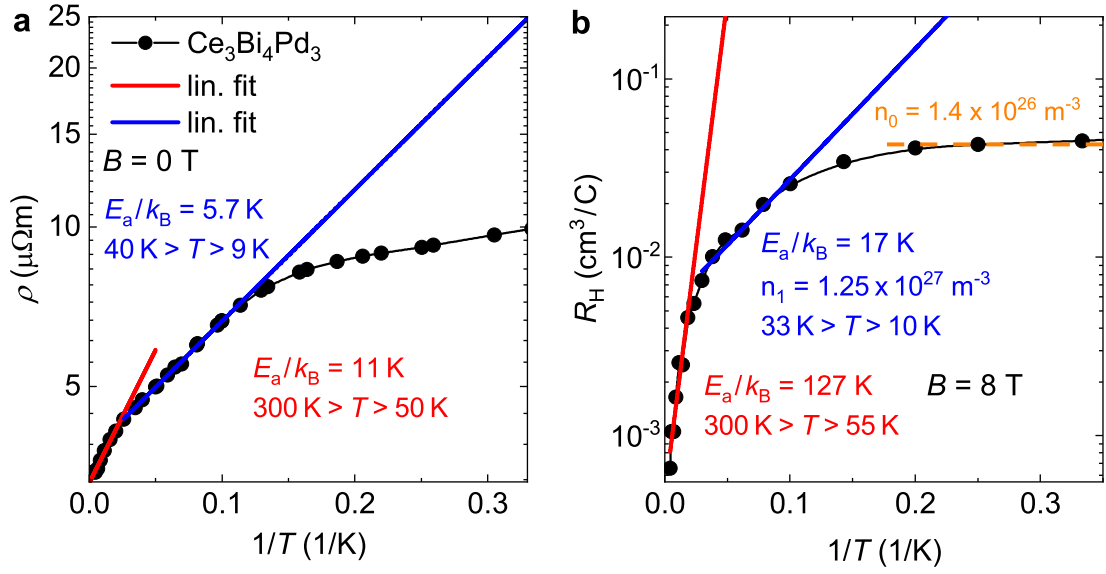


Figure 43: **Analysis of thermally activated transport behaviour.** **a:** Arrhenius plot of the zero-field resistivity of $\text{Ce}_3\text{Bi}_4\text{Pd}_3$ (black symbols). Linear behaviour (red and blue solid lines, corresponding to fits with Eqn. 38) is observed in two different temperature ranges as indicated. **b:** Same plot and analysis as in **a** for the Hall coefficient R_H which is here defined as $\rho_{xy}(B)/B$ at 8 T. Because $\rho_{xy}(B)$ is essentially linear in B for fields up to 8 T and temperatures down to 3 K (Fig. 78 a) this is very similar to the linear-response Hall coefficient. At lower temperatures, an anomalous Hall contribution appears. We then understand the data as the sum of a linear-in- B normal Hall effect, of the magnitude of that at 3 K, plus the anomalous contribution (Fig. 78 a). The fits use Eqn. 39, with the charge carrier concentration $n_1 = 1/(R_{H,1}e)$, which assumes a simple one-band model. Below 9 K, both datasets depart from the activation laws. At low temperatures, the R_H data saturate to a constant value (dashed orange line) which corresponds to the charge carrier concentration n_0 (again in a one-band model). The data are for a sample of the same batch as the $x = 1$ crystal in Figs. 40,42.

5.1.5 Magnetic susceptibility in $\text{Ce}_3\text{Bi}_4(\text{Pt}_{1-x}\text{Pd}_x)_3$

In Kondo insulators, the temperature-dependent magnetic susceptibility shows a Curie-Weiss type behaviour at high temperatures that, after a broad local maximum, is strongly suppressed as the Kondo insulator gap fully develops (see Sect. 4.2). Thus, to investigate the evolution of the Kondo insulator to semimetal

crossover in the substitution series, temperature-dependent magnetic susceptibility measurement were carried out for $\text{Ce}_3\text{Bi}_4(\text{Pt}_{1-x}\text{Pd}_x)_3$. Measurements were done using commercial ^4He DC SQUID and vibrating sample magnetometers (VSM). Measurements below $T = 2\text{ K}$ were performed with a ^3He insert of the DC SQUID magnetometer. A small field of $B = 100\text{ mT}$ was applied to measure the magnetization except for the $x = 0.37$ crystal, where a field of 7 T had to be applied due to the small sample mass. For $\text{Ce}_3\text{Bi}_4\text{Pd}_3$ 13 pieces of crystals from the same batch were measured due to the small crystal size.

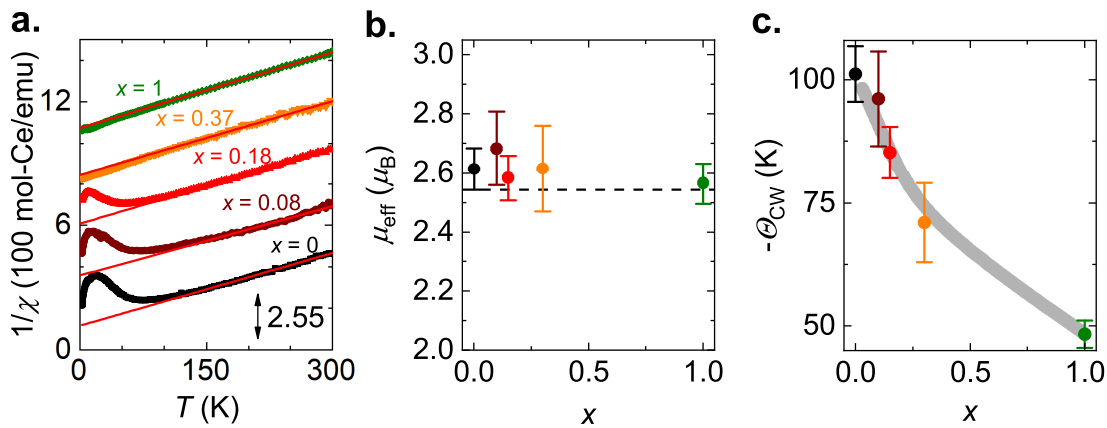


Figure 44: **Curie-Weiss behaviour of $\text{Ce}_3\text{Bi}_4(\text{Pt}_{1-x}\text{Pd}_x)_3$ at high temperatures.** **a:** Inverse magnetic susceptibility of $\text{Ce}_3\text{Bi}_4(\text{Pt}_{1-x}\text{Pd}_x)_3$ vs. T . Curie-Weiss fits were done in the range $T = 150 - 300\text{ K}$ (red lines). The data are shifted successively by an offset of 2.55 for clarity (size is indicated by the double arrow). **b:** The obtained effective moment μ_{eff} vs. the Pd content x . The full Ce^{3+} moment $\mu_{\text{eff}} = 2.54\mu_B$ is indicated by a horizontal dashed line. **c:** The obtained absolute value of the negative Curie-Weiss temperature Θ_{CW} vs. the Pd content x . Gray line is a guide to the eyes. The colour code in panels **b** and **c** corresponds to that of panel **a**. Error bars in panels **b** and **c** reflects errors of the fitting, measurement and sample mass.

The high-temperature ($150\text{--}300\text{ K}$) magnetic susceptibility of crystals corresponding to all substitution values x follows the Curie-Weiss behaviour

$$\chi(T) = \frac{\mu_B^2 \mu_{\text{eff}}^2 N_{\text{Ce}}}{3k_B} \frac{1}{T - \Theta_{\text{CW}}} , \quad (40)$$

as seen in Fig.44 a. Here μ_B is the Bohr magneton, μ_{eff} is the effective magnetic moment, k_B is the Boltzmann constant, N_A is the Avogadro number, N_{Ce} is the number of Ce^{3+} ions in a mol formula unit, and Θ_{CW} is the Curie-Weiss temperature. The obtained μ_{eff} values from high-temperature fits agree within error bars with the value of $2.54 \mu_B$ expected for a free Ce^{3+} ion (Fig. 44 b). Θ_{CW} , which is a measure of the strength of antiferromagnetic (AFM) correlations, decreases continuously in absolute value (Fig. 44 c), but remains sizeable even for the $x = 1$ sample. This is in sharp contrast to the Au-Pt and Cu-Pt substitutions in $\text{Ce}_3\text{Sb}_4\text{Pt}_3$, which suppress Θ_{CW} from 647 K in $\text{Ce}_3\text{Sb}_4\text{Pt}_3$ to less than 3 and 1 K in $\text{Ce}_3\text{Sb}_4\text{Au}_3$ [113] and $\text{Ce}_3\text{Sb}_4\text{Cu}_3$ [114], respectively.

As the Kondo insulator gap is successively suppressed with increasing Pd content, the low-temperature magnetic susceptibility increases (Fig. 45). This is accompanied by a shift of the position of the local maximum T_{max}^x in $\chi(T)$ towards lower temperatures, from $T_{\text{max}}^x = 75$ K in $\text{Ce}_3\text{Bi}_4\text{Pt}_3$ until $T_{\text{max}}^x \sim 10$ K in $\text{Ce}_3\text{Bi}_4\text{Pd}_3$. Here I note that no T_{max}^x can be discerned for the $x = 0.37$ compound. Because of the tiny crystal size of this substitution value, a large magnetic field of $B = 7$ T was applied (opposed to $B = 0.1$ T in case of other x values) to obtain a good quality $\chi(T)$ signal which, in turn, likely suppresses the local maximum feature.

Generally, the occurrence of a maximum at T_{max}^x and the deviation of $\chi(T)$ from a Curie-Weiss law indicates the onset of the heavy fermion state, and specifically in $\text{Ce}_3\text{Bi}_4\text{Pt}_3$ the opening of the Kondo insulator gap (Sect.4.2). Then, the collapse of the gapped state upon going from $x = 0$ to $x = 1$ in $\text{Ce}_3\text{Bi}_4(\text{Pt}_{1-x}\text{Pd}_x)_3$ identifies the appearance of a finite density of states at the Fermi energy, in agreement with the results of the resistivity and Hall effect measurements (Figs.40,42). Further

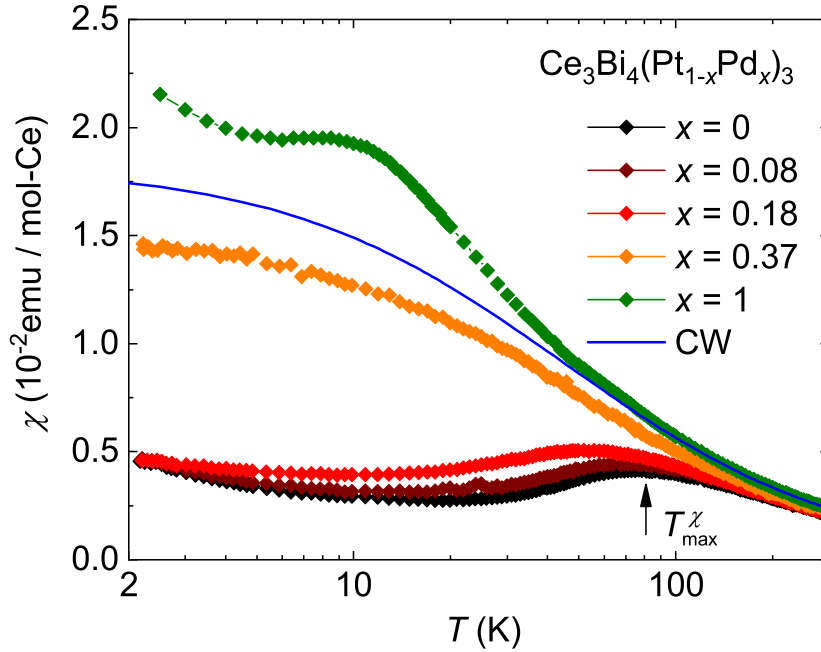


Figure 45: **Temperature-dependent magnetic susceptibility of $\text{Ce}_3\text{Bi}_4(\text{Pt}_{1-x}\text{Pd}_x)_3$.** The data were taken at $B = 100$ mT, except for $x = 0.37$, where $B = 7$ T was applied to obtain a good signal from the tiny single crystals. The blue curve shows the Curie-Weiss behaviour for $x = 0$, obtained from Fig. 44 a. The position of the local maximum T_{max}^χ is indicated for the $x = 0$ curve.

more, the observed $T_{\text{max}}^\chi \sim 10$ K in $\text{Ce}_3\text{Bi}_4\text{Pd}_3$ (Fig. 45) is reflected in the $\rho(T)$ curve as broad Kondo peak at $T \sim 8$ K (Fig. 40), which directly evidences the coupling of magnetic moments to the conduction electrons.

Finally, to address the weak upturn of the magnetic susceptibility below $T = 4$ K of $\text{Ce}_3\text{Bi}_4\text{Pd}_3$ (Fig. 45), measurements of $\chi(T)$ and $M(B)$ curves were extended down to $T = 0.4$ K (Fig. 46 a). They evidence that $\chi(T)$ at 100 mT increases logarithmically with decreasing temperature below $T = 2$ K (Fig. 46 a), and is suppressed at $B = 7$ T to an enhanced, temperature independent Pauli susceptibility expected in heavy fermion metals. In the iso- T $M(B)$ curves, the upturn in $\chi(T)$ manifests as a weak, broad feature at small field (Fig. 46 b), that recovers

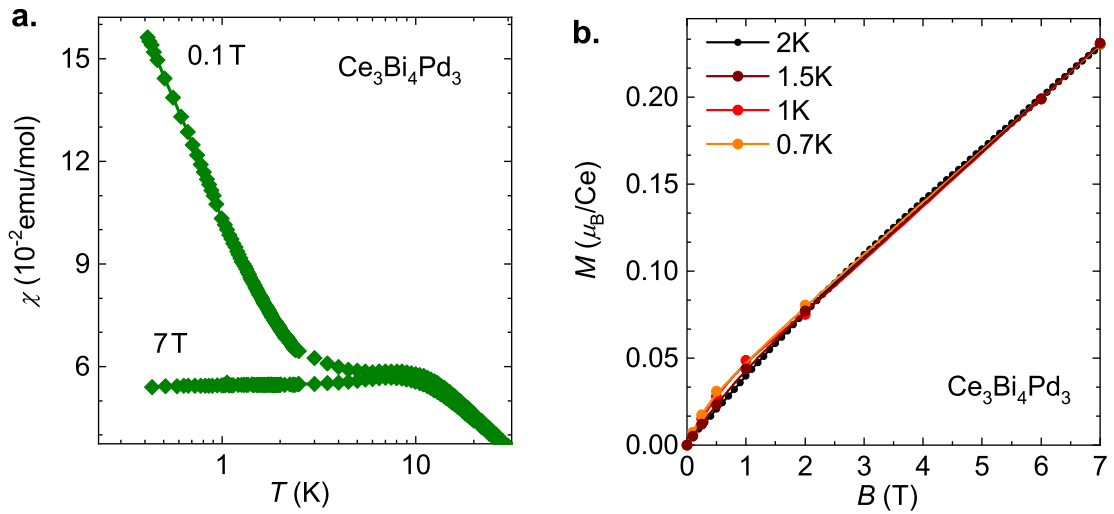


Figure 46: **Magnetic properties of $\text{Ce}_3\text{Bi}_4\text{Pd}_3$ at low temperatures.** **a:** Magnetic susceptibility obtained at $B = 0.1$ and 7 T down to $T = 0.4 \text{ K}$. **b:** Magnetization vs. magnetic field for different temperatures in the range $T = 0.7 - 2 \text{ K}$. The difference in $\chi(T)$ at low temperatures manifests as a small and broad bump in $M(B)$ for $B < 2 \text{ T}$.

a linear $M(B)$ behaviour above $B = 2 \text{ T}$ (Fig 46 b).

In metallic heavy fermion systems, logarithmic divergences are a hallmark of non-Fermi liquid behaviour [123, 124], which is often associated with quantum criticality. Assuming this is also the case for $\text{Ce}_3\text{Bi}_4\text{Pd}_3$, the RKKY interaction in this heavy fermion system can compete against the Kondo coupling and give rise to a nearby magnetic quantum critical point. It is worth noting that similar logarithmic behaviour at low temperatures has recently been observed in another heavy fermion semimetal, namely $\text{CeNi}_{2-\delta}\text{As}_2$ under pressure [125]. The very low-temperature features described above are of great interest on their own and certainly motivate further studies. They show that the presence of strong spin-orbit coupling enriches the global phase diagram of heavy fermion materials [65, 124]. The great tunability of these systems, including the controlled variation of SOC newly demonstrated here, raises the prospect of realizing new phases of

matter.

5.1.6 Conclusions

Substituting Pd in $\text{Ce}_3\text{Bi}_4(\text{Pt}_{1-x}\text{Pd}_x)_3$ represents an iso-structural (Fig. 38), iso-size (Fig. 39), and iso-electronic tuning (high-temperature part in Fig. 42). Thus, changes to the Kondo coupling J_K (via chemical pressure), and chemical potential μ (via doping) can be safely neglected. This, singles out the SOC of conduction electrons λ_{SOC} as the dominating tuning parameter, although the change in the electron wavefunction ($5d$ to $4d$) is also expected to influence the bandstructure of this material [126].

Remarkably, the energy scales of $\text{Ce}_3\text{Bi}_4(\text{Pt}_{1-x}\text{Pd}_x)_3$ and the nature of its ground state changes profoundly with changing λ_{SOC} (Fig. 47): The well-defined Kondo insulator gap observed in $\text{Ce}_3\text{Bi}_4\text{Pt}_3$, gradually closes with increasing x , until it cannot be defined any more. In parallel, both the local maximum in the magnetic susceptibility and the Curie-Weiss temperature stay sizeable, indicating a strong coupling of the conduction electrons to the magnetic moments. Finally, the weak temperature dependence of $\rho(T)$ in $\text{Ce}_3\text{Bi}_4\text{Pd}_3$, and the two orders of magnitude decrease in the low-temperature Hall coefficient between $\text{Ce}_3\text{Bi}_4\text{Pt}_3$ and $\text{Ce}_3\text{Bi}_4\text{Pd}_3$ (Fig. 42) show that with increasing x $\text{Ce}_3\text{Bi}_4(\text{Pt}_{1-x}\text{Pd}_x)_3$ is driven in to a Kondo interaction induced semimetallic state. In the following chapter, I show that it is in fact a novel topologically non-trivial state dubbed Weyl-Kondo semimetal.

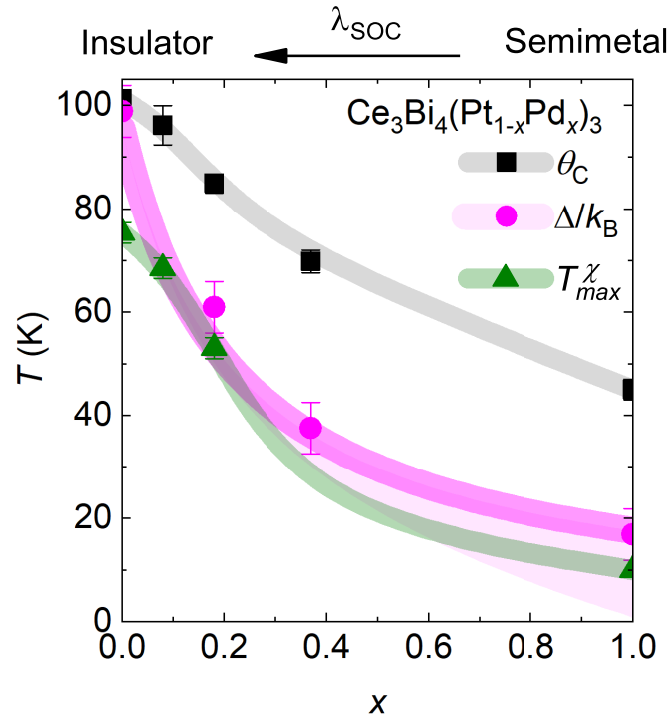


Figure 47: **Characteristic temperature scales for $\text{Ce}_3\text{Bi}_4(\text{Pt}_{1-x}\text{Pd}_x)_3$ as a function of x .** T_{max}^χ and Θ_{CW} are taken from Fig. 45 and the Curie-Weiss fits in Fig. 44, respectively. $\Delta/k_B = 2E_a/k_B$ is taken from the Arrhenius fits in Fig. 41. The full lines are guides to the eyes. The shaded pink area represents the fact that, for $x = 1$, the Arrhenius fit loses significance and $R(T)$ becomes compatible with a gapless state. The dashed green line indicates that the maximum in $\chi(T)$ is suppressed to below 2 K for $x = 0.37$. The arrow on the top axis indicates that an increase of the conduction-electron λ_{SOC} (corresponding to a decrease of x) drives the system from a semimetallic to an insulating state.

5.2 Surface superconductivity in $\text{Ce}_3\text{Bi}_4\text{Pd}_3$

An important question when determining a material's properties, is whether an observed phenomenon is truly intrinsic or whether it is due to extrinsic effects (such as impurities, chemical decomposition, surface oxidation and many more). A significant parameter in this sense is the long-term chemical stability of solids under ambient conditions. This aspect is of great importance for novel materials, whose genuine intrinsic properties are (at first) unknown.

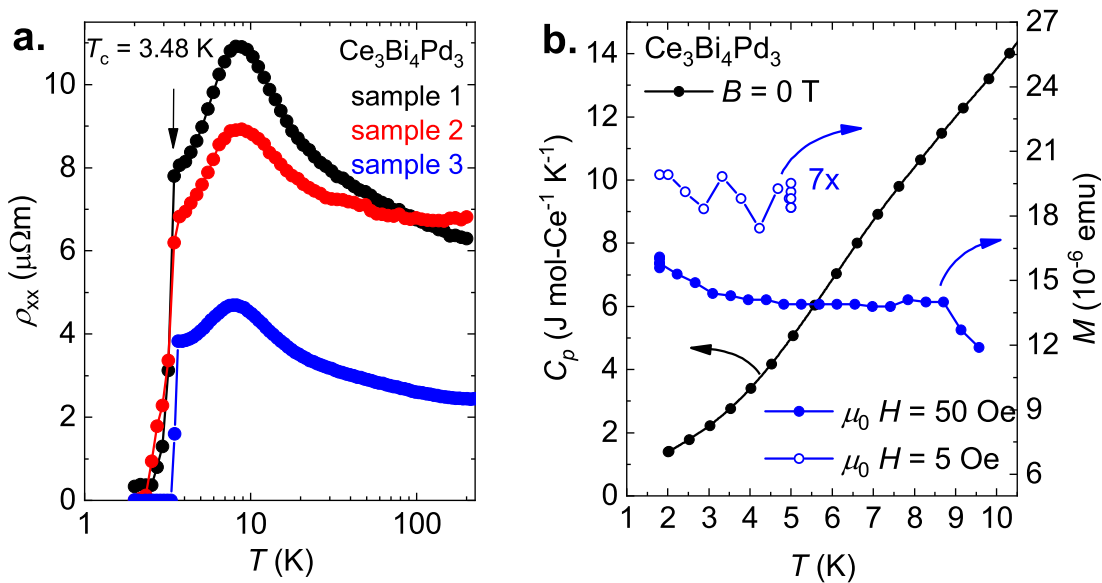


Figure 48: **Superconductivity in $\text{Ce}_3\text{Bi}_4\text{Pd}_3$.** **a:** Temperature-dependent resistivity measurements on three representative single crystals of $\text{Ce}_3\text{Bi}_4\text{Pd}_3$ show the onset of superconductivity, evidenced by the zero resistivity drop at $T_c = 3.5$ K (indicated by arrow). **b:** Zero-field temperature-dependent specific heat (left axis) and magnetization (right axis) in the vicinity of the T_c observed in $\rho(T)$. No bulk signature of superconductivity is observed. Magnetization data were taken with zero-field cooling at field of 5 Oe (open symbols, scaled) and 50 Oe (full symbols)

In $\text{Ce}_3\text{Bi}_4\text{Pd}_3$ initial temperature-dependent resistivity measurements showed superconductivity below $T_c = 3.5$ K, in various single crystals (Fig. 48 a). However, neither a lambda type specific heat anomaly nor a Meissner signal in the

magnetic susceptibility were observed in any of the measured crystals (Fig. 48 b). This firmly rules out the bulk nature of the observed superconductivity in $\rho(T)$. Thus, the question arises whether this is intrinsic but unconventional, or extrinsic superconductivity due to impurities or foreign phases. This is of extreme importance to determine the low-temperature properties of $\text{Ce}_3\text{Bi}_4\text{Pd}_3$.

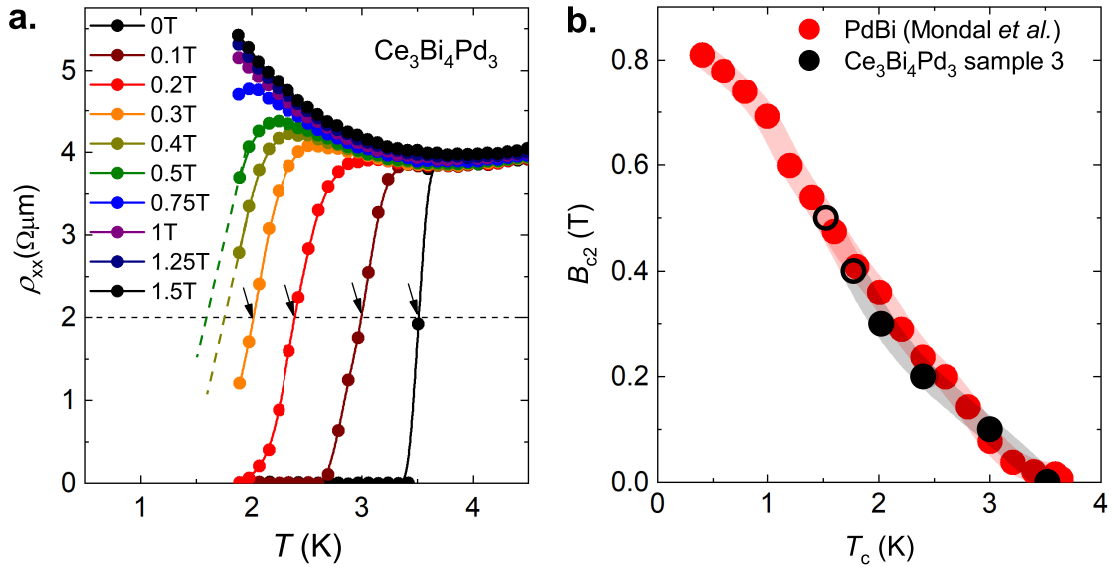


Figure 49: **Superconducting phase diagram of $\text{Ce}_3\text{Bi}_4\text{Pd}_3$.** **a:** iso-field temperature-dependent resistivity of $\text{Ce}_3\text{Bi}_4\text{Pd}_3$ (sample 3 in Fig. 48). Superconductivity persists up to $B = 0.75$ T. The critical temperature T_c is estimated at the temperature where the resistivity reaches half the drop (indicated by horizontal dashed line and arrows). For the curves at $B = 0.4$ T and 0.5 T, T_c is estimated from the crossing of a linear extrapolation to the lowest two points (dark yellow and green dashed lines) with the 50% criteria. **b:** Obtained B - T phase diagram for $\text{Ce}_3\text{Bi}_4\text{Pd}_3$ (black curve) from panel **a**. The last two points at lowest temperatures are estimation (see caption **a**), and are indicated by open symbols. The red curve is the B - T phase diagram of PdBi determined from magnetic susceptibility measurement [127]

To identify putative foreign phases, iso-field temperature-dependent resistivity measurements were carried out on sample 3 (Fig. 49), which showed the sharpest superconducting transition (Fig. 48 a). All possible single elements constituting

$\text{Ce}_3\text{Bi}_4\text{Pd}_3$, binary and ternary superconducting compounds of these elements with similar T_c and $B_{c2}(T)$ phase diagram were searched for in the literature. The close similarity of the phase diagram with that of PdBi [127] suggests that this material might be present in the $\text{Ce}_3\text{Bi}_4\text{Pd}_3$ crystals in form of filaments, domain boundaries or a surface layer. Because SEM images and EDX measurements on $\text{Ce}_3\text{Bi}_4\text{Pd}_3$ single crystal did not detect any foreign phase (Fig. 33) neither in the bulk nor on the surface, all these possibilities had to be ruled out. Of course foreign phases can only be ruled out up to the detection level of SEM/EDX; any amount of foreign phases below this limit would, however, be so small that percolative superconductivity is highly unlikely. An important difference between the single crystals measured by SEM/EDX and by $\rho(T)$ is that in the latter, electrical contacts were initially made by applying high-temperature silver paint that needs a short annealing (2 mins at 100°C at $p = 10^{-5}$ mbar pressure).

Indeed, a $\rho(T)$ measurement made on a pristine (unannealed) single crystal contacted with silver paint at room temperature (without annealing) does not show superconductivity (Fig. 50 black curve). However, when the same crystal is annealed in a second step (in the way described earlier), full superconductivity emerges at $T_c = 3.5$ K (Fig. 50 red curve). Most surprisingly, after polishing the crystal (all surfaces), the onset of superconductivity disappears again, and the resistivity shows semimetallic behaviour down to the lowest temperatures (Fig. 50 blue curve). The polishing was done successively with a 1000 - 2000 - 4000 μm average roughness SiC polishing paper, until the surface was shiny (on average 10-50 μm thick layer was polished away from all surfaces). This is clear evidence that superconductivity appears only at the surface of the crystal, explaining the lack of bulk signals in the specific heat and magnetic susceptibility (Fig. 48). Also, it shows that the effect of annealing in general does not propagate into the bulk, i.e., the bulk properties are retained and can be revealed by polishing the crystal's

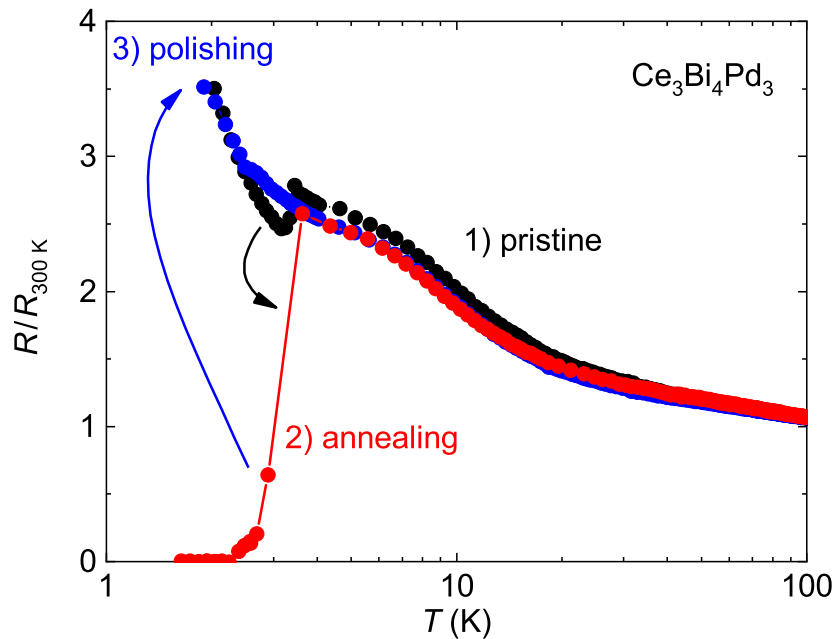


Figure 50: **Zero-field temperature-dependent electrical resistivity of $\text{Ce}_3\text{Bi}_4\text{Pd}_3$.** Pristine, unannealed crystals do not show the superconducting drop (black). After annealing (100 °C, 2 min, 10^{-5} mbar), the superconductivity fully develops at $T_c = 3.5\text{ K}$ (red). After repolishing the surface of the crystal, the superconductivity is absent again (blue).

surface.

In order to identify the cause of the surface superconductivity, and to better understand the chemical change at the surface of the material, time dependent XRD and EDX measurements were carried out. For the former, several mg of $\text{Ce}_3\text{Bi}_4\text{Pd}_3$ single crystals were powderised, and the XRD diffraction was recorded repeatedly for 5.5 hours in several measurements (Fig. 51 a). This is a highly sensitive way to observe the surface degradation, as by powderising the surface-to-bulk ratio is maximized. The measurements show that the main peak of $\text{Ce}_3\text{Bi}_4\text{Pd}_3$ located at $2\theta = 33.3^\circ$ is reduced in amplitude with time, evidencing chemical decomposition. Interestingly, however, this process slows down with time, and shows a tendency to saturation (Fig. 51 b). The time dependence of the amplitude of the

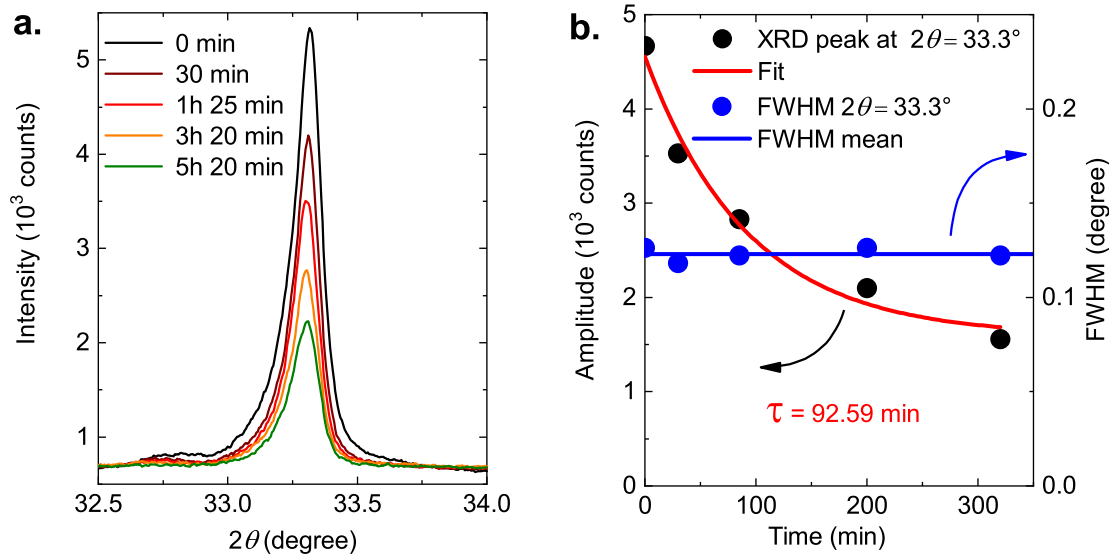


Figure 51: **Time dependent powder XRD measurement of Ce₃Bi₄Pd₃.** **a:** The amplitude of the most intense XRD peak of Ce₃Bi₄Pd₃ located at $2\theta = 33.3^\circ$ for several waiting times up to 5 h 20 mins. **b:** The time dependence of the peak amplitude in panel **a** (left axis) fitted with a saturating exponential relaxation model $A(t) = A_0 + A \exp(-t/\tau)$ (red, τ is indicated). Right axis shows the full width at half maximum of the peaks in panel **a**. It stays constant with time, slightly fluctuating around its mean value (blue line). The data in panel **a** were provided by Xinlin Yan from TU-Vienna.

measured XRD peak can be described qualitatively with a saturating exponential decay (Fig. 51 b), with a time constant of approximately 1.5 h. The quality of the remnant amount of Ce₃Bi₄Pd₃ can then be obtained by analysing the time dependence of the full width at half maximum (FWHM) of the measured XRD peak. The FWHM describes accurately the crystalline quality as its reduction results in peak broadening. Remarkably, the FWHM of the measured XRD peak is constant with time even after 5 hours (Fig. 51 b), despite the peak intensity being considerably reduced. This is a clear indication that although the initial amount of Ce₃Bi₄Pd₃ decreases, the remaining material has pristine quality, and the degradation process stops at the surface. This explains why the intrinsic resistivity can

be easily regained by polishing the surface of the heat-treated crystals (Fig. 50).

Finally, to determine the chemical composition of the surface after the heat treatment, SEM and EDX measurements were performed on heat-treated crystals. Two sets of measurements were made. In a first step, all measured crystals were heat treated for 12 hours at 180 °C and at 10^{-5} mbar pressure (continuous pumping). In the second step, the crystals were separated into two batches. For the first batch, crystals were polished and measured with SEM/EDX. For the second batch, the same measurements were repeated, but now without polishing. While the crystals polished after heat annealing showed the nominal 3:3:4 stoichiometry, and a homogeneous SEM picture (Fig. 52 a), those not polished clearly showed an inhomogeneous surface with the presence of secondary phases (Fig. 52 b). To determine the depth and composition of the surface off-stoichiometry, EDX measurements were performed with two different incident electron energies (15 and 30 keV). The low-energy 15 keV electrons are stopped already below $\sim 1 \mu\text{m}$, whereas the high-energy 30 keV electrons penetrate deeper into the bulk, to $\sim 3 \mu\text{m}$. The low-energy EDX measurement reveals a large off-stoichiometry (Fig. 52 c). Both Pd and Bi are severely suppressed while the Ce content is strongly increased, reaching around 60% atomic ratio. This off-stoichiometry is reduced (but still present) for the high energy measurement (Fig. 52 d), that probes a larger volume. The considerable reduction of the off-stoichiometry on a scale of several μm suggests that the nominal 3:4:3 stoichiometry is recovered on the scale of $\sim 10 \mu\text{m}$ in depth with respect to the surface. Whereas it is currently unknown why the surface is rich in Ce, the following scenario can be suggested: of the three elements – Ce, Pd, Bi – only Ce has a very high chemical affinity to oxygen. It is Ce that oxidises by air even at very low pressure of 10^{-5} mbar as evidenced by the appearance of the EDX oxygen peak at $\sim 0.5 \text{ keV}$ (Fig. 52 e). Ce oxide phases have considerably higher molar volume than Ce itself, so that these phases are extruded to the

surface due to the enhanced internal pressure. The natural consequence is that, below the surface, there must be a layer rich in Bi and Pd. Thus, the similarity in the superconducting phase diagram of the annealed $\text{Ce}_3\text{Bi}_4\text{Pd}_3$ crystals and of PdBi (Fig. 49) is most probably due to the formation of a PdBi crystalline layer below a Ce-rich surface layer due to annealing.

Establishing the extrinsic nature of the superconductivity in $\text{Ce}_3\text{Bi}_4\text{Pd}_3$ and understanding the chemical mechanism allows to develop a sample preparation protocol to avoid this extrinsic effect, and truly determine the bulk transport properties of $\text{Ce}_3\text{Bi}_4\text{Pd}_3$. All transport measurements on $\text{Ce}_3\text{Bi}_4\text{Pd}_3$ presented in the thesis were done as follows:

- Samples are stored in Ar glovebox.
- Samples are polished on all sides before putting electrical contacts.
- All sample preparations (electrical contacts for transport, mounting for experiments) are made within 30 mins.
- Electrical contacts in either 5 or 6 wire configuration (depending on the crystal size) are made by spot welding 12 or 20 μm gold wires using the spot welding technique (30 kW, 30 ms) and a very sharp tungsten tip. For some crystals (e.g., high-field measurements) contacts were made by applying silver paint that dries at room temperature.

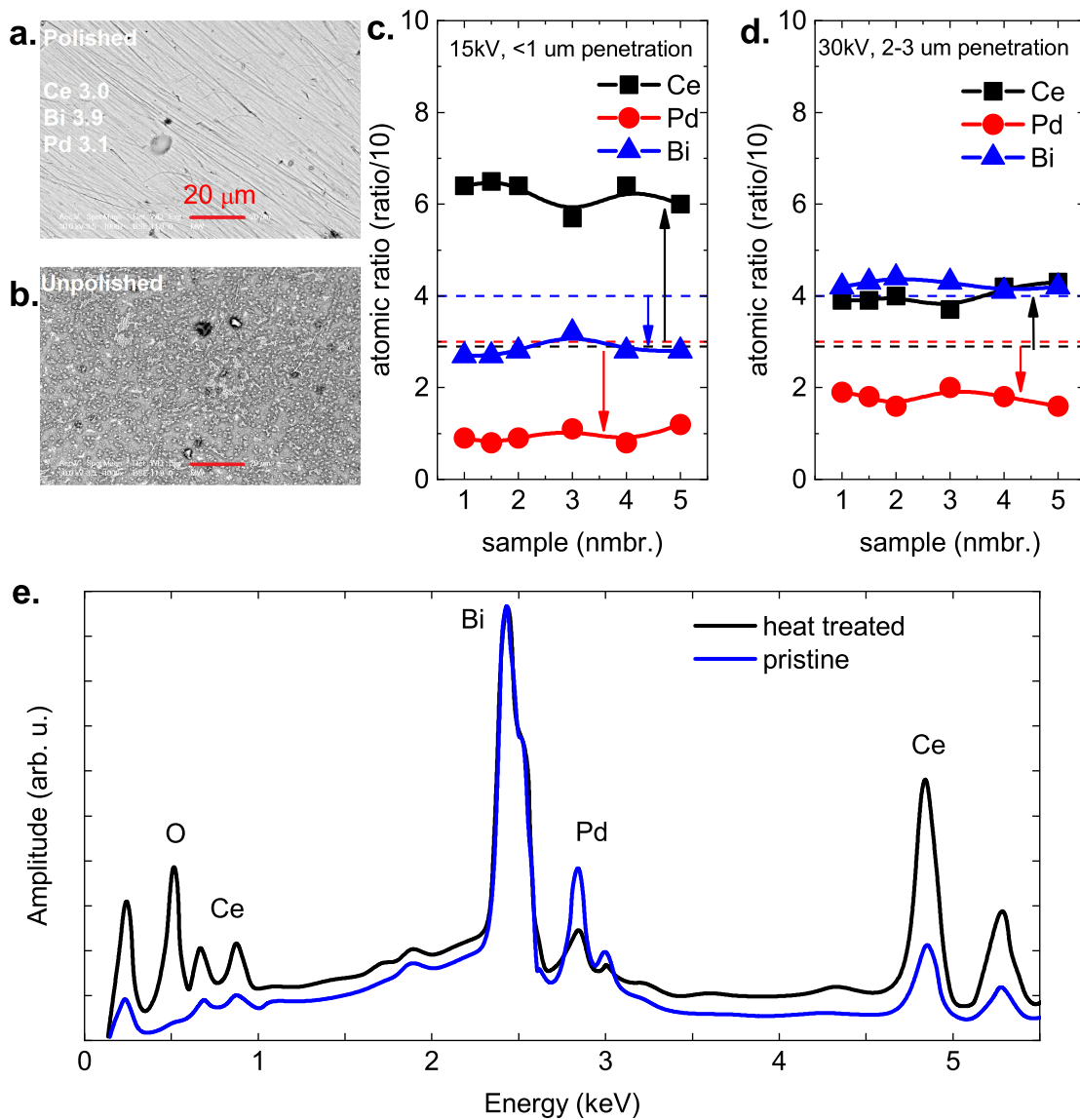


Figure 52: EDX measurements on annealed $\text{Ce}_3\text{Bi}_4\text{Pd}_3$ single crystals. **a:** SEM picture of an annealed, then polished $\text{Ce}_3\text{Bi}_4\text{Pd}_3$ crystal. Indicated is the elemental composition ratio as measured by EDX. **b:** The same as in panel **a** for an annealed and unpolished sample. **c:** EDX compositional results for annealed sample using low-energy (15 keV) incident electrons (shallow penetration). Measured area is approximately $20 \times 20 \mu\text{m}^2$. **d:** Compositional results for annealed, unpolished samples using high-energy (30 keV) incident electrons (deep penetration). The amount of off-stoichiometry in panels **c** and **d** are indicated by arrows with respect to their nominal values (horizontal dashed lines). **e:** EDX spectra of pristine and heat-treated $\text{Ce}_3\text{Bi}_4\text{Pd}_3$ crystals. The latter shows a large oxygen peak at 0.5 keV.

5.3 Probing the Weyl-Kondo semimetal state in $\text{Ce}_3\text{Bi}_4\text{Pd}_3$

As I have shown in the previous section, tuning the SOC in the Kondo insulator $\text{Ce}_3\text{Bi}_4\text{Pt}_3$ by Pd substitution results in the suppression of the Kondo insulating ground state. In particular, the Pd end compound $\text{Ce}_3\text{Bi}_4\text{Pd}_3$ shows a low carrier density, semimetallic behaviour at low temperatures. Thus, the question arises: What stabilizes this semimetallic ground state in $\text{Ce}_3\text{Bi}_4\text{Pd}_3$ and is it topologically nontrivial? To address these questions, I present specific heat and Hall effect measurements in this section. I show that $\text{Ce}_3\text{Bi}_4\text{Pd}_3$ is indeed a novel, strongly correlated Kondo semimetal with linearly dispersing electronic bands, and that it is topologically nontrivial. This novel state of matter is a correlation-driven Weyl system, dubbed Weyl-Kondo semimetal. Thus, before discussing these results, I briefly present the theoretical basics of this new state of matter.

5.3.1 The Weyl-Kondo semimetal

Electronic systems with linear band touching in the bulk are known to exist in lattices with broken inversion symmetry and strong spin-orbit coupling (see Sect. 2.4). Since such states are gapless, they possess arbitrarily small energy excitations in the vicinity of the node and, thus, are particularly susceptible to strong electron correlation effects. In what follows, I present a brief summary based on [107], where such a model was theoretically studied, and Kondo effect-driven Weyl nodes were predicted. It is captured by a periodic Anderson Hamiltonian $H = H_d + H_{cd} + H_c$. Here, H_d and H_{cd} describe the Hamiltonians of the localized electrons and their interaction with conduction electrons, as discussed in Sect. 2.1. The notations c and d correspond to conduction and localized electrons, respectively, where the latter represent the f -electrons of the rare earth atom in a Kondo system. The broken inversion symmetry, that is the key feature here, is captured in the conduction

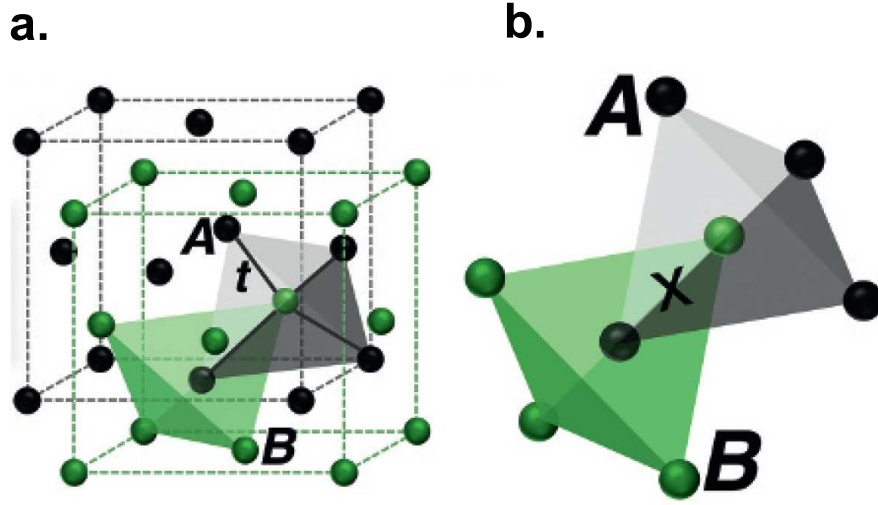


Figure 53: **Structure of the zincblende lattice.** **a:** Inequivalent sublattices labelled A and B (black and green, respectively) of the zincblende lattice. t indicates the nearest neighbour hopping term. **b:** The interlocking tetrahedral structure of sublattices A and B showing how the inversion symmetry is broken with respect to the inversion center of the monoatomic case (black cross). The figure is taken from [107].

electron Hamiltonian H_c

$$\begin{aligned}
 H_c &= \sum_k \Psi_k^\dagger h_k \Psi_k, \\
 \Psi_k^T &= (c_{k\uparrow A}, c_{k\uparrow B}, c_{k\downarrow A}, c_{k\downarrow B}), \\
 h_k &= \sigma_0(u_1(k)\tau_x + u_2(k)\tau_y + m\tau_z) + \lambda(\mathbf{D}(k)\boldsymbol{\sigma}),
 \end{aligned} \tag{41}$$

that is implemented on a noncentrosymmetric zincblende lattice (Fig. 53 a, b), and includes the spin-orbit interaction explicitly via a modified Fu-Kane-Mele model [27]. Here $c_{k\uparrow A}$ denotes the annihilation operator of the conduction electrons with wavevector k , spins \downarrow, \uparrow and sublattice indices A, B of the zincblende structure (Fig. 53 a). $\boldsymbol{\sigma}$ and $\boldsymbol{\tau}$ are Pauli matrices acting on the spin and sublattice space, respectively, where σ_0 is the identity matrix. The broken inversion symmetry is

captured in H_c by the extra potential m , that staggers between the sublattices A and B , whereas the spin-orbit interaction is specified by a Dresselhaus type term with strength λ . The functions $u_1(k)$, $u_2(k)$ and $\mathbf{D}(k)$ are simple trigonometric functions determined by the primitive lattice vectors and the nearest neighbour hopping term t . For more details see [107].

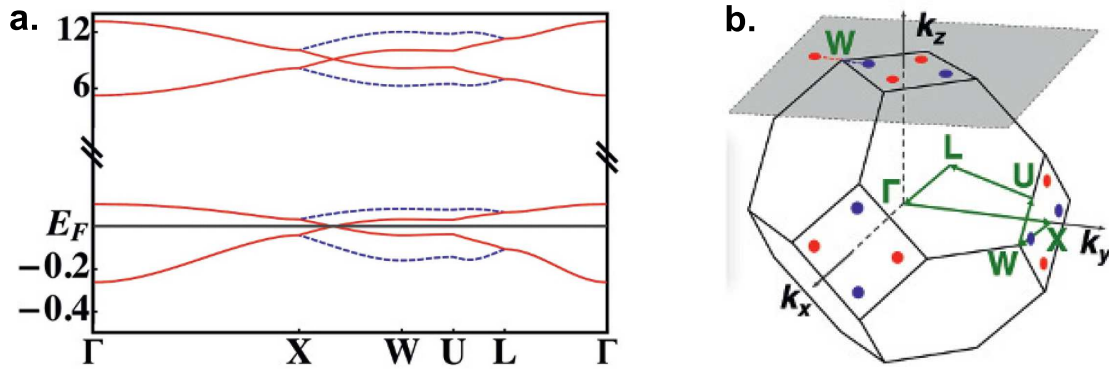


Figure 54: **Energy dispersion of Weyl-Kondo bands.** **a:** Energy dispersion of the Weyl-Kondo model implemented on a zincblende structure (Fig. 53 a) and shown along high symmetry cuts of the Brillouin zone (panel **b**). It displays strongly renormalized band crossing pinned to the Fermi energy. Energy is measured in units of t of the bare conduction electrons, whereas blue dashed lines indicate the absence of Weyl nodes for $m = 0$ (preserved inversion symmetry). Panels **a** and **b** are taken from [107].

The main conclusion of this model is that when the corresponding Schrödinger equation is solved in the strongly interacting limit ($U/t \rightarrow \infty$), and in case of quarter filling (one electron per site), pairs of Weyl nodes with strongly renormalized band width emerge that are pinned to the Fermi energy (Fig. 54 a, Fig. 55 a). It was shown that the band renormalization is governed by the Kondo temperature, and that with suppressing the c - d hybridization the Weyl nodes shift away from the Fermi energy, deep into the valance band. Finally, to asses the band topology of the renormalized band crossings, the associated Berry curvature was calculated:

It shows sources and sinks at the band touching points (Fig. 55 b), thus confirming their Weyl nature.

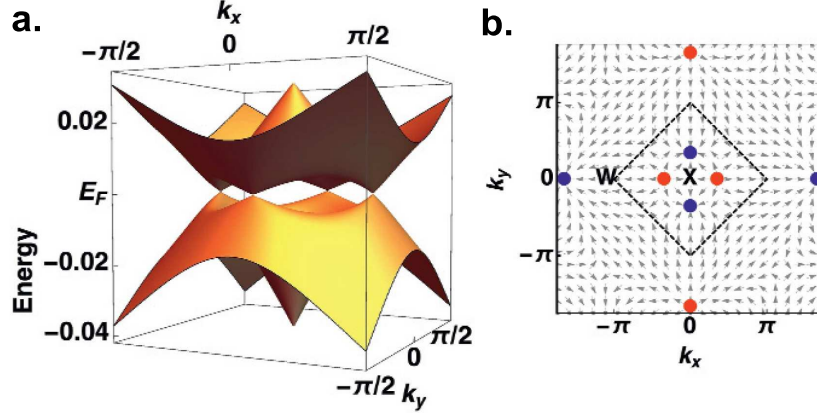


Figure 55: **Dispersion and Berry curvature in Weyl-Kondo semimetal. a:** Low-energy band structure corresponding to the dispersion in Fig. 54 a showing linear dispersion in the vicinity of the Fermi energy E_F . **b:** The distribution of the Berry curvature field in the plane shown in Fig. 54 b showing sources and sinks of the Berry curvature at the linear band touching points (blue and red points). The figure is taken from [107].

A key property of a Weyl-Kondo semimetal is the strong band renormalization that is quantified by the renormalized quasiparticle velocity v^* (slope of the linear dispersion). The latter is determined by the Kondo temperature $T_K \sim 10$ K, as opposed to the Fermi temperature of a weakly correlated metal $T_F \sim 10^4$ K. Thus, v^* is suppressed by a factor of 10^3 with respect to the Fermi velocity v_F of a noninteracting Weyl-semimetal. Then, the associated enhanced density of states dictates a giant entropy release at low temperatures, that can be probed by specific heat experiments. In this case the electronic specific heat C_{el} can be calculated from its definition

$$C_{el} = \left(\frac{\partial u}{\partial T} \right)_V = \frac{\partial}{\partial T} \int_{BZ} \frac{dk^3}{(2\pi)^3} \epsilon(\mathbf{k}) f(\epsilon(\mathbf{k})), \quad (42)$$

which, with the linear dispersion $\epsilon(\mathbf{k}) = \hbar v^* k$, is

$$C_{el} = \frac{7\pi^2}{30} k_B \left(\frac{k_B T}{\hbar v^*} \right)^3. \quad (43)$$

Thus the electronic specific heat of a Weyl-Kondo semimetal is linear in $\sim T^3$ as opposed to $C_{el} \sim T$ in a conventional metal (with quadratic dispersion). Most importantly, the three orders of magnitude renormalization of v^* boosts C_{el} by 9 orders of magnitude in comparison to a noninteracting Weyl semimetal. This makes the specific heat signature readily detectable.

5.3.2 Specific heat

Specific heat measurements on $\text{Ce}_3\text{Bi}_4\text{Pd}_3$ were done in a ^4He *Quantum Design* PPMS equipped with ^3He insert. Measurements were done in an adiabatic calorimeter calibrated for 0 T and 7 T magnetic fields. Due to the small single crystal mass, the heat capacity of 13 representative crystals (the same ones used for the measurement of the magnetization in Sect.5.1.5) were measured using the relaxation time technique.

In Fig. 56 I show the specific heat data up to 100 K. In order to determine the phonon contribution, a simple Debye model

$$C_p = 9R n_D k_B \left(\frac{T}{\Theta_D} \right)^3 \int_0^{\Theta_D/T} \frac{x^4 e^x}{(e^x - 1)^2} dx \quad (44)$$

was fitted to the data in the range $T = 20 - 100$ K. Here R is the universal gas constant, n_D is the number of oscillators per formula unit (C_p is here given by formula units) and Θ_D is the Debye temperature. It yields $n_D = 9.86 \pm 0.05$ and $\Theta_D = (159 \pm 3)$ K, that are in good agreement with the fact that the formula unit has 10 atoms, and that the Debye temperature of $\text{La}_3\text{Bi}_4\text{Pt}_3$ is $\Theta_D = 157$ K [81].

Next, in search for the specific heat signature of a Weyl-Kondo semimetal, I

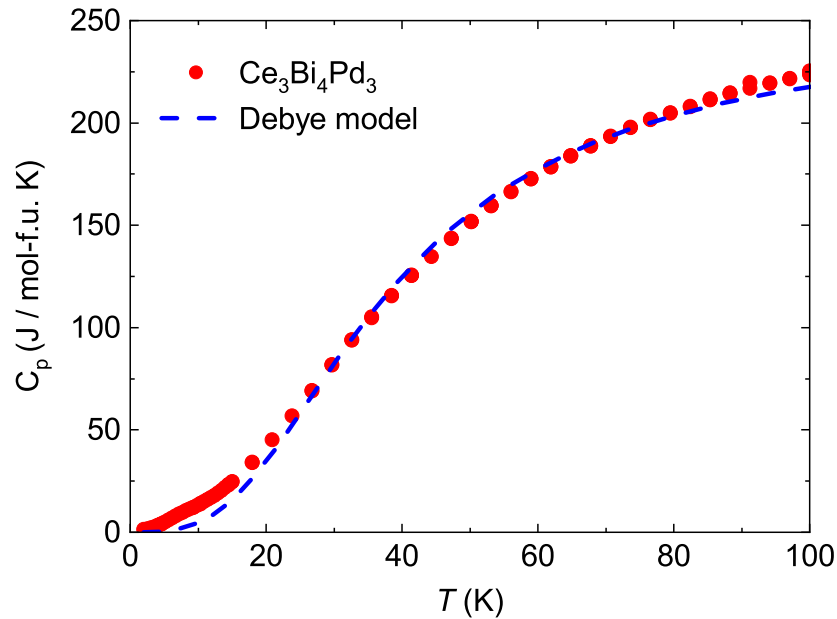


Figure 56: **High-temperature specific heat of $\text{Ce}_3\text{Bi}_4\text{Pd}_3$.** Specific heat measured between 2 and 100 K (red symbols). Blue line shows the best fit of a simple Debye model (Eqn. 44). The curve was fitted to the data between 20 and 100 K. Below 20 K, the lattice model fails to describe the data due to the large electronic specific heat. Also at high temperature the agreement is only fair (due to the simplicity of the model), but sufficient for the purpose here.

turn to the low-temperature data (Fig. 57). It can be described by $C/T = C_{\text{el}}/T + C_{\text{ph}}/T$, i.e., by an electronic and a phononic contribution, respectively. At low temperatures, the phonon contribution is determined by the Debye approximation and reads $C_{\text{ph}}/T = \beta T^2$, where the slope is $\beta = 5 \text{ mJ/mol-f.u. K}^4$ (Fig. 57), and corresponds to a Debye temperature of $\Theta_{\text{D}} = 157 \text{ K}$. This is within excellent agreement with the $\Theta_{\text{D}} = 159 \text{ K}$ obtained from the high-temperature Debye fit (Fig. 56) and with that Debye temperature of $\text{La}_3\text{Bi}_4\text{Pt}_3$ [81]. Interestingly, on top of the phonon background, the electronic contribution C_{el}/T vs. T^2 shows a pronounced anomaly, that is only slightly shifted to lower temperatures in a magnetic field of 7 T (Fig. 57). On the low-temperature side of the anomaly, C/T

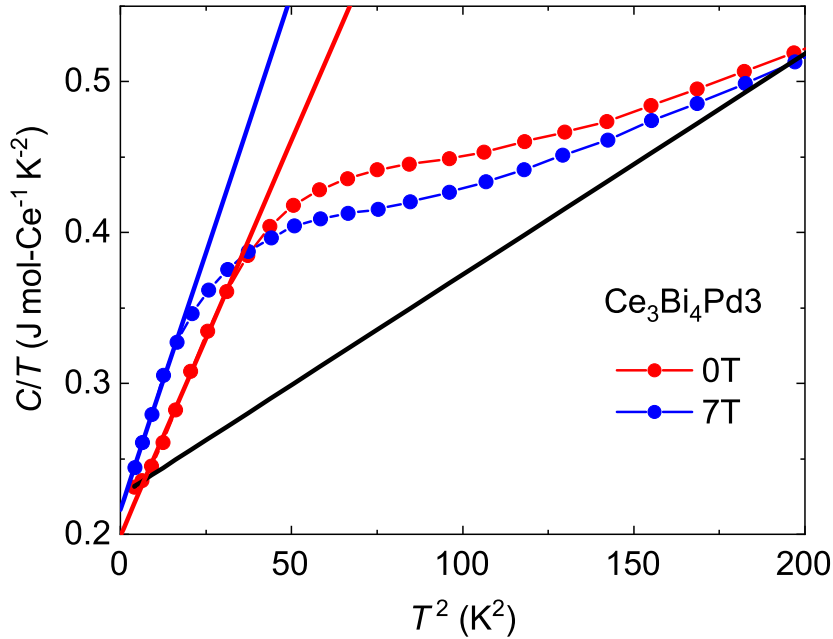


Figure 57: **Low-temperature specific heat of $\text{Ce}_3\text{Bi}_4\text{Pd}_3$.** C/T vs. T^2 plotted for magnetic field of 0 T and 7 T in the range of $T = 2 - 14$ K. The phonon background is denoted by the black line (offsetted with $\gamma = 223$ mJ/mol-Ce K^2 for clarity). At the lowest temperatures the electronic specific heat is proportional to T^3 as indicated by the linear fits (red and blue lines).

is linear in T^2 , with a slope Γ that is sizably larger than that of the phonon contribution (Fig. 57). Below 2 K, the electronic specific heat shows a non-Fermi liquid (NFL) $\ln(1/T)$ upturn and a small Schottky-type anomaly that together constitutes an electronic background for the $C/T \sim T^2$ behaviour (Fig. 58 a). The $\ln(1/T)$ upturn is also seen in the magnetic susceptibility (Figs. 58 a and 46). It therefore likely reflects the physics in the spin sector, and might indicate the proximity to a quantum critical point. This is supported by the fact that at $B = 7$ T the $\ln(1/T)$ contribution to the magnetic susceptibility (Fig. 46 a) and specific heat (data not shown) is suppressed, whereas the $C/T \sim T^2$ behaviour at higher temperatures remains robust (Fig. 57). Because the Schottky-type anomaly is observed in the specific heat but not in the magnetic susceptibility, electronic as

opposed to magnetic degrees of freedom appear to be involved. Thus, this anomaly might be a precursor to the formation of a charge density wave (CDW). Indeed, among the various competing orders that may develop out of a Weyl semimetal, long-range repulsive Coulomb interactions enhance the tendency towards a CDW formation at the wavevector that connects the Weyl nodes [128]. The origin of these low-temperature features (both the $\ln(1/T)$ upturn and the Schottky anomaly) are still under investigation. When these low-temperature contributions are modelled (the orange line in Fig. 58 a) and subtracted from the C_{el}/T data, the ΓT^2 term is seen down to the lowest temperatures, for over more than a decade in temperature (Fig. 58).

The observed $C \sim T^3$ term in the specific heat of $\text{Ce}_3\text{Bi}_4\text{Pd}_3$ is in sharp contrast to the usual $C_{el} \sim T$ electronic specific heat of a metal. In principle, 3D antiferromagnetic (AFM) magnons could give a $C \sim T^3$ contribution, as seen in the cubic heavy fermion antiferromagnet CeIn_3 below its Néel temperature [129, 130]. However, in $\text{Ce}_3\text{Bi}_4\text{Pd}_3$, there is no sign of a magnetic phase transition in the magnetic susceptibility (Fig. 46), and the observed anomalies (Fig. 57) appear too broad in C/T to represent such transitions. In addition, in view of the linear coupling of a magnetic field to a symmetry breaking order parameter, a stronger suppression would be expected if the anomaly represented AFM ordering. In addition, the magnetic field enhances Γ (Fig. 57) but would be expected to reduce it in a 3D AFM magnon scenario [131, 132]. On the other hand, the $C_{el} \sim T^3$ behaviour agrees well with an electronic specific heat originating from strongly renormalized electronic bands with the linear dispersion $\epsilon(k) = \hbar v^* k$ expected in a Weyl-Kondo semimetal (Eqn. 43). The quasiparticle velocities, determined by Eqn. 43, corresponding to the slope of the linear fits in Figs. 57 and 58 yield $v^* = (885 \pm 5)$ m/s and $v^* = (870 \pm 5)$ m/s, respectively. These are indeed significantly smaller than the sound velocity $v_{ph} = 4963$ m/s (corresponding to $\Theta_D = 157\text{K}$), and represent

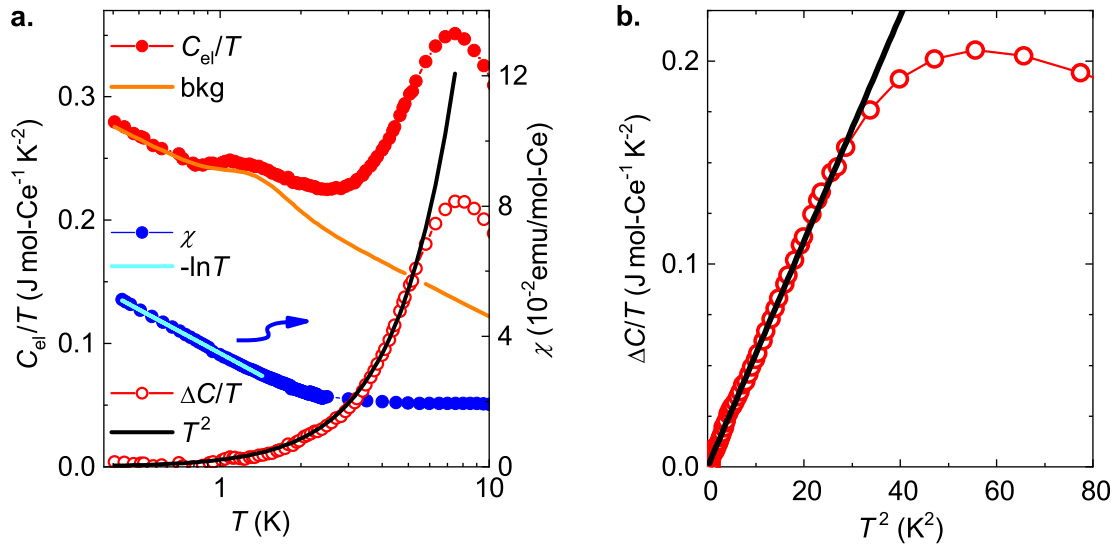


Figure 58: **Specific heat of $Ce_3Bi_4Pd_3$ below 2 K.** **a:** Electronic specific heat coefficient C_{el}/T (left axis) and magnetic susceptibility (right axis) of $Ce_3Bi_4Pd_3$ plotted vs. $\log T$ between 0.4 and 10 K. The orange line describes a Schottky-like anomaly below 2 K, residing on top of an $\ln(1/T)$ upturn. As such they represent an electronic “background” (bkg) to the linear-in- T^2 contribution of the observed $C_{el}/T = \Gamma T^2$ term (Fig. 57). Subtracting the background, $\Delta C/T = C_{el}/T - \text{bkg}$ (empty red symbols), evidences a T^2 law (fit represented by the black line) that extends from 5.5 K to the lowest temperatures. The magnetic susceptibility shows the $\ln(1/T)$ behaviour, but lacks the Schottky-like anomaly, suggesting that the anomaly involves charge as opposed to spin excitations. **b:** The $\Delta C/T$ vs. T^2 data (empty red symbols) and the corresponding linear fit (black line), both obtained from panel **a**, on a lin-lin scale.

a three order of magnitude renormalization compared to a typical Fermi velocity $v_F = 10^6$ m/s of a noninteracting metal. This suggests that the ultra-slow quasiparticle velocities are dictated by the Kondo energy, in agreement with the Weyl-Kondo semimetal scenario.

That the low-temperature specific heat feature is due to a Weyl-Kondo semimetal bandstructure is further confirmed by the low-temperature release of the electronic entropy at zero magnetic field (Fig. 59). In case of a cubic point group at the Ce site, the crystal electric field splits the six-fold degeneracy of the

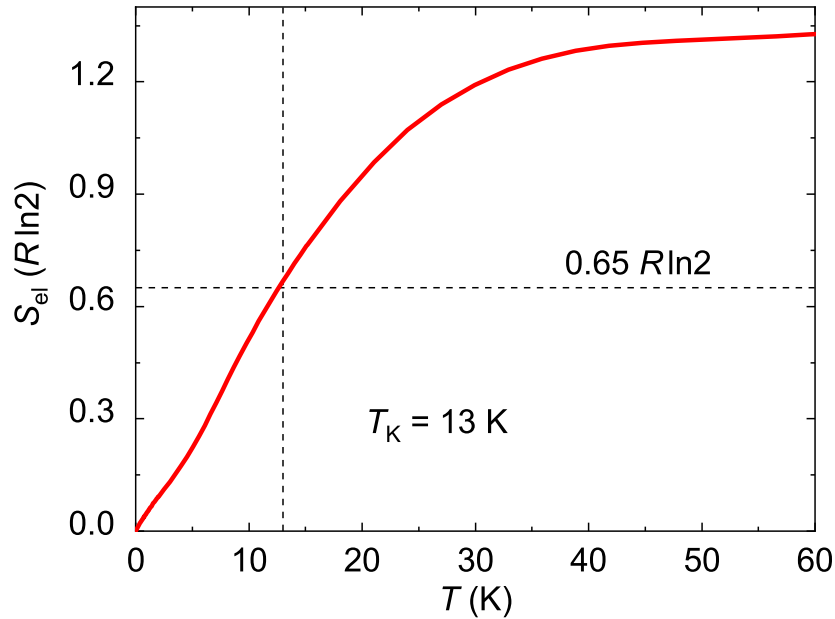


Figure 59: **Low-temperature entropy of $\text{Ce}_3\text{Bi}_4\text{Pd}_3$.** Entropy vs. temperature corresponding to the zero-field curve shown in Fig. 57. Denoted are the $0.65R \ln 2$ criterion and the corresponding Kondo temperature, as described in [133].

z component of the Ce^{3+} ion total angular momentum ($J = 5/2$) into a doublet and a quartet manifold. The ground state degeneracy, and the associated $R \ln 2$ entropy (in case of a doublet ground state) can't be maintained in the $T = 0$ limit, and is quenched by the Kondo interaction. Thus, as both the low-temperature entropy quench and the $\sim T^3$ behaviour in C_{el} are dictated by the Kondo effect, the energy scales obtained from both phenomena must be consistent. In case of a doubly degenerate ground state of a single-ion Kondo regime, the Kondo temperature T_K is determined as the temperature, where the entropy release reaches $0.65R \ln 2$ [133]. In the case of $\text{Ce}_3\text{Bi}_4\text{Pd}_3$, this criterion yields a Kondo temperature of $T_K = 13 \text{ K}$ as shown in Fig. 59. It represents a three order of magnitude renormalization, when compared to the Fermi temperature of a noninteracting metal of $T_F = 10^4 \text{ K}$, which agrees well with the three order of magnitude renor-

malization of v^* as determined from Γ . This is an independent confirmation that the $\sim T^3$ behaviour of C_{el} is indeed the signature of linear bands driven by the Kondo effect.

In conclusion, I showed that the electronic specific heat displays a pronounced $\sim T^3$ behaviour below T_K , that corresponds to an ultra-slow quasiparticle velocity of $v^* = 885$ m/s. The renormalization with respect to a typical Fermi velocity agrees fully with that expected from T_K when compared to T_F , and evidences Kondo-driven nodal excitations, in full agreement with the behaviour expected from a Weyl-Kondo semimetal. Importantly, this specific heat signature sets in at $T \approx 6$ K (36 K² in Fig. 58 b) confirming that the Weyl points are pinned to the Fermi energy within at least 0.5 meV in energy. Nevertheless, whereas specific heat experiments are a powerful tool to ascertain the band dispersion, they contain no information about the Berry curvature distribution, that is the hallmark of nontrivial topology and Weyl semimetals. In the following section, I address this question.

5.3.3 Magnetic field-dependent resistivity

A direct way to probe the nontrivial topology and the associated Berry curvature distribution of a material is electrical transport. As I discussed in Sect.2.4, Weyl nodes give rise to the chiral anomaly in the magnetoresistivity, whereas the associated Berry curvature divergences are expected to drive a spontaneous, nonlinear Hall effect (Sect.3.5).

First, the temperature and magnetic field regime must be delineated where signatures of nontrivial topology are to be expected. The onset of Kondo coherence (the temperature below which the heavy quasiparticles are formed and move coherently through the lattice) is best determined by magnetic field-dependent electrical resistivity measurements. Figure 60 shows the temperature-dependent

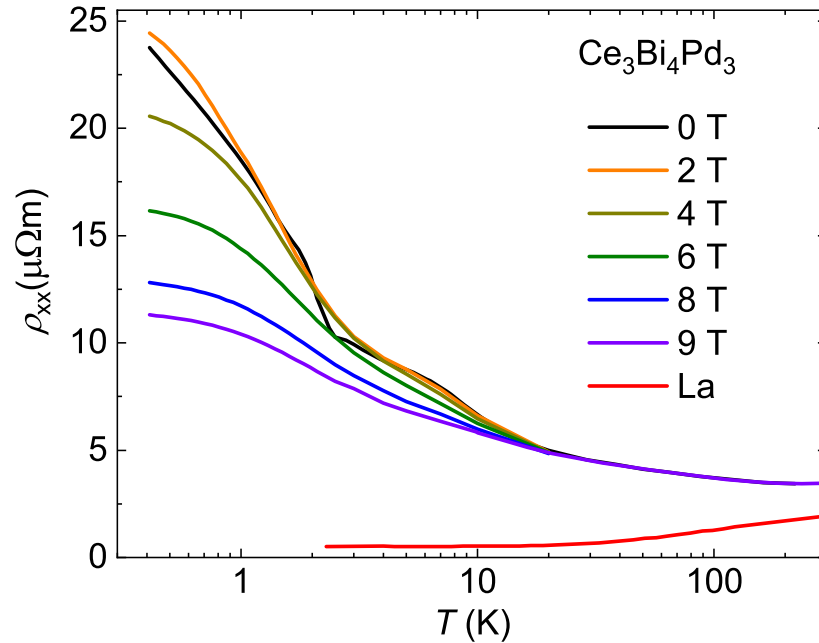


Figure 60: **Iso- B resistivity curves of $\text{Ce}_3\text{Bi}_4\text{Pd}_3$.** Temperature-dependent electrical resistivity under various magnetic fields up to $B = 9$ T in the range of $T = 300 - 0.5$ K. The La reference compound curve is shown in red.

electrical resistivity $\rho(T)$ for $\text{Ce}_3\text{Bi}_4\text{Pd}_3$ for magnetic fields up to 9 T. A substantial deviation of the finite-field $\rho_{xx}(T)$ curves from the one in zero field is observed below about 20 K. The resistivity reduction by the applied field is attributed to the field-suppression of incoherent Kondo scattering, which will be further discussed in what follows (Fig. 62).

In Fig. 61, I show the iso- T MR curves for three distinct temperature regimes. At high temperatures down to $T = 7$ K, they show a simple monotonic decrease with increasing field, that is enhanced at lower temperatures (Fig. 61 a). At intermediate temperatures, for $T = 7 - 2.5$ K, the MR is positive for small fields but changes to a negative MR with a maximum at $B \approx 3$ T (Fig. 61 b). For the lowest temperatures $T < 2$ K, the MR is more complex. A very narrow feature appears around $B = 0$ T at $T = 2$ K that broadens to a double peak structure at lower

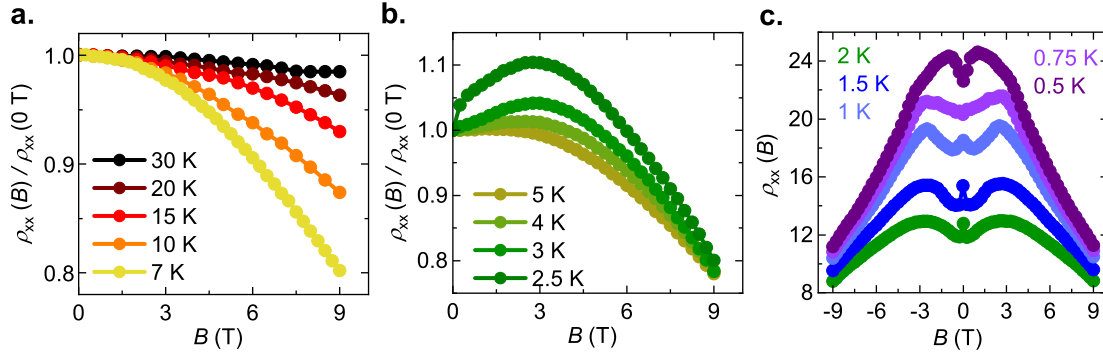


Figure 61: **Iso- T magnetic field-dependent electrical resistivity of $\text{Ce}_3\text{Bi}_4\text{Pd}_3$.** Transverse magnetic field-dependent resistivity normalized to its zero-field value is displayed for the high (panel a), intermediate (panel b) and low-temperature (panel c) regimes.

temperatures (Fig. 61 c). In what follows, I will address all three regimes.

The high-temperature region (Fig. 61 a), featuring the monotonous negative MR, is the hallmark of incoherent Kondo scattering that governs Kondo systems in their single ion regime [132,134]. The $\rho(B)/\rho(0\text{ T})$ vs. B/B^* curves all collapse onto the theoretically predicted curve (Fig. 62 a) for an $S=1/2$ Kondo impurity system [135], provided a suitable scaling field B^* is chosen. The resulting B^* is linear in temperature (Fig. 62 b). Fitting $B^* = B_0^*(1 + T/T^*)$ to the data (Fig. 62 b) yields $B_0^* = 10\text{ T}$ and $T^* = 2.5\text{ K}$, which may be used as estimates of the field and temperature below which the system is fully Kondo coherent. In the intermediate regime below $T = 7\text{ K}$, the scaling fails (Fig. 62 a), as expected when crossing over from the Kondo incoherent to the Kondo coherent regime [134]. The departure from the single ion regime at $T = 7\text{ K}$ is also signalled by the onset of the $C_{el} \sim T^3$ dependence (Fig. 57) and a broad local maximum in $\rho(T)$ (Fig. 60), both at similar temperatures. Indeed, such a broad peak in $\rho(T)$ is a characteristic of the onset of Kondo coherence in heavy fermion metals [134,136]. Thus, the behaviour of both $\rho(T)$ and $\rho(B)$ signals the development of Kondo-

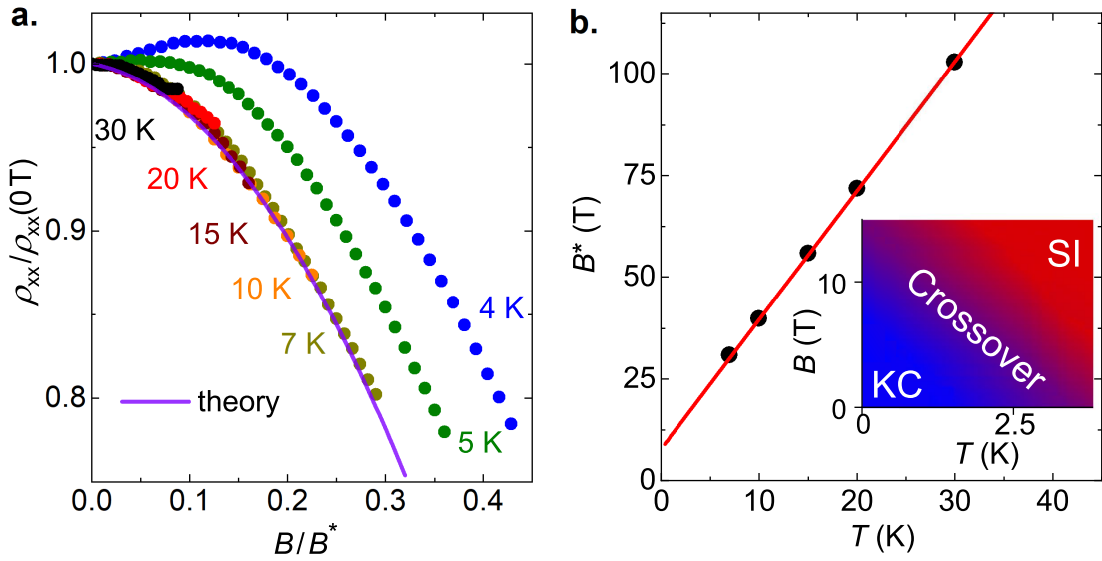


Figure 62: **Schlottman scaling in $\text{Ce}_3\text{Bi}_4\text{Pd}_3$.** **a:** Transverse magnetic field-dependent resistivity scaled to its zero-field value vs. scaled magnetic field B/B^* . The data above 7 K collapse onto the universal curve expected for an $S = 1/2$ Kondo impurity system in the incoherent regime [135] (violet line). At lower temperatures the scaling fails, which is shown here by using B^* from the linear fit in panel **b** (also other choices of B^* cannot achieve scaling). **b:** Values of the scaling magnetic field B^* vs. T (symbols) follow a linear behaviour (red line, linear fit). Inset shows the onset of the Kondo coherent state (KC) out of the single ion regime (SI), via a crossover regime in the B - T phase diagram.

driven, coherent, strongly renormalized bands (inset of Fig. 62 b). In the third regime ($T < 3$ K), well within the Kondo coherent regime, an additional feature appears at small fields in the MR curves (Fig. 61 c). It coincides with the drop of $\rho(T)$ at the same temperature at zero field (Fig. 60) and, thus, these are likely to have a common origin. As I show in the next section, this is closely related to the onset of the spontaneous Hall effect with a large Hall angle.

Finally, I turn to the signatures of nontrivial topology. As I discussed in Sect. 2.4, a key feature of noninteracting Weyl semimetals is the chiral anomaly – charge pumping between a pair of Weyl nodes – which manifests in a large neg-

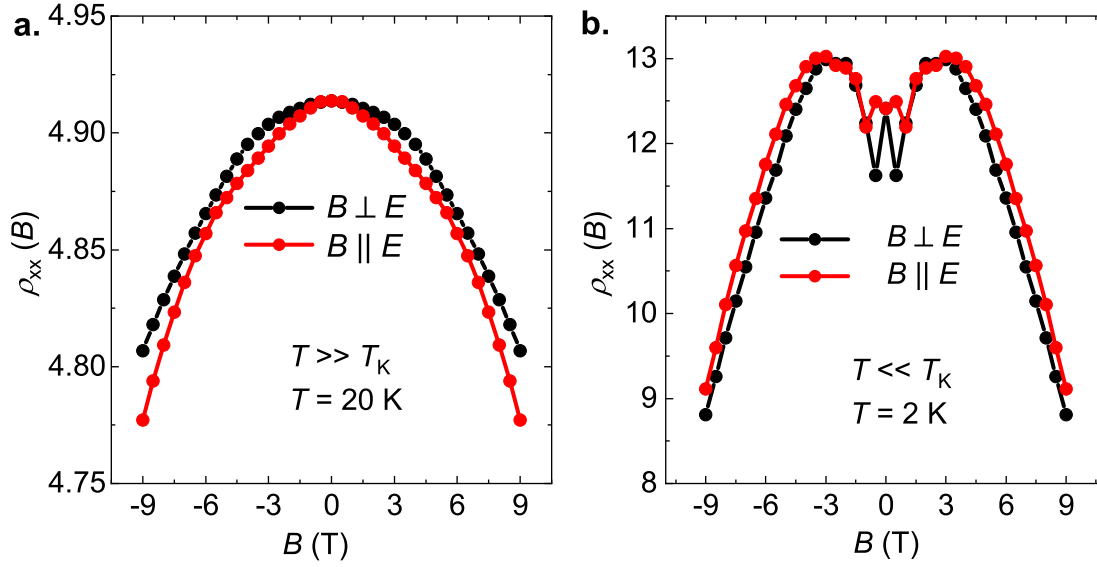


Figure 63: **Probing the chiral anomaly in $\text{Ce}_3\text{Bi}_4\text{Pd}_3$.** Transverse (black) and longitudinal (red) magnetic field-dependent resistivity for temperatures well above (panel a) and well below T_K (panel b). The data were symmetrized to remove any spurious Hall resistivity contribution, and mirrored on the vertical axis for clarity.

ative magnetoresistance for the longitudinal-field configuration ($B \parallel E$), but is absent in the transverse field configuration ($B \perp E$). Because the amplitude c_a of the chiral anomaly is inversely proportional to the density of states [43] and, thus, scales with the third power of the quasiparticle velocity, $c_a \approx (v^*)^3$, it is severely suppressed in interacting Weyl semimetals with low quasiparticle velocity v^* . This is consistent with the experiments: The magnetic-field dependent resistivity shows no discernible extra negative contribution in the longitudinal compared to the transverse field configuration, neither below nor above T_K (Fig. 63). The latter indicates that no Weyl nodes are present at the Fermi energy outside of the Kondo coherent regime.

Because the chiral anomaly is suppressed in the Weyl-Kondo semimetal state, a more suitable transport probe is needed that is independent of v^* and directly reveals the nontrivial topology in heavy fermion compounds. In the following

section I present the striking Hall response observed in the Kondo coherent regime of $\text{Ce}_3\text{Bi}_4\text{Pd}_3$, and show that it proves the nontrivial topological nature of this strongly interacting material.

5.3.4 Spontaneous Hall effect

As I have shown in Sect.3.4 and Sect.3.5, in systems with non-trivial topology the finite Berry curvature $\Omega(\mathbf{k})$ gives rise to an anomalous velocity $\mathbf{v}_a(\mathbf{k})$, that produces a spontaneous Hall effect (SHE) in zero magnetic field. Weyl nodes induce an $\Omega(\mathbf{k})$ that is independent of the Kondo renormalization and, thus, is not suppressed like the chiral anomaly. This makes the Hall effect an ideal transport tool to probe the nontrivial topology in a Weyl-Kondo semimetal.

To study the spontaneous Hall effect in $\text{Ce}_3\text{Bi}_4\text{Pd}_3$, three samples (labelled S1, S2 and S3) corresponding to three different batches and grown with two different techniques were measured (Fig.64). This is to check for reproducibility, and to rule out systematic extrinsic effects, e.g., due to the growth technique.

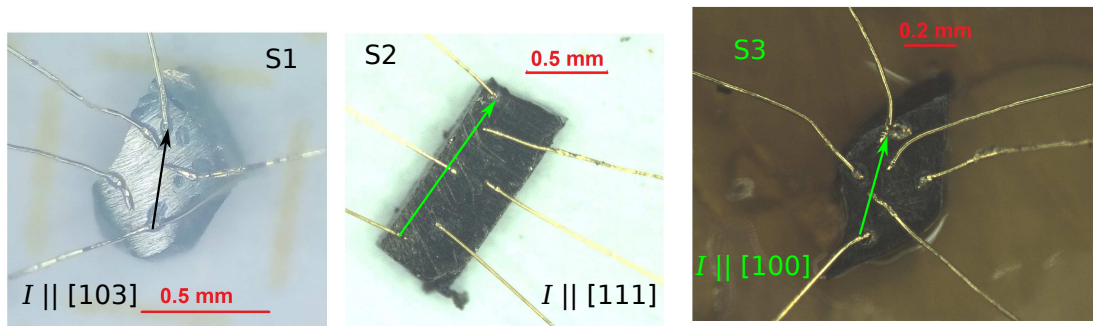


Figure 64: **Photographs of $\text{Ce}_3\text{Bi}_4\text{Pd}_3$ samples used for spontaneous Hall effect measurements.** Contacts were made by the spotwelding technique. Arrows indicate the current direction. Also the crystallographic direction along which the current was applied are indicated.

Sample S1 was grown by the Bi flux technique, and measured in a *Quantum De-*

sign PPMS equipped with a ^3He insert. Measurements were performed with a standard DC resistance bridge using a pseudo AC method, with the current applied in the [103] crystallographic direction. Samples S2 and S3 were grown by the Pb flux method, but correspond to two separate batches with slightly different growth temperature programs. Both were measured in an *Oxford* ^4He cryostat equipped with a 14 T magnet, and with a home built electrical transport sample probe. Resistivity and Hall measurements were performed using a *Stanford Research SR810* lockin amplifier, where both the first (1ω) and second (2ω) harmonic responses were detected. Current was supplied with a voltage controlled *Stanford Research* current supply in the [111] and [100] crystallographic directions for samples S2 and S3, respectively.

In practice, by contacting the (small) samples with the spot welding technique (Fig.64), a perfect Hall geometry cannot be achieved, leading to misalignment contributions for both the resistance and the Hall effect measurements (Fig. 65 b). Thus, in order to obtain the genuine Hall response of the sample, this misalignment contribution must be first determined. In what follows I will demonstrate how this is done in the case of sample S1.

The resistance measured across imperfectly aligned Hall contacts is denoted as R_{xy}^{meas} , the genuine Hall resistance as R_{xy} . The established technique to cancel out misalignment contributions in the normal Hall effect is to measure R_{xy}^{meas} for positive and negative magnetic fields and antisymmetrize the signal as

$$R_{xy} = \frac{R_{xy}^{\text{meas}}(+B_z) - R_{xy}^{\text{meas}}(-B_z)}{2} . \quad (45)$$

For the spontaneous and even-in-field Hall response, however, a different approach is needed. At room temperature and in zero applied magnetic field, where no Hall response exists, the ratio of resistances measured across the (longitudinal) resistivity and Hall contacts (Fig. 65 a) is determined as

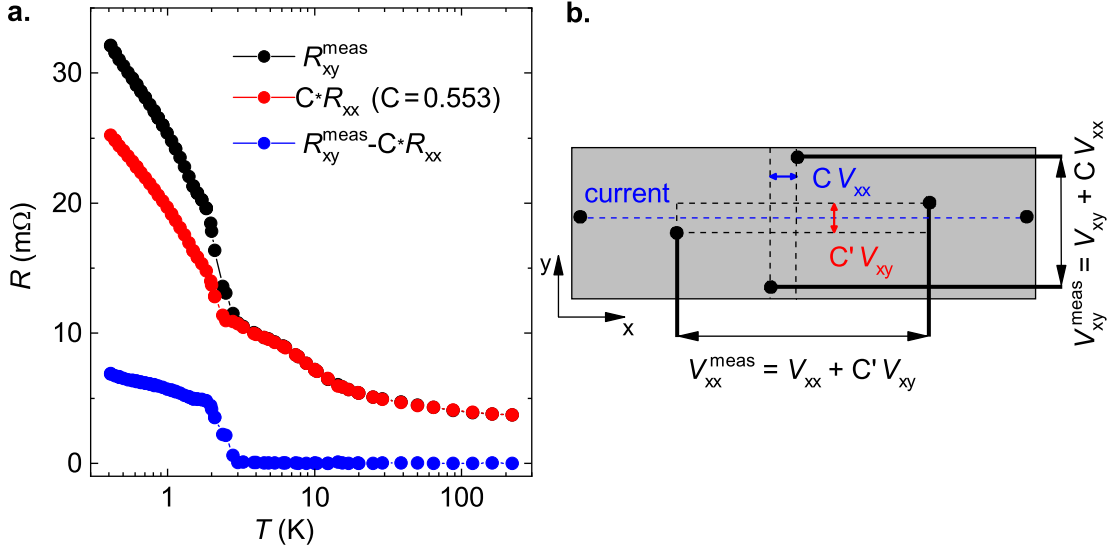


Figure 65: **Misalignment contribution in dc Hall effect measurements of $\text{Ce}_3\text{Bi}_4\text{Pd}_3$.** **a:** Temperature-dependent electrical resistance measured across the Hall contacts R_{xy}^{meas} (black), longitudinal resistance R_{xx} scaled to R_{xy}^{meas} at room temperature (red), and the difference of the two, $R_{xy}(T) = R_{xy}^{\text{meas}}(T) - CR_{xx}(T)$ with $C = 0.553$ (blue), all in zero applied magnetic field and for sample S1. A deviation appears only below $T = 3\text{K}$, where the intrinsic spontaneous Hall response sets in. **b:** Because of unavoidable contact misalignment, the measured voltages across the (longitudinal) resistivity and Hall contacts (V_{xx}^{meas} and V_{xy}^{meas}) contain, in addition to the intrinsic contributions V_{xx} and V_{xy} , the misalignment contributions $C'V_{xy}$ and CV_{xx} , respectively.

$$C = \frac{R_{xy}^{\text{meas}}}{R_{xx}^{\text{meas}}} = \frac{CR_{xx}}{R_{xx}} = 0.553 . \quad (46)$$

As the misalignment factor C is a purely geometrical quantity, and is thus temperature and field independent, the genuine Hall response at arbitrary fields and temperatures is

$$R_{xy}(T, B) = R_{xy}^{\text{meas}}(T, B) - CR_{xx}(T, B) . \quad (47)$$

$R_{xy}(T, B = 0)$ is zero from room temperature down to 3 K (Fig. 65 a). I note that

this contact misalignment correction procedure was adapted both for the DC and the 1ω AC measurements presented in this thesis.

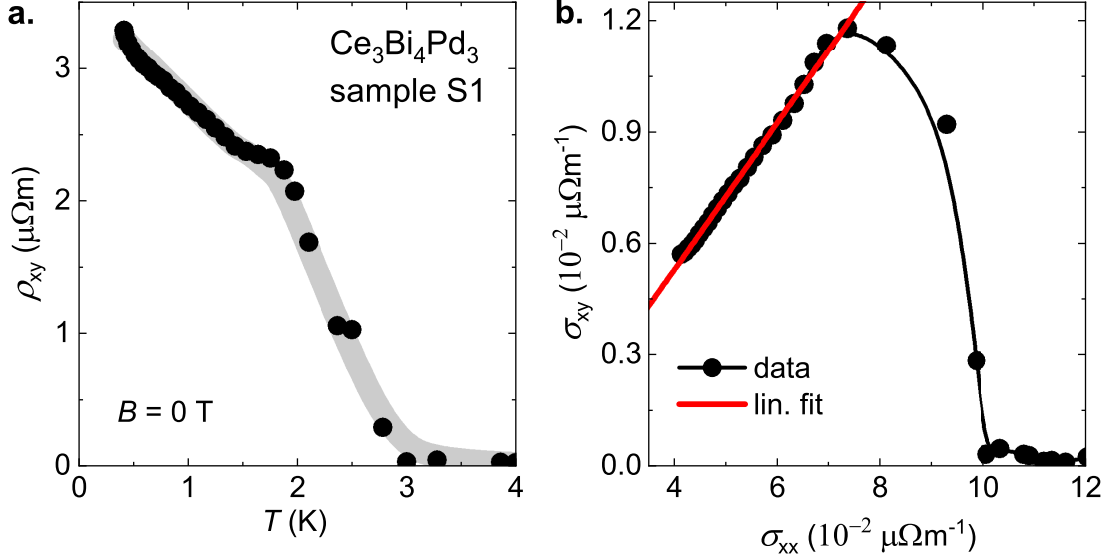


Figure 66: **Spontaneous Hall response in $\text{Ce}_3\text{Bi}_4\text{Pd}_3$.** **a:** Spontaneous Hall resistivity vs. temperature at zero magnetic field. **b:** Spontaneous Hall conductivity σ_{xy} vs. electrical conductivity σ_{xx} with T as an implicit parameter. The red line represents a linear fit, with a slope corresponding to $\tan \Theta_H = 0.2$.

For sample S1 a large spontaneous Hall effect appears below $T = 3$ K (Fig. 66 a and the blue curve in Fig. 65 a). This signal is then clearly not due to a misalignment of the Hall contacts, as was explained before. Instead, that it appears upon entering the Kondo coherent regime (Fig. 62 b inset), and agrees well with the onset of the $\sim T^3$ term in the electronic specific heat (Fig. 58 b), supports the intrinsic origin of this effect. Further more, the experiment was not only carried out in zero external magnetic field, but also without any sample premagnetization process. In fact, the material is entirely nonmagnetic, as evidenced by the absence of magnetic phase transition signatures in the magnetic susceptibility (Fig. 46), specific heat (Fig. 57) and related experiments (Sect. 5.3.5), as well as a careful muon spin rotation investigation (see Sect. 5.3.6). Thus, the observed spontaneous

$\rho_{xy}(T)$ can be assigned to the Berry curvature distribution of this material.

An interesting feature in the spontaneous Hall response of $\text{Ce}_3\text{Bi}_4\text{Pd}_3$ is the linear dependence between the Hall conductivity σ_{xy} and electrical conductivity σ_{xx} (Fig. 66 b). It is a direct evidence that the spontaneous Hall conductivity is proportional to the momentum scattering time τ . Only if $\sigma_{xy} \sim \tau$ is σ_{xy}/σ_{xx} constant [68]. In fact, such a behaviour is one of the hallmarks of a Berry curvature-driven spontaneous Hall effect in a noncentrosymmetric system (Sect.3.5), as therein the Hall current is carried by the out of equilibrium electron distribution (and hence is proportional to τ). This is further supported by the large magnitude of the effect: $\tan \Theta_H$, taken as the slope $\partial\sigma_{xy}/\partial\sigma_{xx}$, assumes the value 0.2 (Fig. 66 b), which is significantly larger than typical values reached in TRS breaking systems with trivial band topology (Fig.19 b). It is unambiguous evidence of a large Berry curvature distribution at the Fermi energy.

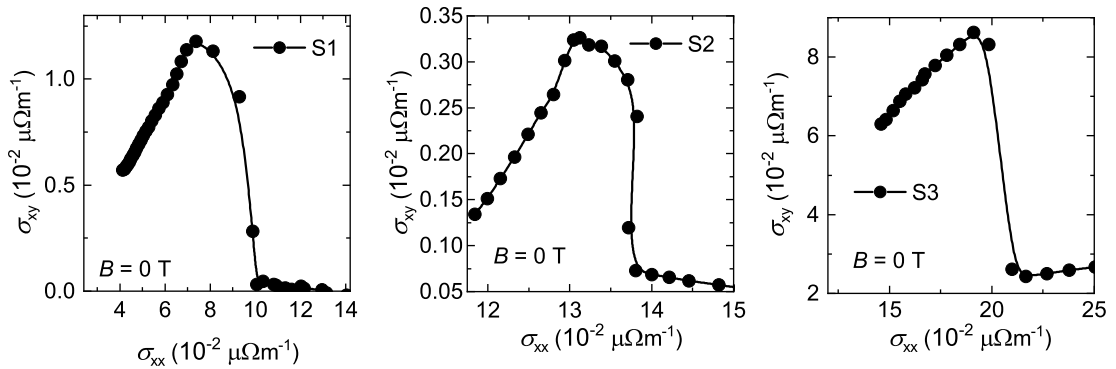


Figure 67: **Reproducibility of the spontaneous Hall effect in $\text{Ce}_3\text{Bi}_4\text{Pd}_3$.** Linear-in-current spontaneous Hall signal for crystals S1, S2, and S3, shown as σ_{xy} vs. σ_{xx} , where temperature is an implicit parameter, for samples from three different growth batches and orientations.

In order to check for the reproducibility of this effect, Hall measurements in zero magnetic field were done on two other samples (Fig. 67). Samples S2 and S3 were measured using AC current excitation, where the 1ω response was detected. They

show the same key features (Fig. 67): A clear enhancement of the spontaneous Hall effect below the coherence temperature (at 4.3 K and 2.5 K for samples S2 and S3, respectively), a clear linear dependence of σ_{xy} vs. σ_{xx} in the Kondo coherent regime, and large Hall angles of $\tan \Theta_H = 0.17$ and 0.52 for samples S2 and S3, respectively. That the Hall angle is different for the different samples is, most likely, due to the different current directions with respect to the crystal axes.

Finally, I turn to the imprint of the large Hall angle on the zero-field electrical resistivity. As discussed in Sect.3.1, a large Hall angle signals a strong reconstruction of the current path in the sample, that changes the bulk resistivity according to Eqn.20, which I rewrite here for convenience as

$$\rho_{xx} = \frac{1}{\sigma_{xx}} \frac{1}{1 + \tan^2 \Theta_H} . \quad (48)$$

Thus, as $\tan \Theta_H$ increases upon the onset of the spontaneous Hall effect, ρ_{xx} should drop.

Before the drop in the resistivity is determined, trivial contributions due to the contact misalignment must be corrected for. The transverse direction misalignment of the contacts (Fig. 65 b) leads to the appearance of an additional resistance $C'R_{xy}$, that adds to the intrinsic longitudinal resistance R_{xx} , so that the total measured resistance is $R_{xx}^{\text{meas}} = R_{xx} + C'R_{xy}$ (with R_{xy} obtained via Eqn. 47). The misalignment factor C' is determined as follows: At a temperature above the onset of the spontaneous Hall effect I measure, on the resistivity contacts, the normal Hall resistance $[R_{xx}^{\text{meas}}(+B) - R_{xx}^{\text{meas}}(-B)]/2$ as function of magnetic field (Fig. 68 a, black data points). At the same temperature, the Hall resistance on the Hall contacts is also measured, and scaled (by the factor C') such that it collapses onto the former curve (Fig. 68 a, red data points). With C' determined in this way, the temperature dependences of $C'R_{xy}$ and, thus, of R_{xx} can be determined in zero

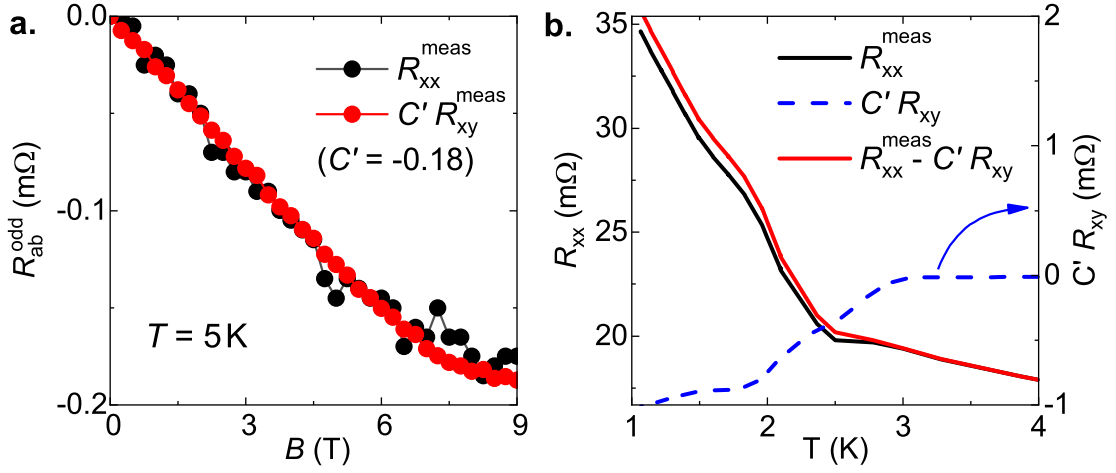


Figure 68: **Misalignment correction of the electrical resistance.** **a:** Measured odd-in- B resistance $R_{ab}^{\text{odd}} = [R_{ab}^{\text{meas}}(+B) - R_{ab}^{\text{meas}}(-B)]/2$ on the electrical resistance contacts ($ab = xx$, black), together with that measured across the Hall contacts and scaled by C' ($ab = xy$, red). The data are plotted for sample S1, and obtained at $T = 5$ K, above the onset of the spontaneous Hall effect. C' is chosen to achieve best overlap of the curves. **b:** With C' obtained from (a), the measured temperature-dependent resistance R_{xx}^{meas} (black) is corrected for the misalignment contribution $C'R_{xy}$ (blue dashed line), to obtain the intrinsic curve (red).

magnetic field. Indeed a drop across the onset of spontaneous Hall effect for sample S1 is discerned (Fig. 68 b), which is also seen in the uncorrected data. Here I note that the correction term used in Eqn. 47 is $R_{xx}^{\text{meas}}(T, B)$ instead of $R_{xx}(T, B)$, thus correcting the effect only to first order. As higher order terms involving the product CC' are very small (for C' see Fig. 68), this is deemed sufficiently accurate.

A clear change of the resistance was observed for all samples (Fig. 69 a-c). To test the scenario proposed by Eqn. 48 quantitatively, I plot the relative change of resistance across the onset of the spontaneous Hall effect as a function of $\tan \Theta_H$ (Fig. 69 d). Indeed, the size of the relative drop increases with $\tan \Theta_H$, and the magnitude and functional form of the dependence (Eqn. 48) are in overall agreement with the data (Fig. 69 d). This provides strong evidence that the drop in R_{xx} is indeed due to this intrinsic effect.

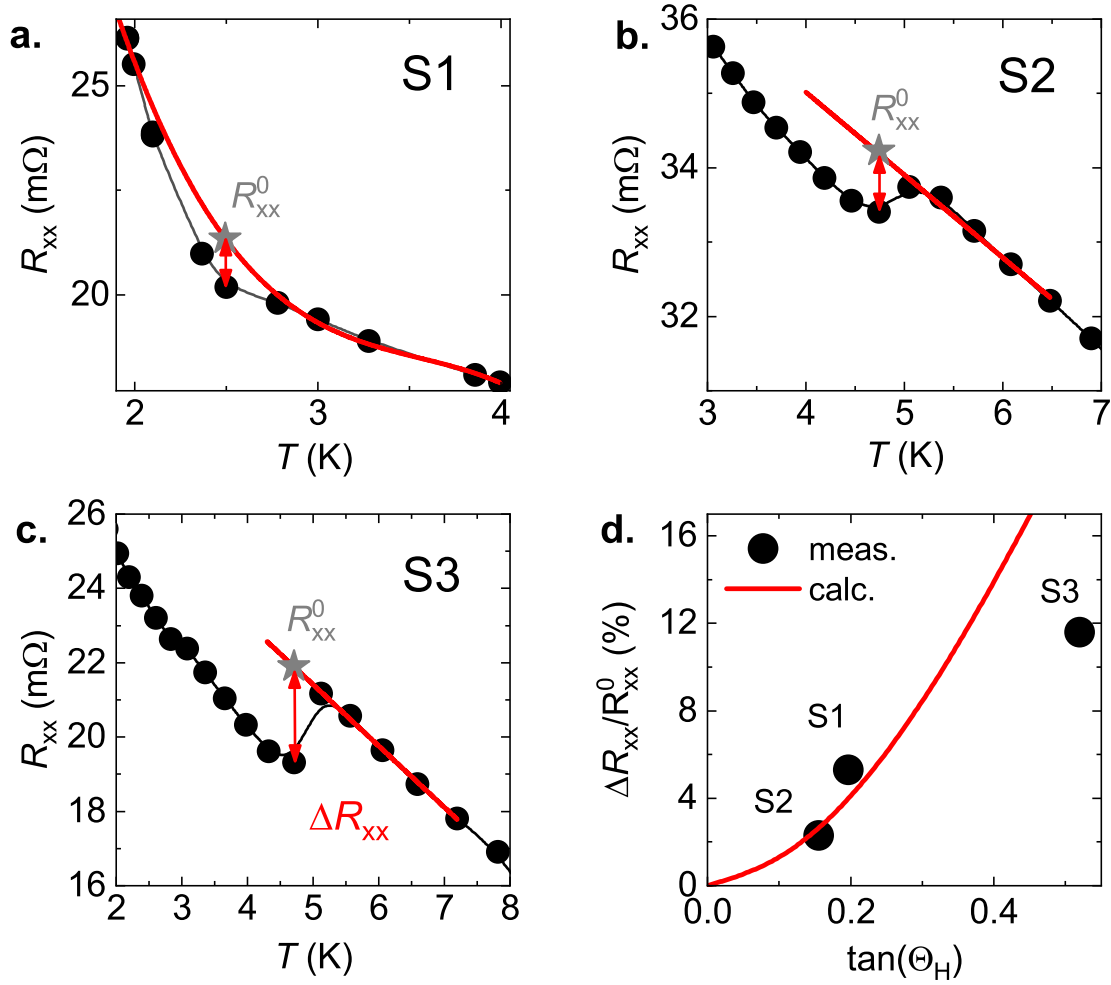


Figure 69: **Resistance change due to large Hall angle.** **a-c:** Longitudinal electrical resistance R_{xx} , corrected for contact misalignment (see text), for samples S1, S2 and S3. With decreasing temperature, a drop of R_{xx} is observed at the onset of the spontaneous Hall effect. For a rough estimate of its magnitude, $R_{xx}(T)$ above the onset temperature is extrapolated to lower T and the difference ΔR_{xx} is read off the data as indicated (red double arrow). **d:** Relative resistance change $\Delta R_{xx}/R_{xx}^0$ of the three sample (symbols) vs. the tangent of the Hall angle. Clearly, $\Delta R_{xx}/R_{xx}^0$ increases with Θ_H . The red line shows the expectation from Eqn.48, $\Delta R_{xx}/R_{xx}^0 = (\rho_{xx}^0 - \rho_{xx})/\rho_{xx}^0 = 1 - 1/(1 + \tan^2 \Theta_H)$, with no adjustable parameter. The overall agreement, both in terms of magnitude and shape, further underpins that the observed signatures in R_{xx} are intrinsic and due to the giant magnitude of the Hall angle.

5.3.5 In search for magnetic phase transition in $\text{Ce}_3\text{Bi}_4\text{Pd}_3$

The appearance of a spontaneous Hall effect in $\text{Ce}_3\text{Bi}_4\text{Pd}_3$ in its Kondo coherent regime is a unique signature of the finite Berry curvature distribution in this system. However, the question remains whether the underlying Berry curvature is associated with a time-reversal breaking mechanism or with an inversion symmetry breaking one that supports the Weyl-Kondo semimetal state. Indeed, I showed that in $\text{Ce}_3\text{Bi}_4\text{Pd}_3$ there is no evidence for a magnetic phase transition at the onset temperature of the spontaneous Hall effect (nor at any other temperature), supported by the lack of related phase transition signatures in the temperature-dependent magnetic susceptibility $\chi(T)$ (Fig. 46 a), magnetization (Fig. 46 b), and specific heat (Fig. 57). This is particularly appealing in light of the huge size of $\tan \Theta_{\text{H}}$ that reaches 0.2 (Fig. 66 b), which is unique even among fully spin polarized ferromagnets (Fig. 19 b) [57].

To corroborate on the lack of time-reversal symmetry breaking transitions with more precise measurements, high data-density and closed-loop field-sweep measurements of the magnetization were carried out at temperatures below the onset of the spontaneous Hall effect (Fig. 70 a, b). Any even spurious ferromagnetic transition would lead to hysteretic behaviour. Clearly, no hysteresis is observed, neither in sweeps up to high fields (up to 2.5 T, panel a), nor in precise very low-field sweeps (up to 0.15 T, panel b). In fact, the $M(H)$ curves in both field ranges show smooth, linear behaviour, as expected for a paramagnetic phase.

In addition, to look for phase transitions, be it with or without TRS breaking, high data-density specific heat measurements at zero field were carried out. The data for the batch of sample S1 (Fig. 70 c) are plotted as C/T vs. T^2 . As seen in Sect.5.3.2, an enhanced $C/T = \Gamma T^2$ term with $\Gamma = 0.008 \text{ J}/(\text{mol-Ce K}^4)$, corresponding to a low quasiparticle velocity of about 1000 m/s is observed. No phase transition anomaly is seen in the data. Most notably, at the onset temperature of

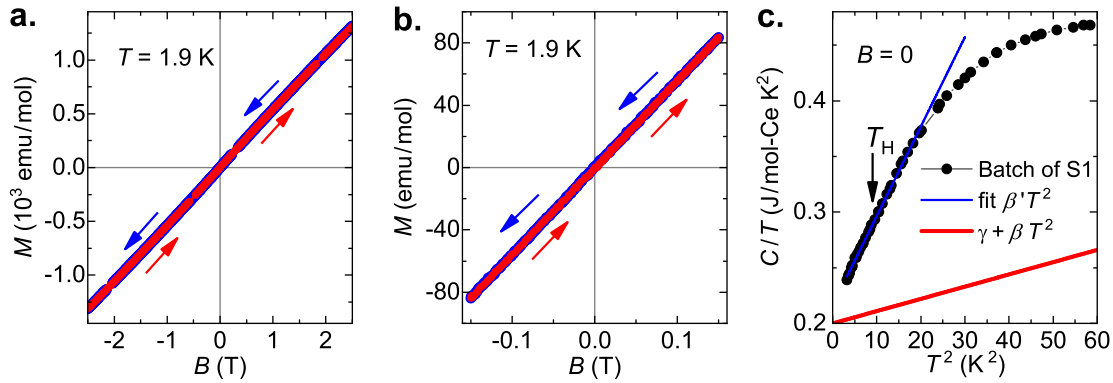


Figure 70: **In search of magnetic phase transition in $\text{Ce}_3\text{Bi}_4\text{Pd}_3$ at low temperatures.** **a-b:** Magnetization loops of $\text{Ce}_3\text{Bi}_4\text{Pd}_3$ in fields up to 2.5 T (a) and higher accuracy measurement in fields up to 150 mT (b), both revealing the absence of any hysteretic behaviour. The symbol sizes for up (red) and down (blue) sweeps are different for better visibility. The initial magnetization curve is contained in the up sweep. **c:** As measured specific heat data in zero magnetic field, plotted as C/T vs. T^2 (black), for the batch of sample S1. The data follow a linear behaviour (blue line) with a slope that overshoots the Debye phonon term (red line, offset for clarity). No phase transition is discerned, neither at the onset of the spontaneous Hall effect (T_H), nor elsewhere. The data were taken and provided by Gaku Eguchi from TU-Vienna [137].

the spontaneous Hall effect (T_H), the data vary smoothly, following the C/T vs. T^2 law (Sect. 5.3.2) without any detectable deviation. In summary, magnetization, and specific heat data rule out that the observed spontaneous Hall effect seen in $\text{Ce}_3\text{Bi}_4\text{Pd}_3$ samples is of magnetic origin.

5.3.6 Muon spin rotation experiments

As I discussed in Sect. 5.3.5, bulk magnetization and specific heat measurements rule out magnetic phase transitions in $\text{Ce}_3\text{Bi}_4\text{Pd}_3$. Nevertheless, such thermodynamic probes are typically sensitive to long range order, whereas a nontrivial Hall effect can also occur in systems that breaks TRS in the absence of long range magnetic order such as in the case of $\text{Pr}_2\text{Ir}_2\text{O}_7$ [79]. Thus, to check whether TRS

is truly preserved in $\text{Ce}_3\text{Bi}_4\text{Pd}_3$, zero-field muon spin rotation (ZF- μSR) is the tool of choice: due to its high sensitivity to tiny magnetic fields (down to $10\ \mu\text{T}$) it can detect even spurious spontaneous TRS breaking, as described in detail in Sect. 2.5.

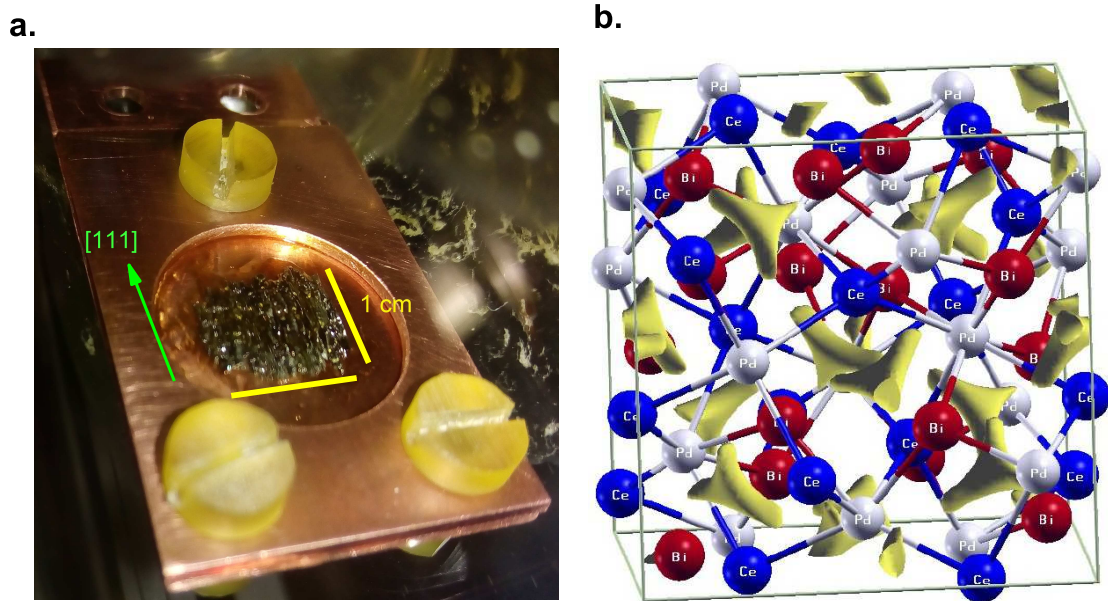


Figure 71: μSR setup for $\text{Ce}_3\text{Bi}_4\text{Pd}_3$. **a**: Photograph of the samples for μSR experiment. A mosaic of long single crystals (growth direction in $[111]$ crystallographic direction). The inplane orientation is random. **b**: DFT calculation of regions with minimum Coulomb potential (yellow areas) that are likely stopping sites for μ^+ . Red atoms denote Bi, blue Ce and grey denotes Pd. The setup in panel **a** was made by Xinlin Yan and Andrey Prokofiev from TU-Vienna. Peter Blaha provided the figure in panel **b** [137].

μSR measurements on $\text{Ce}_3\text{Bi}_4\text{Pd}_3$ were performed at the Dolly spectrometer of the Swiss Muon Source at the Paul Scherrer Institute. The data were taken in collaboration with Toni Shiroka (ETH Zurich) and with the technical support of Jean-Christoph Orain (Paul Scherrer Institute). Single crystals were arranged to form a mosaic with about 1 cm diameter and a thickness of about 0.5 mm, glued on top of a thin copper foil solidly clamped to a copper sample holder (Fig. 71 a), thus optimally using the muon beam cross section, minimizing the background

from the sample holder, and guaranteeing good thermal contact. Crystals for this measurement were synthesized using the Pb flux technique by Xinlin Yan (TU-Vienna), and grow naturally along the [111] crystallographic directions. All single crystals were glued such that the [111] directions were parallel to each other. This setup resulted in very low spurious background signals. A cold-finger Oxford Heliox ^3He system combined with a ^4He Oxford Variox cryostat was used to reach temperatures down to 250 mK. By employing active compensation coils, true zero-field (ZF) conditions could be achieved during the ZF- μSR experiments. DFT calculations to determine the Coulomb potential minima (energy iso-surfaces) were carried out (Fig. 71 b). Such interstitial positions are likely stopping sites for the μ^+ particles.

Figure 72 shows a typical muon spin relaxation curve for $\text{Ce}_3\text{Bi}_4\text{Pd}_3$ measured at the base temperature of $T = 260$ mK, well below the onset of the spontaneous Hall effect. The absence of any oscillating contribution reveals that there is no long range magnetic order present. Instead, the muon spins decohere with time. The ZF data in Fig. 72 are very well described by Eqn. 16, with a nuclear term with the relaxation rate $\sigma = 12 \cdot 10^{-2}/\mu\text{s}$ that dominates the relaxation, and an electronic contribution with a much smaller rate of $\Lambda = 3.9 \cdot 10^{-2}/\mu\text{s}$. The absence of a magnetic ordering is further confirmed by the prompt recovery of the signal in a very small longitudinal magnetic field of $B_{\text{LF}} = 5$ mT (Fig. 72).

Also the temperature dependence of the muon relaxation curves does not show any sign of a magnetic phase transition in $\text{Ce}_3\text{Bi}_4\text{Pd}_3$. As an example, for temperatures above the onset of the spontaneous Hall effect, at $T = 10$ K, the muon relaxation curve coincides with that at $T = 260$ mK (Fig. 73 a). In fact, both the nuclear and the electronic relaxation rates, determined as described above, are temperature independent for the two decades in temperature covered by the measurement (Fig. 73 b). This is strong evidence that TRS is indeed preserved

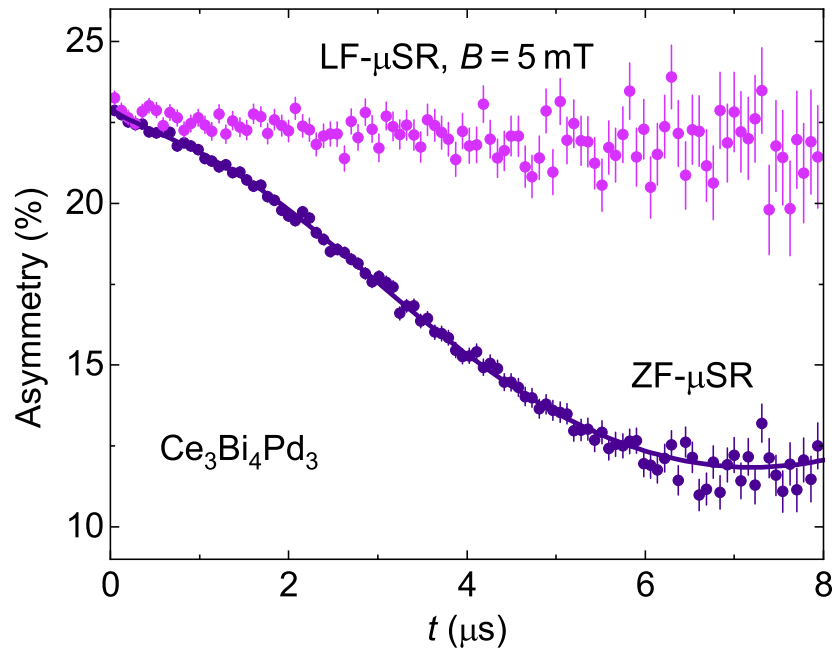


Figure 72: μSR relaxation in $\text{Ce}_3\text{Bi}_4\text{Pd}_3$. High-statistics time dependent relaxation curve was taken at $T = 260$ mK at zero magnetic field indicated by ZF (dark blue symbols), and at 5 mT longitudinal magnetic field indicated denoted by B_{LF} (light violet symbols). Dark blue line denotes best fit according to Eqn. 16. The data and the analysis in the figure were provided by Toni Shiroka (ETH Zurich) see [137].

in $\text{Ce}_3\text{Bi}_4\text{Pd}_3$, excluding a conventional, magnetization induced mechanism as the origin of the observed spontaneous Hall effect.

5.3.7 Magnetic field dependence of the Hall effect

In order to learn more about the mechanism giving rise to the spontaneous Hall effect in $\text{Ce}_3\text{Bi}_4\text{Pd}_3$, Hall resistivity measurements were done as function of an applied magnetic field.

Hall resistivity isotherms $\rho_{xy}(B)$ are fundamentally different for temperatures well above and well below the coherence temperature T^* (Fig. 74). Whereas $\rho_{xy}(B)$ shows a simple linear in magnetic field behaviour for $T \gg T^*$ consistent with a

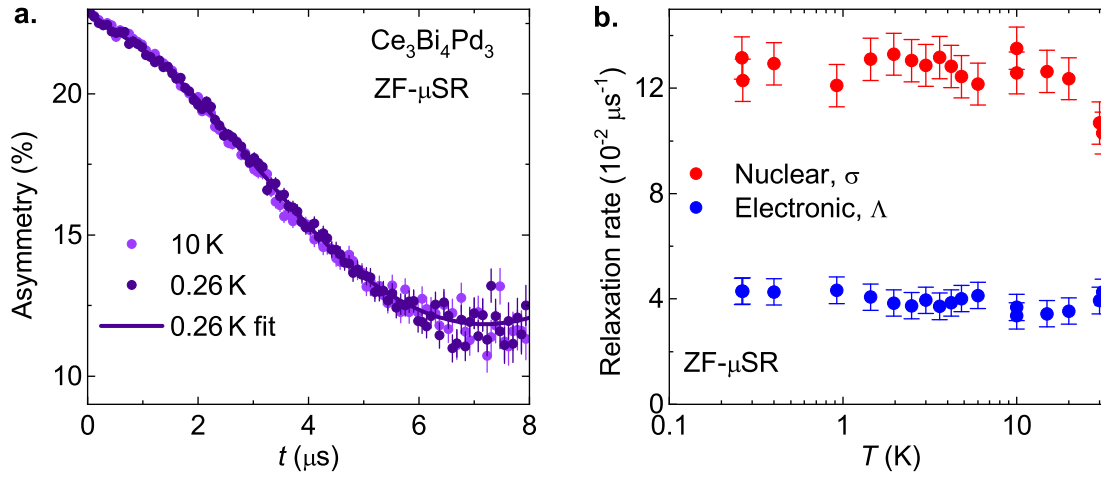


Figure 73: **Temperature-dependent μSR relaxation in $\text{Ce}_3\text{Bi}_4\text{Pd}_3$.** **a:** Representative time dependent relaxation curves taken at $T = 260$ mK and $T = 10$ K at zero magnetic field indicated by ZF (dark and light violet symbols, respectively). Dark violet line denotes best fit to the 260 mK data according to Eqn. 16. **b:** Temperature dependence of the nuclear and electronic contributions to the relaxation rate. The values are obtained from fitting Eqn. 16 to time dependent relaxation curves such as that presented in panel **a**. To confirm whether the error bars indeed reflect the scattering of the extracted relaxation times, relaxation data as in panel **a** were collected twice at 0.26 K, 10 K and about 30 K. The relaxation rates extracted from fits to these two data sets are both plotted in panel **b** (see two data points for these temperatures). Indeed, these data points do agree within the error bars. The data and analysis in this figure were provided by Toni Shiroka (ETH Zurich) see [137].

single hole like band (Fig. 74 a), it shows strong nonlinearities in field for $T \ll T^*$ (Fig. 74 b). Most strikingly, a large even-in-field component $\rho_{xy}^{\text{even}} = [\rho_{xy}(B) + \rho_{xy}(-B)]/2$ is observed that even overwhelms the usual odd-in-field component $\rho_{xy}^{\text{odd}} = [\rho_{xy}(B) - \rho_{xy}(-B)]/2$. As the spontaneous Hall effect in zero field continues as $\rho_{xy}^{\text{even}}(B)$ in finite fields, I first discuss this term. Such even-in- B components are incompatible with the standard (magnetic field or magnetization induced) Hall conductivity mechanism where the elements σ_{xy} of the fully antisymmetric Hall conductivity tensor may couple only to a physical quantity G that breaks time-

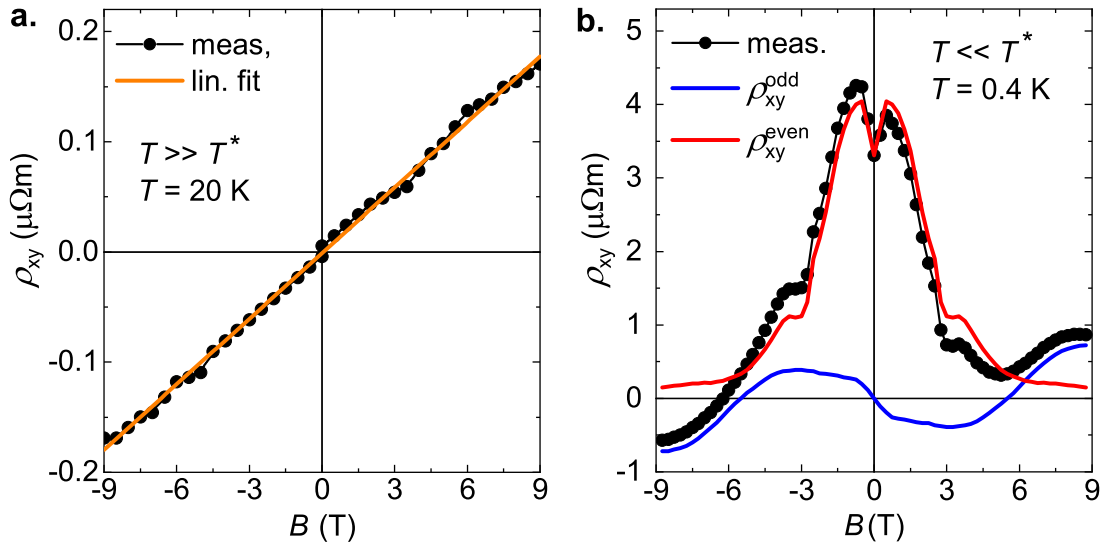


Figure 74: **Magnetic field-dependent Hall effect in $\text{Ce}_3\text{Bi}_4\text{Pd}_3$.** **a:** Hall resistance vs. magnetic field in $\text{Ce}_3\text{Bi}_4\text{Pd}_3$ at $T = 20$ K above the coherence temperature. The measured data are indicated by symbols, whereas the orange line indicates a linear fit to the data. **b:** The same measurement at $T = 400$ mK. The data (black symbols) can be decomposed into an even-in- B ρ_{xy}^{even} and an odd-in- B ρ_{xy}^{odd} components shown as red and blue lines, respectively. These contributions are given by symmetrizing and antisymmetrizing the measured data, respectively. The lines are mirrored to extend to the negative B axis for better clarity.

reversal symmetry and, thus, have to be an odd function of this quantity, e.g., $\sigma_{xy}(B) = -\sigma_{xy}(-B)$ where $G = B$ (Sect. 3.1) [73].

This doesn't mean that the Casimir-Onsager relations are violated, but rather that whatever parameter G describing the Hall effect is, it does not couple to the magnetic field and, thus, it is clearly not of magnetic origin. This rules out trivial mechanisms such as skew scattering or side jump effects that are proportional to the magnetization [68]. Nevertheless, the magnetic field plays an important role, as the amplitude of $\rho_{xy}^{\text{even}}(B)$ is clearly field dependent (Fig. 75). This is to be expected in a Kondo system, where increasing the magnetic field is analogous to increasing the temperature above T^* .

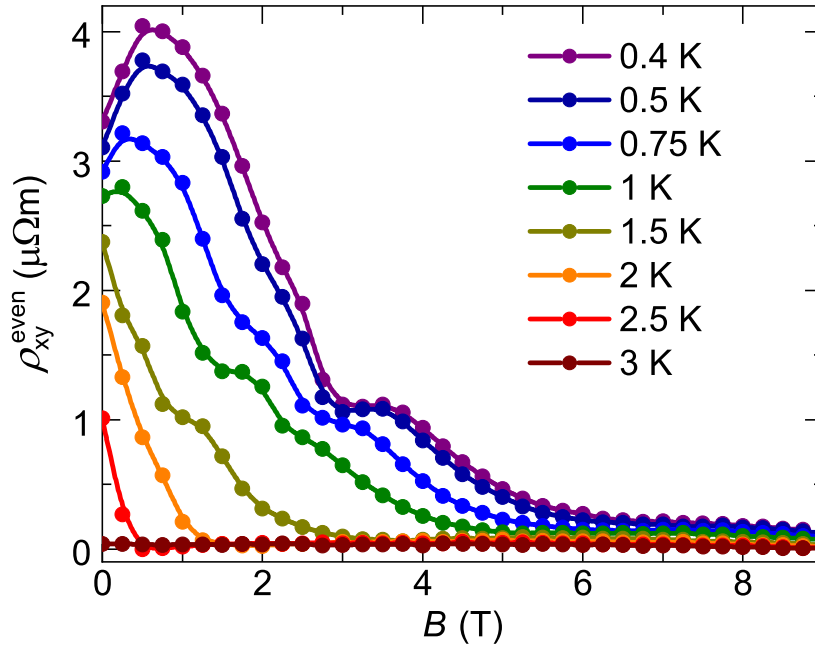


Figure 75: **Even-in-magnetic field Hall resistivity component of $\text{Ce}_3\text{Bi}_4\text{Pd}_3$.** The iso- T $\rho_{xy}^{\text{even}}(B)$ curves were determined by symmetrizing the measured $\rho_{xy}(B)$ curves (see text).

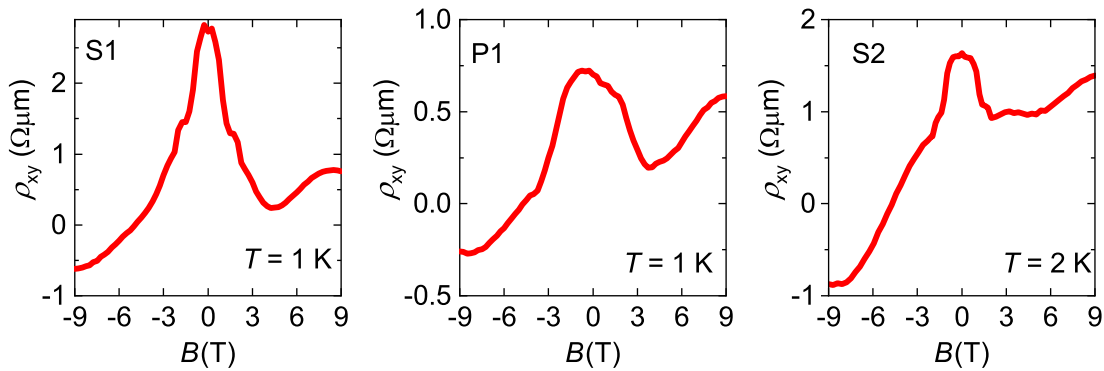


Figure 76: **Qualitative reproducibility of the Hall effect features.** The non-linear-in- B Hall resistivity in three different samples. Samples S1 and S2 are the same as in Fig.67. Samples P1 is from the same batch as S1. All samples show a pronounced even-in- B component.

To check for the reproducibility of this effect, three separate samples were measured (Fig. 76). Clearly, strong nonlinearities of the Hall effect are observed in all crystals, especially the even-in-field, and the nonlinear odd-in- B terms, as seen in Fig. 76. Whereas the qualitative behaviour is reproducible from sample to sample, quantitative differences are most probably due to the effect being sensitive to the crystallographic direction and being directly dependent on the scattering time τ , that is usually different for different samples.

Beside the even-in- B component, the Hall resistivity below T^* also shows an odd-in- B component (the blue curve in Fig. 74 b). In what follows I show that this contribution cannot be produced by two-band effects, and is instead Berry curvature-driven. To demonstrate this, a two-band analysis, corresponding to Eqns. 24, 25, was performed using a recently established robust analysis scheme [74].

The analysis was done on the $\rho_{xy}^{\text{odd}}(B)$ data taken at the lowest temperature of 0.4 K (Fig. 78 a), where the nonlinearity is largest. Though the obtained best fit cannot fully account for the field dependence, it reproduces the overall shape of $\rho_{xy}^{\text{odd}}(B)$ (Fig. 77 a). The obtained charge carrier concentrations and mobilities are $n_1 = 3.39 \times 10^{19} \text{ cm}^{-3}$ and $\mu_1 = 105 \text{ cm}^2/\text{Vs}$ for the (hole) majority carriers and $n_2 = 1.24 \times 10^{17} \text{ cm}^{-3}$ and $\mu_2 = -3820 \text{ cm}^2/\text{Vs}$ for the (electron) minority carriers. In a second step, the transverse magnetic field-dependent resistivity for these parameters is calculated (Eqn. 25, red curve in Fig. 77 b). It completely fails to describe the corresponding data. In fact, no negative magnetic field-dependent resistivity can arise in this setting. Thus, two-band effects are not the cause of the observed nonlinearities in the low-temperature magnetotransport data. Instead, the temperature evolution of $\rho_{xy}^{\text{odd}}(B)$ (Fig. 78) suggests that it consists of two terms: a Lorentz force-driven linear-in-magnetic field term, that is also observed at higher temperature (Fig. 74 a), and an intrinsic anomalous Hall effect. The latter

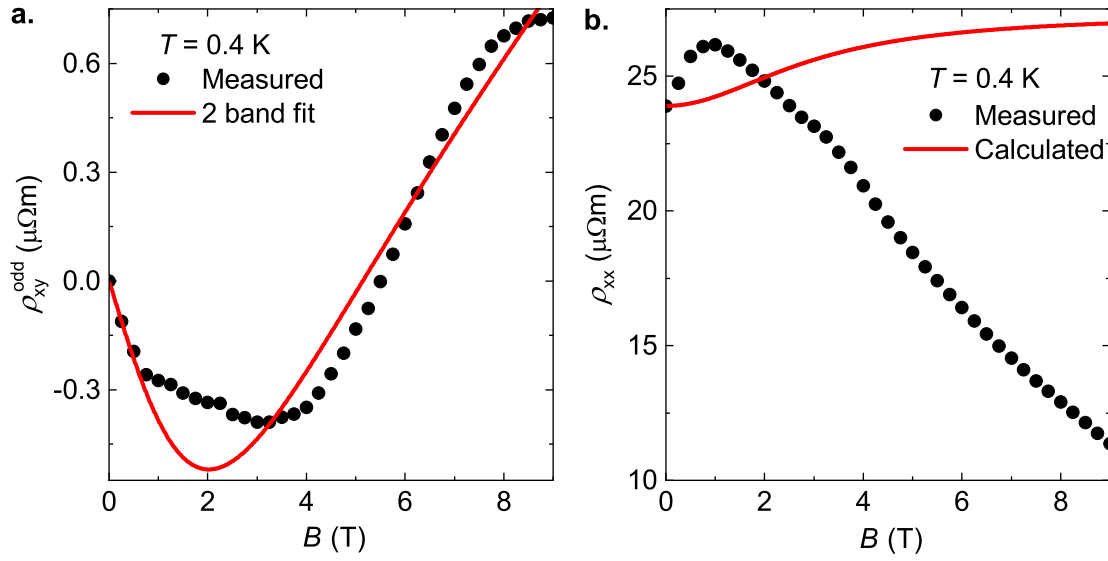


Figure 77: **Two-band analysis of magnetotransport data of $\text{Ce}_3\text{Bi}_4\text{Pd}_3$.** **a:** Odd-in-field Hall resistivity at 0.4 K (from Fig. 78 a) with best fit of a two-band model (red line, see text). **b:** Transverse magnetic field-dependent resistivity at 0.4 K with corresponding curve calculated from the parameters obtained in (a), showing that a two-band model cannot account for the experimental curves. The analysis in this figure was done by Gaku Eguchi from TU-Vienna.

term is consistent with a Berry curvature-driven AHE due to broken TRS [68], which is in this case due to the applied magnetic field.

In such a scenario, the AHE is carried by the equilibrium Fermi-Dirac distribution (Sect.3.4) and, thus, is independent of the scattering time τ (Sect.3.4). As a consequence, the corresponding Hall resistivity must scale quadratically with the electrical resistivity, i.e., $\rho_{xy}^{\text{odd}} \sim \rho_{xx}^2$ (Sect.3.4), which is indeed the case for $\text{Ce}_3\text{Bi}_4\text{Pd}_3$ (Fig. 78 b). The AHE contribution to ρ_{xy}^{odd} extracted with respect to the normal (linear) Hall background at $T = 4$ K as $\rho_{xy}^{\text{odd}} - \rho_{xy}^{\text{odd}}(4 \text{ K})$, scales quadratically with the corresponding contribution of the electrical resistivity $\rho_{xx} - \rho_{xx}(4 \text{ K})$ (Fig. 78 b).

Finally, I discuss the linear-in- B , ordinary Hall effect. As seen in Fig. 74 a, it is

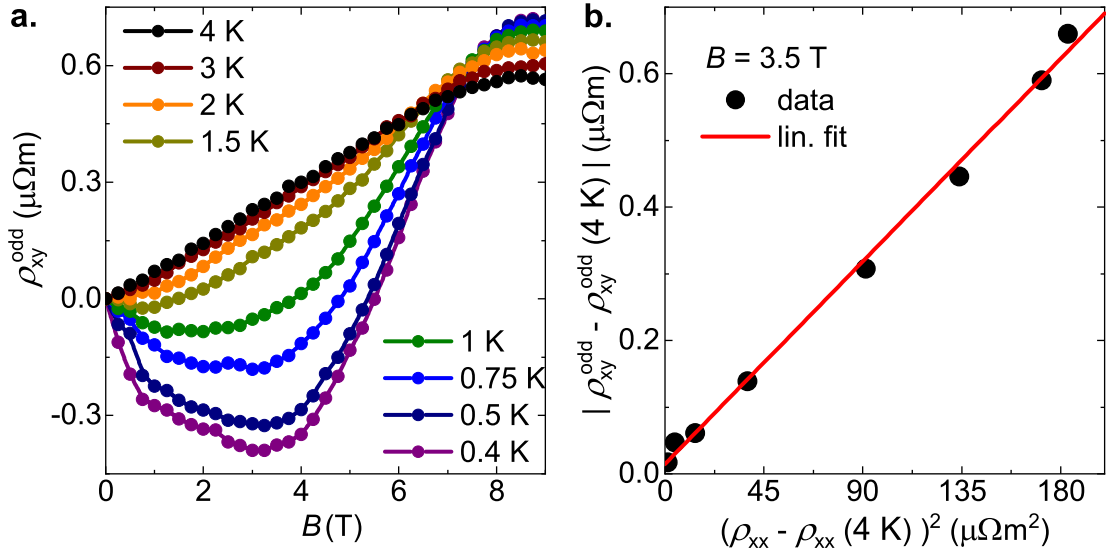


Figure 78: **Odd-in-magnetic field Hall resistivity component of $\text{Ce}_3\text{Bi}_4\text{Pd}_3$.** **a:** The iso- T $\rho_{xy}^{\text{odd}}(B)$ curves were determined by antisymmetrizing the measured $\rho_{xy}(B)$ curves (see text). Below T^* it displays an intrinsic anomalous Hall effect, in addition to a linear background. **b:** The amplitude of the anomalous Hall effect with respect to the linear background at 4 K, $\rho_{xy}^{\text{odd}} - \rho_{xy}^{\text{odd}}(4\text{ K})$, is linear in the square of the corresponding electrical resistivity $\rho_{xx} - \rho_{xx}(4\text{ K})$.

characterized by a positive Hall coefficient R_{H} , indicating hole type conduction. At low temperatures, a slight nonlinearity appears above $B = 8\text{ T}$ (Fig. 78 b) that, as will be discussed in Sect. 5.4, is due to the proximity to a field induced topological phase transition. Thus, I will define R_{H} as $\rho_{xy}^{\text{odd}}(B)/B$ at $B = 8\text{ T}$.

The temperature dependence of R_{H} , similar to $\rho_{xy}(B)$, is markedly different below and above the onset of Kondo coherence (Fig. 79 a). At high temperatures, a monotonic increase of R_{H} is seen, where below $T = 7\text{ K}$ R_{H} saturates, indicating the presence of a finite Fermi surface.

To check whether $R_{\text{H}}(T)$ in $\text{Ce}_3\text{Bi}_4\text{Pd}_3$ is governed by a temperature-dependent charge carrier concentration or by skew scattering (Sect. 3.3), I plot R_{H} vs. $\rho_{\text{mag}}\chi^*$ (Fig. 79 b), with temperature as an implicit parameter. In the fully incoherent

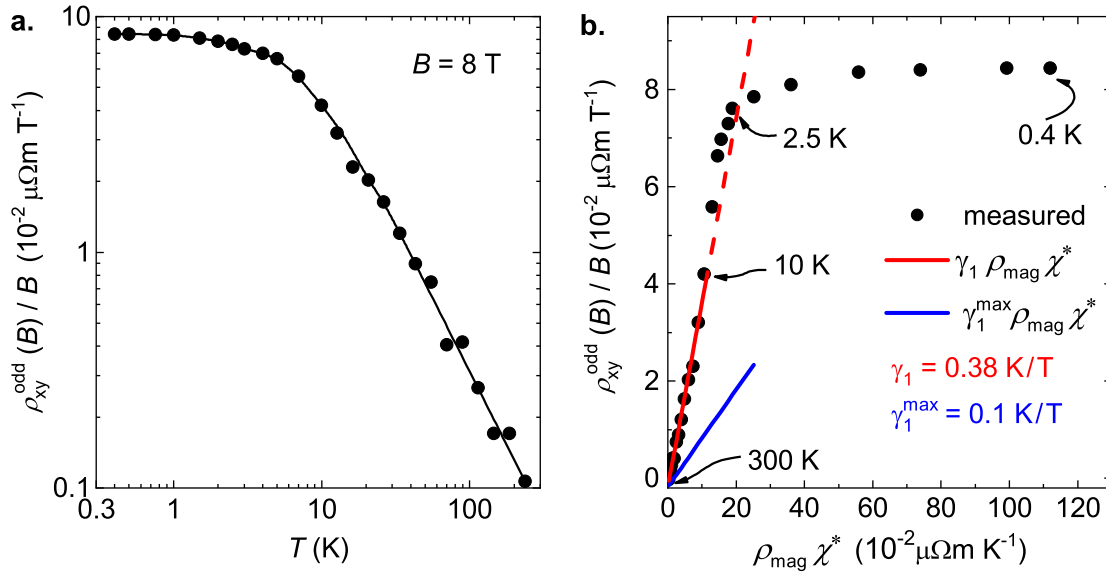


Figure 79: **Temperature-dependent normal Hall coefficient of $\text{Ce}_3\text{Bi}_4\text{Pd}_3$.** **a:** R_H defined as ρ_{xy}^{odd}/B at $B=8\text{ T}$ vs. T on a log-log scale. **b:** The same quantity now expressed vs. the product of the magnetic contribution to the zero-field resistivity (see text) and reduced magnetic susceptibility (χ^* , see Sect. 3.3) to check for possible skew scattering effects (Sect. 3.3). The red line denotes a linear fit to the data at high temperatures with slope γ_1 . Indicated with a red dashed line is its extension to low temperatures. The blue line indicates the theoretical maximum possible contribution due to skew scattering (see text).

regime above $T = 10\text{ K}$, a linear relationship with the slope $\gamma_1 = 0.38\text{ K/T}$ is observed (Fig. 79 b). At first, this seems to suggest that the Hall response of this material is dominated by skew scattering. However, such a large γ_1 value is not only incompatible with the Ce^{3+} case of $\gamma_1 < 0.1$ (see Fig. 79 b and Sect. 3.3), but is also inconsistent with skew scattering in heavy fermion compounds for any phase shift δ , as $|\gamma_1| \leq 0.21$ (Sect. 3.3). Therefore, skew scattering plays at best a minor role in $R_H(T)$ in the incoherent regime. In the Kondo coherent regime skew scattering is known to freeze out with decreasing temperature. In $\text{Ce}_3\text{Bi}_4\text{Pd}_3$, however, the magnitude of R_H continues to increase below T^* . Thus, skew scattering does not play an important role in $R_H(T)$, neither above nor below T^* .

Thus, $R_H(T)$ should be interpreted in terms of a change in the charge carrier concentration: At high temperatures, it decreases with decreasing temperature, consistent with the opening of a pseudo-gapped electronic density of states. At the lowest temperatures, it saturates to a constant value, indicating that the system assumes a semimetallic ground state, with a very small but finite Fermi surface. Indeed, the corresponding hole concentration reaches $8 \times 10^{19} \text{ cm}^{-3}$, or 0.002 charge carriers per atom.

5.3.8 Nonlinearity in the Hall effect

As discussed in the previous sections (Sect.5.3.4 and Sect.5.3.7) both the spontaneous Hall effect in $\text{Ce}_3\text{Bi}_4\text{Pd}_3$ and the corresponding even-in-magnetic field Hall resistivity cannot be explained by the conventional time-reversal symmetry breaking Hall effect. In fact, that they are determined by the scattering rate in a nonmagnetic ground state evidences their nonequilibrium nature. Indeed, it was shown that the Berry curvature in TRS preserving noncentrosymmetric systems induces a Hall effect that is carried by the nonequilibrium electron distribution function (Sect.3.5). Therein, the salient feature was shown to be its nonlinearity in the driving electric field or electrical current (Eqn.31, Sect.3.5). Thus, to conclude whether such a mechanism is at the heart of the observed effects in $\text{Ce}_3\text{Bi}_4\text{Pd}_3$, and whether it is directly determined by the Berry curvature distribution, the dependence of the spontaneous Hall signal on the driving current was systematically investigated.

Measurements were performed in an *Oxford* ^4He cryostat equipped with a 14 T magnet, and a home made electrical transport probe. $I - V$ curves on samples S2, S3 (Fig.64 b,c) and S4 (from the same batch as S3) were obtained in two subsequent set of experiments. In the first set of experiments, the DC Hall voltage response to a DC current drive was measured with a *Keithley* nanovoltmeter. In

the second set of experiments, the AC voltage response to an AC current excitation (with angular frequency of 1ω) was measured using the standard lock-in technique. Voltage components were detected in the 0ω , 1ω and 2ω channels. To increase the precision of the measurements, a *Stanford Research* voltage controlled current supply was used. In both sets of experiments, at first data were collected at base temperature ($T \approx 2\text{K}$) and at zero magnetic field. Then, data acquisition was extended to higher temperatures and at finite magnetic fields. Here I note that in case of the AC measurements presented below, no contact misalignment correction was adapted for the 0ω and 2ω measurements, as the electrical resistivity at these components is zero.

First I present results on current-voltage measurement using DC current excitations. Whereas $I_{\text{DC}} - V_{ij}^{\text{DC}}$ curves obtained at the lowest temperature and zero magnetic field are linear for the electrical resistance ($ij = xx$, Fig. 80 a), as expected from an Ohmic sample, the Hall voltage V_{xy}^{DC} is clearly nonlinear-in- I_{DC} (Fig. 80 b). The nonlinearity of the V_{xy}^{DC} can be uniquely decomposed, as evidenced by fitting (Fig. 80 b), into a linear-in- I_{DC} contribution with a slope of R_{xy} , and a quadratic-in- I_{DC} contribution with amplitude α^{DC} . The presence of the $V_{xy}^{\text{DC}} = \alpha^{\text{DC}} I_{\text{DC}}^2$ term is in good agreement with the theoretically predicted nonlinear Hall effect (Eqn. 31, Sect. 3.5), whereas the origin of the novel, linear-in- I_{DC} term will be addressed later in the next section.

To gain further insight on the details of the nonlinearity of the $I - V$ curve, I now turn to the AC experiment. Here, the Hall voltage naturally decomposes into a purely quadratic-in- I component with an angular frequency of 2ω (Fig. 81 a) and a linear-in- I component with an angular frequency of 1ω (Fig. 81 b) measured in the respective frequency channels. Importantly, the second-harmonic nature of the former term was theoretically predicted as the hallmark of the nonlinear Hall effect in noncentrosymmetric systems (Sect. 3.5) [53] and, thus, is strong evidence

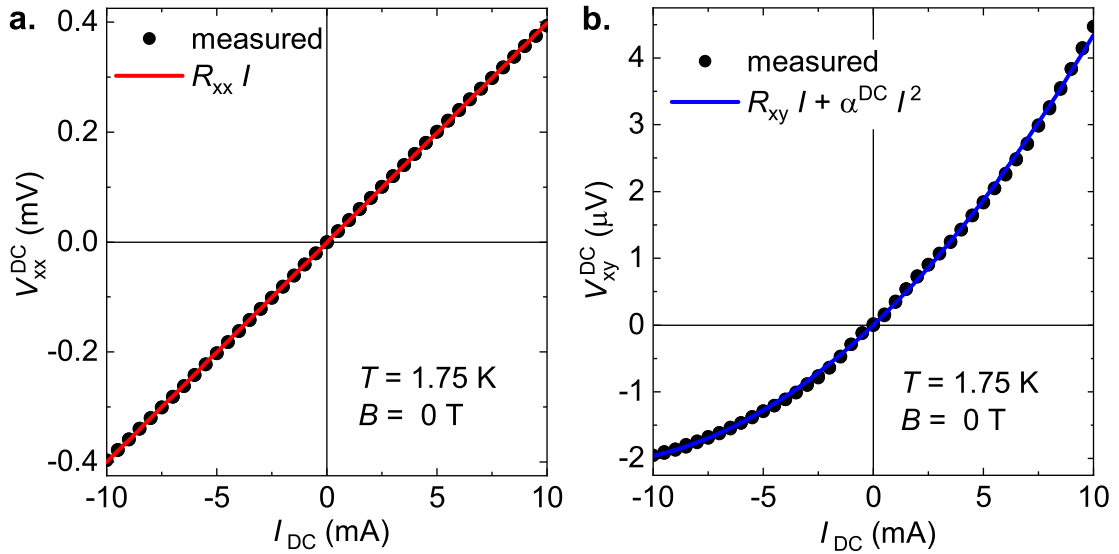


Figure 80: **DC longitudinal and transverse current-voltage curves of $\text{Ce}_3\text{Bi}_4\text{Pd}_3$.** **a:** Measured $I - V$ curve corresponding to the electrical resistance (black symbols) shows linear dependence expected for an Ohmic sample. Linear fit with slope R_{xx} is shown as red line. **b:** Measured $I - V$ curve corresponding to the Hall voltage (black symbols) shows strong nonlinearity. It corresponds to a superposition of a linear- and a quadratic-in-current component as indicated by the fit with the parameters R_{xy} and α^{DC} , respectively (blue line). The data were measured at $T = 1.75$ K, in zero magnetic field and on sample S2.

that the spontaneous Hall effect in $\text{Ce}_3\text{Bi}_4\text{Pd}_3$ is Berry curvature-driven.

A further fingerprint of the nonlinear Hall effect beside the 2ω response is the presence of a rectified 0ω component with respect to an AC drive (Eqn. 34, Sect. 3.5). In search for this component in $\text{Ce}_3\text{Bi}_4\text{Pd}_3$, the 0ω Hall voltage response was measured at the same temperature as the 2ω response. Indeed, a clear, quadratic-in-current Hall response was detected (Fig. 82), which confirms the theoretical prediction, further demonstrating the intrinsic nature of this effect.

To further confirm the intrinsic nature of the second-harmonic Hall effect, the 2ω $I - V$ curve corresponding to V_{xx} was measured in parallel to that corresponding to V_{xy} (Fig. 83 a). I note that the V_{xx} curve was obtained by correcting for the

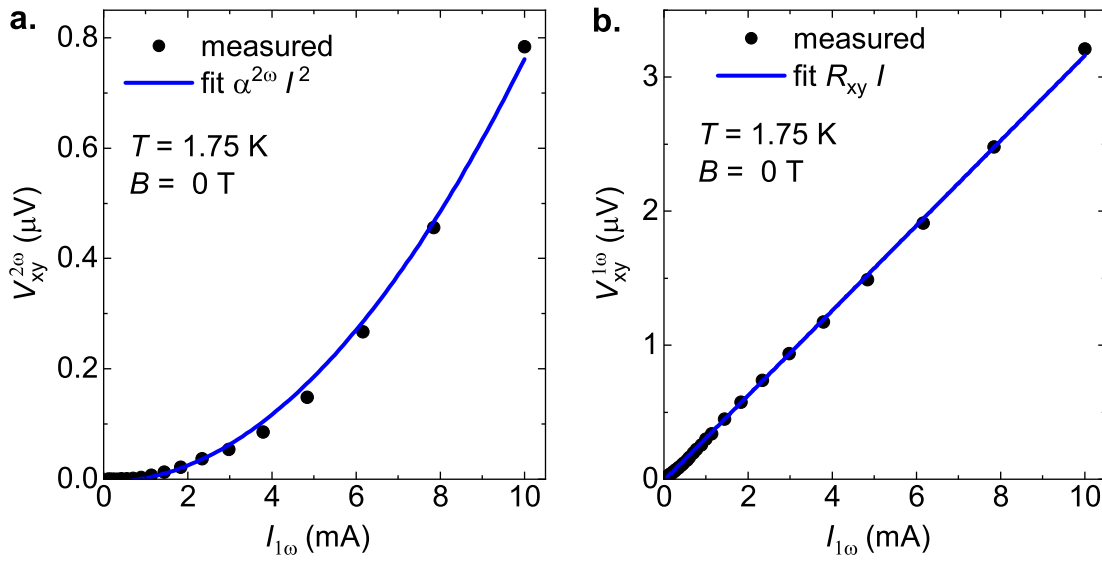


Figure 81: **AC current-voltage curves of $\text{Ce}_3\text{Bi}_4\text{Pd}_3$.** **a:** Second-harmonic Hall voltage (black symbols) shows a clear quadratic-in-current behaviour (fit, blue line) with amplitude $\alpha^{2\omega}$. **b:** First-harmonic Hall voltage (black symbols) shows a clear linear-in-current behaviour (fit, blue line) with amplitude R_{xy} .

trivial contribution due to the misalignment of the longitudinal voltage contacts (see Fig. 68 and the corresponding part in Sect. 5.3.4). The measured V_{xx} curve is spurious, confirming that the nonlinearity appears only in the Hall voltage. In addition, this measurements proves that the system remains in the Ohmic regime in agreement with the linear $V_{xx} - I$ curve seen in DC transport (Fig. 80 a).

Furthermore, frequency dependent measurements of the 2ω signal in V_{xy} show that it is frequency independent (Fig. 83 b), which rules out bad contact quality (inductive and capacitive elements in an AC experiment) as the sources of the observed effect. Finally, to rule out current inhomogeneities, the 2ω Hall voltage was checked on two different contact configurations on the same sample (Fig. 83 c). This reveals, that the detected signal is independent of the contact position (see Fig. 83 c, a lower contact quality merely increases the noise of the signal). Finally, another principal aspect concerning the intrinsic nature of the observed Hall effect

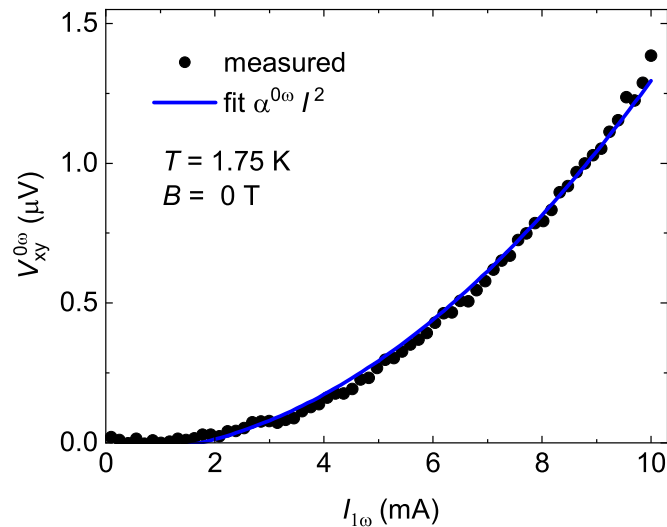


Figure 82: 0ω current-voltage curves of $\text{Ce}_3\text{Bi}_4\text{Pd}_3$. The Hall response to an AC excitation shows a clear quadratic-in-current component in the 0ω channel (black symbols). A quadratic fit with amplitude $\alpha^{0\omega}$ is shown by the blue line.

in $\text{Ce}_3\text{Bi}_4\text{Pd}_3$ is its reproducibility. Not only the 1ω Hall voltage is reproducible as I have previously shown (Fig. 67), but also all investigated samples show a quadratic-in-current 2ω Hall voltage (Fig. 84).

The quadratic-in-current 2ω and 0ω Hall voltages discussed so far are indeed the predicted salient features of the nonlinear Hall effect (Sect. 3.5) [53]. The linear 1ω contribution (Fig. 81 b), by contrast, points out the necessity to go beyond this treatment. In fact, this component even dominates the Hall response, e.g., $V_{xy}^{1\omega} = 1.5 \mu\text{V}$ compared to $V_{xy}^{2\omega} = 0.15 \mu\text{V}$ at $I = 5 \text{ mA}$ (Fig. 81). Thus, the first obvious question is how are the two contributions related to one another and to the Kondo energyscale? To answer this question, isothermal $I - V$ curves were measured in zero magnetic field.

DC $I - V$ curves (corresponding to Fig. 80) obtained in the temperature range $T = 1.75 - 20 \text{ K}$ clearly show that both the linear- and the quadratic-in-current contributions disappear together with increasing temperature (Fig. 85 a) as the sys-

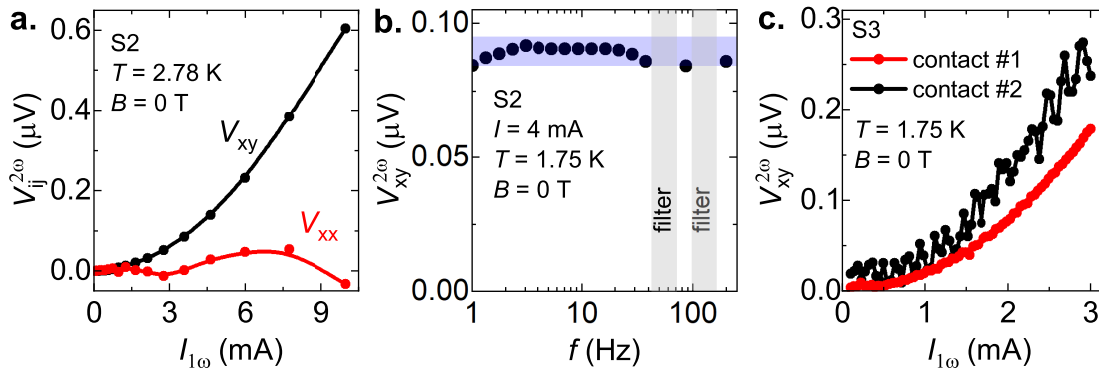


Figure 83: **Intrinsic nature of the 2ω Hall signal in $\text{Ce}_3\text{Bi}_4\text{Pd}_3$.** **a:** Measured 2ω longitudinal voltage, plotted together with the 2ω Hall voltage. The longitudinal voltage (electrical resistivity) is spurious and without any recognizable trend. **b:** Frequency dependence of the 2ω Hall voltage obtained at $T = 1.75$ K, $I = 4$ mA and in zero magnetic field. The measured voltage is independent of the excitation frequency over two orders of magnitude. Measurements around 50 Hz and 100 Hz are not possible due to the built-in line filters for noise reduction (gray bars). **c:** Measured 2ω Hall voltage on two different sets of contacts. A small difference in the amplitude corresponds to the small difference in the distance between the contacts. The larger noise in contact # 2 is due to lower contact quality. Measurements were done on different samples indicated, as in the legends.

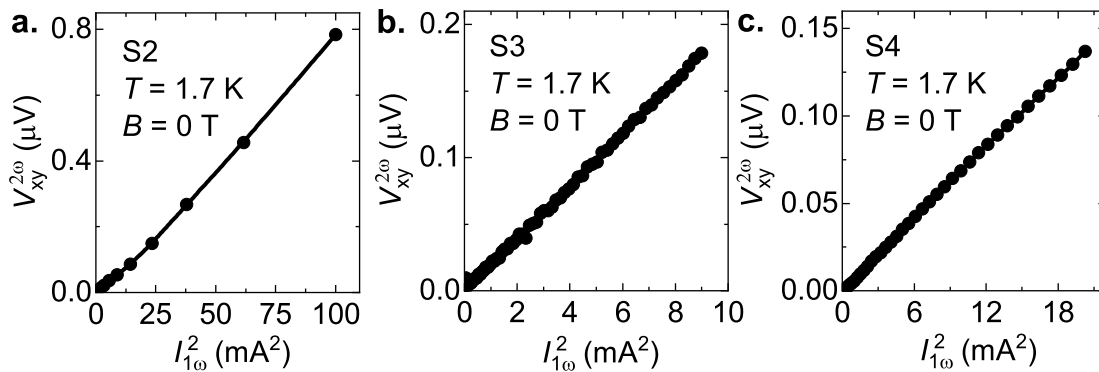


Figure 84: **Reproducibility of the 2ω Hall signal in $\text{Ce}_3\text{Bi}_4\text{Pd}_3$.** Second-harmonic 2ω Hall voltage measured for 3 representative sample, from two different growth batches (S2, S3 and S4). Measurements were done at the lowest temperature and in zero magnetic field.

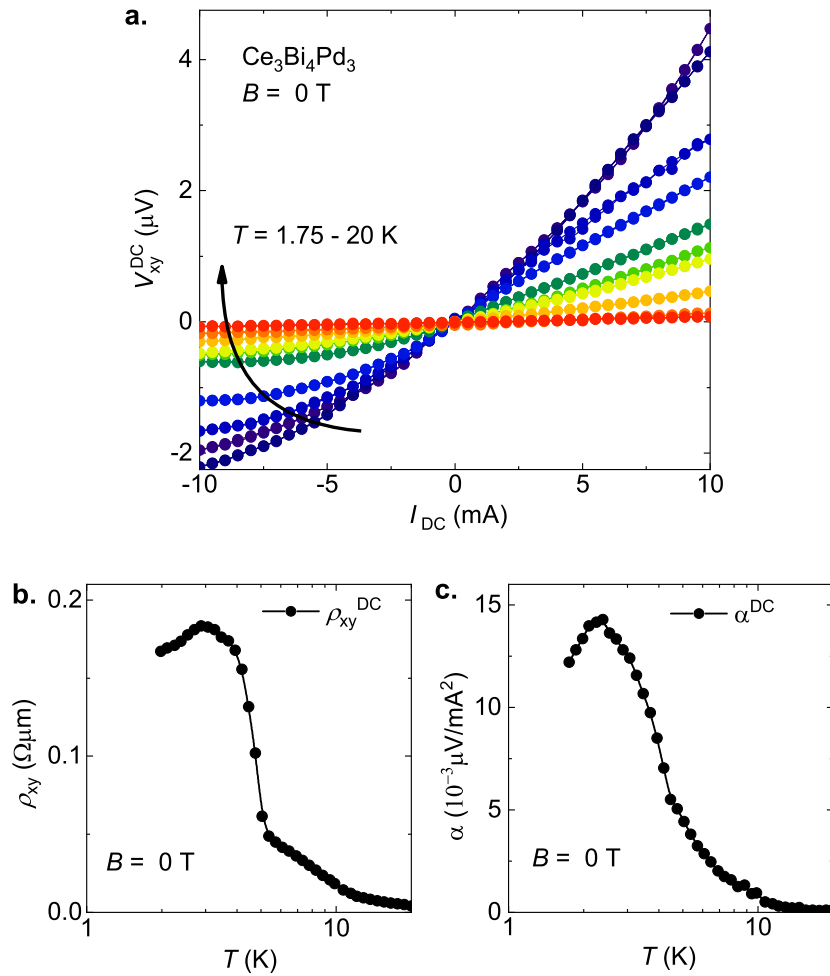


Figure 85: **Isothermal DC current-voltage curves for the spontaneous Hall response in $\text{Ce}_3\text{Bi}_4\text{Pd}_3$.** **a:** The DC Hall voltage as function of current for sample S2 at various temperatures between 1.75 and 20 K and for $B = 0$ T. Each curve can be decomposed to a linear- and quadratic-in-current component as shown in Fig. 80 b. **b-c:** The linear-in-current ρ_{xy} and quadratic in current α^{DC} amplitudes vs. temperature. The data are extracted from fits similar to that shown in Fig. 80 b.

tems is pushed out of its Kondo coherent regime (Fig. 62 b-inset). This, together with the qualitative similarity of their temperature dependence (Fig. 85 b,c), indicates that both components are Kondo-driven and have a common origin.

Finally, these observations in the DC limit are confirmed by AC current drive

experiments at various temperatures and magnetic fields: As temperature is increased above $T = 4$ K, both the 2ω and the related 0ω contribution are suppressed rapidly as Kondo coherence is lost (Fig. 86 a,b and Fig. 87 a,b, respectively), in close similarity with the behaviour observed in the DC limit (Fig. 85 c). Also, applying a magnetic field has a similar effect as increasing temperature: Following an initial increase of the nonlinear 2ω and 0ω coefficients $\alpha^{2\omega}$ and $\alpha^{0\omega}$, respectively, both are completely suppressed at $B = 9$ T (Fig. 86 c,d and Fig. 87 c,d, respectively). Again, this agrees well with the behaviour observed in the DC limit (Fig. 75).

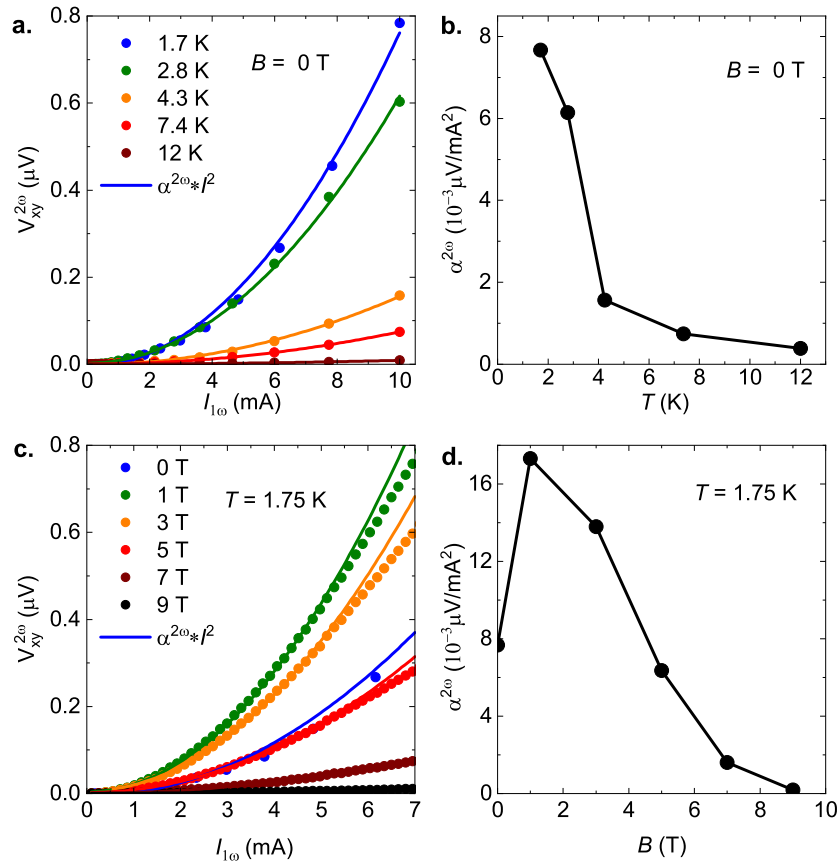


Figure 86: **Temperature and magnetic field dependence of the 2ω Hall response in $\text{Ce}_3\text{Bi}_4\text{Pd}_3$.** **a:** Second-harmonic $I - V$ curves at various temperatures show a suppression of the 2ω Hall voltage with increasing temperature. The measured data are shown as full symbols, quadratic fits are denoted by solid lines. **b:** The amplitude of the quadratic fit $\alpha^{2\omega}$ (panel **a**) shows a marked enhancement below $T = 4$ K. **c:** Second-harmonic $I - V$ curves at various magnetic fields show a suppression of the 2ω Hall voltage with increasing field. The measured data are shown as full symbols, quadratic fits are denoted by solid lines. At higher currents, a slight deviation from an $\sim I^2$ law is observed. **d:** The amplitude of the quadratic fit $\alpha^{2\omega}$ (panel **c**) is completely suppressed at 9 T. The measurements were done on sample S2.

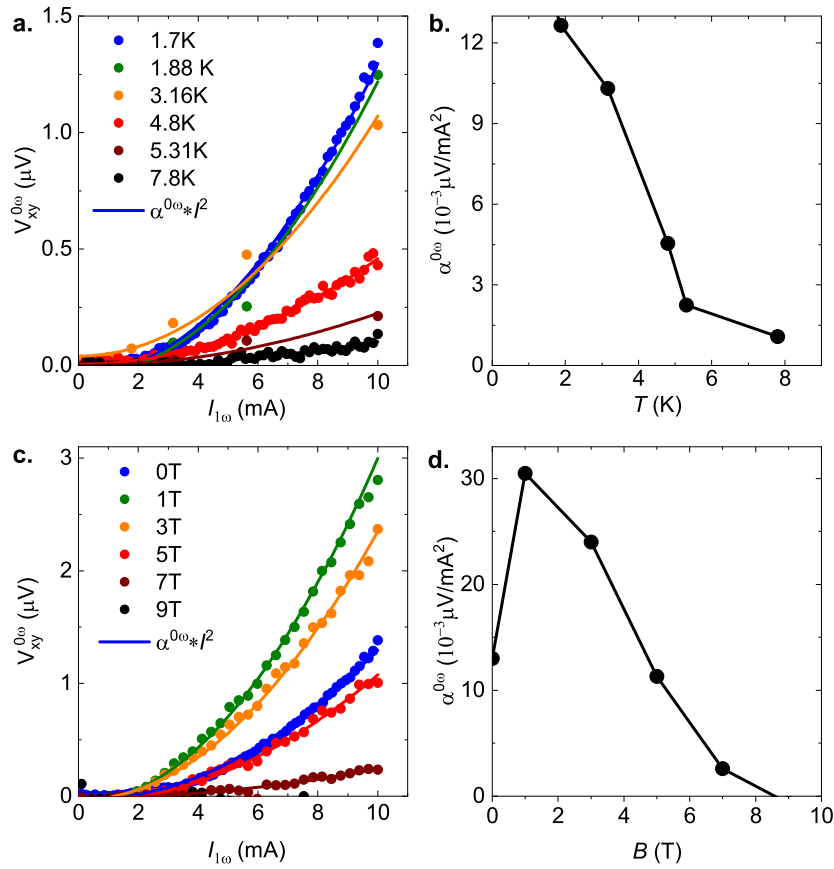


Figure 87: **Temperature and magnetic field dependence of the 0ω Hall response in $\text{Ce}_3\text{Bi}_4\text{Pd}_3$.** **a:** Zeroth harmonic $I - V$ curves at various temperatures show a suppression of the Hall effect with increasing temperature. The measured data are shown as full symbols, quadratic fits are denoted by solid lines. **b:** The amplitude of the quadratic fit $\alpha^{0\omega}$ (panel a) shows a marked enhancement below 5 K. **c:** Zeroth harmonic $I - V$ curves at various magnetic fields show a suppression of the Hall effect with increasing field. The measured data are shown as full symbols, quadratic fits are denoted by solid lines. **d:** The amplitude of the quadratic fit $\alpha^{0\omega}$ (panel c) is completely suppressed at 9 T. The measurements were done on sample S2.

5.3.9 Density functional theory for $\text{Ce}_3\text{Bi}_4\text{Pd}_3$

The nonlinear spontaneous Hall effect in $\text{Ce}_3\text{Bi}_4\text{Pd}_3$ directly evidences the nonzero Berry curvature at the Fermi energy. In light of the specific heat signature of the Weyl-Kondo semimetal state in this material (Sec. 5.3.2), these Hall effect results suggest that the Berry curvature in $\text{Ce}_3\text{Bi}_4\text{Pd}_3$ is associated with Weyl nodes close to the Fermi energy. In what follows, I discuss DFT bandstructure calculation results for $\text{Ce}_3\text{Bi}_4\text{Pd}_3$ that show that tilted Weyl cones are present already in the noninteracting bandstructure of this material. Weyl-Kondo semimetal model calculations then show that such Weyl nodes are pushed to the Fermi energy by the Kondo interaction.

The DFT band structure calculations of $\text{Ce}_3\text{Bi}_4\text{Pd}_3$ were performed by Peter Blaha from TU-Vienna. The Weyl-Kondo semimetal model calculations were performed by Sarah E. Grefe, Hsin-Hua Lai and Qimiao Si from Rice University (Houston / USA). For the DFT calculations all-electron augmented-plane-wave code WIEN2k was used [138] with the Perdew, Burke, Ernzerhof (PBE) functional [139]. The experimentally determined structure (powder XRD, Fig. 38 and Fig. 39) was used with space group $I\bar{4}3d$, $a = 10.052 \text{ \AA}$, and Ce, Pd, and Bi at the $12a$, $12b$, and $16c$ (with $x = 0.0839$) positions, respectively. As DFT cannot treat many body effects such as the Kondo interaction of the Ce $4f$ electrons with the conduction electrons derived from s , p , and d orbitals, it is used here to describe the conduction electron part only. For this purpose, the open-core approximation is used, where one Ce $4f$ electron is included as noninteracting core state, but the $4f$ basis functions are removed from the band structure calculations and, thus, cannot hybridize with other orbitals. As such, this approach is the *ab initio* counterpart of H_c in the periodic Anderson Hamiltonian of the Weyl-Kondo model (Eqn. 41).

The calculation was done with atomic sphere radii of 3.0, 2.5, and 2.5 Bohr for

Ce, Pd and Bi, respectively, and a plane wave cutoff parameter of $RK_{\max} = 8.5$, where $R = 2.5$ and K_{\max} restricts the plane wave expansion. Inside the atomic spheres an angular momentum expansion up to $l_{\max} = 10$ is used, while for the nonspherical matrix elements l_{\max} is restricted to 6. The k -space integration was done with an $18 \times 18 \times 18$ k mesh. Spin-orbit coupling was included in a second variational procedure [138].

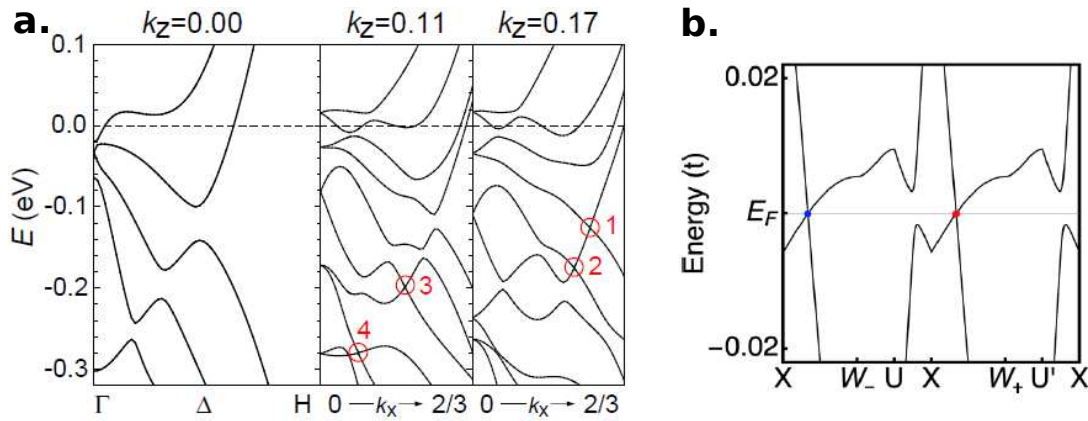


Figure 88: **Theoretical description of Weyl-Kondo physics in $\text{Ce}_3\text{Bi}_4\text{Pd}_3$.** **a:** *Ab initio* band structure of $\text{Ce}_3\text{Bi}_4\text{Pd}_3$, with $4f$ electrons in the core. In the k_x - k_z plane, four different Weyl nodes (1-4) are identified. 1 and 4 are most strongly tilted. This band structure describes the noninteracting part of the Weyl-Kondo semimetal Hamiltonian. This figure (and the corresponding calculations, see [137]) was provided by Peter Blaha (TU-Vienna) **b:** Dispersion across a pair of Weyl (blue) and anti-Weyl (red) nodes for a Weyl-Kondo model with tilted Weyl cones (figure taken from [94]). Energy is expressed in units of the conduction electron bandwidth t . The Kondo interaction pushes Weyl nodes of the noninteracting conduction bands that are far away from the Fermi energy (such as in panel a) to the Fermi energy.

To identify the Weyl nodes, a modified version of BerryPI [140] was used that calculates the Berry curvature of Wilson loops around candidate Weyl nodes [36]. Within the k_x - k_z plane of the Brillouin zone, four Weyl nodes were identified (Fig. 88 a) with the coordinates and energies given in Table 2.

All identified Weyl nodes are situated at least 100 meV away from the Fermi

Table 2: Coordinates of Weyl nodes in the k_x - k_z plane of the Brillouin zone of $\text{Ce}_3\text{Bi}_4\text{Pd}_3$, in units of $2\pi/a$, where $a = 10.052 \text{ \AA}$, and their energies with respect to the Fermi energy in eV. Due to the cubic symmetry of the system, all coordinates occur in both signs and all x, y, z permutations, leading to a multiplicity of 24. This table (and the corresponding calculations, see [137]) was provided by Peter Blaha (TU-Vienna).

Weyl node	k_x	k_y	k_z	E
1	0.517	0	0.174	-0.127
2	0.447	0	0.164	-0.174
3	0.372	0	0.112	-0.196
4	0.172	0	0.087	-0.282

level. Then, the Kondo interaction is expected to pin (part of) these Weyl nodes to the Fermi level, just as it does in the Weyl-Kondo model (Sect. 5.3.1). As the nonlinear anomalous Hall effect occurs in tilted Weyl semimetals (Sect. 3.5), the Weyl node 1 (Fig. 88) with sizeable tilt might be a good candidate for this process. Whereas in previous DFT + dynamical mean field theory (DMFT) calculations for $\text{Ce}_3\text{Bi}_4\text{Pd}_3$ [126] topologically nontrivial band crossings were not considered, a very recent study [122] suggests that nodal lines are also present in the uncorrelated (DFT) bandstructure, far above the Fermi level. The low-temperature specific heat of $\text{Ce}_3\text{Bi}_4\text{Pd}_3$ (Sect. 5.3.2), however, is consistent with a scenario where Weyl point (as opposed to line) nodes are driven by the Kondo effect to the immediate vicinity of the Fermi energy (as described by the Weyl-Kondo model, Sect. 5.3.1).

5.3.10 Discussion

The nonlinear spontaneous Hall voltage terms ($V_{xy}^{2\omega}, V_{xy}^{0\omega}, V_{xy}^{\text{DC}} \sim I^2$) observed in $\text{Ce}_3\text{Bi}_4\text{Pd}_3$ are expected within a perturbative treatment of the nonlinear Hall effect (Eqn. 34, Sect. 3.5) [53]. Indeed, *ab initio* calculations for several weakly interacting Weyl semimetals have reproduced this effect [54], which can be used

as a direct comparison with the observed Hall effect in $\text{Ce}_3\text{Bi}_4\text{Pd}_3$. For the non-interacting systems within the perturbative approach [53, 54], the Berry curvature dipole D_{xz} (Eqn. 33, Sect. 3.5) as well as the nonlinear Hall conductivity $\sigma_{xy} = e^3\tau D_{xz}/(2\hbar^2) \cdot E_x$ can be computed from the electronic band structure as function of the chemical potential. The tangent of the Hall angle $\tan \Theta_H$ in terms of the normal (1ω) longitudinal conductivity σ_{xx} was found to be at maximum of the order 10^{-4} for a scattering time $\tau = 10$ ps and an electric field of $E_x = 10^2$ V/m, corresponding to $\tan \Theta_H/E_x \leq 10^{-6}$ m/V [54]. For $\text{Ce}_3\text{Bi}_4\text{Pd}_3$, values as large as 3×10^{-3} m/V for this ratio in the second-harmonic channel were measured (Fig. 81 a). An effect that is at least three orders of magnitude smaller would be difficult to resolve experimentally, explaining why for weakly interacting nonmagnetic Weyl semimetals it has not been reported so far. The giant value observed for $\text{Ce}_3\text{Bi}_4\text{Pd}_3$ is even more surprising as it is obtained in a bulk semimetal, without any chemical potential tuning. Experimentally, such tuning is limited to the case of low-carrier density (quasi) 2D materials such as bilayer [141] and few-layer [142] WTe_2 , where 2ω Hall voltages were reported at the same time of our posting of this result on arXiv, and attributed to a large (but not divergent) Berry curvature. The maximum values reached there are estimated to be $\tan \Theta_H \approx 5 \times 10^{-3}$ and 10^{-4} , and $\tan \Theta_H/E_x \approx 3 \times 10^{-6}$ m/V and 10^{-8} m/V, respectively, thus again at least three orders of magnitude smaller than what is observed for $\text{Ce}_3\text{Bi}_4\text{Pd}_3$.

The linear-in-current DC as well as the (first-harmonic) 1ω AC contribution to V_{xy} , by contrast, have not been considered in the perturbative approach of [53]. Before addressing this term, I demonstrate (within the perturbative regime) that odd-in-current terms can appear in general.

As discussed in Sect. 3.5, the Berry curvature-driven Hall current density in an inversion symmetry breaking but time-reversal symmetry preserving material is

given by Eqn.31, which is rewritten below for convenience as

$$j_y = \frac{e^2}{\hbar} \int \frac{d^3k}{(2\pi)^3} g(\mathbf{k}) \underbrace{\Omega_z^{\text{odd}}(\mathbf{k}) E_x}_{v_y} . \quad (49)$$

Here $g(\mathbf{k})$ is the out-of-equilibrium contribution to the distribution function associated with an applied electric field E_x and v_y is the anomalous velocity. Then, the specific dependence of the Hall voltage on the current, $V_{xy}(I_x)$, associated with Eqn. 49, depends on the form of $g(\mathbf{k})$. As discussed in Sect. 3.5, in a linearised Boltzmann approximation used in [53, 54], $g(\mathbf{k})$ corresponds to the equilibrium (Fermi-Dirac) distribution function $f_0(\mathbf{k})$ rigidly shifted in the direction of E_x , that is $f(\mathbf{k}) = f_0(\mathbf{k}) + \partial f_0 / \partial k_x \cdot \delta k_x$, with $\delta k_x = (e\tau/\hbar) \cdot E_x$. Here $f(\mathbf{k})$ is the total distribution function, and $g(\mathbf{k})$ is the second term of the sum. In this case, Eqn. 49 simplifies to Eqn. 33, rewritten here for convenience as

$$j_y^{(2)} = \frac{e^3 \tau E_x^2}{\hbar^2} \int \underbrace{\frac{d^3k}{(2\pi)^3} \frac{\partial f_0(\mathbf{k})}{\partial k_x} \Omega_z^{\text{odd}}(\mathbf{k})}_{D_{zx}} . \quad (50)$$

D_{zx} is the Berry curvature dipole and the superscript (2) makes it explicit that this is a 2nd order effect in E_x , i.e., j_y is quadratic and, thus, even in E_x . However, this picture fails to consider the boundary condition of a Hall effect experiment, namely that no net current can flow in the y -direction (see Sect. 3.1, Eqn. 18). To fulfil this condition, the above current $j_y^{(2)}$ must be compensated by an equal current of opposite sign, that can only be generated by a shift of the Fermi surface in the k_y direction by $\delta k_y = (e\tau/\hbar) \cdot E_y^{(2)}$, with $E_y^{(2)} = -\rho_{xx} j_y^{(2)}$. In a second step, this shift then leads to an additional Berry curvature-driven Hall current density $j_y^{(3)}$, by populating states with finite anomalous velocity $v_y(\mathbf{k})$. To be explicit, the

extra shift of the total distribution function $f(\mathbf{k})$ by δk_y ,

$$f(\mathbf{k} + \delta \mathbf{k}_y) = f^0(\mathbf{k}) + \delta k_x \frac{\partial f^0(\mathbf{k})}{\partial k_x} + \delta k_y \frac{\partial f^0(\mathbf{k})}{\partial k_y} , \quad (51)$$

results in an extra contribution (3rd term) which, through Eqn. 49 and with $\delta k_y = -(e^4 \tau^2 \rho_{xx} / \hbar^3) \cdot D_{zx} E_x^2$, drives the (3rd order) Hall current density

$$j_y^{(3)} = -\left(\frac{e^3 \tau}{\hbar^2}\right)^2 \rho_{xx} D_{zx} D_{zy} E_x^3 , \quad (52)$$

where $D_{zy} = \int d^3 k / (2\pi)^3 (\partial f_0(\mathbf{k}) / \partial k_y) \Omega_z^{\text{odd}}(\mathbf{k})$ is the corresponding Berry curvature dipole. Combining Eqns. 50 and 52, the Hall voltage V_{xy} will be the sum of both even-in- I_x and odd-in- I_x contributions.

In what follows, I address the linear-in- I contributions in $\text{Ce}_3\text{Bi}_4\text{Pd}_3$. Intriguingly, such contributions, with $\tan \Theta_H$ up to 0.5 taken as the local slope $\partial \sigma_{xy} / \partial \sigma_{xx}$ (Fig. 67), are even much larger than the 2ω effect quantified above. In what follows I show that the striking deviations from simple expectations [53, 54], most notably the giant enhancement of the spontaneous nonlinear Hall effect, and the appearance of a linear-in-field (first-harmonic) contribution arise naturally in a Weyl-Kondo semimetal picture.

The giant magnitude of the spontaneous Hall effect in $\text{Ce}_3\text{Bi}_4\text{Pd}_3$, and the presence of a linear-in-current 1ω term, point to the necessity to go beyond the simple perturbative treatment of the effect in [53]. Therein, the nonequilibrium electron distribution was obtained using a simple linearised Boltzmann equation with relaxation time approximation. As discussed in Sect. 3.5, the validity of such an approximation relies on two crucial assumptions

- The expansion parameter $\delta k = E_x e \tau / \hbar$ is negligible on the scale of the Fermi wavevector k_F , that is $\delta k \ll k_F$.
- The anomalous velocity $v_a(\mathbf{k})$ does not vary considerably on the scale of δk .

Noninteracting Weyl semimetals generally fulfil these requirements (Sect. 3.5), as therein the Fermi energy is typically not in the immediate vicinity of the Weyl points (Fig. 89 a,b); in this case a perturbative treatment is expected to capture the nonlinear Hall effect correctly. By contrast, for a Weyl-Kondo semimetal, the Kondo resonance strongly renormalizes the Weyl dispersion and pins the Weyl nodes to the Fermi energy [107], which was also demonstrated to be the case for tilted Weyl cones [94]. As a consequence, firstly, the Fermi surfaces around the Weyl nodes are small, and a situation where $k_F \sim \delta k$ can arise. Indeed, the presence of small pockets in $\text{Ce}_3\text{Bi}_4\text{Pd}_3$ is supported by the small carrier concentration ($8 \times 10^{19} \text{ cm}^{-3}$, or 0.002 charge per atom) obtained from the normal Hall coefficient (see Fig. 79 a and the corresponding part in Sect. 5.3.7). Secondly, as a finite nonlinear spontaneous Hall effect in Weyl semimetals occurs only if the Weyl cones are tilted (see Fig. 20 and the corresponding part in Sect. 3.5), k_F will have a minimum around the Weyl node denoted by \mathbf{k}_W . Close to that point the Berry curvature is diverging, and the associated anomalous velocity $v_a(\mathbf{k}_W)$ cannot be considered constant on the scale of δk (Fig. 89 c, d). Thus, a linearised Boltzmann approximation will fail, and a nonperturbative approach to determine the electron distribution function $f(\mathbf{k})$ (that is at the heart of this effect, see Eqn. 31 and the corresponding part in Sect. 3.5) is needed. Indeed, this is most likely the case in $\text{Ce}_3\text{Bi}_4\text{Pd}_3$. While indeed tilted Weyl cones are present already in the noninteracting bandstructure of $\text{Ce}_3\text{Bi}_4\text{Pd}_3$ (Fig. 88 a), it is the Kondo interaction that pushes them to the immediate vicinity of the Fermi level (Fig. 88 b, Sect. 5.3.9), as demonstrated by Weyl-Kondo semimetal model calculations with tilted Weyl cones in the bare conduction electron band [94]. Indeed, for the specific bandstructure of $\text{Ce}_3\text{Bi}_4\text{Pd}_3$, such a picture was confirmed by *ab-initio* based DFT+DMFT calculations [122], capable of capturing (in part) the Kondo interaction. They show that high-energy linear band crossings in the DFT bandstructure are renormalized

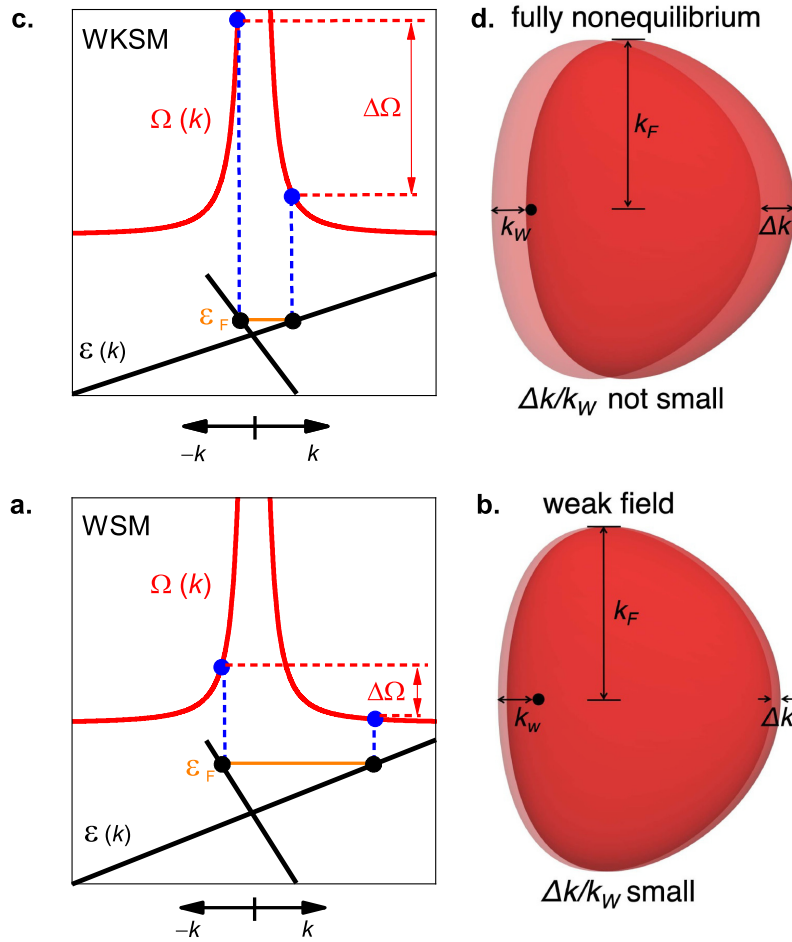


Figure 89: **Schematic Berry curvature and Fermi surface in a tilted Weyl semimetal.** **a:** Schematic energy dispersion ($\epsilon(k)$, black line), and Berry curvature ($\Omega(k)$, red line) for a noninteracting Weyl semimetal (WSM) or for a Weyl-Kondo semimetal (WKSM) in the weak-field regime that could, however, not be reached in our experiments. In such a case, the Fermi energy (ϵ_F , orange line) is away from the band crossing. As a result, the Fermi surface avoids the diverging part of $\Omega(k)$ (blue dots, blue dashed lines). The difference $\Delta\Omega$ of $\Omega(k)$ at the two opposite extremes of the Fermi surface, that determines the nonlinear Hall effect in a WSM, is also small. **b:** The corresponding (rigid) shift Δk of the Fermi surface due to an applied electric field is much smaller than the minimum k_W of the Fermi wavevector k_F measured with respect to the Weyl point (black dot). This constitutes the weak field limit. **c:** The same as (a) but now for a WKSM. There, ϵ_F is pinned to the Weyl point (practically very close to it, with a minimal offset). As a consequence, the Fermi surface samples the diverging part of $\Omega(k)$ at the position of k_W . $\Delta\Omega$ is significantly enhanced compared to a generic WSM

(panel **a**) resulting in an enhanced nonlinear Hall effect (the difference between a WSM and a WKSM is much larger – orders of magnitude as discussed in the text – than what can be sketched). **d**: Same as **b** but now for a Weyl-Kondo semimetal. There Δk cannot be considered to be small compared to k_W . This constitutes the fully nonequilibrium case. Panels **b** and **d** were provided by Sarah E. Grefe from Rice University [137].

and pinned to the Fermi energy only below the Kondo coherence temperature of few K [122].

Whereas a fully developed approach in the strong interaction limit is yet to be developed, two immediate consequences of the failure of a perturbative approach can be seen. Firstly, in the perturbative approach (weak electric field), the Hall resistance itself is linear-in- I giving rise to a quadratic, 2ω Hall voltage. When the system is driven to the nonperturbative regime, R_{xy} will deviate from its initial linear-in- I dependence, naturally giving rise to a constant term in R_{xy} and, thus, a linear, 1ω Hall voltage (Fig. 91) as observed for $\text{Ce}_3\text{Bi}_4\text{Pd}_3$. Secondly, the symmetry considerations of the Hall conductivity in the nonperturbative approach [53], that otherwise dictate a vanishing effect in $\text{Ce}_3\text{Bi}_4\text{Pd}_3$, will not hold. Such symmetry constraints originate from the assumption that the σ_{xy} can be directly connected to the equilibrium Fermi distribution $f_0(\mathbf{k})$. As this distribution inherits the symmetries of the lattice, they will be forwarded to σ_{xy} . Clearly, in the fully nonequilibrium case, where $f(\mathbf{k})$ is not directly determined by $f_0(\mathbf{k})$, such symmetry considerations are not valid. This corresponds to the fact that the applied electric field cannot be considered as a probing one only, and instead introduces an additional directionality to the system and to σ_{xy} , thus breaking the lattice symmetry.

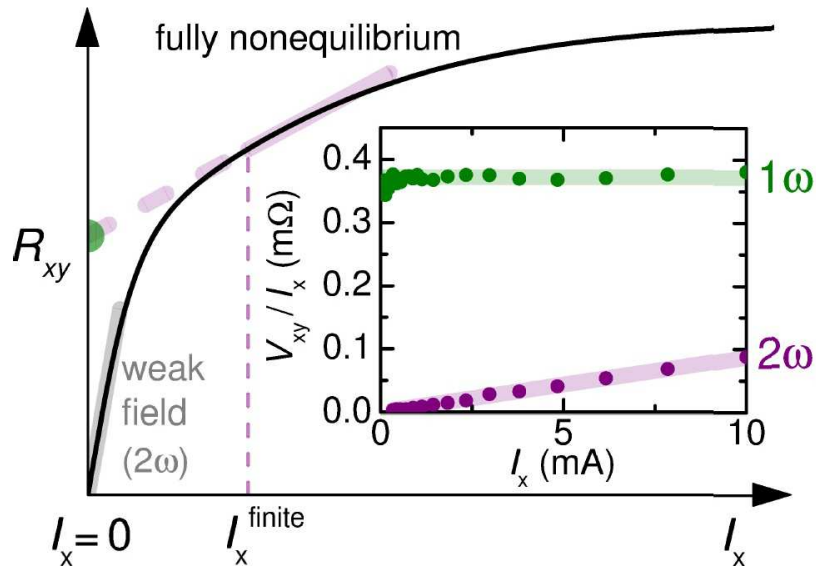


Figure 91: **Schematic Berry of the nonlinear quantum Hall resistance in a fully nonequilibrium state.** In the weak field limit, the Hall resistance is linear in current (grey line), giving rise to only a quadratic, second-harmonic Hall voltage (2ω). In the fully nonequilibrium state the system can be expanded around a finite current (I_{finite}). Whereas the linear contribution to R_{xy} still produces a 2ω signal (transparent, purple thick line), its abscissa gives rise to a constant R_{xy} (green transparent dot) and, thus, a linear 1ω voltage. Inset shows that both contributions are evidenced in the zero-field Hall response of $\text{Ce}_3\text{Bi}_4\text{Pd}_3$.

5.4 Collapse of the Weyl-Kondo semimetal state in $\text{Ce}_3\text{Bi}_4\text{Pd}_3$ in high magnetic fields

Key to understand the richness of phenomena displayed by strongly correlated electron systems has been a systematic exploration of their low-temperature phase diagrams [123, 143–145]. It has also led to the discovery of emergent phases stabilized by quantum critical fluctuations, most notably unconventional superconductivity [146–149]. In the previous sections, I showed that in $\text{Ce}_3\text{Bi}_4\text{Pd}_3$ the Kondo interaction gives rise to a semimetallic state, that displays thermodynamic and transport fingerprints of the recently proposed Weyl-Kondo semimetal. Thus, the question arises: What is the mechanism stabilizing this novel ground state? Due to the low-energy scales in heavy fermion systems, varying a non-thermal control parameter such as applied magnetic field, pressure, or chemical composition has been instrumental in delineating phases defined by a Landau order parameter [14]. In the following section, I show that this approach is versatile also for strongly correlated topological phases, and in particular for $\text{Ce}_3\text{Bi}_4\text{Pd}_3$. I present Hall effect, magnetic field-dependent resistivity and torque magnetometry measurements to probe how the ground state of $\text{Ce}_3\text{Bi}_4\text{Pd}_3$ transforms under magnetic field tuning. An intriguing two-stage transition is detected, which is associated with the annihilation of the Weyl nodes, making the system more insulating, and a consecutive transition to a heavy fermion metal phase.

5.4.1 Magnetic field-dependent electrical resistivity

Magnetotransport measurements in DC fields up to 37 T were performed at the HFML-EMFL high magnetic field facility at Nijmegen. The measurement and data acquisition was set up in collaboration with Alix McCollam, Lucas M. K. Tang and Bryan Vlaar from the HFML-EMFL and Diego A. Zocco from TU-Vienna. Data

were taken using *Stanford Research SR830* lockin amplifiers, with the measured voltage signal pre-amplified 100 times using *Princeton Applied Research* low-noise transformers. Electrical contacts were made by either spot welding or gluing with silver paint 12 μm diameter gold wires to the samples in a 5-wire configuration. Resistivity curves were obtained by symmetrizing the measured $\rho_{xx}(B)$ curves. Additional low-temperature electrical resistivity measurements down to 70 mK and in magnetic fields up to 15 T were performed in an Oxford dilution refrigerator at TU-Wien.

Iso-magnetic field temperature-dependent resistance curves show that applying large magnetic fields suppresses the semimetallic state, and drives it into a metallic one above $B \approx 14$ T (Fig. 92 a). Interestingly, the ultimate metallic curve at $B = 37$ T shows a higher resistivity than in the nonmagnetic reference compound $\text{La}_3\text{Bi}_4\text{Pd}_3$, that has a distinctly different temperature dependence (Fig. 92 a), suggesting that the Kondo interaction is still at play.

Further insight to the evolution of the metallic state is offered by iso- T magnetic field-dependent resistivity measurements (Fig. 92 b). They show that the transition to the final metallic state happens in two stages. At the first field denoted $B_{c1} \sim 9$ T, the magnetic field-dependent resistivity develops a “shoulder” where the curve changes slope (Fig. 92 b). Then, in a second step at $B_{c2} \sim 14$ T, a crossover to an almost field-independent behaviour is observed, that is typical for a metal [150], in agreement with the metallic behaviour observed in the temperature dependence (Fig. 92 a).

To corroborate the presence of two transitions in the high-field magnetoresistivity curves, $\rho_{xx}(B)$ and $\rho_{xx}(T)$ measurements were extended, across the relevant field range, down to 120 mK (Fig. 93 a, Fig. 94). The $\rho_{xx}(B)$ data reveal that the shoulder detected at B_{c1} (Fig. 92 b) is clearly enhanced. Therein, a Schlottmann type behaviour is seen both in the low-field range below B_{c1} and

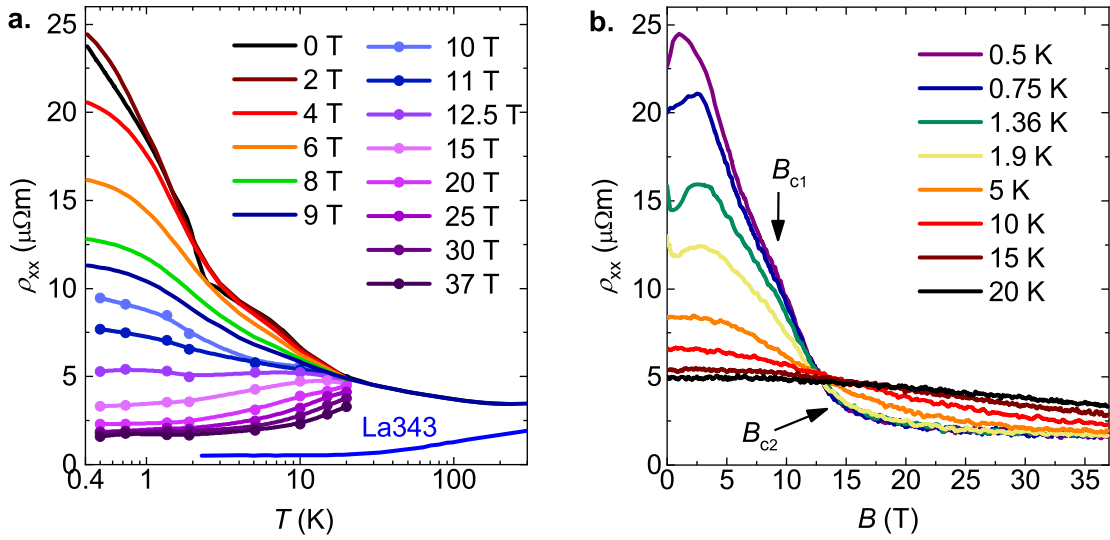


Figure 92: **Electrical resistivity of $\text{Ce}_3\text{Bi}_4\text{Pd}_3$ in high magnetic fields.** **a:** Temperature-dependent electrical resistivity at various fixed magnetic fields. For $B > 9$ T, iso- B cuts (dots) were taken from panel **b**. The zero-field resistivity of the nonmagnetic reference compound $\text{La}_3\text{Bi}_4\text{Pd}_3$ is shown for comparison (blue line denoted La343). The low-field data are taken from Fig. 60. High-field measurements were obtained on the same sample. **b:** Resistivity isotherms in fields up to $B = 37$ T for various temperatures between 0.5 and 20 K. At the lowest temperatures, a shoulder is identified at about 9 T (at B_{c1}) and a crossover to a very weak field dependence at about 14 T (at B_{c2}). Arrows indicate the position of the critical fields. Here, they point to the crossover fields of the 0.5 K Hall resistivity isotherm (Fig. 99 a), that are defined via the fit with Eqn.53. The curves in panel **b**, as well as data points in panel **a** above 9 T, were obtained at the HFML-EMFL in Nijmegen in collaboration with Alix McCollam, Diego A. Zocco, Lucas M. K. Tang and Bryan Vlaar.

in the intermediate-field range between B_{c1} and B_{c2} (see shaded lines in Fig. 93 a). The “double decay” shape, separated by B_{c1} , naturally suggests that the magnetic field-dependent resistivity of $\text{Ce}_3\text{Bi}_4\text{Pd}_3$ is governed by two different scales, one of the Weyl-Kondo semimetal below B_{c1} and one of the intermediate phase between B_{c1} and B_{c2} .

To identify the transition at B_{c1} in the temperature-dependent iso-field curves,

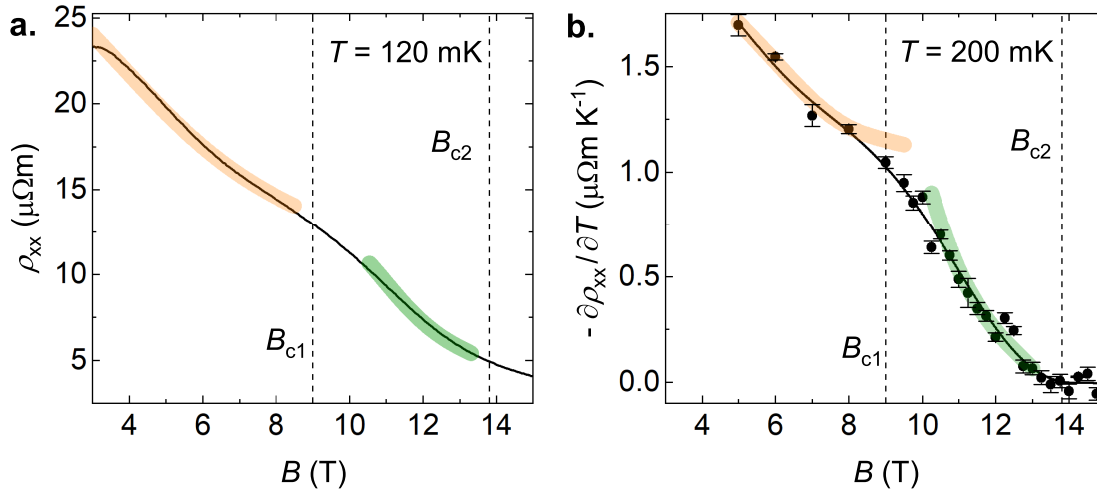


Figure 93: **Field-dependent electrical resistivity at low temperatures.** **a:** Electrical resistivity vs. magnetic field at 120 mK (full black line), together with Schottmann-type curves (orange and green lines, see also Fig. 62 a). Their purpose is merely to indicate what type of magnetic field-dependent resistivity might be expected in a Kondo system. Below B_{c1} , and between B_{c1} and B_{c2} , the measured curve indeed resembles the overall behaviour. However, it is clear that the entire curve cannot be attributed to a Kondo system with a single energy scale. Instead, the observed double-decay structure suggests that B_{c1} separates two regimes with different ground states. **b:** Temperature derivatives (full symbols) of $\rho_{xx}(T)$ iso-field curves at 200 mK, defined as the slopes of the linear fits in Fig. 94. The error bars represent the standard error of the slope of these fits. The lines are guides to the eyes (they also have Schottmann shape). Vertical dashed lines indicate the position of B_{c1} and B_{c2} , where a change of behaviour is observed.

I plot, in Fig. 93 b, their temperature derivative taken at 200 mK, vs. magnetic field (see Fig. 94 for how the derivative is determined). In this plot, the transition between the two regimes is even more pronounced than for the fields-dependent resistivity isotherms. This confirms the non-monotonous change of the ground state across B_{c1} , and the metallization of the system B_{c2} , indicated by a vanishing slope at fields beyond B_{c2} (Fig. 93 b).

In search for a characteristic temperature scale of the metallic high-field phase, the temperature-dependent electrical resistivity of $\text{Ce}_3\text{Bi}_4\text{Pd}_3$ was examined at the

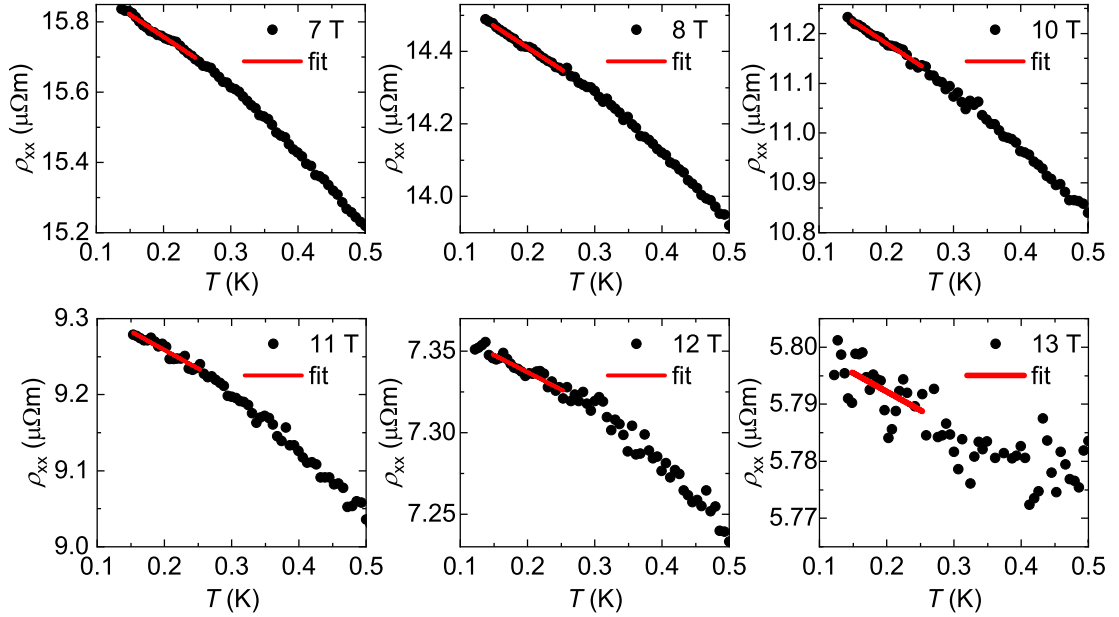


Figure 94: **Temperature-dependent iso-field electrical resistivity curves at low temperatures.** The red lines are linear fits to the data (full symbols) in the range (200 ± 50) mK. Their slopes correspond to the local derivative of $\rho(T)$ at 200 mK and are plotted vs. field in Fig. 93 b.

lowest temperatures. Interestingly, a $\rho(T) = \rho_0 + AT^2$ behaviour is observed at the largest fields (Fig. 95), which is a characteristic of Fermi liquid behaviour [151] (Sect. 2.2). To check whether the obtained A coefficient at $B = 15$ T of $A = 8.75 \mu\Omega\text{cm}/\text{K}^2$ (Fig. 95) is consistent with a heavy fermion Fermi liquid state, I compare it to that expected from the compounds Fermi temperature using the Kadowaki-Woods ratio $A/\gamma^2 = 10\mu\Omega\text{cm mol}^2\text{K}^2\text{J}^{-2}$ [151]. Because γ is not well-defined in a Weyl-Kondo semimetal (and because no specific heat data are yet available in such high fields), an effective value is estimated by substituting the Kondo temperature ($T_K = 13$ K, see Sect. 5.3.2) for the Fermi temperature T_F in the (molar) specific heat relation $C_V = (\pi^2/2)Rk_B(T/T_F) = (\pi^2/2)Rk_B(T/T_K)$ [80], where R is the universal gas constant and k_B is the Boltzmann constant. This yields an effective $\gamma^2 = 1.7 \text{ J}^2/(\text{mol}^2\text{K}^4)$ and an estimated $A = 17 \mu\Omega\text{cm}/\text{K}^2$, which

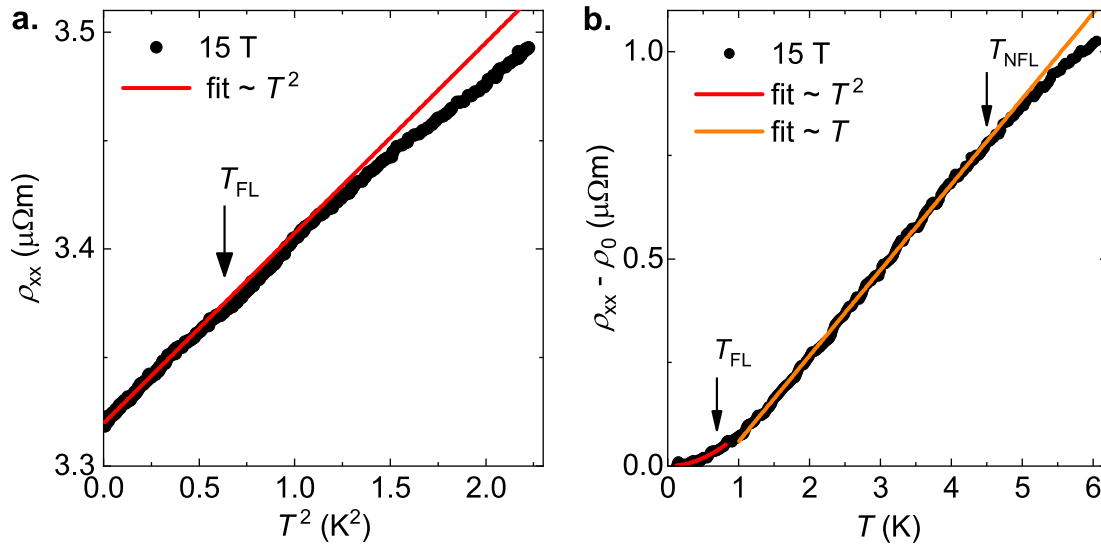


Figure 95: **Low-temperature electrical resistivity of $\text{Ce}_3\text{Bi}_4\text{Pd}_3$ at 15 T.** **a:** Electrical resistivity vs. temperature squared in the metallic phase at $B = 15$ T (black symbols). The data display a linear in T^2 behaviour at the lowest temperatures as indicated by the $\sim T^2$ fit (red line) up to $T_{\text{FL}} = 0.79$ K (arrow). T_{FL} is determined as the temperature above which the data deviate by more than 5% from the $\sim T^2$ law. **b:** Temperature-dependent part of $\rho(T)$ vs. T up to 6 K, in a magnetic field of 15 T. Above T_{FL} and up to T_{NFL} , the non-Fermi liquid form $\rho \sim T$ is observed (orange line). This indicates that a quantum critical point is nearby. The residual resistivity ρ_0 is about $4 \Omega\mu\text{m}$, which is slightly different from that in panel **a** due to a different set of contacts used for remeasuring the curve.

is within a factor of 2 of the observed A coefficient. This indicates that magnetic field somewhat suppresses the correlation strength, but has by far not suppressed the Kondo interaction even at 15 T. Confirming the heavy fermion metal ground state of $\text{Ce}_3\text{Bi}_4\text{Pd}_3$ at high fields allows to estimate a characteristic temperature $T_{\text{FL}} = 0.79$ K (at $B = 15$ T), which is the upper bound where an $\sim AT^2$ behaviour is observed in $\rho(T)$ (Fig. 95 a). Interestingly, above T_{FL} , $\rho(T)$ displays linear-in- T behaviour (Fig. 95 b) characteristic of non-Fermi liquid behaviour in the vicinity of a quantum critical point [15, 152, 153], and providing evidence for such a point at B_{c2} . In fact, starting deep in the metallic phase (Fig. 96), A of $\text{Ce}_3\text{Bi}_4\text{Pd}_3$ is

strongly enhanced with decreasing field, suggesting a divergence near B_{c2} that follows an $A(B) = C / (B - B_{c2})^p$ law (Fig. 97) with $B_{c2} = 13.82 \pm 0.02$ T and $p = 0.98 \pm 0.03$. Indeed, this form of a diverging A coefficient has been associated with quantum criticality [154]. However, below $B = 15$ T, a rapid suppression of A is seen, leading to a crossover to T^2 behaviour with a negative slope (Figs. 96 and 97); it is associated with the non-metallic phase below B_{c2} and, thus, it should not be interpreted in a Fermi liquid picture.

Finally, whereas the low-field state is identified as a Weyl-Kondo semimetal and the high-field state (above B_{c2}) as a heavy fermion metal, little is known about the intermediate state between B_{c1} and B_{c2} . In the following sections, I show that Hall effect and torque magnetometry measurements clarify the nature of this phase.

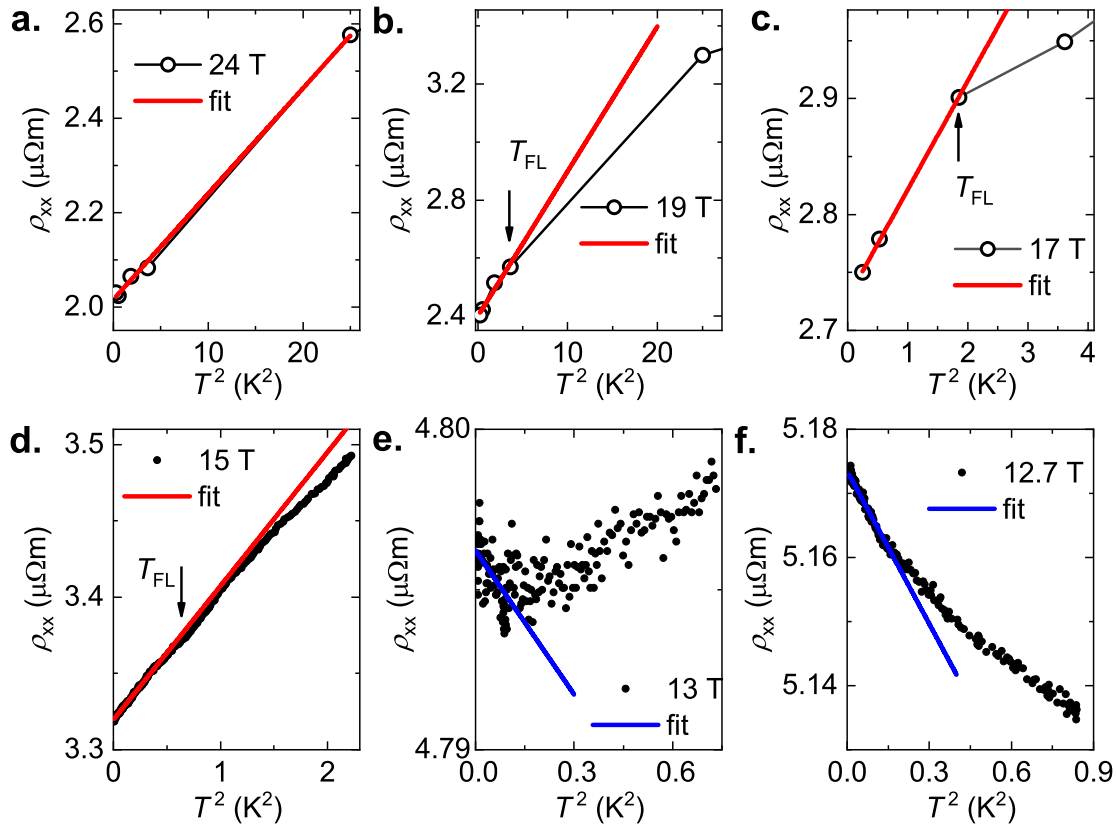


Figure 96: **Fermi liquid behaviour of $\text{Ce}_3\text{Bi}_4\text{Pd}_3$.** Iso- B temperature-dependent electrical resistivity vs. T^2 in high magnetic fields. The data in panels **a-c** (open symbols) were taken from constant B cuts in Fig.92 b. The data in panels **d-f** (full symbols) were obtained in a dilution refrigerator. Red line (panels **a-d**) denotes linear fit with positive slope reflecting Fermi liquid behaviour. Blue lines in panels **e, f** denotes linear fits with negative slopes.

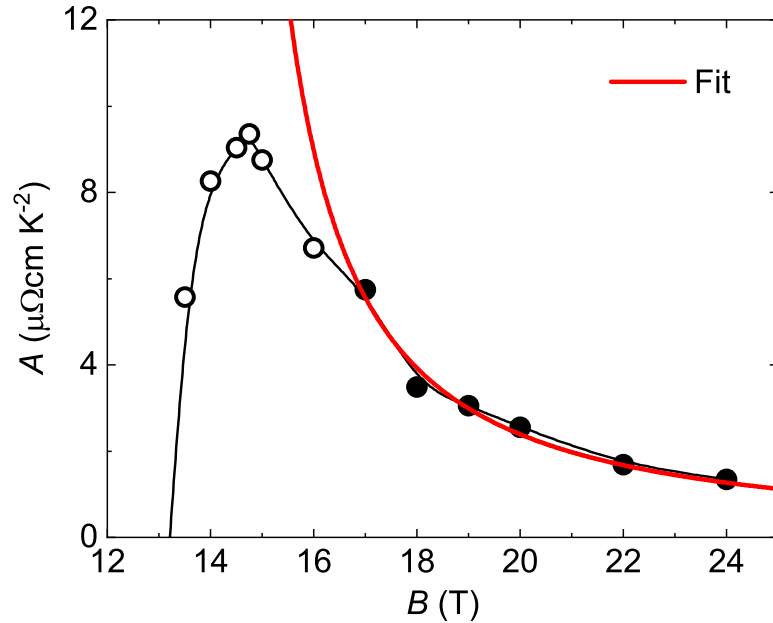


Figure 97: **Field-dependent A coefficient in $\text{Ce}_3\text{Bi}_4\text{Pd}_3$.** A coefficient obtained from Fig. 96. Full data points are taken deep in the metallic regime, and are consistent with a diverging behaviour at B_{c2} (red curve see text). Open symbols indicate data where the proximity of the non-metallic phase influences the resistivity curve and that were, thus, not taken in account in the fitting. The data points above 15 T are obtained from magnetic field-dependent resistivity isotherms (Fig. 92 b) obtained at the HFML-EMFL in Nijmegen in collaboration with Alix McCollam, Diego A. Zocco, Lucas M. K. Tang and Bryan Vlaar.

5.4.2 Hall effect and quantum criticality

The Hall resistivity of $\text{Ce}_3\text{Bi}_4\text{Pd}_3$ up to $B = 37\text{ T}$ was measured simultaneously with the magnetoresistivity, thus, using the same setup, equipment and technique explained in Sect. 5.4.1. The presented $\rho_{xy}(B)$ curves are obtained by the standard antisymmetrizing procedure of the measured resistivity ρ_{xy}^{meas} , i.e., $\rho_{xy}(B) = [\rho_{xy}^{\text{meas}}(+B) - \rho_{xy}^{\text{meas}}(-B)]/2$. This cancels out both the spontaneous Hall effect (zero-field signal) and any even-in-field component. These Hall effect data (Fig. 98) reveal the two-stage transition observed in magnetoresistivity (Fig. 92 b)

most clearly. At the highest temperature ($T = 20$ K), the iso- T $\rho_{xy}(B)$ curve is linear in B at low fields, as expected for a normal Hall effect, and shows only a weak deviation from linearity at the highest fields; the latter corresponds to a change of slope (kink). With decreasing temperature, two well visible kinks develop at B_{c1} and B_{c2} (Fig. 98). In addition, the previously discussed anomalous Hall contribution (Fig. 78) develops in small fields at lowest temperatures.

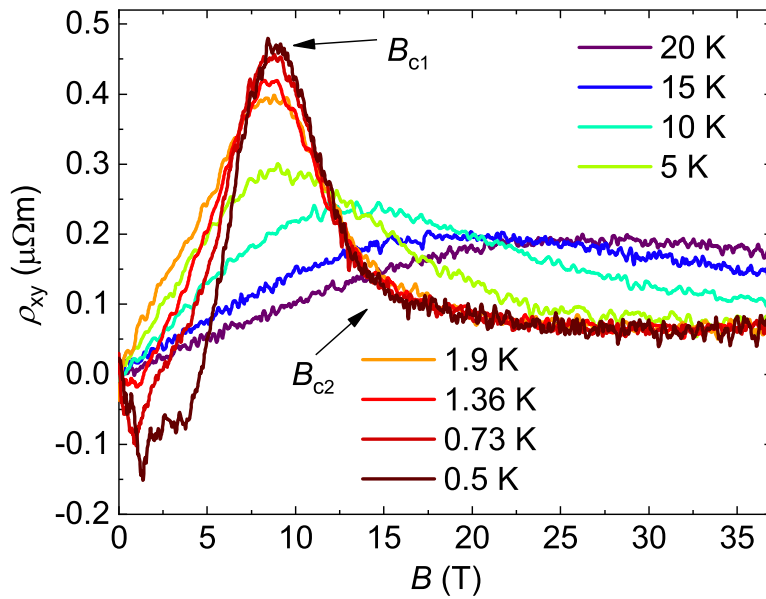


Figure 98: **Hall resistivity isotherms of $\text{Ce}_3\text{Bi}_4\text{Pd}_3$ in high magnetic fields.** Isothermal Hall resistivity curves up to $B = 37$ T at different temperatures display a marked change of slopes at B_{c1} and B_{c2} (arrows). Here, they point to the crossover fields of the 0.5 K Hall resistivity isotherm (Fig. 99 a), that are defined via the fit with Eqn.53. At these fields, signatures are also seen in the magnetic field-dependent resistivity (Fig. 92 b). The curves were obtained at the HFML-EMFL in Nijmegen in collaboration with Alix McCollam, Diego A. Zocco, Lucas M. K. Tang and Bryan Vlaar.

In what follows, I present a quantitative analysis of the Hall resistivity isotherms. As explained in Sect. 3.6, when magnetic field drives transitions between ground states with different Fermi volume, the resulting (finite tempera-

ture) crossovers manifest as (broadened) kinks in $\rho_{xy}(B)$, and (broadened) steps in the differential Hall coefficient $\tilde{R}_H(B)$, which is the local slope of $\rho_{xy}(B)$. Such behaviour was observed in a number of heavy fermion metals [13, 64–66] driven by magnetic field across quantum critical points. As other origins of the nonlinearities in $\rho_{xy}(B)$ of $\text{Ce}_3\text{Bi}_4\text{Pd}_3$, notably skew scattering and two band effects, can be ruled out (see end of this section), the two kinks seen at B_{c1} and B_{c2} in the $\rho_{xy}(B)$ data of $\text{Ce}_3\text{Bi}_4\text{Pd}_3$ (Fig. 98) do indeed seem to evidence two consecutive Fermi volume changing quantum phase transitions.

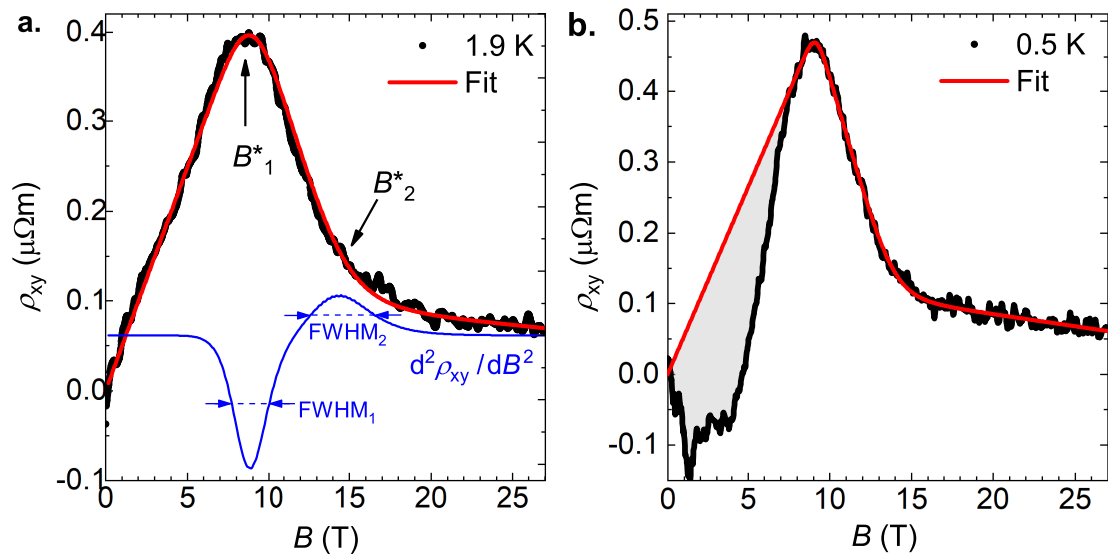


Figure 99: **Successive Fermi surface reconstruction in $\text{Ce}_3\text{Bi}_4\text{Pd}_3$ at high magnetic fields.** **a:** Hall resistivity isotherm at $T = 2$ K (black) fitted with a phenomenological two crossover model (red line, Eqn. 53). The blue curve denotes the second derivative of the fitted $\rho_{xy}(B)$ curve. It captures the transition widths characterized by their FWHM (blue horizontal dashed line and arrows). **b:** Same as panel **a** at $T = 0.5$ K. The low-field anomalous Hall contribution is denoted by grey shaded area.

To quantify these two transitions, the phenomenological model describing a single transition (Eqn. 35, Eqn. 36) is extended to a two-stage crossover scenario defined as

$$\begin{aligned}
\tilde{R}_H &= R_2 - (R_2 - R_{H,1}) \left[1 + \left(\frac{B}{B_2^*} \right)^{p_2} \right]^{-1}, \\
\text{where } R_{H,1} &= R_1 - (R_1 - R_0) \left[1 + \left(\frac{B}{B_1^*} \right)^{p_1} \right]^{-1}, \\
\text{and } \rho_{xy}(B_0) &= \int_0^{B_0} \tilde{R}_H(B) dB.
\end{aligned} \tag{53}$$

Here R_0 , R_1 and R_2 are the differential Hall coefficients related to the low-field, intermediate and high-field phases, respectively, whereas B_1^* and B_2^* denote the (finite-temperature) transition positions. The parameters p_1 and p_2 are related to transition widths that are quantified by the full width at half maximum (FWHM) of their second derivative (see blue curve in Fig. 99 a). Fitting Eqn. 53 for a representative isotherm at $T = 2$ K reproduces the measured data perfectly (Fig. 99 a). For lower temperatures, where the anomalous Hall effect sets in, care must be taken at low fields; Eqn. 53 is fitted only above $B = 8.4$ T, where this contribution is negligible (Fig. 99 b). Fits of similar quality are obtained at all temperatures up to $T = 10$ K (Fig. 100). At higher temperatures, no sign of the upper transition can be discerned within the accessed field range and, thus, the obtained fit parameters are no longer meaningful.

The temperature evolution of all fitted parameters is plotted in Fig. 101. The two crossover fields B_1^* and B_2^* (Fig. 99 a), determined for all available isotherms, are plotted as characteristic temperatures $T_1^*(B)$ and $T_2^*(B)$ in Fig. 101 a. In the zero-temperature limit, they extrapolate to B_{c1} and B_{c2} , respectively, in good agreement with the two characteristic fields observed in the magnetic field-dependent resistivity (Fig. 92). Both crossovers sharpen considerably with decreasing temperature (Fig. 101 c, d), indicating that the phase diagram of magnetic field-tuned $\text{Ce}_3\text{Bi}_4\text{Pd}_3$ comprises three phases with distinct Fermi volume: a phase below B_{c1} with a small hole-like Fermi volume, an intermediate-field phase between B_{c1} and B_{c2} with an even smaller electron-like Fermi surface, and a high-

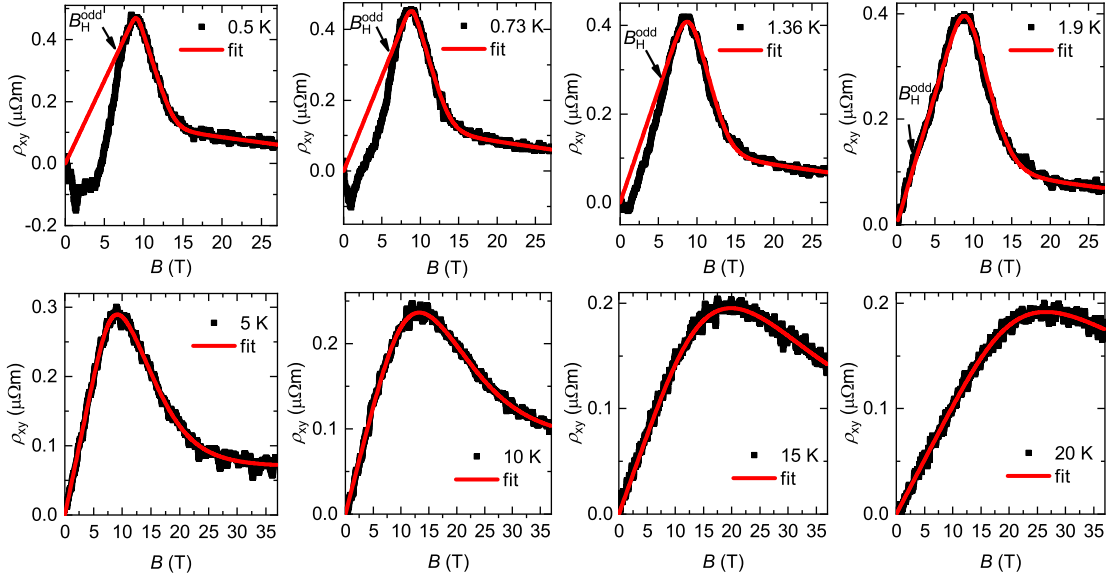


Figure 100: **Two-stage crossover fits to the Hall resistivity of $\text{Ce}_3\text{Bi}_4\text{Pd}_3$ at high magnetic fields.** Hall resistivity data for various temperatures between 0.5 and 20 K (black symbols), and the corresponding two-stage transition fits (red lines). Below 1.9 K, the fit range is between 8.4 and 27 T, to avoid influence of the anomalous Hall effect. Arrows indicate the field $B_{\text{H}}^{\text{odd}}$ above which the deviation from the initial linear behaviour, as imposed by the fit, drops below 15%.

field phase beyond B_{c2} with a much larger Fermi volume (Fig. 101 b). Note that, in the simplest case, the Fermi volume is inversely proportional to \tilde{R}_{H} .

Finally, I corroborate the assignment of the high-field nonlinearities observed in the $\rho_{xy}(B)$ curves of $\text{Ce}_3\text{Bi}_4\text{Pd}_3$ by demonstrating that other sources of such nonlinearities, most notably skew scattering and two-band effects, can be safely ruled out or neglected. As discussed in Sect. 3.3, a skew scattering-driven anomalous Hall effect is expected to appear in heavy fermion systems. Such a contribution is frequently estimated by $\rho_A(B) \sim \rho(B)M(B)$ [76]. This is, however, only valid if the field dependence of ρ is dominated by that of the scattering time [68]. If the Fermi surface undergoes an abrupt change, as is the case in the Kondo destruction scenario of heavy fermion metals [13], and as observed for $\text{Ce}_3\text{Bi}_4\text{Pd}_3$ at

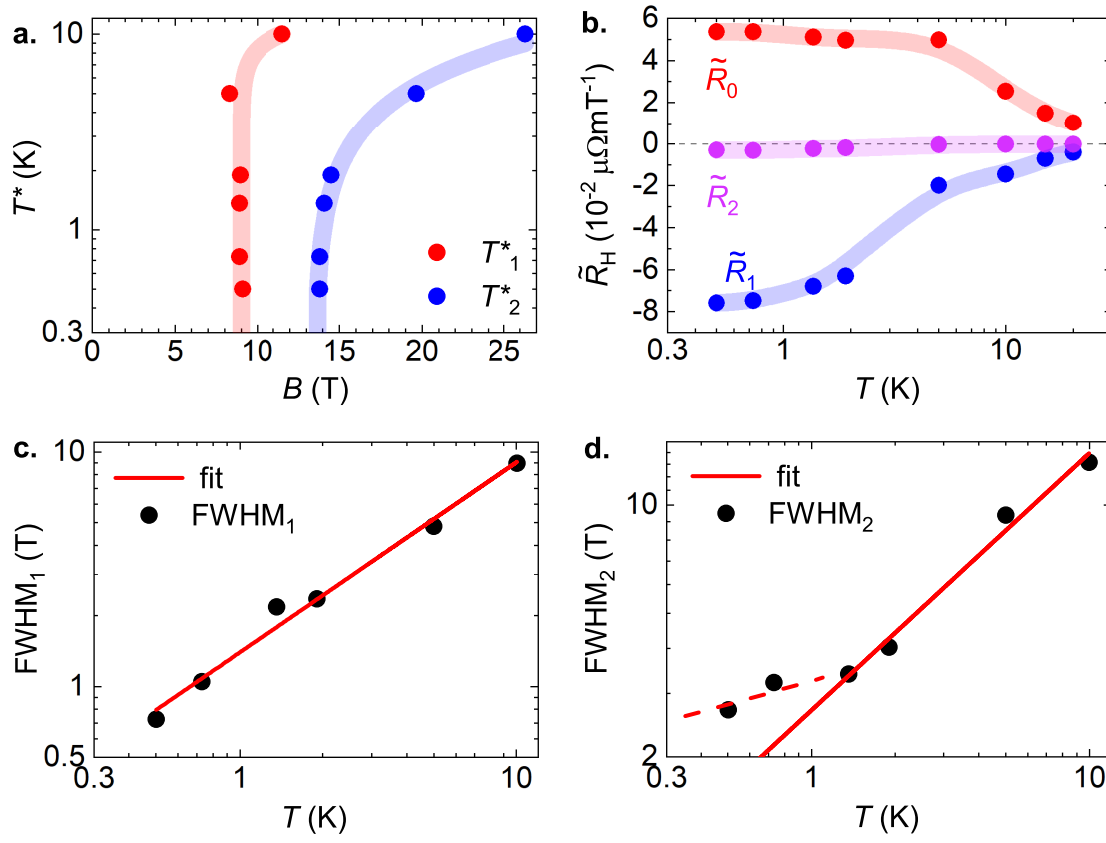


Figure 101: **Analysis of Hall resistivity isotherms of $\text{Ce}_3\text{Bi}_4\text{Pd}_3$ at high magnetic fields.** **a:** The crossover fields $B_1^*(T)$ and $B_2^*(T)$ determined from the $\rho_{xy}(B)$ fits (Fig.99) are plotted as $T_1^*(B)$ and $T_2^*(B)$, respectively, in a temperature–magnetic field phase diagram. Both extrapolate to critical fields B_{c1} and B_{c2} in the zero temperature limit. **b:** The three differential Hall coefficients separated by B_{c1} and B_{c2} vs. temperature. **c, d:** Double-logarithmic plot of the full widths at half maximum of the two transitions (black symbols) determined from the 2nd derivative (Fig.99 a) of the fits in Fig.100. Red lines represent linear fits ($\text{FWHM}_i \sim T^{m_i}$) with power exponents of $m_1 = 0.81 \pm 0.05$ and $m_2 = 0.71 \pm 0.06$ for FWHM_1 and FWHM_2 , respectively. The temperature dependence of FWHM_2 shows the tendency to a weaker slope denoted by the dashed red line at the lowest temperatures.

B_{c1} and B_{c2} , the field dependence of ρ may be dominated by that of the charge carrier concentration. In this situation, the expression $\rho_A(B) \sim M(B)$ [155,156] is more appropriate. Thus, in Fig.102, $\rho_{xy}(B)$ is plotted together with the mag-

netization $M(B)$ [157], scaled by γ_2 to fit $\rho_{xy}(B)$ at low ($B < B_{c1}$), intermediate ($B_{c1} < B < B_{c2}$), and high ($B > B_{c2}$) fields. It is clear that none of the characteristic features of $\rho_{xy}(B)$ is seen in $M(B)$. Thus, skew scattering is not at the origin of the observed high magnetic field dependence of ρ_{xy} in $\text{Ce}_3\text{Bi}_4\text{Pd}_3$.

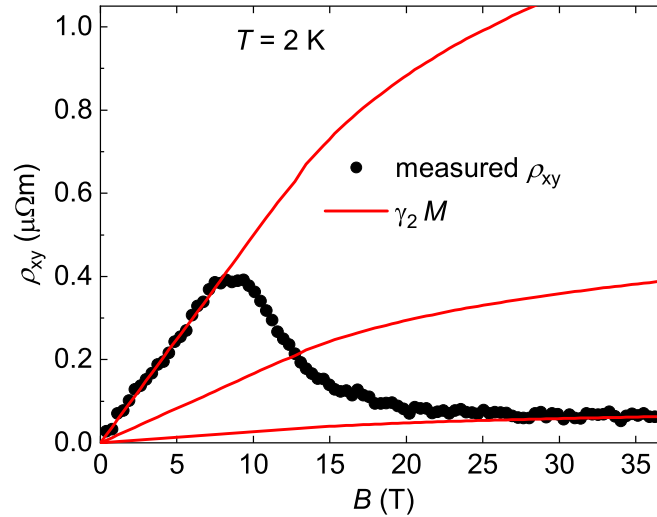


Figure 102: **Estimation of skew scattering contribution to Hall effect from magnetization.** Field-dependent Hall resistivity at 1.9 K, together with magnetization data at 1.5 K taken from [157] and scaled by γ_2 to match ρ_{xy} at low, intermediate, and high fields. The fact that $\gamma_2 M(B)$ does not reproduce the shape of $\rho_{xy}(B)$ reveals that the anomalous Hall effect due to skew scattering is unimportant in $\text{Ce}_3\text{Bi}_4\text{Pd}_3$ at 2 K.

In the next step, despite the above argument, the form $\rho_A(B) = \gamma \rho(B) M(B)$ [76] is used as an estimate of the absolute maximum skew scattering contribution. Here $\gamma = 0.08 \text{ K/T}$ is used ($\gamma = 0.05 \text{ Ce}/\mu_B$ when M is in units of μ_B/Ce), which is the upper limit seen for Ce-based heavy fermion materials [76]. Then $\rho_A(B)$ is subtracted from the $\rho_{xy}(B)$ data, and the two-crossover fit is redone at several representative temperatures (Fig. 103). The results show that the skew scattering contribution to the initial Hall coefficient is at most $\sim 20\%$ (Fig. 103 d). Importantly, neither the crossover positions nor their width change considerably

(Fig. 103 c, e-f). Thus, in conclusion, skew scattering does not contribute appreciably to the crossover behaviour observed in $\text{Ce}_3\text{Bi}_4\text{Pd}_3$.

Finally, to investigate whether the feature observed in the high-field Hall resistivity $\rho_{xy}(B)$ at B_{c1} (Fig. 98) might, alternatively, be a multiple band effect, an effective two-band analysis has been performed on a representative $\rho_{xy}(B)$ curve

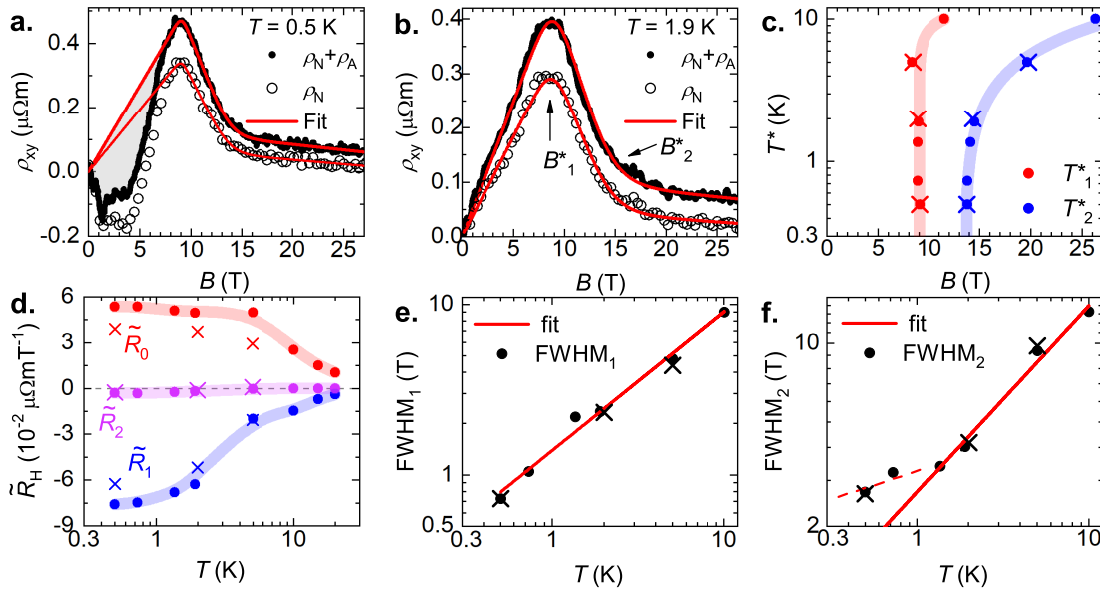


Figure 103: **Estimation of skew scattering contribution to Hall effect from magnetization and electrical resistivity.** Analysis of the two-crossover behaviour, redone under the (unrealistic, see text) assumptions that, firstly, the field dependence of the electrical resistivity is due to skew scattering only, and that thus the anomalous Hall effect is given by $\rho_A(B) = \gamma_2 \rho(B) M(B)$ and that, secondly, the prefactor γ_2 assumes the maximum possible value. **a, b:** As-measured Hall resistivity isotherms (full black points) and data with the (hypothetical) skew scattering contribution ρ_A subtracted, leaving only the normal contribution ρ_N (open symbols). Red line denote the respective two-transition fits (Eqn. 53). **c-f:** Fit parameters obtained for the as-measured (full circles) and (hypothetical) skew scattering corrected data (crosses). The fact that the key fit parameters quantifying the crossovers (T^* and FWHM) are essentially unchanged shows that even the maximum estimated anomalous Hall contribution does not have any appreciable effect on the Hall crossovers.

at $T = 1.9$ K. The analysis was done in three different fit ranges (Fig. 104), to test up to which field a two-band model can capture the observed behaviour.

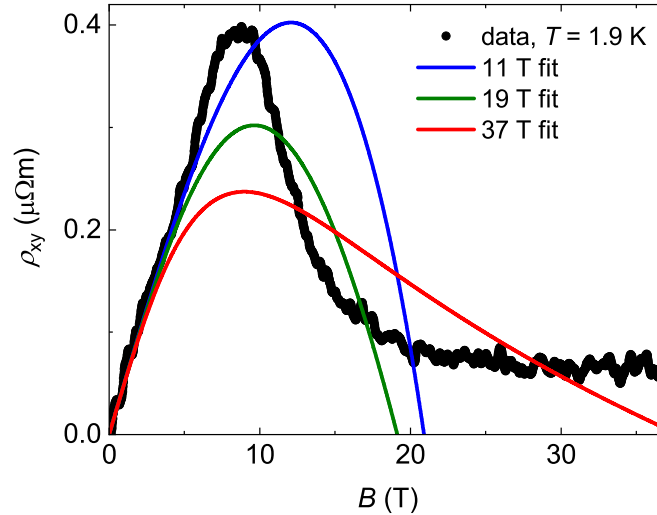


Figure 104: **Estimation of contribution to Hall effect from multiband effects.** Two-band analysis of the Hall resistivity vs. field isotherm of $\text{Ce}_3\text{Bi}_4\text{Pd}_3$ at 1.9 K, using the robust analysis scheme of [74]. The three curves represent fits from zero field up to 11, 19, and 37 T, respectively, to test whether in any of these field ranges the experimental $\rho_{xy}(B)$ curve can be reproduced. The failure shows that the pronounced nonlinearity of $\rho_{xy}(B)$ cannot be due to two-band (or multiband) effects. The analysis in this figure was done by Gaku Eguchi from TU-Vienna.

Even the fit up to 11 T has very poor quality, showing that a two-band model cannot reproduce the sharp bending at B_{c1} . Also the parameters obtained for this fit (one electron and one hole band with $|n_1| \approx |n_2| \approx 1 \times 10^{18} \text{ cm}^{-3}$, $|\mu_1| \approx |\mu_2| \approx 2000 \text{ cm}^2/\text{Vs}$) appear rather unrealistic. Extending the field range does not bring any improvement. Thus, it is highly unlikely that the observed nonlinearity is due to two- or multiband effects (even in the generic multiband situation, typically two bands are found to dominate). The fact that the feature in $\rho_{xy}(B)$ at B_{c1} coincides with the anomalies in $\rho_{xx}(B)$ and $d\rho_{xx}/dT$ (Fig. 93) as well as all other temperature scales reported in Fig. 110 supports, instead, that it is due to a crossover between

phases with different Fermi volume.

Table 3: Fitting parameters for two-band analysis done in Fig. 104. All values are rounded up to the first digit and, thus, must be regarded as approximate values. A positive (negative) sign of the mobility denotes a hole-like (electron-like) band.

parameters	11 T	19 T	37 T	units
n_1	$9 \cdot 10^{23}$	$7 \cdot 10^{25}$	$1 \cdot 10^{27}$	$1/\text{m}^3$
n_2	$9 \cdot 10^{23}$	$1 \cdot 10^{24}$	$1 \cdot 10^{23}$	$1/\text{m}^3$
μ_1	-2000	-40	-3	cm^2/Vs
μ_2	2000	500	1000	cm^2/Vs

5.4.3 Torque magnetometry

The two step transition observed in $\text{Ce}_3\text{Bi}_4\text{Pd}_3$ was further studied by torque magnetometry experiments in high magnetic fields. Angular-dependent magnetic torque measurements for $\text{Ce}_3\text{Bi}_4\text{Pd}_3$ single crystals in pulsed fields up to 65 T were obtained at the NHMFL-LANL Los Alamos in collaboration with the Franziska Weickert, Ross McDonald, Laurel E. Winter and Marcello Jaime from NHMFL-LANL Los Alamos and Diego A. Zocco from TU-Vienna. Magnetic torque data up to 37 T were obtained at the HFML-EMFL Nijmegen high magnetic field facilities in collaboration with Alix McCollam, Diego A. Zocco, Lucas M. K. Tang and Bryan Vlaar. Piezoresistive levers of dimensions $120 \mu\text{m} \times 50 \mu\text{m} \times 4 \mu\text{m}$ and unloaded resonant frequencies of 250 to 300 kHz were used. Due to inherent limitations of the piezo technique small samples were cut from previously characterized single crystals, resulting in the loss of the crystallographic alignment.

In addition, field-dependent torque magnetometry and magnetization measurements were also performed on the Kondo insulator $\text{Ce}_3\text{Bi}_4\text{Pt}_3$. The magnetization data were obtained using an extraction magnetometer and the “sample-in/sample-out” technique to separate the sample signal from the background. Such measure-

ments were performed for comparative reasons as, firstly, $\text{Ce}_3\text{Bi}_4\text{Pd}_3$ is related to the extensively studied compound $\text{Ce}_3\text{Bi}_4\text{Pt}_3$ (Sect. 5.1), secondly, both compounds feature a field induced metallization at high magnetic fields (Sects. 4.3, 5.4.1 and 5.4.2).

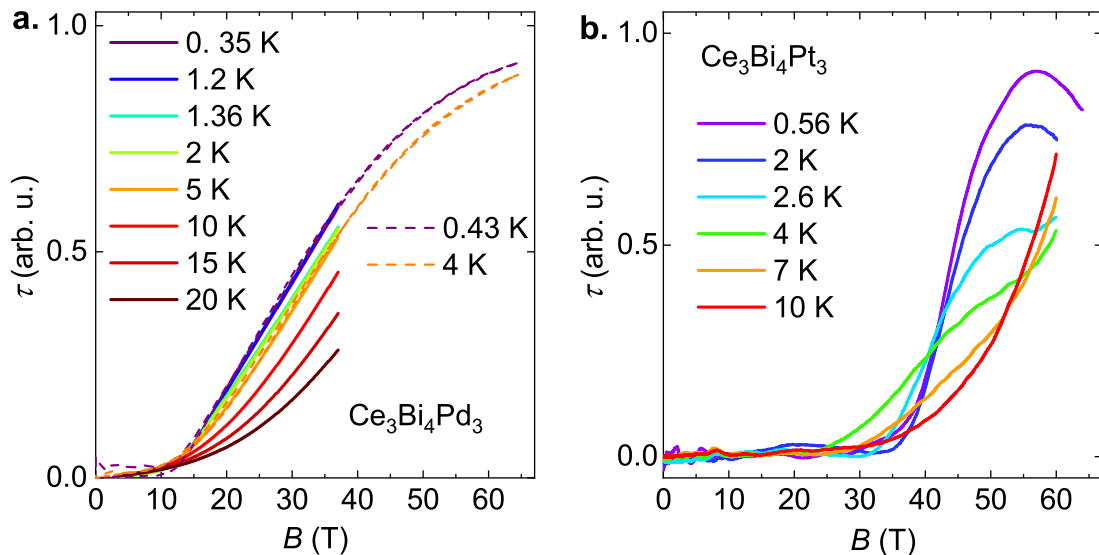


Figure 105: **High-field torque magnetometry of $\text{Ce}_3\text{Bi}_4\text{Pd}_3$ and $\text{Ce}_3\text{Bi}_4\text{Pt}_3$.** **a:** Magnetic torque isotherms of $\text{Ce}_3\text{Bi}_4\text{Pd}_3$ at various temperatures as function of applied magnetic field up to 37 T and, for low temperatures, up to 65 T. **b:** Same as in panel **a** for the Kondo insulator $\text{Ce}_3\text{Bi}_4\text{Pt}_3$. The data up to 37 T were obtained at the HFML-EMFL in Nijmegen in collaboration with Alix McCollam, Diego A. Zocco, Lucas M. K. Tang and Brian Vlaar. The data up to 60 T were obtained at the NHMFL-LANL Los Alamos in collaboration with the Franziska Weickert, Diego A. Zocco, Ross McDonald, Laurel E. Winter and Marcello Jaime.

For $\text{Ce}_3\text{Bi}_4\text{Pd}_3$ at low magnetic fields, essentially no torque signal is detected (Fig. 105 a). This is what is expected for a cubic, magnetically isotropic system, with a linear-in-field magnetization [158]. A sizeable torque signal appears only above about 14 T in the close vicinity of B_{c2} and, thus, coincides with the metallization of the system. Indeed similar behaviour, albeit with a much larger magnetic field scale, is also seen in the canonical Kondo insulator $\text{Ce}_3\text{Bi}_4\text{Pt}_3$ (Fig. 105 b).

There, the onset of sizeable torque produces characteristic signatures in both the first and second derivative of the torque with respect to magnetic field. In the first derivative, this is a step-like increase which, at the lowest temperatures, reaches half height at 13.5 and 38.9 T for $\text{Ce}_3\text{Bi}_4\text{Pd}_3$ and $\text{Ce}_3\text{Bi}_4\text{Pt}_3$, respectively (Fig. 106 a).

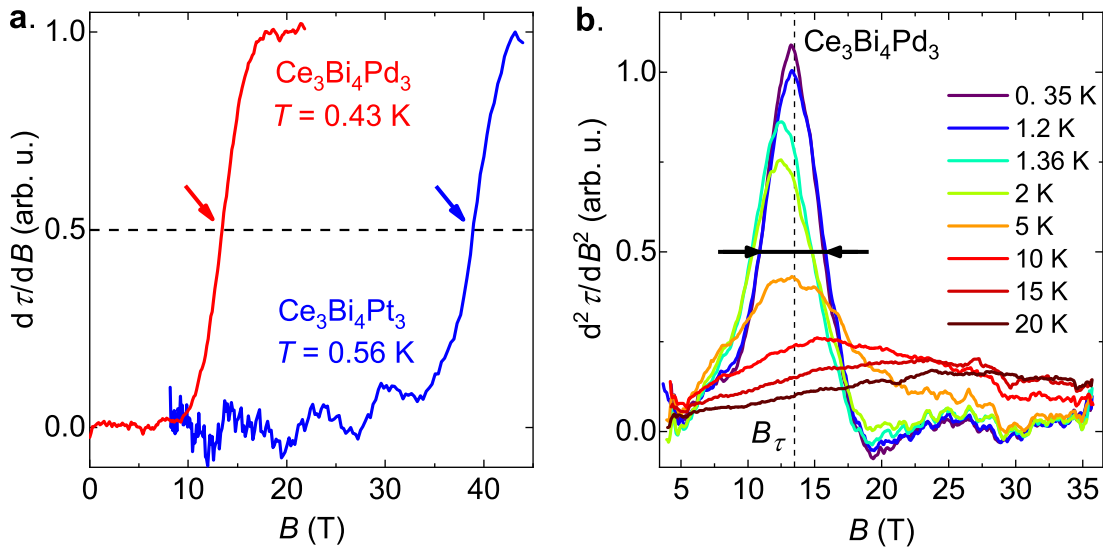


Figure 106: **Magnetic transition in $\text{Ce}_3\text{Bi}_4\text{Pd}_3$ and $\text{Ce}_3\text{Bi}_4\text{Pt}_3$.** **a:** Field derivative of the magnetic torque isotherms of $\text{Ce}_3\text{Bi}_4\text{Pd}_3$ and $\text{Ce}_3\text{Bi}_4\text{Pt}_3$ at the lowest temperatures of 0.43 K and 0.56 K, respectively, revealing similar characteristics, albeit at different fields (the fields where the step-like increases reach half height are indicated by arrows). **b:** Second field derivative of the torque signal of $\text{Ce}_3\text{Bi}_4\text{Pd}_3$. The characteristic field of the torque signal B_τ is defined as the center of the full width at half maximum, as indicated by the dashed vertical line and the horizontal arrows for the 0.35 K isotherm.

For $\text{Ce}_3\text{Bi}_4\text{Pt}_3$, the abrupt appearance of the torque signal at high fields, with the step half height at $B = 38.9$ T, appears to be related to the Kondo insulator to metal transition observed previously between $B = 30$ -40 T in transport [91] and specific heat experiments [92]. By analogy, it seems reasonable to associate the corresponding signature in $\text{Ce}_3\text{Bi}_4\text{Pd}_3$, with the half-height field of 13.5 T, with the

metallization transition seen in the magnetic field-dependent resistivity (Fig. 92b) and Hall resistivity data (Fig. 98) at $B_{c2} = 13.8$ T. In the second derivative of $\tau(B)$ (Fig. 106 b), the signature is a maximum, and the middle field at half height is used as its characteristic field scale B_τ . This analysis shows that the torque signal of $\text{Ce}_3\text{Bi}_4\text{Pd}_3$ only picks up the high-field metallization transition at B_{c2} , but is insensitive to the low-field transition at B_{c1} .

In order to confirm that the torque signal is indeed due to the onset of nonlinearities in $M(B)$, angle dependent torque measurements were carried out. Here the angle θ is between the applied magnetic field and the normal vector of the cantilever (Fig. 107 a inset). For cubic, magnetically isotropic systems M is always parallel to B and, thus, $\tau(B)$ is forced to vanish. However, the first nonvanishing higher order term in the magnetization, that is $M \sim B^3$, will lead to a $\tau \sim B^4$ dependence, which means that the angle dependence follows a $\tau(\theta) \sim \sin(4\theta)$ rule [158]. This is the case for $\text{Ce}_3\text{Bi}_4\text{Pt}_3$ at $B = 55$ T and $T = 0.5$ K (Fig. 107 a). Indeed, the onset of the torque signal coincides with the departure of the $M(B)$ curve from its initial linear behaviour (Fig. 107 b). Beside the dominant 4θ component, a smaller 2θ term is necessary to describe the full angle dependence of τ (Fig. 107a). It arises unavoidably due to the field gradient on the sample that results in a linear-in- B force term (hence $\tau \sim B^2$). Similar to the case of $\text{Ce}_3\text{Bi}_4\text{Pt}_3$, the $\tau(\theta)$ data for $\text{Ce}_3\text{Bi}_4\text{Pd}_3$ at $B = 15$ T show a pronounced 4θ component, evidencing the onset of nonlinearities in $M(B)$ at B_{c2} .

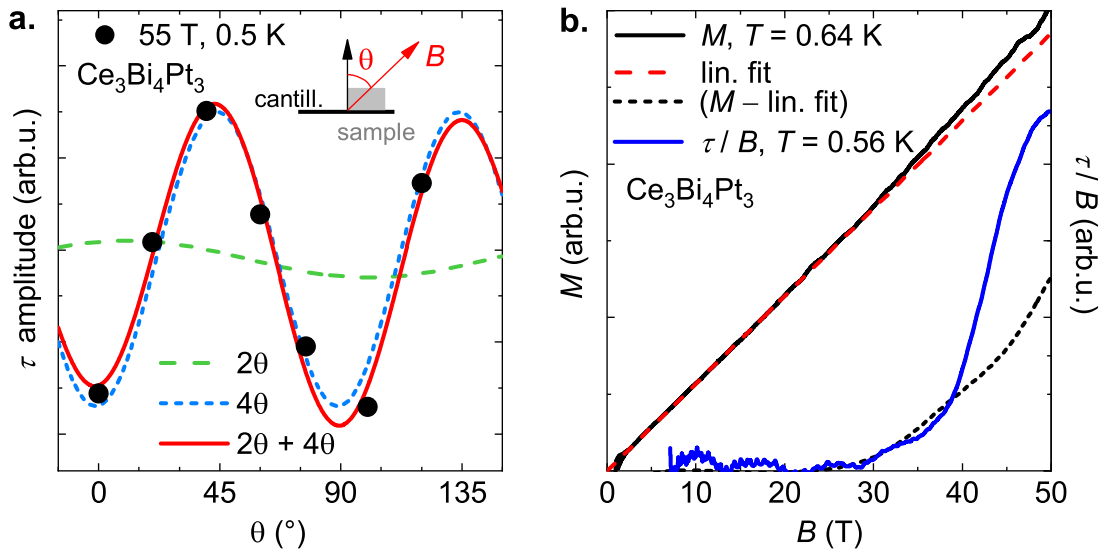


Figure 107: **Nonlinear magnetization of $\text{Ce}_3\text{Bi}_4\text{Pt}_3$.** **a:** Angular dependence of the torque signal of $\text{Ce}_3\text{Bi}_4\text{Pt}_3$ at 0.5 K, obtained at $B = 55$ T (black dots). The red solid line is the best fit to the data, and it corresponds to the superposition of a dominant 4θ component (blue dashed line) and a much smaller 2θ contribution (green dashed line). The definition of the angle θ is sketched in the inset. **b:** High-field magnetization (black curve, left axis) at 0.64 K and magnetic torque divided by applied magnetic field (blue curve, right axis) at 0.56 K, both for $\text{Ce}_3\text{Bi}_4\text{Pt}_3$. Above $B = 30$ T, the magnetization departs from linear-in- B behaviour (red dashed line, linear fit to the data below 30 T). The difference is plotted as black dotted curve on the right axis. The data in both panels were obtained at the NHMFL-LANL Los Alamos in collaboration with the Franziska Weickert, Diego A. Zocco, Ross McDonald, Laurel E. Winter and Marcello Jaime.

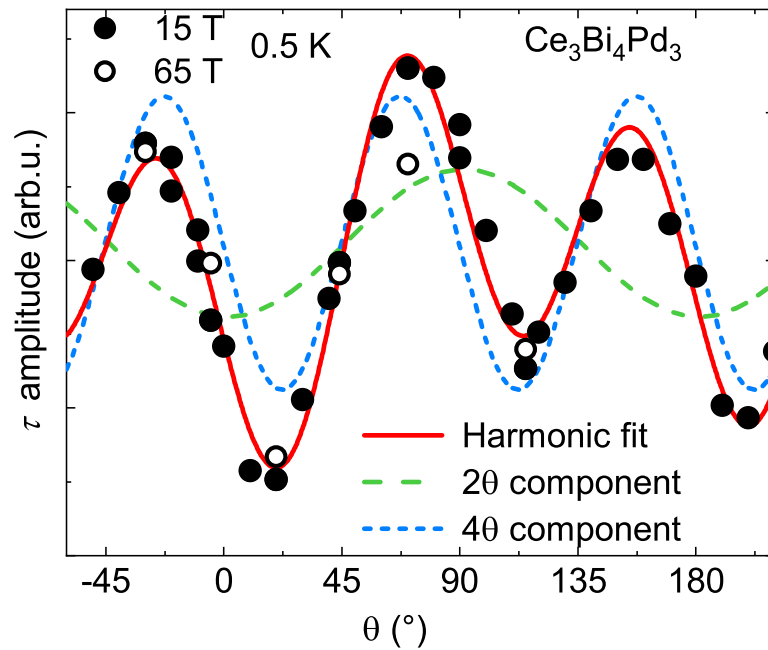


Figure 108: **Nonlinear magnetization in $\text{Ce}_3\text{Bi}_4\text{Pd}_3$.** Angular dependence of the torque signal of $\text{Ce}_3\text{Bi}_4\text{Pd}_3$ at 0.5 K, obtained for magnetic field-sweeps up to 15 T (black dots) and 65 T (white dots). The red solid line is the best fit to the 15 T data, and it corresponds to the superposition of a dominant 4θ component (blue dashed line) and a smaller 2θ contribution (green dashed line). The data were obtained at the NHMFL-LANL Los Alamos in collaboration with the Franziska Weickert, Diego A. Zocco, Ross McDonald, Laurel E. Winter and Marcello Jaime.

5.4.4 Discussion

Having established the structure of the magnetic field-tuned phase diagram of $\text{Ce}_3\text{Bi}_4\text{Pd}_3$ allows to address the pertinent questions: What is the nature of the different delineated phases and what are the mechanisms stabilizing them? Which design strategies for strongly correlated topological phases can be derived from the new understanding? The semimetallic phase at low fields has been identified, via thermodynamic and transport signatures (Sect. 5.3), as a Weyl-Kondo semimetal. The magnetic field dependence of both the onset temperature $T_{C/T}$ of the $\sim T^3$

specific heat signature (Fig. 109 a), and that (T_H^{even}) of the Berry curvature-driven even-in-field Hall signal (Fig. 109 b) suggest that the Weyl-Kondo semimetal is suppressed at $B \sim 9$ T (Fig. 110 a). This is further reinforced by the Fermi surface reconstruction observed in the field-dependent Hall effect at B_{c1} (Fig. 101a).

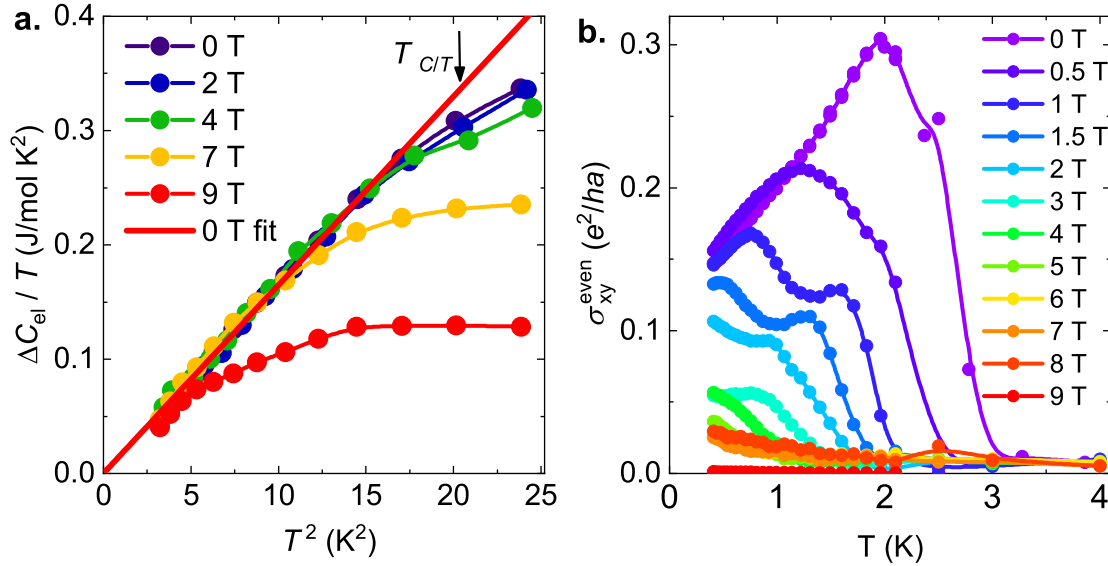


Figure 109: **Weyl-Kondo semimetal state in $\text{Ce}_3\text{Bi}_4\text{Pd}_3$ vs. magnetic field.** **a:** The Weyl-Kondo semimetal $\sim T^3$ contribution to the specific heat defined similar to that in Fig. 58 b at different magnetic fields. $T_{C/T}$ denotes the temperature where the $\Delta C_{\text{el}}/T$ data differ from the $\sim T^2$ law by more than 5%. Red line denotes linear fit for the $B = 0$ T data. **a:** The temperature Berry curvature-driven even-in-field Hall conductivity at different magnetic fields. Its onset temperature defines T_H^{even} .

The metallic high-field phase evidences signatures of a partially field-polarized moderately heavy Fermi liquid, whose characteristic quantities (A coefficient, T_{FL}) show that it collapses at a quantum critical point at B_{c2} (Fig. 110 a). Indeed, this is further underpinned by the Fermi surface reconstruction observed in the Hall resistivity at the same field (Figs. 101 a). What remains to be clarified is the nature of the intermediate phase. Magnetic field in Kondo systems is expected to predominantly provide Zeeman coupling, and according to calculations in a

magnetic field-tuned Weyl-Kondo semimetal model, a critical field exists where the Weyl nodes annihilate and are thus gapped out [107], thereby giving rise to a topological phase transition [30]. The electronic structure of the intermediate phase, while topologically clearly distinct, therefore differs from the Weyl-Kondo semimetal only by the opening of gaps at the Weyl nodes.

The proximity of $\text{Ce}_3\text{Bi}_4\text{Pd}_3$ to a Kondo insulator, realized in $\text{Ce}_3\text{Bi}_4(\text{Pt}_{1-x}\text{Pd}_x)_3$ up to at least $x \leq 0.4$ (Sect. 5.1), as well as its torque feature at B_{c2} (Fig. 106 a) closely resembling that observed at the Kondo insulator to metal transition [91, 92] in $\text{Ce}_3\text{Bi}_4\text{Pt}_3$ (Fig. 106 b), suggest that the “background” to the low and intermediate-field phases is a Kondo insulator. The high-magnetic field study then suggests that the Weyl nodes, which are created in zero field by the inversion symmetry breaking of the noncentrosymmetric crystal structure of $\text{Ce}_3\text{Bi}_4\text{Pd}_3$ and are gapped-out at the critical magnetic field B_{c1} , are positioned within the gap of a Kondo insulator. This Kondo insulator then, with further increasing field, collapses to a heavy fermion metal at B_{c2} .

The analysis of the Hall resistivity underpins this interpretation. The charge carrier concentration per Ce, determined at 0.5 K from a simple single-band model, changes from about 0.01 holes in the Weyl-Kondo semimetal, via 0.007 electrons in the more insulating phase, to 0.2 electrons in the heavy fermion metal (Fig. 110 b). The application of magnetic field gives rise to a two-stage quantum phase transitions (Fig. 110 c). The first transition, that is associated with the annihilation of the Weyl nodes, and that hence is topological in nature, leads to a jump in the extrapolated zero-temperature Hall coefficient. Whereas such a feature is expected for Kondo destruction quantum criticality, this is unlikely the cause here: in $\text{Ce}_3\text{Bi}_4\text{Pd}_3$ the Kondo interaction is gradually suppressed only for fields much higher than B_{c2} (Fig. 97), and no magnetic order is observed in the entire field range. Thus, the zero-temperature jump in the Hall coefficient suggests that the

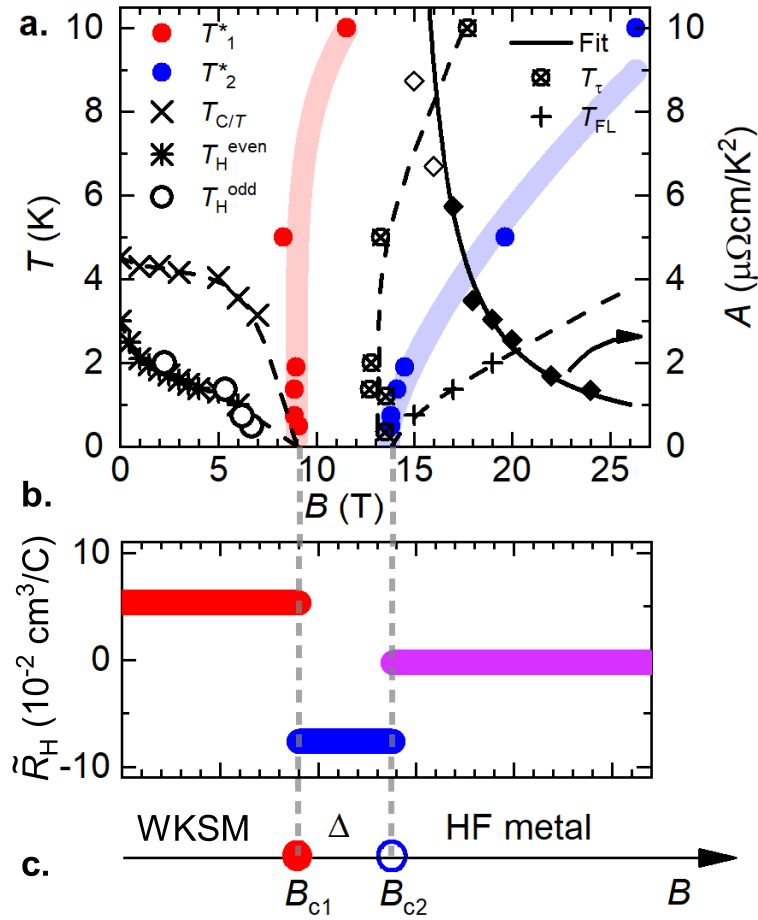


Figure 110: **Magnetic field-tuned phase diagram of $\text{Ce}_3\text{Bi}_4\text{Pd}_3$.** **a:** Temperature–magnetic field phase diagram with the crossover temperatures T_1^* and T_2^* from Fig. 101 a, the temperature $T_{C/T}$ below which the electronic specific heat coefficient C/T displays the T^2 law representing the linear Weyl dispersion (Fig. 109 a), the onset temperature T_H^{even} of the Berry curvature-related contribution to the even-in-field Hall resistivity taken from Fig. 109 b, the temperature T_H^{odd} below which the Berry curvature-related contribution to the odd-in-field Hall resistivity sets in (Fig. 100), the characteristic scale T_τ for the change in character of the torque signal (Fig. 106 b), and the temperature T_{FL} below which the $\rho \sim T^2$ Fermi liquid law sets in (all left axis). The A coefficient of this law is plotted on the right axis. Above 16 T, it is well described by $A/(B - B_{c2})^{-p}$, with $B_{c2} = 13.82 \pm 0.02$ T and $p = 0.98 \pm 0.03$, suggesting that the effective mass diverges at a quantum critical point situated at B_{c2} . **b:** Differential Hall coefficient vs. B in the zero temperature limit obtained from Fig. 101. **c:** Schematic ground state of $\text{Ce}_3\text{Bi}_4\text{Pd}_3$ vs. magnetic field with the three experimentally resolved phases shown. WKSM denotes the Weyl-Kondo semimetal state, Δ denotes gapped Weyl nodes and HF metal denotes the heavy fermion metal state.

first quantum phase transition is not continuous. The second transition, by contrast, displays signatures of quantum criticality and, thus, must be (at least nearly) continuous. Indeed, evidence for quantum criticality at a Kondo insulator to metal transition has previously been seen in pressure-tuned SmB_6 [159, 160].

In conclusion, high magnetic field studies show that a Weyl-Kondo semimetal is quenched in two stages of quantum phase transition, annihilating and gapping-out the Weyl nodes in a Kondo insulator background in a topological first step, and collapsing the underlying Kondo insulator gap to form a (heavy fermion) metal in a second step. This sequence is both a confirmation of the Weyl-Kondo semimetal assignment for $\text{Ce}_3\text{Bi}_4\text{Pd}_3$ and a recipe to find other correlation-driven Weyl semimetals in strongly correlated materials and theoretical models in general.

6 Summary and outlook

In this thesis, I discussed the crystal growth, physical properties and high-magnetic field study of the novel compound $\text{Ce}_3\text{Bi}_4\text{Pd}_3$. In the first part of the results (Sect. 5), I demonstrate that Pd-Pt substitution is an ideal tool to tune the spin-orbit coupling in the Kondo insulator $\text{Ce}_3\text{Bi}_4\text{Pt}_3$. Powder XRD measurements confirm that varying the concentration x in $\text{Ce}_3\text{Bi}_4(\text{Pt}_{1-x}\text{Pd}_x)_3$ realizes an iso-structural and iso-size substitution series. In addition, because Pd and Pt have the same number of valence electrons, such a series is also iso-electronic. Indeed, Hall effect measurements at room temperature – where electron correlation effects are negligible – confirm this scenario. Temperature-dependent measurements, on the other hand, reveal surprising behaviour. Electrical resistivity, Hall resistivity and magnetic susceptibility data evidence a reduction of the Kondo gap and a transformation of the ground state to a Kondo interaction-driven semimetal.

In the second part of Sect. 5, I present thermodynamic and Hall effect results.

Contrary to the $C \sim T$ law expected for the electronic specific heat of metals, $\text{Ce}_3\text{Bi}_4\text{Pd}_3$ evidences a $C = \Gamma T^3$ behaviour that is the hallmark of 3D electron systems with linear dispersion. Most interestingly, the coefficient Γ is orders of magnitude enhanced over values expected for weakly correlated semimetals, and in fact, is determined by the Kondo energy scale of this material. This discovery establishes a new class of heavy fermion compounds named Weyl-Kondo semimetals. Such systems host Weyl nodes pinned to the Fermi energy by the Kondo interaction and exhibit linearly-dispersing bands which are severely renormalized.

Whereas specific heat experiments provide valuable information about the band dispersion, they tell little about the electronic topology of the system. In search for a unique fingerprint of the newly proposed Weyl-Kondo semimetal state, attention was given to the Hall effect. The divergent Berry curvature at the Weyl nodes is expected to drive a novel type of Hall effect that occurs in the absence of a magnetic field but is nonlinear in the driving electric field. Indeed, temperature-dependent Hall resistivity measurements in $\text{Ce}_3\text{Bi}_4\text{Pd}_3$ show a clear spontaneous Hall effect in the Kondo coherent regime. Remarkably, it occurs not only in the absence of an external magnetic field, but also in a nonmagnetic groundstate as evidenced by state-of-the-art μSR experiments. Instead, the effect is clearly driven by the nonequilibrium electron distribution function, is an even function of an external magnetic field, and is nonlinear in the driving current, all in agreement with theoretical expectations. However, the spontaneous Hall effect in $\text{Ce}_3\text{Bi}_4\text{Pd}_3$ points beyond the case of noninteracting Weyl semimetals. The detected second-harmonic contribution surpasses that predicted for noninteracting Weyl semimetals by orders of magnitude. In addition, a linear-in-electric field, first-harmonic component appears that has so far not been considered theoretically. I demonstrate that all these aspects arise naturally when Weyl nodes are in the extreme vicinity of the Fermi energy, where perturbation type calculations are expected to break down.

This constitutes a strong evidence for the proposed Weyl-Kondo semimetal state.

In the third part of Sect. 5 I present a magnetotransport and torque magnetometry study on $\text{Ce}_3\text{Bi}_4\text{Pd}_3$ in high magnetic fields. Isothermal magnetic field-dependent electrical resistivity curves at the lowest temperatures evidences a two-stage transition, with critical fields of $B_{c1} \sim 9 \text{ T}$ and $B_{c2} \sim 13.8 \text{ T}$ from an initial semimetallic to a high-field metallic state. This is corroborated by iso-field temperature-dependent resistivity measurements. The first transition displays marked changes of $\rho(B)$ and the low-temperature derivative of $\rho(T)$, albeit non of the behaviours are metallic. Measurements across B_{c2} , on the other hand, reveal the transition to a heavy Fermi-liquid state across a quantum critical point. Indeed the extracted A -coefficient is consistent with a divergence at B_{c2} . It is accompanied by a vanishing Fermi-liquid temperature T_{FL} , above which $\rho(T)$ shows non-Fermi liquid behaviour. Hall resistivity isotherms confirm this scenario. They display two successive kinks at the same magnetic field values where the resistivity showed the two-staged transition. The differential Hall coefficients associated with the three regimes (below B_{c1} , between B_{c1} and B_{c2} , and above B_{c2}) show a transition from an initial state with low, via an intermediate one with even lower to a final metallic state with much higher carrier density. Whereas the corresponding values of the initial and final state support an initial semimetallic and a final metallic ground state, respectively, the reduced value for the intermediate phase points to an annihilation and gapping of the Weyl nodes. Indeed, both the $C = \Gamma T^3$ behaviour and the finite spontaneous Hall resistivity disappear at B_{c1} . Remarkably, torque magnetometry displays a clear onset of magnetisation at B_{c2} , similar to previously seen Kondo insulator-to-metal transition in $\text{Ce}_3\text{Bi}_4\text{Pt}_3$. These results suggest that the Weyl nodes in $\text{Ce}_3\text{Bi}_4\text{Pd}_3$ emerge within a small Kondo insulator gap. Applying a finite magnetic field then leads to the annihilation of the Weyl nodes at a first critical field, and to a subsequent transition to a field-polarized

heavy fermion state at the second critical field.

Finally, establishing the Weyl-Kondo semimetal phase in $\text{Ce}_3\text{Bi}_4\text{Pd}_3$ opens up new perspectives in harnessing the synergy between strong electron interactions and nontrivial topology. For example, motivated by the unique spontaneous Hall effect, exploring related effects in thermal and thermoelectric transport holds promise for novel quantum phenomena unseen so far. On the other hand, the fate of the surface Fermi arcs in the limit of strong electron interactions remains an open and exciting question. Due to the large surface-to-volume ratio of thin film structures, their production either by appropriate growth techniques (e.g., molecular beam epitaxy) or by microfabrication methods is certainly a promising way forward. Such approaches may directly expose nontrivial surface states to well established transport techniques allowing to capture their specific signatures.

7 List of abbreviations

ARPES – Angle-resolved photoemission spectroscopy

AHE – Anomalous Hall effect

DFT – Density functional theory

EDX – Energy-dispersive X-ray spectroscopy

FC – Field cooling

FWHM – Full width at half maximum

LF- μ SR – Longitudinal-field muon spin rotation

μ SR – Muon spin rotation.

ZF- μ SR – Zero-field muon spin rotation

NFL – Non-Fermi liquid

PPMS – Physical Property Measurement System

QCP – Quantum critical point

QHE – Quantum Hall effect

QPT – Quantum phase transition

SEM – Scanning electron microscopy. TRS – Time reversal symmetry

WKSM – Weyl-Kondo semimetal

WDX – Wavelength-dispersive X-ray spectroscopy

XRD – X-ray diffraction

ZFC – Zero-field cooling

8 Contributions of collaborators

The experiments and calculations presented in this thesis could not have been done without the effort of many collaborators. Their contributions to this PhD thesis are detailed in what follows.

Lukas Prochaska from TU-Vienna contributed to the electrical transport measurements presented in Sect. 5.1.4. Gaku Eguchi from TU-Vienna contributed to the electrical transport, specific heat and magnetization experiments presented in Sects. 5.1.4, 5.3.2, and 5.3.5, respectively. Andrey Sidorenko from TU-Vienna contributed to the magnetic susceptibility and magnetization experiments presented in Sect. 5.1.5. Robert Svagera and Monika Waas performed all SEM/EDX experiments, and provided all related data presented in this thesis. Andrey Prokofiev from TU-Vienna contributed to all crystal growth experiments presented in this thesis.

Xinlin Yan from TU-Vienna grew the lead flux grown $\text{Ce}_3\text{Bi}_4\text{Pd}_3$ single crystals used for the second harmonic current-voltage measurements presented in Sect. 5.3 and the muon spin rotation experiments presented in Sect. 5.3.6. He also performed the time-dependent XRD measurements presented in Fig. 51 a. Mathieu Taupin from TU-Vienna contributed to the data acquisition of the spontaneous Hall effect and related current-voltage measurements of $\text{Ce}_3\text{Bi}_4\text{Pd}_3$ presented in Sects. 5.3.4 and 5.3.8. Toni Shiroka from ETH Zurich performed the muon spin rotation experiments with me and provided related data and their analysis presented in Sect. 5.3.6. Jean-Christophe Orain from the Paul Scherrer Institute provided the technical support for these measurements. Peter Blaha from TU-Vienna carried out the density functional theory calculations for $\text{Ce}_3\text{Bi}_4\text{Pd}_3$ and provided related figures discussed in Sect. 5.3.9. Sarah E. Grefe, Hsin-Hua Lai and Qimiao Si from Rice University (Houston / USA) performed the Weyl-Kondo semimetal model calculations and provided related data discussed in Sects. 5.3.1 and 5.3.10.

Diego A. Zocco from TU-Vienna contributed to all high magnetic field experiments presented in Sect. 5.4. He carried out the magnetic field-dependent magnetization experiments and angle-dependent magnetic torque magnetometry for $\text{Ce}_3\text{Bi}_4\text{Pt}_3$ and $\text{Ce}_3\text{Bi}_4\text{Pd}_3$, all presented in Sect. 5.4.3. Mathieu Taupin and Diego A. Zocco from TU-Vienna contributed to the magnetic field and temperature-dependent resistivity experiments on $\text{Ce}_3\text{Bi}_4\text{Pd}_3$ done in the dilution refrigerator at TU-Vienna (Sect. 5.4). Electrical resistivity, Hall resistivity and torque magnetometry experiments performed on $\text{Ce}_3\text{Bi}_4\text{Pd}_3$ and $\text{Ce}_3\text{Bi}_4\text{Pt}_3$ (Sect. 5.4) at the High Field Magnet Laboratory (HFML-EMFL), Radboud University (Nijmegen, the Netherlands) were done in collaboration with Alix McCollam, Lucas M. K. Tang and Bryan Vlaar from HFML-EMFL, Radboud University. Torque magnetometry and magnetization experiments performed on $\text{Ce}_3\text{Bi}_4\text{Pd}_3$ and $\text{Ce}_3\text{Bi}_4\text{Pt}_3$ (Sect. 5.4) at the National High Magnetic Field Laboratory (Los Alamos / USA) were done in collaboration with Franziska Weickert, Ross McDonald, Laurel E. Winter and Marcelo Jaime from the Los Alamos National Laboratory (see Sect. 5.4).

All contributions, data and analysis provided by collaborators are indicated at the respective part in the text and also in the related figure captions.

References

- [1] de Haas, W. J., de Boer, J. & van den Berg, G. J. The electrical resistance of gold, copper and lead at low temperatures. *Physica* **1**, 1115 (1934).
- [2] Kondo, J. Resistance minimum in dilute magnetic alloys. *Progr. Theor. Phys.* **32**, 37 (1964).
- [3] Abrikosov, A. A. Electron scattering on magnetic impurities in metals and anomalous resistivity effects. *Phys. Phys. Fiz.* **2**, 5 (1965).
- [4] Hewson, A. C. *The Kondo Problem to Heavy Fermions* (Cambridge University Press, Cambridge, 1997).
- [5] Horvatić, B., Sokcević, D. & Zlatić, V. Finite-temperature spectral density for the Anderson model. *Phys. Rev. B* **36**, 675 (1987).
- [6] Schrieffer, J. R. & Wolff, P. A. Relation between the Anderson and Kondo Hamiltonians. *Phys. Rev. B* **149**, 491 (1966).
- [7] Y. Onuki and T. Komatsubara. Heavy Fermion state in CeCu₆. *J. Magn. Magn. Mater.* **63-64**, 281 (1987).
- [8] Coleman, P. *Handbook of Magnetism and Advanced Magnetic Materials, Vol 1: Fundamentals and Theory*, chap. “Heavy Fermions: electrons at the edge of magnetism.”, 95–148 (Eds. H. Kronmüller and S. Parkin, John Wiley and Sons, West Sussex, UK, 2007).
- [9] Doniach, S. The Kondo lattice and weak antiferromagnetism. *Physica B+C* **91**, 231 (1977).
- [10] Hertz, J. Quantum critical phenomena. *Phys. Rev. B* **14**, 1165 (1976).

- [11] Millis, A. J. Effect of a nonzero temperature on quantum critical points in itinerant fermion systems. *Phys. Rev. B* **48**, 7183 (1993).
- [12] Si, Q., Rabello, S., Ingersent, K. & Smith, J. Locally critical quantum phase transitions in strongly correlated metals. *Nature* **413**, 804 (2001).
- [13] Paschen, S., Lühmann, T., Wirth, S., Gegenwart, P., Trovarelli, O., Geibel, C., Steglich, F., Coleman, P. & Si, Q. Hall-effect evolution across a heavy-fermion quantum critical point. *Nature* **432**, 881 (2004).
- [14] Gegenwart, P., Si, Q. & Steglich, F. Quantum criticality in heavy-fermion metals. *Nature Phys.* **4**, 186 (2008).
- [15] Custers, J., Gegenwart, P., Wilhelm, H., Neumaier, K., Tokiwa, Y., Trovarelli, O., Geibel, C., Steglich, F., Pépin, C. & Coleman, P. The break-up of heavy electrons at a quantum critical point. *Nature* **424**, 524 (2003).
- [16] Riseborough, P. S. Heavy fermion semiconductors. *Adv. Phys.* **49**, 257 (2000).
- [17] Landau, L. D. On the theory of phase transitions. *Zh. Eksp. Teor. Fiz.* **7**, 19 (1937).
- [18] v. Klitzing, K., Dorda, G. & Pepper, M. New method for high-accuracy determination of the fine-structure constant based on quantized Hall resistance. *Phys. Rev. Lett.* **45**, 494 (1980).
- [19] Thouless, D. J., Kohmoto, M., Nightingale, M. P. & den Nijs, M. Quantized hall conductance in a two-dimensional periodic potential. *Phys. Rev. Lett.* **49**, 405 (1982).
- [20] Hasan, M. Z. & Kane, C. L. Colloquium: Topological insulators. *Rev. Mod. Phys.* **82**, 3045 (2010).

REFERENCES

- [21] Chang, C.-Z., Zhang, J., Feng, X., Shen, J., Zhang, Z., Guo, M., Li, K., Ou, Y., Wei, P., Wang, L.-L., Ji, Z.-Q., Feng, Y., Ji, S., Chen, X., Jia, J., Dai, X., Fang, Z., Zhang, S.-C., He, K., Wang, Y., Lu, L., Ma, X.-C. & Xue, Q.-K. Experimental observation of the quantum anomalous Hall effect in a magnetic topological insulator. *Science* **340**, 167 (2013).
- [22] Berry, M. V. Quantal phase factors accompanying adiabatic changes. *Proc. R. Soc. London, Ser. A* **392**, 45 (1984).
- [23] Halperin, B. I. Quantized hall conductance, current-carrying edge states, and the existence of extended states in a two-dimensional disordered potential. *Phys. Rev. B* **25**, 2185 (1982).
- [24] Cooper, D., D’Anjou, B., Ghattamaneni, N., Harack, B., Hilke, M., Horth, A., Majlis, N., Massicotte, M., Vandsburger, L., Whiteway, E. & Yu, V. Experimental review of graphene. *ISRN Condens. Matter Phys.* **2012** (2011).
- [25] Kane, C. L. & Mele, E. J. Z_2 topological order and the quantum spin hall effect. *Phys. Rev. Lett.* **95**, 146802 (2005).
- [26] König, M., Wiedmann, S., Brüne, C., Roth, A., Buhmann, H., Molenkamp, L. W., Qi, X. & Zhang, S. Quantum spin Hall insulator state in HgTe quantum wells. *Science* **318**, 766 (2007).
- [27] Fu, L., Kane, C. L. & Mele, E. J. Topological insulators in three dimensions. *Phys. Rev. Lett.* **98**, 106803 (2007).
- [28] Hsieh, D., Qian, D., Wray, L., Xia, Y., Hor, Y. S., Cava, R. J. & Hasan, M. Z. A topological Dirac insulator in a quantum spin Hall phase. *Nature* **452**, 970 (2008).

- [29] Xia, Y., Qian, D., Hsieh, D., Wray, L., Pal, A., Lin, H., Bansil, A., Grauer, D., Hor, Y. S., Cava, R. J. & Hasan, M. Z. Observation of a large-gap topological-insulator class with a single Dirac cone on the surface. *Nature Phys.* **5**, 398 (2009).
- [30] Armitage, N. P., Mele, E. J. & Vishwanath, A. Weyl and Dirac semimetals in three-dimensional solids. *Rev. Mod. Phys.* **90**, 015001 (2018).
- [31] Weyl, H. Elektron und Gravitation. I. *Z. Phys.* **56**, 330 (1929).
- [32] Xiao, D., Chang, M.-C. & Niu, Q. Berry phase effects on electronic properties. *Rev. Mod. Phys.* **82**, 1959 (2010).
- [33] Hui, L., He, H., Lu, H.-Z., Huachen, Z., Liu, H., Ma, R., Fan, Z., Shen, S.-Q. & Wang, J. Negative Magnetoresistance in Dirac Semimetal Cd_3As_2 . *Nat. Commun.* **7**, 10301 (2016).
- [34] Ojanen, T. Helical fermi arcs and surface states in time-reversal invariant weyl semimetals. *Phys. Rev. B* **87**, 245112 (2013).
- [35] Huang, S.-M., Xu, S.-Y., Belopolski, I., Lee, C.-C., Chang, G., Wang, B., Alidoust, N., Bian, G., Neupane, M., Zhang, C., Jia, S., Bansil, A., Lin, H. & Hasan, M. Z. A Weyl Fermion semimetal with surface Fermi arcs in the transition metal monpnictide TaAs class. *Nat. Commun.* **6**, 7373 (2015).
- [36] Weng, H., Fang, C., Fang, Z., Bernevig, B. A. & Dai, X. Weyl semimetal phase in noncentrosymmetric transition-metal monophosphides. *Phys. Rev. X* **5**, 011029 (2015).
- [37] Xu, S.-Y., Alidoust, N., Belopolski, I., Yuan, Z., Bian, G., Chang, T.-R., Zheng, H., Strocov, V. N., Sanchez, D. S., Chang, G., Zhang, C., Mou, D.,

REFERENCES

- Wu, Y., Huang, L., Lee, C.-C., Huang, S.-M., Wang, B., Bansil, A., Jeng, H.-T., Neupert, T., Kaminski, A., Lin, H., Jia, S. & Zahid Hasan, M. Discovery of a Weyl fermion state with Fermi arcs in niobium arsenide. *Nat. Phys.* **11**, 748 (2015).
- [38] Xu, N., Weng, H. M., Lv, B. Q., Matt, C. E., Park, J., Bisti, F., Strocov, V. N., Gawryluk, D., Pomjakushina, E., Conder, K., Plumb, N. C., Radovic, M., Autès, G., Yazyev, O. V., Fang, Z., Dai, X., Qian, T., Mesot, J., Ding, H. & Shi, M. Observation of Weyl nodes and Fermi arcs in tantalum phosphide. *Nat. Commun.* **7**, 11006 (2016).
- [39] Xu, S. Y., Belopolski, I., Alidoust, N., Neupane, M., Bian, G., Zhang, C. L., Sankar, R., Chang, G. Q., Yuan, Z. J., Lee, C. C., Huang, S. M., Zheng, H., Ma, J., Sanchez, D. S., Wang, B. K., Bansil, A., Chou, F. C., Shibayev, P. P., Lin, H., Jia, S. & Hasan, M. Z. Discovery of a Weyl fermion semimetal and topological Fermi arcs. *Science* **349**, 613 (2015).
- [40] Adler, S. L. Axial-vector vertex in spinor electrodynamics. *Phys. Rev.* **177**, 2426 (1969).
- [41] Bell, J. S. & Jackiw, R. A PCAC puzzle: $\pi^0 \rightarrow \gamma\gamma$ in the σ -model. *Il Nuovo Cimento A* **60**, 47 (1969).
- [42] Nielsen, H. B. & Ninomiya, M. The Adler-Bell-Jackiw Anomaly and Weyl Fermions in Crystals. *Phys. Lett.* **130 B**, 389 (1983).
- [43] Zhang, C.-L., Xu, S.-Y., Belopolski, I., Yuan, Z., Lin, Z., Tong, B., Bian, G., Alidoust, N., Lee, C.-C., Huang, S.-M., Chang, T.-R., Chang, G., Hsu, C.-H., Jeng, H.-T., Neupane, M., Sanchez, D. S., Zheng, H., Wang, J., Lin, H., Zhang, C., Lu, H.-Z., Shen, S.-Q., Neupert, T., Zahid Hasan, M. & Jia,

- S. Signatures of the Adler–Bell–Jackiw chiral anomaly in a Weyl fermion semimetal. *Nat. Commun.* **7**, 10735 (2016).
- [44] Hu, J., Liu, J. Y., Graf, D., Radmanesh, S. M. A., Adams, D. J., Chuang, A., Wang, Y., Chiorescu, I., Wei, J., Spinu, L. & Mao, Z. Q. π Berry phase and Zeeman splitting of Weyl semimetal TaP. *Sci. Rep.* **6**, 18674 (2016).
- [45] Li, C.-Z., Wang, L.-X., Liu, H., Wang, J., Liao, Z.-M. & Yu, D.-P. Giant negative magnetoresistance induced by the chiral anomaly in individual Cd₃As₂ nanowires. *Nat. Commun.* **6**, 10137 (2015).
- [46] Li, Q., Kharzeev, D. E., Zhang, C., Huang, Y., Pletikosić, I., Fedorov, A., Zhong, R., Schneeloch, J., Gu, G. & Valla, T. Chiral magnetic effect in ZrTe₅. *Nat. Phys.* **12**, 550 (2016).
- [47] dos Reis, R. D., Ajeesh, M. O., Kumar, N., Arnold, F., Shekhar, C., Naumann, M., Schmidt, M., Nicklas, M. & Hassinger, E. On the search for the chiral anomaly in Weyl semimetals: the negative longitudinal magnetoresistance. *New J. Phys.* **18**, 085006 (2016).
- [48] Wan, X., Turner, A. M., Vishwanath, A. & Savrasov, S. Y. Topological semimetal and Fermi-arc surface states in the electronic structure of pyrochlore iridates. *Phys. Rev. B* **83**, 205101 (2011).
- [49] Moll, P. J. W., Nair, N. L., Helm, T., Potter, A. C., Kimchi, I., Vishwanath, A. & Analytis, J. G. Transport evidence for Fermi-arc-mediated chirality transfer in the Dirac semimetal Cd₃As₂. *Nature* **535**, 266 (2016).
- [50] Zhang, C., Zhang, Y., Yuan, X., Lu, S., Zhang, J., Narayan, A., Liu, Y., Zhang, H., Ni, Z., Liu, R., Choi, E. S., Suslov, A., Sanvito, S., Pi, L., Lu, H.-Z., Potter, A. C. & Xiu, F. Quantum Hall effect based on Weyl orbits in Cd₃As₂. *Nature* **565**, 331–336 (2019).

REFERENCES

- [51] Potter, A. C., Kimchi, I. & Vishwanath, A. Quantum oscillations from surface Fermi arcs in Weyl and Dirac semimetals. *Nat. Commun.* **5**, 5161 (2014).
- [52] Burkov, A. A. Anomalous Hall effect in Weyl metals. *Phys. Rev. Lett.* **113**, 187202 (2014).
- [53] Sodemann, I. & Fu, L. Quantum nonlinear Hall effect induced by Berry curvature dipole in time-reversal invariant materials. *Phys. Rev. Lett.* **115**, 216806 (2015).
- [54] Zhang, Y., Sun, Y. & Yan, B. Berry curvature dipole in Weyl semimetal materials: An *ab initio* study. *Phys. Rev. B* **97**, 041101 (2018).
- [55] Suzuki, T., Chisnell, R., Devarakonda, A., Liu, Y.-T., Feng, W., Xiao, D., Lynn, J. & Checkelsky, J. Large anomalous Hall effect in a half-Heusler antiferromagnet. *Nat. Phys.* **12**, 1119 (2016).
- [56] Liang, T., Lin, J., Gibson, Q., Kushwaha, S., Liu, M., Wang, W., Xiong, H., Sobota, J. A., Hashimoto, M., Kirchmann, P. S., Shen, Z.-X., Cava, R. J. & Ong, N. P. Anomalous Hall effect in ZrTe_5 . *Nat. Phys.* **14**, 451 (2018).
- [57] Liu, E., Sun, Y., Kumar, N., Muechler, L., Sun, A., Jiao, L., Yang, S.-Y., Liu, D., Liang, A., Xu, Q., Kroder, J., Süß, V., Borrmann, H., Shekhar, C., Wang, Z., Xi, C., Wang, W., Schnelle, W., Wirth, S., Chen, Y., Goennenwein, S. T. B. & Felser, C. Giant anomalous Hall effect in a ferromagnetic kagome-lattice semimetal. *Nat. Phys.* **14**, 1125 (2018).
- [58] Luke, G. M., Fudamoto, K. M., Y. and Kojima, Larkin, M. I., Merrin, J., Nachumi, B., Uemura, Y., Y. J. Maeno, Mao, Z. Q., Mori, Y., Nakamura, H. & Sigrist, M. Time-reversal symmetry-breaking superconductivity in Sr_2RuO_4 . *Nature* **394** (1998).

- [59] Hillier, A. D., Quintanilla, J. & Cywinski, R. Evidence for time-reversal symmetry breaking in the noncentrosymmetric superconductor LaNiC_2 . *Phys. Rev. Lett.* **102** (2009).
- [60] Shang, T., Pang, G. M., Baines, C., Jiang, W. B., Xie, W., Wang, A., Medarde, M., Pomjakushina, E., Shi, M., Mesot, J., Yuan, H. Q. & Shiroka, T. Nodeless superconductivity and time-reversal symmetry breaking in the noncentrosymmetric superconductor Re_{24}Ti . *Phys. Rev. B* **97** (2018).
- [61] Elvezio Morenzoni. Introduction to μSR Muon Spin Rotation/Relaxation. <https://www.psi.ch/sites/default/files/import/lmu/EducationLecturesEN/MuonSpinRotation-An-Introduction-print-em-2012.pdf> (2012).
- [62] Yaouanc, A. & de Reotier, P. D. *Muon Spin Rotation, Relaxation, and Resonance: Applications to Condensed Matter*, vol. 147, 1-504 of *International Series of Monographs on Physics* (Oxford University Press, 2010).
- [63] Prokofiev, A., Eisenmenger, C. & Lientsching, G. *Material Synthesis, Lectures at the Technical University of Vienna Nr. 138.065* (Technical University of Vienna, Institute of Solid State Physics, 2019).
- [64] Friedemann, S., Oeschler, N., Wirth, S., Krellner, C., Geibel, C., Steglich, F., Paschen, S., Kirchner, S. & Si, Q. Fermi-surface collapse and dynamical scaling near a quantum-critical point. *Proc. Natl. Acad. Sci. USA* **107**, 14547 (2010).
- [65] Custers, J., Lorenzer, K., Müller, M., Prokofiev, A., Sidorenko, A., Winkler, H., Strydom, A. M., Shimura, Y., Sakakibara, T., Yu, R., Si, Q. & Paschen, S. Destruction of the Kondo effect in the cubic heavy-fermion compound $\text{Ce}_3\text{Pd}_{20}\text{Si}_6$. *Nat. Mater.* **11**, 189 (2012).

REFERENCES

- [66] V. Martelli and A. Caib and E. M. Nicab and M. Taupin and, A. Prokofieva and C.-C. Liub and H.-H. Lai and, R. Yub and K. Ingersente and R. K uchler and A.M. Strydom and D. Geiger and J. Haenel and J. Larrea and Q. Si and S. Paschen. Sequential localization of a complex electron fluid. *Proc. Natl. Acad. Sci. USA* **116**, 17701 (2019).
- [67] Tsui, D. C., Stormer, H. L. & Gossard, A. C. Two-dimensional magneto-transport in the extreme quantum limit. *Phys. Rev. Lett.* **48**, 1559 (1982).
- [68] Nagaosa, N., Sinova, J., Onoda, S., MacDonald, A. H. & Ong, N. P. Anomalous Hall effect. *Rev. Mod. Phys.* **82**, 1539 (2010).
- [69] Ritz, R., Halder, M., Wagner, M., Franz, C., Bauer, A. & Pfeiderer, C. Formation of a topological non-Fermi liquid in MnSi. *Nature* **497**, 231 (2013).
- [70] Franz, C., Freimuth, F., Bauer, A., Ritz, R., Schnarr, C., Duvinag, C., Adams, T., Bl ugel, S., Rosch, A., Mokrousov, Y. & Pfeiderer, C. Real-Space and Reciprocal-Space Berry Phases in the Hall Effect of $\text{Mn}_{1-x}\text{Fe}_x\text{Si}$. *Phys. Rev. Lett* **112**, 186601 (2014).
- [71] Nakatsuji, S., Kiyohara, N. & Higo, T. Large anomalous Hall effect in a non-collinear antiferromagnet at room temperature. *Nature* **527**, 212 (2015).
- [72] Ueland, B., Mielea, C., Kato, Y., Ayala-Valenzuela, O., McDonald, R., Okazaki, R., Tobash, P., Torrez, M., Ronning, F., Movshovich, R., Fisk, Z., Bauer, E. D., Martin, I. & Thompson, J. D. Controllable chirality-induced geometrical hall effect in a frustrated highly correlated metal. *Nat. Commun.* **3**, 1067 (2012).
- [73] Casimir, H. B. G. On Onsager’s principle of microscopic reversibility. *Rev. Mod. Phys.* **17**, 343 (1945).

- [74] Eguchi, G. & Paschen, S. Robust scheme for magnetotransport analysis in topological insulators. *Phys. Rev. B* **99**, 165128 (2019).
- [75] Tafti, F. F., Gibson, Q., Kushwaha, S., Krizan, J. W., Haldolaarachchige, N. & Cava, R. J. Temperature-field phase diagram of extreme magnetoresistance. *Proc. Natl. Acad. Sci. U.S.A.* **113**, 25 (2016).
- [76] Fert, A. & Levy, P. M. Theory of the Hall effect in heavy-fermion compounds. *Phys. Rev. B* **36**, 1907 (1987).
- [77] Hundley, M. F., Malinowski, A., Pagliuso, P. G., Sarrao, J. L. & Thompson, J. D. Anomalous f -electron Hall effect in the heavy-fermion system $CeTIn_5$ ($T=Co, Ir, \text{ or } Rh$). *Phys. Rev. B* **7** (2004).
- [78] Yao, Y., Kleinman, L., MacDonald, A. H., Sinova, J., Jungwirth, T., sheng Wang, D., Wang, E. & Niu, Q. First Principles Calculation of Anomalous Hall Conductivity in Ferromagnetic bcc Fe. *Phys. Rev. Lett.* **92**, 037204 (2004).
- [79] Machida, Y., Nakatsuji, S., Onoda, S., Tayama, T. & Sakakibara, T. Time-reversal symmetry breaking and spontaneous Hall effect without magnetic dipole order. *Nature* **463**, 210 (2010).
- [80] Ashcroft, N. W. & Mermin, N. D. *Solid State Physics* (Saunders College Publishing, Fort Worth, ISBN 0-03-083993-9, 1976).
- [81] Hundley, M. F., Canfield, P. C., Thompson, J. D., Fisk, Z. & Lawrence, J. M. Hybridization gap in $Ce_3Bi_4Pt_3$. *Phys. Rev. B* **42**, 6842 (1990).
- [82] Hundley, M., Canfield, P., Thompson, J., Fisk, Z. & Lawrence, J. Evidence for a ‘coherence’ gap in $Ce_3Bi_4Pt_3$. *Physica B* **171**, 254 (1991).

REFERENCES

- [83] Hundley, M., Lacerda, A., Canfield, P., Thompson, J. & Fisk, Z. Magnetoresistance of the Kondo insulator $\text{Ce}_3\text{Bi}_4\text{Pt}_3$. *Physica B* **186-188**, 425 (1993).
- [84] Hundley, M. F., Thompson, J. D., Canfield, P. C. & Fisk, Z. Electronic transport in $\text{Ce}_3\text{Bi}_4\text{Pt}_3$: evidence for a temperature-dependent hybridization gap. *Physica B* **199-200**, 443 (1994).
- [85] Bucher, B., Schlesinger, Z., Canfield, P. C. & Fisk, Z. Kondo coupling induced charge gap in $\text{Ce}_3\text{Bi}_4\text{Pt}_3$. *Phys. Rev. Lett.* **72**, 522 (1994).
- [86] Reyes, A. P., Heffner, R. H., Canfield, P. C., Thompson, J. D. & Fisk, Z. ^{209}Bi NMR and NQR investigation of the small-gap semiconductor $\text{Ce}_3\text{Bi}_4\text{Pt}_3$. *Phys. Rev. B* **49**, 16321 (1994).
- [87] Kwei, G. H., Lawrence, J. M. & Canfield, P. C. Temperature dependence of the $4f$ occupation of $\text{Ce}_3\text{Bi}_4\text{Pt}_3$. *Phys. Rev. B* **49**, 14708 (1994).
- [88] Severing, A., Thompson, J. D., Canfield, P. C., Fisk, Z. & Riseborough, P. Gap in the magnetic excitation spectrum of $\text{Ce}_3\text{Bi}_4\text{Pt}_3$. *Phys. Rev. B* **44**, 6832 (1991).
- [89] Hundley, M. F., Canfield, P. C., Thompson, J. D. & Fisk, Z. Substitutional effects on the electronic transport of the Kondo semiconductor $\text{Ce}_3\text{Bi}_4\text{Pt}_3$. *Phys. Rev. B* **50**, 18142 (1994).
- [90] Cooley, J. C., Aronson, M. C. & Canfield, P. C. High pressures and the Kondo gap in $\text{Ce}_3\text{Bi}_4\text{Pt}_3$. *Phys. Rev. B* **55**, 7533 (1997).
- [91] Boebinger, G. S., Passner, A., Canfield, P. C. & Fisk, Z. Studies of the Kondo insulator $\text{Ce}_3\text{Bi}_4\text{Pt}_3$ in 61 T pulsed magnetic fields. *Physica B* **211**, 227 (1995).

- [92] Jaime, M., Movshovich, R., Stewart, G., Beyermann, W., Berisso, M., Hundley, M., Canfield, P. & Sarrao, J. Closing the spin gap in the Kondo insulator $\text{Ce}_3\text{Bi}_4\text{Pt}_3$ at high magnetic fields. *Nature* **405**, 160 (2000).
- [93] Mirrman, R. *Point Groups, Space Groups, Crystals, Molecules*, chap. III.5.a, 163 (World Scientific, 1999).
- [94] Grefe, S. E., Lai, H.-H., Paschen, S. & Si, Q. Weyl-Kondo semimetals in nonsymmorphic systems. *Phys. Rev. B* **101**, 075138 (2020).
- [95] Chang, P.-Y., Erten, O. & Coleman, P. Möbius Kondo insulators. *Nat. Phys.* **13**, 794 (2017).
- [96] Pietrus, T., Löhneysen, H. & Schlottmann, P. Kondo-hole conduction in the La-doped Kondo insulator $\text{Ce}_3\text{Bi}_4\text{Pt}_3$. *Phys. Rev. B* **77**, 115134 (2008).
- [97] Riseborough, P. S. Theory of the dynamic magnetic response of $\text{Ce}_3\text{Bi}_4\text{Pt}_4$: A heavy-fermion semiconductor. *Phys. Rev. B* **45**, 13984 (1992).
- [98] Wirth, S. & Steglich, F. Exploring heavy fermions from macroscopic to microscopic length scales. *Nat. Rev. Mater.* **1**, 16051 (2016).
- [99] Xiang, Z., Kasahara, Y., Asaba, T., Lawson, B., Tinsman, C., Chen, L., Sugimoto, K., Kawaguchi, S., Sato, Y., Li, G., Yao, S., Chen, Y. L., Iga, F., Singleton, J., Matsuda, Y. & Li, L. Quantum oscillations of electrical resistivity in an insulator. *Science* **362**, 65 (2019).
- [100] Sugiyama, K., Iga, F., Kasaya, M., Kasuya, T. & Date, M. Field-Induced Metallic State in YbB_{12} under High Magnetic Field. *J. Phys. Soc. Jpn.* **57**, 3946 (1988).

REFERENCES

- [101] Terashima, T. T., Matsuda, Y. H., Kohama, Y., Ikeda, A., Kondo, A., Kindo, K. & Iga, F. Magnetic-field-induced Kondo metal realized in YbB_{12} . *Phys. Rev. Lett.* **120**, 257206 (2018).
- [102] Cooley, J., Mielke, C., Hulst, V., Goettee, J., Honold, M., Modler, R., Lacerda, A., Rickel, D. & Smith, J. High field gap closure in the Kondo insulator SmB_6 . *J. Supercond.* **12**, 171 (1999).
- [103] Dzero, M., Sun, K., Galitski, V. & Coleman, P. Topological kondo insulators. *Phys. Rev. Lett.* **104**, 106408 (2010).
- [104] Dzero, M., Xia, J., Galitski, V. & Coleman, P. Topological Kondo insulators. *Annu. Rev. Condens. Matter Phys.* **7**, 249 (2016).
- [105] Feng, X.-Y., Dai, J., Chung, C.-H. & Si, Q. Competing topological and Kondo insulator phases on a honeycomb lattice. *Phys. Rev. Lett.* **111**, 016402 (2013).
- [106] Feng, X.-Y., Zhong, H., Dai, J. & Si, Q. Dirac-Kondo semimetals and topological Kondo insulators in the dilute carrier limit, arXiv:1605.02380 (2016).
- [107] Lai, H.-H., Grefe, S. E., Paschen, S. & Si, Q. Weyl-Kondo semimetal in heavy-fermion systems. *Proc. Natl. Acad. Sci. USA* **115**, 93–97 (2018).
- [108] Wakeham, N., Rosa, P. F. S., Wang, Y. Q., Kang, M., Fisk, Z., Ronning, F. & Thompson, J. D. Low-temperature conducting state in two candidate topological Kondo insulators: SmB_6 and $\text{Ce}_3\text{Bi}_4\text{Pt}_4$. *Phys. Rev. B* **94**, 035127 (2016).
- [109] Shanavas, K. V., Popović, Z. S. & Satpathy, S. Theoretical model for Rashba spin-orbit interaction in d electrons. *Phys. Rev. B* **90**, 165108 (2014).

- [110] Takeda, Y., Arita, M., Okamura, Y., Sato, H., Shimada, K., Mamiya, K., Namatame, H., Taniguchi, M., Katoh, K., Iga, F. & Takabatake, T. Low-Temperature High-Resolution Resonant Photoemission Study of Kondo Insulator $\text{Ce}_3\text{Bi}_4\text{Pt}_3$. *Jpn. J. Appl. Phys.* **38**, 209 (1999).
- [111] Nishigori, S., Goshima, H., Suzuki, T., Fujita, T., Nakamoto, G., Takabatake, T., Fujii, H. & Sakurai, J. Energy gap suppression by alloying in $\text{CeNi}_{1-x}\text{Pt}_x\text{Sn}$. *Physica B* **186 & 188**, 406 (1993).
- [112] Kasaya, M., Tani, T., Iga, F. & Kasuya, T. Electrical resistivity, Hall constant and magnetic susceptibility in the Kondo states $\text{Ce}(\text{Ni}_{1-x}\text{Pd}_x)\text{Sn}$ and YbNiSn . *J. Magn. Magn. Mater.* **76**, 278–280 (1988).
- [113] Katoh, K. & Kasaya, M. Magnetic and transport properties of $\text{Ce}_3\text{Au}_{3-x}\text{Pt}_x\text{Sb}_4$. *J. Phys. Soc. Jpn.* **65**, 3654 (1996).
- [114] Jones, C. D. W., Regan, K. A. & DiSalvo, F. J. $\text{Ce}_3\text{Cu}_x\text{Pt}_{3-x}\text{Sb}_4$: Modifying the properties of a Kondo insulator by substitutional doping. *Phys. Rev. B* **60**, 5282 (1999).
- [115] Schlottmann, P. Impurity bands in kondo insulators. *Phys. Rev. B* **46**, 998 (1992).
- [116] Harima, H. & Yanase, Y. private communications (2020).
- [117] Canfield, P. C. & Fisk, Z. Growth of single crystals from metallic fluxes. *Philos. Mag. B* **65**, 1117 (1992).
- [118] Goraus, J., Slebarski, A. & Fijalkowski, M. Experimental and theoretical study of CePdBi . *J. Phys. Condens. Matter* **25**, 176002 (2013).
- [119] Han, F., Wan, X., Phelan, D., Stoumpos, C. C., Sturza, M., Malliakas, C. D., Li, Q., Han, T.-H., Zhao, Q., Chung, D. Y. & Kanatzidis, M. G.

- Antiferromagnetic Kondo lattice in the layered compound $\text{CePd}_{1-x}\text{Bi}_2$ and comparison to the superconductor $\text{LaPd}_{1-x}\text{Bi}_2$. *Phys. Rev. B* **92**, 045112 (2015).
- [120] Hermes, W., Linsinger, S., Mishra, R. & Pöttgen, R. Structure and properties of $\text{Ce}_3\text{Pd}_3\text{Bi}_4$, CePdBi , and CePd_2Zn_3 . *Monatsh. Chem.* **139**, 1143 (2008).
- [121] Tomczak, J. M. Isoelectronic tuning of heavy fermion systems: Proposal to synthesize $\text{Ce}_3\text{Sb}_4\text{Pd}_3$. *Phys. Rev. B* **101**, 035116 (2020).
- [122] Cao, C., Zhi, G.-X. & Zhu, J.-X. From trivial Kondo insulator $\text{Ce}_3\text{Pt}_3\text{Bi}_4$ to topological nodal-line semimetal $\text{Ce}_3\text{Pd}_3\text{Bi}_4$. *Phys. Rev. Lett.* **124**, 166403 (2020).
- [123] v. Löhneysen, H., Rosch, A., Vojta, M. & Wölfle, P. Fermi-liquid instabilities at magnetic quantum critical points. *Rev. Mod. Phys.* **79**, 1015 (2007).
- [124] Si, Q. & Paschen, S. Quantum phase transitions in heavy fermion metals and Kondo insulators. *Phys. Status Solidi B* **250**, 425 (2013).
- [125] Luo, Y., Ronning, F., Wakeham, N., Lu, X., Park, T., Xu, Z.-A., & Thompson, J. D. Pressure-tuned quantum criticality in the antiferromagnetic Kondo semimetal $\text{CeNi}_{2-\delta}\text{As}_2$. *Proc. Natl. Acad. Sci.* **112**, 13520 (2015).
- [126] Tomczak, J. M. Thermoelectricity in correlated narrow-gap semiconductors. *J. Phys.: Condens. Matter* **30**, 183001 (2018).
- [127] Mondal, M., Joshi, B., and Anand Kamlapure, S. K., Ganguli, S. C., Thamizhavel, A., Mandal, S. S., Ramakrishnan, S. & Raychaudhuri, P. Andreev bound state and multiple energy gaps in the noncentrosymmetric superconductor BiPd . *Phys. Rev. B* **86**, 094520 (2012).

- [128] H. Wei and S.-P. Chao and V. Aji. Long-range interaction induced phases in Weyl semimetals. *Phys. Rev. B* **89** (2014).
- [129] Berton, A., Chaussy, J., Chouteau, G., Cornut, B., Flouquet, J., Odin, J., Palleau, J., Peyrard, J. & Tournier, R. Magnetization and specific heat of abnormal cerium compounds. *J. Phys. Colloq.* **40**, 326 (1979).
- [130] Cornelius, A. L., Pagliuso, P. G., Hundley, M. F. & Sarrao, J. L. Field-induced magnetic transitions in the quasi-two-dimensional heavy-fermion antiferromagnets Ce_nRhIn_{3n+2} ($n = 1$ or 2). *Phys. Rev. B* **64**, 144411 (2001).
- [131] Deonaraine, S. & Joshua, S. J. Magnetic Field Effects on the Spin Wave Spectra and Magnon Specific Heat of Antiferromagnetic NtF_2 . *Phys. Stat. Solidi B* **57**, 767 (1973).
- [132] Maple, M. B., Butch, N. P., Frederick, N. A., Ho, P.-C., Jeffries, J. R., Saylesa, T. A., Yanagisawa, T., Yuhasz, W. M., Chi, S., Kang, H. J., Lynn, J. W., Dai, P., McCall, S. K., McElfresh, M. W., Fluss, M. J., Henkie, Z. & Pietraszko, A. Field-dependent ordered phases and Kondo phenomena in the filled skutterudite compound $PrOs_4As_{12}$. *Proc. Natl. Acad. Sci. USA* **103**, 6783 (2006).
- [133] Desranges, H.-U. & Schotte, K. D. Specific heat of the Kondo model. *Phys. Lett. A* **91**, 240 (1982).
- [134] Singh, Y. P., Haney, D. J., Huang, X. Y., Lum, I. K., White, B. D., Dzero, M., Maple, M. B. & Almasan, C. C. From local moment to mixed-valence regime in $Ce_{1-x}Yb_xCoIn_5$ alloys. *Phys. Rev. B* **89**, 115106 (2014).
- [135] Schlottmann, P. Bethe-Ansatz solution of the ground-state of the $SU(2j+1)$ Kondo (Coqblin-Schrieffer) model: Magnetization, magnetoresistance and universality. *Z. Phys. B* **51**, 223 (1983).

REFERENCES

- [136] C. Petrovic and P. G. Pagliuso and M. F. Hundley and R. Movshovich and J. L. Sarrao and J. D. Thompson and Z. Fisk and P. Monthoux. Heavy-fermion superconductivity in CeCoIn₅ at 2.3 K. *J. Phys. Condens. Mater.* **13**, 337 (2001).
- [137] Dzsaber, S., Yan, X., and Gaku Eguchi, M. T., Prokofiev, A., Shiroka, T., Blaha, P., Rubel, O., Grefe, S. E., Lai, H.-H., Si, Q. & Paschen, S. Giant spontaneous Hall effect in a nonmagnetic Weyl-Kondo semimetal. *arXiv:1811.02819* (2019).
- [138] P. Blaha, *et al.* Wien2k, an augmented plane wave plus local orbital program for calculating the crystal properties. *TU Vienna*, <http://www.wien2k.at>, Austria (2018).
- [139] Perdew, J. P., Burke, K. & Ernzerhof, M. Generalized gradient approximation made simple. *Phys. Rev. Lett.* **77**, 3865 (1996).
- [140] Ahmed, S. J., Kivinen, J., Zaporzan, B., Curiel, L., Pichardo, S. & Rubel, O. BerryPI: A software for studying polarization of crystalline solids with WIEN2k density functional all-electron package. *Comput. Phys. Commun.* **184**, 647 (2013).
- [141] Ma, Q., Xu, S.-Y., Shen, H., MacNeill, D., Fatemi, V., Chang, T.-R., Mier Valdivia, A. M., Wu, S., Du, Z., Hsu, C.-H., Fang, S., Gibson, Q. D., Watanabe, K., Taniguchi, T., Cava, R. J., Kaxiras, E., Lu, H.-Z., Lin, H., Fu, L., Gedik, N. & Jarillo-Herrero, P. Observation of the nonlinear Hall effect under time-reversal-symmetric conditions. *Nature* **565**, 337 (2019).
- [142] Kang, K., Li, T., Sohn, E., Shan, J. & Mak, K. F. Nonlinear anomalous Hall effect in few-layer WTe₂. *Nat. Mater.* **18**, 324 (2019).

- [143] Tokura, Y. & Nagaosa, N. Orbital physics in transition-metal oxides. *Science* **288**, 462 (2000).
- [144] Si, Q. & Steglich, F. Heavy fermions and quantum phase transitions. *Science* **329**, 1161 (2010).
- [145] Keimer, B., Kivelson, S. A., Norman, M. R., Uchida, S. & Zaanen, J. From quantum matter to high-temperature superconductivity in copper oxides. *Nature* **518**, 179 (2015).
- [146] Mathur, N., Grosche, F., Julian, S., Walker, I., Freye, D., Haselwimmer, R. & Lonzarich, G. Magnetically mediated superconductivity in heavy fermion compounds. *Nature* **394**, 39 (1998).
- [147] D. J. Scalapino. A common thread: The pairing interaction for unconventional superconductors. *Rev. Mod. Phys.* **84**, 1383 (2012).
- [148] Kuo, H.-H., Chu, J.-H., Palmstrom, J. C., Kivelson, S. A. & Fisher, I. R. Ubiquitous signatures of nematic quantum criticality in optimally doped Fe-based superconductors. *Science* **352**, 958 (2016).
- [149] B. Michon and C. Girod and S. Badoux and J. Kačmarčík and Q. Ma and M. Dragomir and H. A. Dabkowska and B. D. Gaulin and J.-S. Zhou and S. Pyon and T. Takayama and H. Takagi and S. Verret and N. Doiron-Leyraud. Thermodynamic signatures of quantum criticality in cuprate superconductors. *Nature* **567**, 218 (2019).
- [150] A. B. Pippard. *Magnetoresistance in Metals* (Cambridge University Press, 1989).

REFERENCES

- [151] Kadowaki, K. & Woods, S. B. Universal relationship of the resistivity and specific heat in heavy-fermion compounds. *Solid State Commun.* **58**, 507 (1986).
- [152] R. Daou and N. Doiron-Leyraud and D. LeBoeuf and S. Y. Li and F. Laliberté and O. Cyr-Choinière and Y. J. Jo and L. Balicas and J.-Q. Yan and J.-S. Zhou and J. B. Goodenough. Linear temperature dependence of resistivity and change in the Fermi surface at the pseudogap critical point of a high- T_c superconductor. *Nat. Phys.* **5**, 31 (2009).
- [153] S. Kasahara and T. Shibauchi and K. Hashimoto and K. Ikada and S. Tonegawa and R. Okazaki and H. Shishido and H. Ikeda and H. Takeya and K. Hirata and T. Terashima and Y. Matsuda. Evolution from non-Fermi- to Fermi-liquid transport via isovalent doping in $\text{BaFe}_2(\text{As}_{1-x}\text{P}_x)_2$ superconductors. *Phys. Rev. B.* **81**, 184519 (2010).
- [154] Friedemann, S., Westerkamp, T., Brando, M., Oeschler, N., Wirth, S., Gegenwart, P., Krellner, C., Geibel, C. & Steglich, F. Detaching the anti-ferromagnetic quantum critical point from the Fermi-surface reconstruction in YbRh_2Si_2 . *Nat. Phys.* **5**, 465–469 (2009).
- [155] Arushanov, E., Kloc, C., Hohl, H. & Bucher, E. The Hall effect in $\beta\text{-FeSi}_2$ single crystals. *J. Appl. Phys.* **75**, 5106 (1994).
- [156] O’Handley, R. C. *Hall effect formulae and units*, 417–419 (Plenum Press, New York, 1980).
- [157] Kushwaha, S. K., Chan, M. K., Park, J., Thomas, S. M., Bauer, E. D., Thompson, J. D., Ronning, F., Rosa, P. F. S. & Harrison, N. Magnetic field-tuned Fermi liquid in a Kondo insulator. *Nat. Commun.* **10**, 5487 (2019).

- [158] Michelutti, B. & Morin, P. Paramagnetic torque in cubic rare-earth compounds. *Phys. Rev. B* **46**, 14213 (1992).
- [159] Gabáni, S., Bauer, E., Berger, S., Flachbart, K., Paderno, Y., Paul, C., Pavlík, V. & Shitsevalova, N. Pressure-induced Fermi-liquid behavior in the Kondo insulator SmB_6 : Possible transition through a quantum critical point. *Phys. Rev. B* **67**, 172406 (2003).
- [160] Y. Zhou and Q. Wu and P.F. Rosa and R. Yu and J. Guo and W. Yi and S. Zhang and Z. Wang and H. Wang and S. Cai and K. Yang and A. Li and Z. Jiang and S. Zhang and X. Wei and Y. Huang and P. Sun and Feng Yang and Z. Fisk and Q. Si and Z. Zhao and L. Sun. Quantum phase transition and destruction of Kondo effect in pressurized SmB_6 . *Science Bulletin* **62**, 1439–1444 (2017).